# Development and application of methods for out-of-equilibrium quantum many-body systems

A Thesis
Submitted for the Degree of
**Doctor of Philosophy**
in the Faculty of Science

by

**Anirudha Mirmira**

JNCASR

THEORETICAL SCIENCES UNIT
JAWAHARLAL NEHRU CENTRE FOR ADVANCED SCIENTIFIC RESEARCH
Bangalore – 560 064

AUGUST 2023

## DECLARATION

I hereby declare that the matter embodied in the thesis entitled **"Development and application of methods for out-of-equilibrium quantum many-body systems"** is the result of investigations carried out by me at the Theoretical Sciences Unit, Jawaharlal Nehru Centre for Advanced Scientific Research, Bangalore, India under the supervision of Prof. N. S. Vidhyadhiraja and that it has not been submitted elsewhere for the award of any degree or diploma.

In keeping with the general practice in reporting scientific observations, due acknowledgement has been made whenever the work described is based on the findings of other investigators.

Anirudha Mirmira

# CERTIFICATE

I hereby certify that the matter embodied in this thesis entitled **"Development and application of methods for out-of-equilibrium quantum many-body systems"** has been carried out by Mr. Anirudha Mirmira at the Theoretical Sciences Unit, Jawaharlal Nehru Centre for Advanced Scientific Research, Bangalore, India under my supervision and that it has not been submitted elsewhere for the award of any degree or diploma.

Prof. N. S. Vidhyadhiraja
(Research Supervisor)

# Acknowledgements

It is often said that you take up parts of your thesis advisor's attitudes to research and to life in general. If that is indeed so, I couldn't have asked for a better person than Prof. N.S. Vidhyadhiraja to be my thesis advisor. As all of his students would attest, the academic freedom he gives and the rigour in his formulation of scientific questions is almost superlative. This accompanied by his calm and reassuring demeanour has ensured that all my discussions with him were motivating and stimulating. I'm grateful for his scientific acuity and willingness to get his hands dirty.

Joining the centre as a wide-eyed, inexperienced graduate student, I am thankful for the courses by Prof. Swapan Pati, Prof. Subir K Das, Prof. Balasubramanian S, Prof. A. Chakraborti, Prof. Rajesh Ganapathy, Prof. Srikanth Sastry, Prof. Chandrabhas Narayana, Prof. N.S. Vidhyadhiraja, Prof. Ranjan Dutta, Prof. Umesh Waghmare, Prof. Shivaprasad S.M. at the centre and Prof. Vijay Shenoy and Prof. Sachindeo Vaidya at IISc. Their courses not only armed me with the required knowledge but also the attitude required to approach my research problem. I'm also thankful to Prof. Subir K Das and Prof. N.S. Vidhyadhiraja for their guidance during my winter and summer projects in their groups respectively.

I have had the opportunity to learn from some of the most competent and dedicated members of the strongly-correlated electron systems group including Dr Nagamalleswara Rao Dasari, Dr Sudeshna Sen, Dr Rukhsan Ul Haq, Dr Wasim Raja Mondal, Vinayak Kulkarni, Gurshidali P, Gunjan Sharma and Aashish Kumar. Thanks are also due to Syam Sadan and Chakradhar Rangi, who were my mentees as part of their summer projects for the wide-ranging and intense discussions we had.

It has been my good fortune to come across and discuss my work with some of the keenest minds in condensed matter physics like Prof. Mark Jarell, Prof. David Logan, Prof. Krishnendu Sengupta, Dr Hanna Terletska, Dr Arijit Dutta, Dr Sudeshna Sen, and Dr Wasim Raja Mondal, each of whom has given invaluable inputs and contributed to a better understanding of condensed matter physics and research problems both included in and excluded from the thesis.

I am thankful for the great atmosphere and camaraderie in the theoretical sciences unit, possible only due to the attitudes and dedication of each of its members. In particular, the TSU seminars, the unit day, and the trip to Sakleshpur have been memorable. Thanks in particular to Prof. Shobhana Narasimhan for her crossword puzzles and Prof. Subir Das' humour, which I've always looked forward to.

A great initiative by the centre has been the student mentorship programme and I'm grateful for the opportunity to be a part of this noble outreach endeavour. I'm thankful to Dr Indumati Rao for her guidance and Mr Praveen, and Mr Vinayak Pattar for their dedication and enthusiasm. I'm also thankful to Dr Arun K, Dr Shivaram Kubakaddi, Dr Rajendra Kumar, Dheemahi and Anjali Gaur for their dedication and patience in mentoring the participants.

The small community of students in the centre has allowed me to interact and make friends from a wide variety of subjects, backgrounds and attitudes. I'm especially thankful for the whole range of experiences I have had as a part of this community both as a participant and in organising activities. I'm thankful to the quiz club members Dr Arun Panchapakesan, Rutvij Kulkarni, Riddhimoy Pathak and Jayendra Singh for their support and hard work in organising quizzes.

I am grateful to Dr Asutosh Bellur, Dr Chakradhar (Chakri), Dr Aditya Mahadevan and Shaurya Kaushal, who were my mentors, ride/run partners, and friends on my athletic journey. They have been beacons of motivation and great sources of knowledge. I'm also thankful to Karthik sir and Manjunath sir at Swimlife who taught me how to swim well. Thanks in particular to Asutosh for not only getting me to start on this journey but being invested in me through thick and thin, both figuratively and literally.

Dungeons & Dragons has been a source of great fun and solace and I'm grateful to Azog the scarlet hunter (Dr Prateek Anand), Soggoth the herald of Celephaïs, (Srikant Venkitachalam) and Drayk (Rutvij Kulkarni) for their wonderful roleplay and keeping me on my toes. I'm thankful to Matt Colville and his videos on running the game for getting me into the hobby.

I've had the opportunity to make some of the finest memories through my PhD journey thanks to my good friends. In particular, Arun Panchapakesan, Neelakshi Varma and Srikant Venkitachalam have been fast friends from the very beginning of my time in the centre and have inspired, entertained and comforted me in more ways than I can express. Asutosh Bellur has been a source of motivation and his incredible open-mindedness has allowed me to explore parts of myself I would have never had otherwise. I'm grateful to Wasim Mondal and Gurshidali for their friendship and as travel companions.

I'm thankful to the past and present members of HIV Lab and HB Lab who considered me an honorary group member and included me in many of their group outings and activities. I'm thankful also for the small campus for allowing me an opportunity to interact and become friends with a whole bunch of people, which would take too long to list.

Coming to the campus, the centre has been a great place to get on with my research thanks to its wonderfully maintained environment and the availability of good coffee. Thanks are due to the staff of the Hostel, Dining Hall, and Utility for providing the facilities to nourish both the body and mind. Thanks to the staff of the Academic and administration departments who make paperwork seem almost effortless. I'm grateful to the Security and Gardening departments for taking such good care of the campus. I'm thankful to JNCASR for being the place where I've had some of the very best experiences of my life.

I wouldn't be here today if not for the efforts and encouragement from Madhusudhan sir, the HV sir and KMR sir. I'm eternally grateful to them for building up my skills and inculcating a passion for scientific research. I'm also thankful to the REAP Programme organised by the Jawaharlal Nehru Planetarium for exposure to scientific research and the various opportunities to learn about physics, both the subject and philosophy behind it.

I'm thankful to have found a friend like Pragya Sharma, who has not only been a great source of joy and comfort but has also been an inspiration in her organisation and critical thinking skills. I wholeheartedly thank Amma and Anna, my parents, for encouraging my curiosity and providing me with the best atmosphere and opportunities.

# List of Publications

- Mirmira, A., & Vidhyadhiraja, N. S., “Steady-state dc transport through an Anderson impurity coupled to leads with spin-orbit coupling”. Physical Review B, **107**(8), 085107 (2023).
- Mirmira, A., & Vidhyadhiraja, N. S., “Exact time evolution of Kitaev chain subjected to temporal noise”. *Manuscript under preparation*

# Synopsis

In this thesis, we have looked at the development and application of both computational and analytical methods to study quantum many-body systems out of equilibrium. The thesis consists of six chapters and two appendices.

In Chapter 1, we introduce and motivate the subject matter of the thesis from both the phenomenological and method aspects. In Chapter 2, we implement the steady-state Keldysh second order perturbation theory (KPT2) and study the transport through a quantum dot connected to leads with spin-orbit coupling (SOC) with a DC bias. In Chapter 3, we look at the effect of valence fluctuations which arise through the gate voltage of the quantum dot connected to leads with SOC by applying the steady-state interpolative approximation (SSIPA). In Chapter 4, we develop the steady-state local moment (SSLMA) approach by generalizing the LMA out of equilibrium. In Chapter 5, we implement and use the transfer matrix method to study the effect of piecewise constant driving protocols on the topology and dynamical quantum phase transitions in the Kitaev chain. In Chapter 6, we derive the time-dependent projection operator method to obtain the effective Kondo Hamiltonian of a single impurity Anderson model (SIAM). We summarise and conclude in Chapter 7. The appendices consist of an introduction to the Keldysh field-theoretic method and the detailed calculation of the second-order self energies used in chapters 2 and 3.

Chapter 1 is an introduction to quantum many-body systems out of equilibrium. We begin with the motivation for studying such systems including the applicability to a wide variety of systems and the possibility of novel phases of matter not present in equilibrium. We next move to phenomenology and explain the general differences between equilibrium and non-equilibrium quantum many-body systems with a detailed look at some experimental results. The third section of the chapter deals with the extant methods and the motivates the need for development of methods in the thesis. We conclude with an overview of the structure of the thesis.

In Chapter 2, we implement the KPT2 method to the SIAM coupled to leads with SOC. We begin with extensive benchmarking of the method in both equilibrium and out of equilibrium. Next, we study the scaling and universality in the linear response regime of the system. The system has two parameter regimes viz. a weak-intermediate coupling and strong coupling regimes. We calculate the spectral function and conductance in both these regimes and are able to explain the experimental observations in an equivalent system.

In Chapter 3, we apply the SSIPA method to the system considered is in Chapter 2 along with a gate-voltage applied on the quantum dot. This takes the system away from the particle-hole symmetric limit and controls the cost for valence fluctuations. We evaluate the IPA ansatz self-consistently and derive the self-energy. This is followed by evaluation of the current and the details of the numerical implementation. We conclude with the results including benchmarks and the effect of particle-hole asymmetry both in equilibrium and when a DC bias is applied across the leads.

Chapter 4 deals with the development of the SSLMA method which is a generalization of the equilibrium LMA, and its application to the steady-state SIAM. The formalism of the method is presented followed by some analytical limits of the theory and details of the numerical implementation. The method is extensively benchmarked in both zero and finite temperatures with the equilibrium results. Some results concerning the transport and universality calculated by the application of the method are also presented.

In Chapter 5, the transfer matrix method has been used to study the effect of piecewise constant driving in the Kitaev chain. The chapter firstly deals with the details of the Kitaev chain, including the topological phase diagram and the general form of the ground state. This is followed by a derivation of the transfer matrices for the square wave, noise and quench driving protocols. The definition of the Loschmidt echo and characterization of dynamical quantum phase transitions follows. In the last part, the results including benchmarking and for the three driving protocols are presented.

Chapter 6 involves the derivation and application of the time-dependent projection operator method (TDPOM) to the driven SIAM. We begin with the derivation of the TDPOM in the general case and use it to calculate the effective Hamiltonian of the driven SIAM. In particular, we consider the case of sinusoidal driving and look at the effect of driving on the nature of the emergent Kondo model and calculate the time-dependent Kondo coupling. We look at the dependence of the Kondo coupling on the parameters of the driving in the $U = \infty$ limit and at specific values.

Chapter 7 consists of the summary of the thesis and concludes with the major findings of all the chapters. We also look at the future outlook.

# List of Figures

# List of Tables

# Contents

# Chapter 1

# Out-of-Equilibrium: Phenomenology and Methods

## 1.1 Motivation

While it has been almost a century since the time-dependent Schrödinger equation was proposed, the field of non-equilibrium quantum physics is still in its nascency with multiple groups exploring a wide variety of systems with even more fundamental questions remaining unresolved definitively. Non-equilibrium quantum phenomena are ubiquitous from nuclear particle physics, to both Fermionic and Bosonic condensed matter physics, all the way up to early universe cosmology[1]. In particular, many-body quantum systems are all the more ubiquitous since most realistic systems involve interaction or correlation between their constituent particles.

Non-equilibrium many-body quantum physics not only makes an appearance in all sorts of phenomena across time, energy and length scales but also leads to novel phases of matter not present in or near equilibrium. Given the ubiquity, these phenomena have naturally seen much sustained interest from both the theoretical and experimental quarters. In particular, recent experimental methods like optical lattices[2], quantum point contacts[3], ultrafast spectroscopy[4], etc. have opened new avenues for exploration. These phenomena are not just of interest to the academic but also have a large number of applications in diverse fields like spintronics, quantum information, heat/charge transport in electronic devices, etc.

## 1.2 Phenomenology

A question which immediately arises when one begins research into non-equilibrium quantum phenomena is: *what are the general differences between equilibrium and non-equilibrium systems?* While the question can be answered in a large number of ways with varying levels of detail, let us consider a few phenomena which will make the answer a bit more apparent. The first phenomenon of interest would be the origin of irreversibility out of equilibrium, given that the microscopic laws that govern the systems are time-reversal symmetric. Another phenomenon is the non-ergodicity of systems out of equilibrium compared to their equilibrium counterparts. A defining feature of non-equilibrium systems is the presence of particle and/or energy currents either within the system (closed systems) or with external baths (open systems). Non-equilibrium systems can also vary from equilibrium due to the presence of noise, fluctuation and other such stochastic processes.

Each of the phenomena considered above leads to a class of systems and correspondingly a class of methods to solve the said systems. While the general comparison is fruitful, non-equilibrium systems also allow for specific novel phenomena which do not have any equilibrium counterparts. Consider the prototypical example of a quantum dot connected to leads across which a source-drain bias has been applied and is subject to a split-gate voltage. While a detailed analysis of this model is carried out in chapters 2 and 3, the experimental findings in quantum point contacts (QPCs) in heterostructures like $LaAlO_3/SrTiO_3$ see the presence of both integer and half-integer quantization in the conductance in units of $2e^2/h$. This is seen in Fig. 1.1 and the presence of half-integer plateaus is only possible out of equilibrium when the source-drain bias is finite.

Another possibility is the emergence of new phases which have no equilibrium counterparts when systems are subjected to driving. A great example of such a phenomenon is the observation of time crystals. Both discrete[6] and continuous time crystals[7] have been experimentally observed when systems are subject to specific driving protocols. In particular, driving a chain of Yb atoms with inter-atomic coupling as seen in Fig. 1.2 in a tripartite periodic protocol which involved a global rotation, interaction and disordered parts, resulted in a discrete time crystal. This was characterized by the magnetizations of each of the individual ions getting locked into the sub-harmonic response, i.e. the peak of the Fourier transform of the time-dependent magnetizations is at $\omega/2$, where $\omega$ is the driving frequency.

Thus depending on the system under consideration, the phenomenology

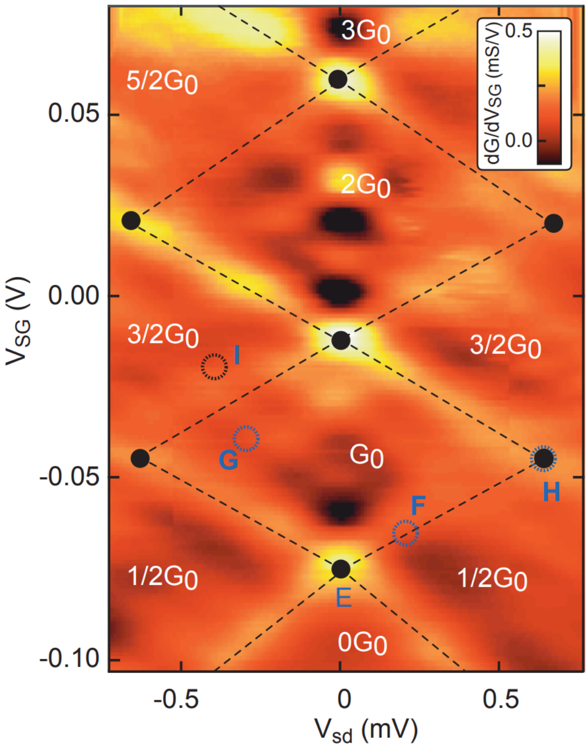

Figure 1.1: The differential conductance plotted as a colour map with varying source-drain voltage $V_{\rm sd}$ and split-gate voltage $V_{\rm sg}$ for the LaAlO$_3$/SrTiO$_3$ quantum point contacts. Notice the integer quantization of conductance (in units of $G_0 = 2e^2/h$) in the $V_{sd} = 0$ case and the appearance of half-integer plateaus when $V_{sd} \neq 0$. Figure taken from A. Jouan et al.[5]

would involve getting an accurate theoretical description of various quantities like current and conductance (for transport) or time-evolved states and effective Hamiltonians (for novel phases), etc. Each such quantity is best calculated using one of the various methods that exist to study systems out of equilibrium.

## 1.3 Methods

Let us now focus on the theoretical methods to study quantum systems out of equilibrium. In trying to study non-equilibrium systems, we see that the familiar aspects like fluctuation-dissipation theorem, time-reversal symmetry, conservation laws, Luttinger theorem, Ward identity, Gell-Mann Low theorem, Wick's theorem, etc. are either absent or need to be modified to a

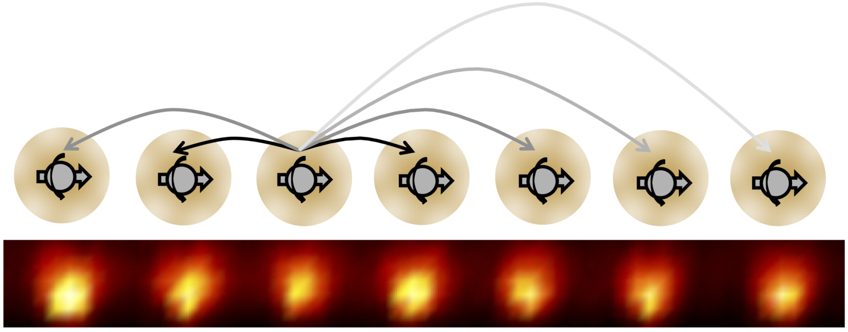

Figure 1.2: A discrete time crystal was observed by J. Zhang et al.[6] in a Yb spin chain (shown in the bottom) with interatomic interactions as shown (top part) when subject to a tripartite periodic driving protocol. The time crystal was characterized by a sub-harmonic response in the individual magnetizations of the ions. Image taken from Prof. N. Yao's research page

large extent. Thus, generalising equilibrium methods to non-equilibrium is a non-trivial task and hence has seen sustained interest across the fields of condensed matter physics, nuclear physics, atomic physics, high energy physics and cosmology. The challenges in the generalization of equilibrium methods have also led to a lack of definitive conclusions and a lack of consensus in the resolution of many fundamental questions.

For example, unlike in equilibrium, where the methods of Bethe ansatz and numerical renormalization group (NRG) act as benchmarks in the study of Kondo physics, there have not been any such defining methods in the case of non-equilibrium. Even the generalizations of the Bethe ansatz[8] and NRG[9] to out-of-equilibrium systems have their limitations either in the ability to capture all the energy scales or in computational limits due to the exponentially growing density matrices. While quite a bit of progress has been made in the steady-state case, the time-dependent driving is even more difficult to tackle due to the increased size of matrices required or in the case of Floquet theory[10], to truncate the Magnus expansion to $\mathcal{O}(\Omega^{-1})$ terms. Accounting for interactions in the Floquet method is especially hard due to the occurrence of higher-order terms in the Magnus expansion.

Another class of methods which allows access to both closed and open systems are the methods based on the quantum kinetic equations or Boltzmann transport. While these methods capture the relaxation to a thermal state, they involve weak-coupling perturbation in addition to a semi-classical approximation or a gradient expansion[11]. Thus it is the need of the hour for the development of novel methods to study even simple non-equilibrium systems.

## 1.4 Outline of the thesis

While the plethora of methods which already exist to study non-equilibrium quantum systems may seem more than sufficient at first glance, the shortcomings of each method warrant the development of novel methods which can tackle at least some of these shortcomings. In this thesis, we develop and apply methods to study transport, the effect of driving on topology, noise and emergent effective Hamiltonians.

In chapter 2, we numerically implement and apply the steady-state interpolative approximation[12] (ssIPA) to study transport through a quantum dot coupled to leads with spin-orbit coupling across which a DC bias is applied. The system described above is generalized to include valence fluctuations through the means of a gate voltage in chapter 3 and requires a modification to the ssIPA ansatz. Chapter 4 deals with the generalization of the local moment approach[13] (LMA), a very successful and inexpensive method in equilibrium to study steady-state transport in the single impurity Anderson model (SIAM). We change gears in chapter 5 where we implement the Transfer Matrix method[14] to study the effect of piecewise constant driving (including square-wave driving, noise and quenches) on the topology of the Kitaev chain[15]. In chapter 6, we derive the time-dependent effective Hamiltonian for the SIAM subject to sinusoidal driving using a generalization of the projection operator method to nonequilibrium.

# Bibliography

[1] E. A. Calzetta and B.-L. B. Hu, *Nonequilibrium quantum field theory* (Cambridge University Press, 2009).

[2] M. Lewenstein, A. Sanpera, V. Ahufinger, B. Damski, A. Sen(De), and U. Sen, Advances in Physics **56**, 243 (2007).

[3] H. van Houten and C. Beenakker, Physics Today **49**, 22 (1996).

[4] A. Zong, B. R. Nebgen, S.-C. Lin, J. A. Spies, and M. Zuerch, Nature Reviews Materials **8**, 224 (2023).

[5] A. Jouan, G. Singh, E. Lesne, D. C. Vaz, M. Bibes, A. Barthélémy, C. Ulysse, D. Stornaiuolo, M. Salluzzo, S. Hurand, J. Lesueur, C. Feuillet-Palma, and N. Bergeal, Nature Electronics **3**, 201 (2020).

[6] J. Zhang, P. W. Hess, A. Kyprianidis, P. Becker, A. Lee, J. Smith, G. Pagano, I.-D. Potirniche, A. C. Potter, A. Vishwanath, N. Y. Yao, and C. Monroe, Nature **543**, 217 (2017).

[7] P. Kongkhambut, J. Skulte, L. Mathey, J. G. Cosme, A. Hemmerich, and H. Keßler, Science **377**, 670 (2022).

[8] P. Mehta and N. Andrei, Phys. Rev. Lett. **96**, 216802 (2006).

[9] F. Schwarz, I. Weymann, J. von Delft, and A. Weichselbaum, Phys. Rev. Lett. **121**, 137702 (2018).

[10] M. Bukov, L. D'Alessio, and A. Polkovnikov, Advances in Physics **64**, 139 (2015).

[11] H. Aoki, N. Tsuji, M. Eckstein, M. Kollar, T. Oka, and P. Werner, Rev. Mod. Phys. **86**, 779 (2014).

[12] A. A. Aligia, Phys. Rev. B **74**, 155125 (2006).

[13] D. E. Logan, M. P. Eastwood, and M. A. Tusch, Journal of Physics: Condensed Matter **10**, 2673 (1998).

[14] D. Nghiem and R. Joynt, Phys. Rev. A **73**, 032333 (2006).

[15] A. Y. Kitaev, Physics-Uspekhi **44**, 131 (2001).

# Chapter 2

# Steady-state dc transport through an Anderson impurity coupled to leads with spin-orbit coupling

## 2.1 Introduction

The Kondo effect and its interplay with bias in the leads is a rich and well-studied problem. This non-equilibrium Kondo effect has been observed in a wide variety of systems such as quantum dots[1–3], molecular systems[4;5], carbon nano tubes[6–9], and quantum point contacts[10–14]. Correspondingly, experiments also observe a wide range of phenomena in these systems such as quantum interference[15], spin-selective transport[16], etc. The single impurity Anderson model (SIAM) has been the standard paradigm for modelling such systems both in and out of equilibrium. The SIAM in equilibrium has been studied extensively using methods such as the Bethe ansatz[17] and numerical renormalization group[18;19].

In recent years, a whole range of theoretical methods has been developed and used to study Kondo systems out of equilibrium. However, unlike in the case of equilibrium, where a reasonable consensus has been achieved, the physics of nonequilibrium interacting systems is still under debate. In the case of the SIAM, the splitting of the Kondo peaks, the effects of magnetic field and spin-orbit coupling (SOC) on the Kondo effect, and the effects of bias and temperature have been studied using various methods such as numerical renormalization group[20–23], non-crossing approximation[24], perturbative methods[25–27], quantum Monte Carlo methods[28], exact diagonalization methods[29], Bethe ansatz[30], hierarchical equation of motion[31] and master equation approaches[32] among many others.

SOC is an important parameter, and is well known to be an integral aspect of exotic materials such as topological insulators, and topological magnets and is useful in many spintronics applications. Quantum dot systems have been studied both with SOC on the dot and with SOC in the leads. Experiments with the SOC on the dot include directly measuring the SOC in two-atom quantum dots[33], the observation of an anomalous Josephson current[34], and controlling the SOC using magnetic field direction[35] among many others. The case with SOC in the leads has also been studied with phenomena such as the gate voltage tunability of SOC[14;36], magnetotransport[37], etc. having been observed.

In equilibrium, the effect of the SOC on the Kondo resonance has been theoretically studied in detail[38–40]. A driven quantum dot, coupled to normal metallic leads, with SOC on the dot has been investigated using the finite-$U$ slave boson method[41] and the findings show that the Rashba spin-orbit coupling (RSOC) introduces new conductance peaks next to the Kondo peak while suppressing the Kondo peak. Quantum wire systems have also been studied and interesting observations, such as the destruction of spin accumulation due to an impurity[42] and multichannel effects[43] have been made. A quantum dot connected to a nanoribbon with SOC has also been studied using the Hubbard III approximation[26].

A powerful tool in experimentally studying the effect of bias on quantum systems is the paradigm of quantum point contacts (QPCs). QPCs are realized by constricting a two-dimensional (2D) electron gas between contacts which have a source-drain and gate voltage applied. Multiple experiments on QPCs have observed quantized conductance along with some well-known anomalies[44–46]. Recent experiments in systems with quantum point contacts have also seen the interplay of SOC and Kondo physics. In particular, Smith *et al.*[14], have realized a QPC setup where they can tune the SOC and have observed a two-peak conductance in the large SOC regime along with an increase in the zero bias conductance (ZBC) with temperature.

In this chapter, we study the interplay between Rashba spin-orbit coupling on the leads, a constant bias and interactions on the steady-state dc transport through a quantum dot system. As mentioned before, the effect of Rashba SOC in the leads on the Kondo effect in equilibrium has received significant attention[38–40]. When subjected to a dc bias, the studied system will be out of equilibrium and the interplay of bias and SOC in the leads becomes an important consideration. We employ the interpolative approximation(IPA)[47] , which reduces in the particle-hole (p-h) symmetric limit to the Keldysh second-order perturbative theory (KPT2), to investigate transport through the dot with Rashba SOC on normal metallic two-dimensional leads. Since the method is approximate, we begin with a benchmarking of the method against exact methods such as the time-evolving block decimation (TEBD)[29] and identify the regimes within which the results from KPT2 are reliable. We have investigated the effect of SOC on (i) universality and scaling in the linear response regime and, subsequently, on (ii) differential conductance in the non-linear bias regime. We find the equilibrium universal scale, i.e. the quasiparticle weight controls the extent of the linear response regime and is also crucial in determining the thermal scaling of the system when comparing the theoretical and experimental results. The features in differential conductance are investigated in a wide parameter space, and characteristic signatures of the interplay of bias, interactions, Rashba SOC and temperature are identified. Finally, we compare some of our results corresponding to the strong coupling regime to recent experiments, and offer a qualitative explanation for some of the observations.

## 2.2 Formalism

The Hamiltonian for a quantum dot system connected to two leads with Rashba spin-orbit coupling (RSOC) can be written as

$$H = H_0 + H_{\mathrm{d}} + H_{\mathrm{RSOC}} + H_{\mathrm{hyb}}\,, \tag{2.1}$$

where the two-dimensional conduction band reservoirs (L/R) are represented by $H_0 = \sum_{\alpha\mathbf{k}\sigma} \epsilon_{\alpha\mathbf{k}} c^\dagger_{\alpha\mathbf{k}\sigma} c_{\alpha\mathbf{k}\sigma}$ and the Hamiltonian for the quantum dot is given by $H_{\mathrm{d}} = \sum_\sigma \epsilon_d d^\dagger_\sigma d_\sigma + U n_{d\uparrow} n_{d\downarrow}$, where $\alpha = L/R$ and $\sigma = \uparrow / \downarrow$ are the lead and spin indices respectively. The RSOC term is represented by[38]

$$H_{\mathrm{RSOC}} = \sum_{\alpha\mathbf{k}} \lambda \psi^\dagger_{\alpha\mathbf{k}} (\mathbf{k} \times \vec{\sigma})_z \psi_{\alpha\mathbf{k}}\,, \tag{2.2}$$

where $\mathbf{k} = (k_x, k_y)$, and $\psi^\dagger_{\alpha\mathbf{k}} = (c^\dagger_{\alpha\mathbf{k},\uparrow}\; c^\dagger_{\alpha\mathbf{k},\downarrow})$. Finally, the hybridization between the quantum dot and the leads is given by

$$H_{\mathrm{hyb}} = \sum_{\alpha\mathbf{k}\sigma} \left( V_{\mathbf{k}} c^\dagger_{\alpha\mathbf{k}\sigma} d_\sigma + \mathrm{h.c} \right)\,. \tag{2.3}$$

The conduction band terms, namely, $H_0$ and $H_{\mathrm{RSOC}}$, may be combined[38], which leads to the emergence of chiral conduction bands. This is accomplished using the angular momentum expansion (details in Appendix B) to obtain the following form of the Hamiltonian:

$$\begin{aligned} H = &\sum_{khm} \tilde{\epsilon}_{kh} (c_{kh}^{m+\frac{1}{2}})^\dagger c_{kh}^{m+\frac{1}{2}} \\ &+ \sum_{khm} \delta_{m,0} \tilde{V}_k \left( (c_{kh}^{m+\frac{1}{2}})^\dagger d_\uparrow + h (c_{kh}^{m-\frac{1}{2}})^\dagger d_\downarrow + \text{h.c} \right) \\ &+ H_d \, , \end{aligned} \tag{2.4}$$

where $h = \pm 1$ is an emergent chiral quantum number. This also allows us to define an emergent angular momentum quantum number, given by $j_m = m + \frac{h}{2}$, with only the bands corresponding to $j_m = \pm\frac{1}{2}$ coupling to the dot, while the rest of the bands are decoupled. The renormalized dispersion $\tilde{\epsilon}_{kh}$, now depends on $h$ and the spin-orbit interaction $\lambda$, as given by the expression $\tilde{\epsilon}_{kh} = (\epsilon_k + h\lambda k)/k = \tilde{\epsilon}_k + h\lambda$. For a free-electron like dispersion, $\tilde{\epsilon}_k$ will be linear in $k$. Hence RSOC introduces a Zeeman-type splitting of the conduction band, without breaking the time-reversal symmetry. Further, the hybridization matrix elements are assumed to be isotropic, i.e, $V_{\mathbf{k}} = V_k$, and $\tilde{V}_k = V_k \sqrt{2\pi/k}$.

In order to study the interplay between the RSOC and a constant voltage bias, we consider the left and right leads to have a lead-dependent chemical potential $\mu_\alpha$ applied to all the emergent $h, j_m$ channels in each lead, such that the voltage bias is given by $V_{sd} = \mu_L - \mu_R$. This leads to the Hamiltonian

$$H_{eff} = \sum_{\alpha=L,R} H_\alpha + H_{hyb} + H_{dot} \, , \tag{2.5}$$

where the individual terms are given by

$$H_\alpha = \sum_{khj_m} \tilde{\epsilon}_{k\alpha h} c^\dagger_{\alpha k h j_m} c_{\alpha k h j_m} \, , \tag{2.6}$$

$$H_{hyb} = \sum_{\alpha k h} \tilde{V}_{k\alpha} \left[ c^\dagger_{\alpha k h \frac{+1}{2}} d_\uparrow + h c^\dagger_{\alpha k h \frac{-1}{2}} d_\downarrow + h.c. \right] , \tag{2.7}$$

$$H_{dot} = \sum_\sigma \epsilon_d n_\sigma + U n_\uparrow n_\downarrow \, , \tag{2.8}$$

with $\tilde{\epsilon}_{k\alpha h} = \tilde{\epsilon}_{kh} + \mu_\alpha$. The model described above can be visualized by the schematic in fig. 2.1. We note that this model was investigated using a quantum master equation (QME) approach in a recent work[14], and the results were used to explain specific experimental observations of differential conductance reported in the same work. The present work, using the IPA, provides a different perspective and fresh insight into these experiments[14] and hence may be viewed as complementary to the QME results.

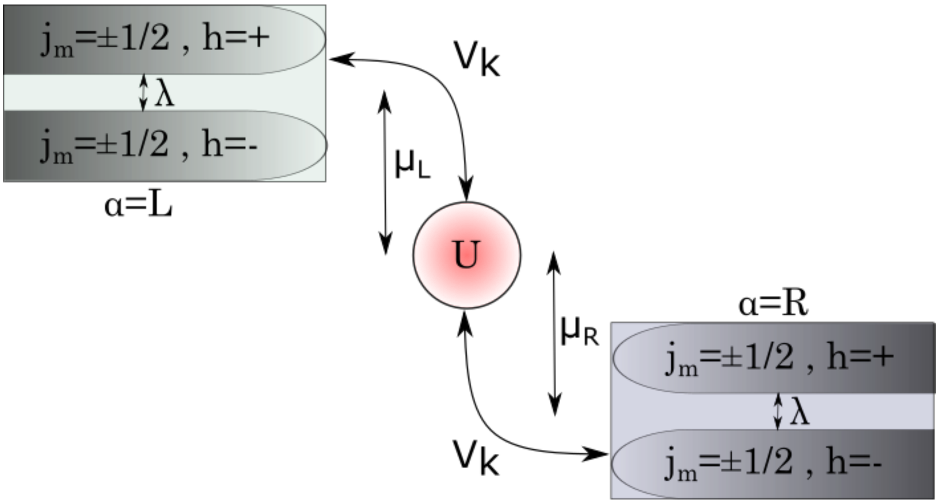

Figure 2.1: Schematic of the correlated quantum dot connected to two leads, split further by spin-orbit coupling into chiral bands, subject to a voltage bias, $V_{sd} = \mu_L - \mu_R$.

In the presence of a finite bias, ensuring particle-hole symmetry by setting $\mu_L = \frac{V_{sd}}{2} = -\mu_R$, we can compute the symmetrized the steady-state current ($J$) can be computed using the Meir-Wingreen formula, given by[48]

$$\begin{aligned} J =& \frac{2ie}{h} \sum_{\sigma} \int d\omega \Big[ \left(\Delta_L(\omega) - \Delta_R(\omega)\right) G^{<}_{d\sigma}(\omega) \\ &+ 2i \left(f_L(\omega)\Delta_L(\omega) - f_R(\omega)\Delta_R(\omega)\right) \mathrm{Im} G^{r}_{d\sigma}(\omega) \Big] \,. \end{aligned} \tag{2.9}$$

In the above, the $G^{<}_{d\sigma}$ and $G^{r}_{d\sigma}$ represent the lesser and retarded dot Green's functions computed within Keldysh formalism, and $f_\alpha$ is the Fermi-Dirac distribution function of the $\alpha^{\text{th}}$ lead. The $\Delta_\alpha(\omega)$ represents the dot-lead coupling and is given by

$$\Delta_\alpha(\omega) = -\mathrm{Im}\Gamma_\alpha(\omega) \,, \tag{2.10}$$

where the hybridization function for the $\alpha^{\text{th}}$ lead, $\Gamma_\alpha(\omega)$, is given by

$$\begin{aligned} \Gamma_\alpha(\omega) &= \sum_{kh} \frac{\tilde{V}_k^2}{\omega^+ - \epsilon_{k\alpha h}} \\ &= \sum_{k} \tilde{V}_k^2 \left[ \frac{1}{\omega^+ - \tilde{\epsilon}_{k\alpha} + \lambda} + \frac{1}{\omega^+ - \tilde{\epsilon}_{k\alpha} - \lambda} \right] \\ &= \sum_{h} \Delta_{h\alpha}(\omega) \, = E_\alpha(\omega) - i\Gamma_\alpha(\omega). \end{aligned} \tag{2.11}$$

With a suitable choice of the $\tilde{V}_k$-dependence on $k$ as $\tilde{V}_k^2 = V_0^2 f(k)$, we can transform the summation over $k$ into an integral that has the form of a Hilbert transform, and hence the hybridization function can be obtained as:

$$\Gamma_{h\alpha}(\omega) = V_0^2 \mathrm{H}\left[\omega^+ - \mu_\alpha - h\lambda\right] \tag{2.12}$$

where H$[z]$ is the Hilbert transform with respect to a "density of states" (DOS), $\rho_0(\epsilon)$, given by

$$\mathrm{H}[z] = \int d\epsilon \, \frac{\rho_0(\epsilon)}{z - \epsilon} \, . \tag{2.13}$$

Note that the $\rho_0(\epsilon)$ in the above equation stems from the $k$-dependence of the hybridization matrix element. The conduction band density of states is already incorporated through the electron dispersion of a free-electron form (see the discussion below Eq. (4)). We have explored three types of $\rho_0(\epsilon)$: (i)a Gaussian (G), which is not bounded, but can be interpreted as having an effective finite bandwidth, (ii) a semi-elliptic (S) form which has a compact support, and (iii) a wide, flat form (F). The expressions for the three forms are

$$\rho_0^{\mathrm{G}}(\epsilon) = \frac{1}{\sqrt{\pi} t_*} \exp\left(-\frac{\epsilon^2}{t_*^2}\right) \tag{2.14}$$

$$\rho_0^{\mathrm{S}}(\epsilon) = \frac{1}{\pi t_*}\left(1 - \frac{\epsilon^2}{4t_*^2}\right)^{1/2} \tag{2.15}$$

$$\rho_0^{\mathrm{F}}(\epsilon) = \frac{1}{2t_*}\theta(t_* - |\epsilon|) \, . \tag{2.16}$$

We define an energy scale, $\Delta_0 = \pi V_0^2 \rho_0(0)$ which is known to determine the scaling of dynamics and transport properties in equilibrium[49], and hence can be expected to play an important role in the steady-state as well. In terms of this scale, the dot-lead coupling is given by, $\Delta_{h\alpha}(\omega) = \Delta_0 \rho_0(\omega - \mu_\alpha - h\lambda)/\rho_0(0)$. For all our calculations, we have used the semi-elliptic or the Gaussian forms with $t_* = 1$, except for benchmarking where we have used the flat-DOS form with a large $t_*$, but a finite $\Delta_0$. In all the calculations described in this work, we have chosen $\Delta_0 = 0.1$, implying that the choice of $V_0$ is not the same for the three forms. The infinitely wide flat-DOS hybridization is obtained by using the limit $t_* \to \infty$, and a concomitant scaling of $V_0 \sim \sqrt{t_*}$, such that $\Delta_0 = 0.1$. Thus, in such a limit, the hybridization does not have a bias or spin-orbit coupling dependence while the semi-elliptic and the Gaussian forms do, and this difference leads to several observable consequences as we will discuss in Sec. III.

The dot Green's functions used in the current expression, given by Eq. 2.9, may be computed using the Dyson's equations given by[47]

$$[G^r_d(\omega)]^{-1} = [g^r_d(\omega)]^{-1} - \Sigma^r(\omega)\,, \tag{2.17}$$

$$G^<_d(\omega) = |G^r_d(\omega)|^2\left(\frac{g^<_d(\omega)}{|g^r_d(\omega)|^2} - \Sigma^<(\omega)\right), \tag{2.18}$$

where $g^r_d, g^<_d$ represent the non-interacting ($U = 0$) Green's functions of the dot, and $\Sigma^r, \Sigma^<$ are the retarded and lesser self-energies respectively. Obtaining the self-energies represents the greatest challenge in computing the current. We have employed the interpolative perturbative approximation (IPA), introduced by Aligia[47], which is equivalent to the second-order Keldysh perturbation theory (KPT2) in the steady-state p-h symmetric limit, and to the iterative perturbation theory IPT[50] in the equilibrium limit, to get the self-energies. The second-order expressions for the retarded and lesser self-energies are as follows[47] (see appendix B):

$$\Sigma^r(\omega) = U^2\int\left(\prod_{i=1}^{3} d\epsilon_i D(\epsilon_i)\right)(\omega^+ + \epsilon_3 - \epsilon_2 - \epsilon_1)^{-1} \\ \times\left[\tilde{f}(-\epsilon_1)\tilde{f}(-\epsilon_2)\tilde{f}(\epsilon_3) + \tilde{f}(\epsilon_1)\tilde{f}(\epsilon_2)\tilde{f}(-\epsilon_3)\right] \tag{2.19}$$

and

$$\Sigma^<(\omega) = -2i\pi U^2\int d\epsilon_1 d\epsilon_2 D(\epsilon_1)D(\epsilon_2)D(\epsilon_1+\epsilon_2-\omega) \\ \times\left[\tilde{f}(\epsilon_1)\tilde{f}(\epsilon_2)\tilde{f}(\omega-\epsilon_1-\epsilon_2)\right] \tag{2.20}$$

where $D(\omega) = -(1/\pi)\,\mathrm{Im}\{\tilde{g}^r_d(\omega)\}$ is the spectral function calculated from the Hartree-corrected, retarded dot Green's function given by

$$[\tilde{g}^r_{d\sigma}(\omega)]^{-1} = \omega^+ - \sum_\alpha \Gamma_\alpha(\omega)\,, \tag{2.21}$$

and $\tilde{f}(\omega) = \sum_\alpha \Delta_\alpha(\omega)f_\alpha(\omega)/\sum_\alpha \Delta_\alpha(\omega)$ is the weighted Fermi function, with $\Delta_\alpha(\omega) = -\mathrm{Im}\Gamma_\alpha(\omega)$ (Eq. 2.11), and $f_\alpha(\omega) = f(\omega-\mu_\alpha)$ is the Fermi function for the $\alpha^{\mathrm{th}}$ lead. In writing the above, we have assumed the p-h symmetric limit, where $\epsilon_d = -U/2$ cancels the first order Hartree contribution. To obtain the lesser Green's function $[G^<_d(\omega)]$, we need the Hartree-corrected lesser Green's function of the dot, which is given by

$$\tilde{g}^<_{d\sigma}(\omega) = 2i|\tilde{g}^r_{d\sigma}(\omega)|^2\sum_\alpha \Delta_\alpha(\omega)f_\alpha(\omega)\,. \tag{2.22}$$

Solutions of Eqs. 2.9 to 2.22 yield the physical picture of the interplay of bias, interactions and SOC on the spectra and current-voltage characteristics. The self-energies in Eq. (2.19) and (2.20) are evaluated as convolutions using the Fourier transform. The details of the numerical implementation of the convolution can be found in earlier works[51]. The differential conductance is calculated as $G = dJ/dV_{sd}$, and numerically implemented through a derivative of the splined current[1]. We present our results for spectra and transport quantities in the next section.

## 2.3 Results

In equilibrium studies of the p-h symmetric Anderson model, the IPT[50], based on the second-order perturbation theory, is a good approximation in the weak coupling limit, and by coincidence also reproduces the atomic limit. Hence, the IPT has been extensively used as an interpolating approximation for lattice models such as the Hubbard model and the periodic Anderson model within the dynamical mean-field theory to investigate Mott transition and heavy fermion physics[52]. Various Keldysh perturbation theory based approximations including IPA have been used quite widely in the out-of-equilibrium case as well[25;27;47]. In this work, we carry out a simple benchmarking exercise to ascertain the regime of validity of the IPA and subsequently use it to investigate the effect of spin-orbit coupling.

### 2.3.1 Benchmarking

As a first benchmark, we compare the current-voltage (IV) curves for the flat-DOS and the semi-elliptic DOS cases with the steady state results from Nuss *et al.*[29] who have used the time-evolving block decimation (TEBD) method on a model with 150 sites comprising two leads and a quantum dot subjected to a dc bias. As shown in fig. 2.2 we find that the $J - V_{sd}$ curves match the TEBD results very well[2]. The presence of a peak in the current at a specific bias roughly around half the bandwidth is seen in the case of the finite bandwidth semi-elliptic DOS case. The peak position moves to higher bias values for increasing interaction strength and concomitantly the peak current magnitude decreases. In the case of the infinitely wide, flat

---

[1] Codes for reproducing the IPA data in figs. 2.2 and 2.6 are provided at the GitHub link (`https://github.com/nsvraja/ssIPA_ZF_phsym`). A README is also included for ease of use.

[2] For a fixed energy scale $\Delta_0$, the hybridisation strength $V_0$, needs to have a multiplicative factor of $\sqrt{2}$ for a quantitative comparison with the TEBD results

hybridization function, we see a saturation of the current at high bias values and the saturation current decreases with increasing $U$. Both of these results show that the IPA captures the current characteristics very well over a wide range of interaction strengths.

As a second benchmark, we compare our results with fourth-order perturbation theory by Fujii *et al.* [25] (for a flat/uniform hybridization, with $U = 6\Delta_0$ and SOC strength $\lambda = 0$) in fig. 2.3 and see that the interacting dot DOS matches very well with their results. We see that there is a reduction in the zero frequency weight with increasing bias and also splitting and broadening of the central peak. Next, we examine the effect of equilibrium scales on transport characteristics in the linear response regime.

### 2.3.2 Linear response regime: scaling and universality

The excellent agreement with TEBD and fourth-order perturbation theory yield strong confidence in the validity of IPA in a wide bias and interaction range. We now explore the extent of the linear response regime and examine if equilibrium quantities describe the response of the system at finite bias, but close to equilibrium.

As we can see from fig. 2.2, the linear dependence of the current at low values of bias agrees well with the TEBD calculations and the extent of the linear response regime depends on the value of the interaction and SOC strengths. In equilibrium, the quasiparticle weight, which can be calculated as $Z_0 = [1 - \mathrm{Re}(d\Sigma(\omega)/d\omega|_{\omega=0})]^{-1}$, where $\Sigma(\omega)$ is the self energy, happens to be proportional to the Kondo scale, and hence determines the extent of the universal regime[49]. In order to understand the dependence of the self-energy on SOC and bias, we have carried out a simple analysis (details in the Appendix) of the second-order expression (Eq. 2.19) assuming that the Hartree-corrected density of states is not varying rapidly in the neighbourhood of $\omega = 0$ for low values of bias, and SOC, i.e $D(\omega) \simeq D_0 = -\,\mathrm{Im}\{\tilde{g}^r_{d\sigma}(\omega = 0)\}$ for $|\omega|, |V_{sd}|, \lambda << t_*$. $D_0$ may be found by considering the expressions for the retarded Green's functions in Sec. II, as shown below. From Eq. 2.21, we see that

$$[\tilde{g}^r_{d\sigma}(\omega = 0)]^{-1} = V_0^2 \sum_{\alpha h} \int d\epsilon \, \frac{\rho_0(\epsilon)}{\mu_\alpha + h\lambda + \epsilon - i\eta} \tag{2.23}$$

where $\eta \to 0^+$. Using the above expression, we note that at $\omega = 0$, the Hartree-corrected non-interacting Green's function $\tilde{g}^r_{d\sigma}$ is purely imaginary, since

$$\mathrm{Re}\,(\tilde{g}^r_{d\sigma}(\omega = 0))^{-1} = V_0^2 \sum_{\alpha h} \mathcal{P} \int d\epsilon \, \frac{\rho_0(\epsilon)}{\mu_\alpha + h\lambda + \epsilon} = 0 \tag{2.24}$$

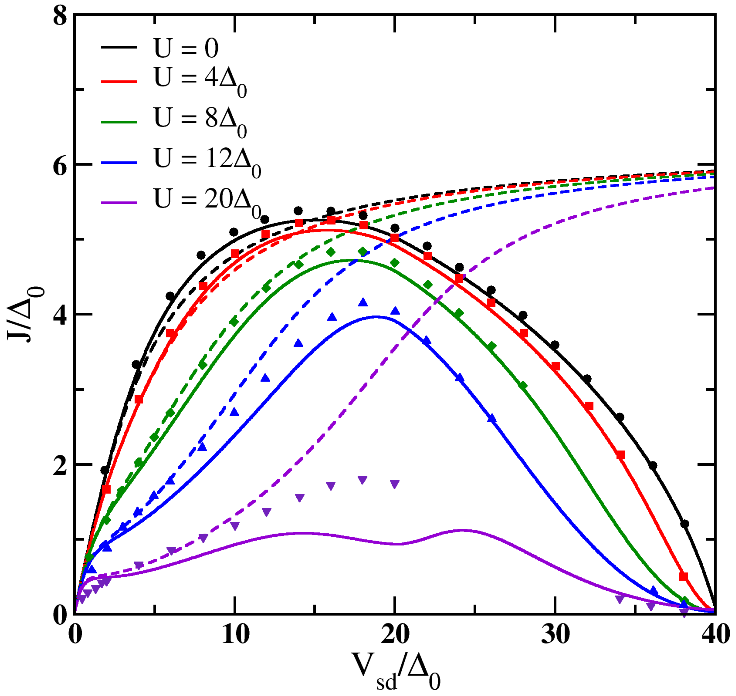

Figure 2.2: The current-voltage curves computed within IPA ($\lambda = 0$) for various values of $U$ (mentioned as legends) compared to TEBD results of Nuss *et al.*[29]. The solid lines represent the current computed for a semi-elliptic hybridization, while the dashed lines correspond to the flat hybridization. The symbols are data extracted from Nuss *et al.*[29] and the current is scaled by a factor of 3.33.

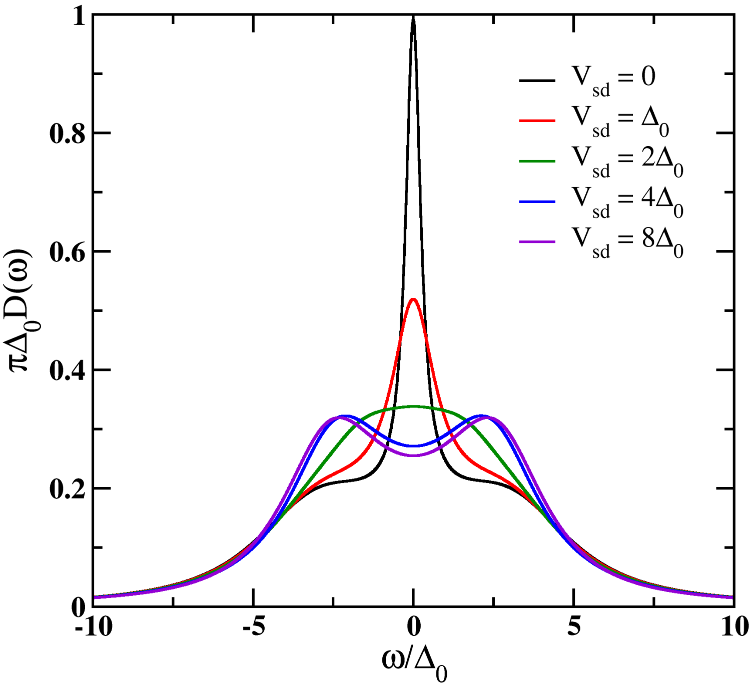

Figure 2.3: The DOS of the dot computed within IPA for $U = 6\Delta_0$ and the flat hybridization in the absence of SOC. A splitting of the zero frequency peak with increasing bias (indicated as legend) is seen, which matches with the results of a fourth-order calculation of Fujii *et al.*[25].

for a p-h symmetric $\rho_0(\epsilon)$. In the above equations, $\mu_L = V_{sd}/2, \mu_R = -V_{sd}/2, h = \pm 1$, and $\mathcal{P}$ denotes the principal value. Thus,

$$\tilde{g}^r_{d\sigma}(\omega = 0) = -\frac{i}{\pi V_0^2 \sum_{h\alpha} \rho_0(\mu_\alpha + h\lambda)} \tag{2.25}$$

using which we can write, for zero bias, $D_0 = (4\pi^2 V_0^2 \rho_0(\lambda))^{-1}$. We find that the imaginary part of the retarded self-energy in terms of $D_0$ is given by (for $\omega \to 0$ and $T = 0$, details are provided in the Appendix)

$$-\frac{1}{\pi} \operatorname{Im} \Sigma^r(\omega) = \frac{U^2 D_0^3}{2} \left[\omega^2 + \frac{3V_{sd}^2}{4}\right] \tag{2.26}$$

Using the Kramers-Krönig transformation, the real part of the retarded self-energy is given by

$$\operatorname{Re} \Sigma^r(\omega) = -\frac{U^2 D_0^3}{\Lambda} \left[\Lambda^2 - \frac{3V_{sd}^2}{4}\right] \omega \,, \tag{2.27}$$

where $\Lambda$ is a high-energy cutoff that represents the extent of the quadratic dependence of the imaginary part of the self-energy.

Thus, using the definition of the quasiparticle weight as $\operatorname{Re} \Sigma^r(\omega) = \omega(1 - \frac{1}{Z})$ we get the analytical expression (please refer to the Appendix for details of the calculation),

$$Z(U, \lambda, V_{sd}) = \left(1 + \frac{U^2 D_0^3}{\Lambda} \left[\Lambda^2 - \frac{3V_{sd}^2}{4}\right]\right)^{-1} \,. \tag{2.28}$$

Using this, we note that, since the IPA is based on second-order perturbation theory, the equilibrium quasiparticle weight, $Z_0 = Z(U, \lambda, V_{sd} = 0)$ decays algebraically with increasing interaction strength (at zero bias) as $U^{-2}$. The dependence on SOC enters through $D_0$. For a flat density of states, since $D_0$ does not depend on $\lambda$, the quasiparticle weight, $Z_0$ will be independent of SOC. The Kondo scale is proportional to the product of bandwidth and $Z_0$, and since the chiral bands move outward with increasing $\lambda$, the effective bandwidth will increase and hence will give rise to a linearly increasing Kondo scale.

However, for a frequency-dependent density of states such as the semi-elliptic or Gaussian density of states, $D_0$ increases as $\rho_0^{-3}(\lambda)$. For example, for the Gaussian and semi-elliptic forms of the hybridization, the $D_0$ is proportional to $\exp(3\lambda^2/t_*^2)$ and $(1 - \lambda^2/4t_*^2)^{-3/2}$ respectively. Hence the quasiparticle weight will decrease sharply with increasing $\lambda$ as $Z_0 \propto D_0^{-3}$ [from Eq. 2.28]. So, even though the effective bandwidth increases linearly with increasing SOC in parallel to the flat hybridization case, the strong decrease due to the factor of $D_0^{-3}$ dominates. The equilibrium quasiparticle weight, $Z_0$ shown in the bottom left panel of fig. 2.4, for the semi-elliptic and the Gaussian hybridization functions (denoted as SE and G respectively), is seen to decrease sharply with increasing $\lambda/\Delta_0$ in agreement with the arguments above.

Consistent with the decrease of $Z_0$ with $\lambda$, the linear response regime in the current-voltage $(J - V_{sd})$ relationship shrinks considerably with increasing interaction strength (for $\lambda = 0$) as seen in the top left panel of fig. 2.4 and with increasing $\lambda$ for $U = 20\Delta_0$ as seen in the top right panel. However, when the current and bias are scaled by $Z_0$, all the curves of the top two panels collapse up to a bias of $V_{sd} \simeq Z_0\Delta_0$ (shown in the bottom right panel), which confirms that the equilibrium quasiparticle weight, or equivalently, $T_K$, determines the extent of the linear response regime[53].

Equilibrium investigations of the SIAM have shown that the Kondo scale decreases exponentially with increasing $U$ for $\lambda = 0$[17]. In the presence of $\lambda$ on the leads and $U$ on the dot, the Kondo scale has been shown to increase or decrease depending on whether the leads have a wide, flat form or a finite bandwidth[38;40] respectively.

In our work, we have shown [see Eq. 2.28] that the quasiparticle weight, and hence the Kondo scale depends on $U$ algebraically (decreasing as $U^{-2}$) and on $\lambda$ through the density of states, namely as $(\rho_0(\lambda))^3$. The algebraic decrease of the scale with $U$ is known to be an artefact of the perturbative approximation employed to obtain the self-energy, while exact methods such as Bethe ansatz[17] find an exponential decrease. Since $\rho_0(\epsilon)$ is usually chosen to have a maximum at the chemical potential, and decreases monotonically with increasing $|\epsilon|$, the Kondo scale will also decrease monotonically with increasing $\lambda$ as discussed above. The precise form of this decrease will depend on the form of the density of states.

We see from fig. 2.4, (bottom-left panel) that the quasiparticle weight scale decreases sharply with increasing $\lambda$. Although the qualitative trend is the same for the semi-elliptic and the Gaussian hybridization, the scale decreases much more rapidly for the latter. For the same value of the parameters, the scale corresponding to the Gaussian hybridization is much smaller than that of the semi-elliptic case. Hence for the strong coupling regime, we choose to work with the Gaussian hybridization.

Additionally, in the strong coupling[3] ($T_K \to 0$) regime, a clear separation

---

[3] In practice, we consider the system to be in the strong coupling regime when the $Z_0 \lesssim 0.1$, since the low-temperature scale, i.e $T_K \sim Z_0\Delta_0$ will be at least one order of magnitude smaller than the non-universal scales, $\Delta_0$, bandwidth, $U$, etc.

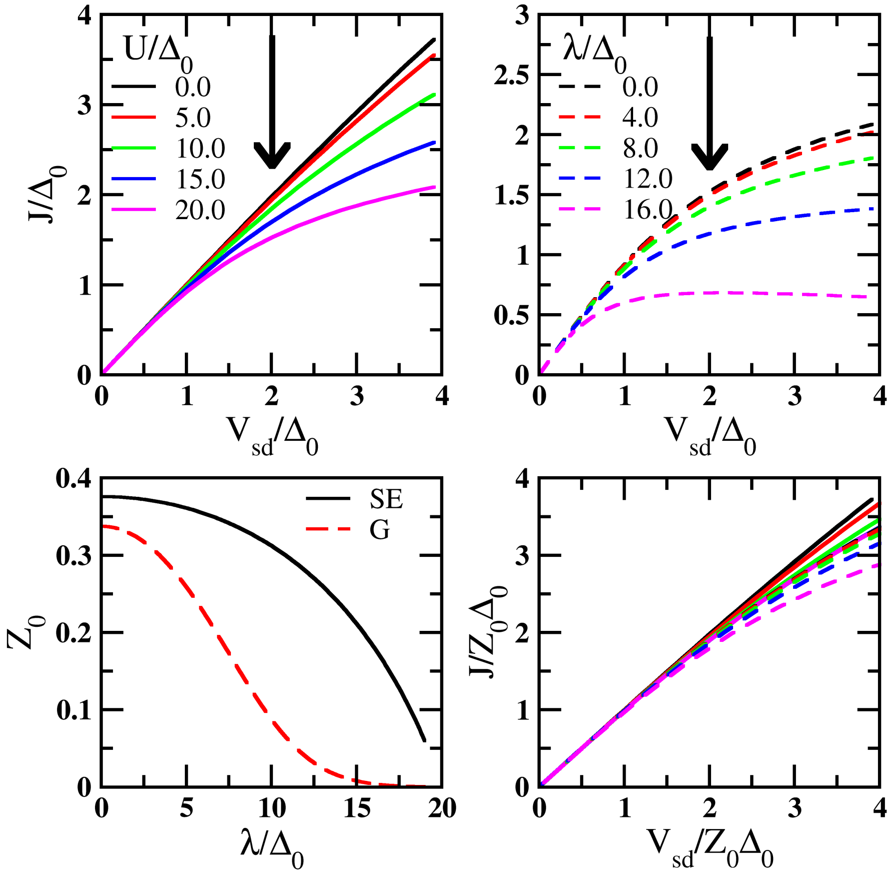

Figure 2.4: Current ($J/\Delta_0$) as a function of bias ($V_{sd}/\Delta_0$) is shown in the top two panels. The left panel shows the result for various values of interaction strength $U/\Delta_0$, and SOC strength $\lambda = 0$, while the right panel shows the result for $U = 20\Delta_0$ and various values of $\lambda/\Delta_0$. The bottom left panel shows the dependence of equilibrium ($V_{sd} = 0$) quasiparticle weight $Z_0$ on the spin-orbit coupling for the semi-elliptic (SE) and Gaussian (G) forms of hybridization. The bottom right panel shows the collapse of all the curves in the top two panels up to a bias given by $V_{sd} \simeq Z_0\Delta_0$, when the current and bias are scaled by $Z_0$, thus determining the linear response regime.

of scales ($T_K$ *vs* bandwidth, $U$) occurs, which is the best distinguishing feature of this regime, and will be seen to have important consequences on the evolution of spectra and conductance with increasing temperature, and will be discussed later.

Subsequent to the benchmarking and a study of the scales and the linear response regime, we now present the main results of our work, which focus on the interplay of spin-orbit coupling and electron-electron interactions on the single-particle spectra and the differential conductance. Since the SOC does not alter the hybridization functions in the case of the infinitely wide, flat/uniform DOS, the results do not show any dependence on $\lambda$. Therefore, we will consider the semi-elliptic and Gaussian hybridization forms where the effective bandwidth is modified by $\lambda$ as seen from Eqs. 2.12- 2.16.

### 2.3.3 Evolution of density of states with interactions, SOC, bias, and temperature

Since the separation of scales is an important consideration in our analysis, we will investigate the transfer of spectral weight in the weak/intermediate coupling and strong coupling regimes separately.

**Weak/intermediate coupling regime**

In order to be in the weak/intermediate coupling regime, we will choose $U = 20\Delta_0, \lambda = 15\Delta_0$ and the semi-elliptic hybridization, for which, as the bottom left panel of fig. 2.4 shows, the $Z_0 \simeq 0.2$. At equilibrium (zero bias), and in the absence of SOC, but with finite $U$ ($\gtrsim$ bandwidth), the dot spectral function acquires Hubbard bands at $\omega \gtrsim \pm U/2$ as the top panel of fig. 2.5 shows. For a flat/uniform hybridization, the Hubbard bands are known to lie close to $\pm U/2$[54], but for a dispersive DOS such as semi-elliptic or Gaussian, these incoherent peaks lie somewhat beyond $\pm U/2$. If we now turn on SOC, keeping $V_{sd} = 0$, then as the middle panel shows, the left, and right lead hybridization functions broaden significantly. This is because the chiral bands that are split by the SOC, when superimposed give rise to a hybridization, that has a width equal to $D + 2\lambda$, and for the middle panel, since $D = 40\Delta_0$, and $\lambda = 15\Delta_0$, the band-edges are at $\pm(D/2+\lambda) = \pm 35\Delta_0$. Since, for this larger bandwidth, the hybridization appears less dispersive and appears similar to a uniform DOS, the Hubbard bands become more prominent, and their location is almost at $\pm U/2$.

Next, as bias is turned on and raised to $20\Delta_0$, the band centres (chemical potentials) of the two leads move apart ($\mu_L = V_{sd}/2$ and $\mu_R = -V_{sd}/2$), and concomitantly, the dot spectrum (solid black line in the bottom panel of fig. 2.5) goes over to a two-peak structure in non-equilibrium from a three-peak structure at equilibrium. In the same panel, the red dashed and blue dot-dashed lines, which are the left and right lead hybridizations, have small bumps at precisely these energies for $V_{sd} = 20\Delta_0$. Since the Hubbard bands are also at $\pm U/2$, which are $\pm 10\Delta_0$ in fig. 2.5, a maximum in conductance may be expected to occur when the bias becomes equal to the peak position difference of the Hubbard bands[25]. Indeed, this will be confirmed in Sec. III D-1.

### Strong coupling regime

In parallel to the previous section, we will analyze the changes in the spectra and hybridization as we sequentially turn on SOC, temperature, and bias for $U = 20\Delta_0$. The strong coupling regime will be accessed through a choice of the value of the SOC, and the hybridization function, as $\lambda = 18\Delta_0$, and the Gaussian, for which as the left bottom panel of fig. 2.4 shows, the scale is $Z_0 \sim 10^{-3}$.

Figure 2.6 (please see footnote[4]) shows the left lead and the right lead hybridization functions as $\Gamma_L$ and $\Gamma_R$ in black and blue colours respectively. The dot spectral function is shown in the centre as a red solid line. The vertical axis is energy/frequency. Figure 6(a) represents a situation where $U = 20\Delta_0$, but $\lambda = T = V_{sd} = 0$. The dot spectral function has a three-peak structure, with the central peak being the Kondo peak, and the other two being the Hubbard bands at $\pm U/2$. As we turn on $\lambda = 18\Delta_0$, keeping $T = V_{sd} = 0$, Fig. 6(b) shows that the central peak in the dot spectral function becomes extremely narrow (width$\simeq Z_0\Delta_0 \sim 10^{-4}$), while $\Gamma_L$ and $\Gamma_R$ show the development of chiral bands due to the SOC. The clear separation of the Kondo peak and the Hubbard bands is evident and is a characteristic of the strong coupling regime. When we turn on a small, but finite temperature of $T = 0.05\Delta_0$, Fig. 6(c) shows that the central peak melts leaving the Hubbard bands as the only distinct features in the spectrum. Finally, when a bias of $V_{sd} = 25\Delta_0$ is turned on, there are minor changes in the positions of the spectral peaks, while the $\Gamma_L$ and $\Gamma_R$ move up and down respectively. The occupied region of the left lead is seen to overlap with the region between the Hubbard bands, and the unoccupied region of the right lead. This overlap can very likely lead to finite bias peaks in the conductance. Next, we analyze the dependence of the differential conductance on the bias, SOC, interactions

---

[4] The figure has been made to appear as a schematic, but it has been made using data obtained from IPA, and the curves in the four panels are not mere sketches. The purpose of this figure is to allow a direct comparison of the calculated results with the schematic shown in Fig. 1 of Ref[14]

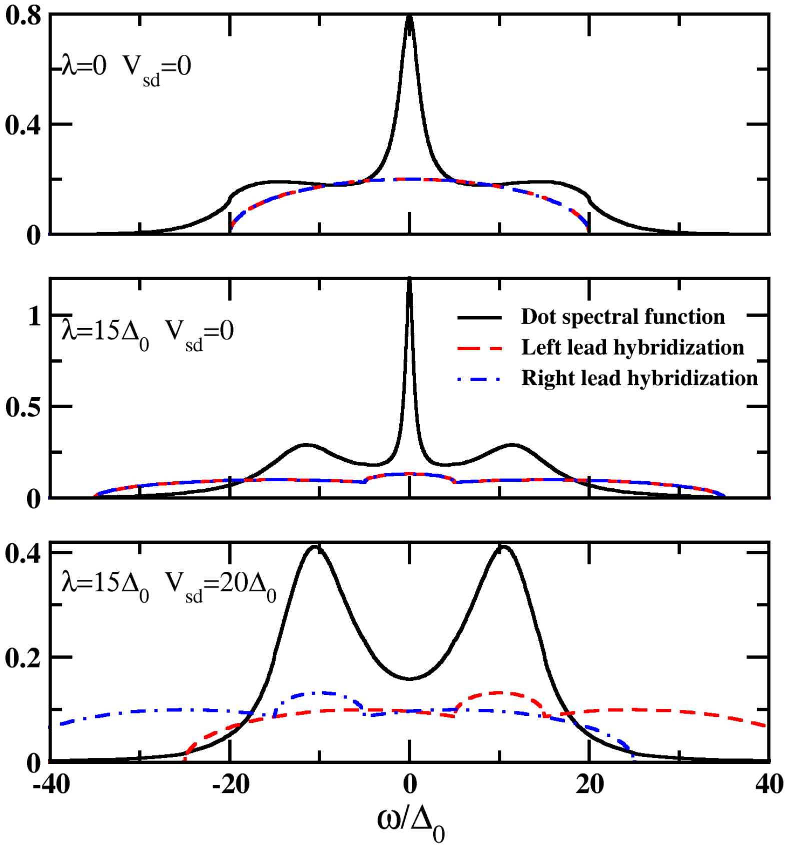

Figure 2.5: The dot spectral function (solid black line), and the left and right lead hybridization functions (red dashed and blue dot-dashed lines respectively) as a function of $\omega/\Delta_0$ showing the variation of spectral features with increasing SOC and bias for a fixed interaction strength, $U = 20\Delta_0$. The top panel is for $\lambda = V_{sd} = 0$, while $\lambda = 15\Delta_0$ is turned on in the middle panel keeping bias zero, and the bottom panel has $\lambda = 15\Delta_0$ and $V_{sd} = 20\Delta_0$. The semi-elliptic hybridization function has been used here.

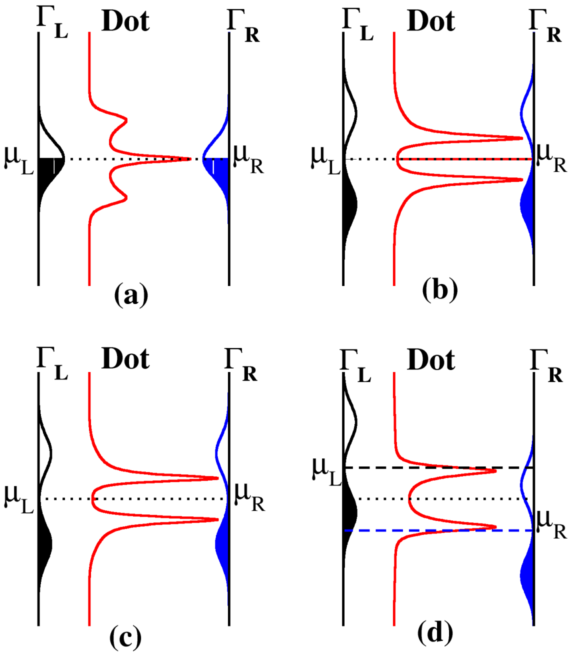

Figure 2.6: The hybridization and the dot density of states, for the Gaussian hybridization function in the strong coupling regime. $\Gamma_\alpha$ is the lead hybridization with $\alpha = L/R$ for left (black)/right (blue), and the central (red) curve shows the dot density of states. Similarly, $\mu_\alpha$ represents the chemical potential of the $\alpha^{\text{th}}$ lead. The interaction strength is fixed at $U = 20\Delta_0$, while SOC, temperature and bias are turned on sequentially from (a)-(d) as follows: (a) $\lambda = T = V_{sd} = 0$; (b) $\lambda = 18\Delta_0$, $T = V_{sd} = 0$; (c) $\lambda = 18\Delta_0, T = 0.05\Delta_0$, $V_{sd} = 0$; (d)$\lambda = 18\Delta_0, T = 0.05\Delta_0$, $V_{sd} = 25\Delta_0$. The shaded regions represent the $T = 0$ occupied states. The dotted and dashed lines are guides to the eye.

and temperature.

### 2.3.4 Conductance

We have divided the conductance results into two sections. In the first section, we present the differential conductance in the weak/intermediate coupling regime focusing on the evolution of various features with $U, \lambda$, SOC and $T$. The second section focuses on the strong correlation regime and qualitative comparison to experimental results.

#### Weak/Intermediate coupling regime

Figure 2.7 shows colour contour plots of the conductance for various values of $U \in [0, 20]\Delta_0$ and $\lambda \in [0, 15]\Delta_0$ at $T = 0$, computed with the semi-elliptic hybridization function. Within this range of parameters, the quasiparticle weight is in the range of $Z_0 \in [0.2, 1]$, so the choice of the range of parameters corresponds to the weak/intermediate coupling regime. The conductance is computed by fitting a cubic spline to the current *vs* $V_{sd}$ data and taking the first derivative. The colour bar on the right of each panel shows the association of a given colour with the value of the conductance. The top left and right panels represent varying interaction strength on the y-axis, but fixed SOC of zero and $15\Delta_0$ respectively, while the bottom left and right panels represent varying SOC on the $y$-axis, but fixed $U$ of zero and $15\Delta_0$ respectively. The ZBC peak is seen to be a universal feature in all panels, and it is interesting to note that the width of this peak decreases with increasing $U$ with or without $\lambda$, while the effect of $\lambda$ on the peak width at $U = 0$ is very weak (bottom left panel), but in the presence of $U$, $\lambda$ leads to a sharp narrowing of the zero bias peak (bottom right panel), which is consistent with the bottom left panel of fig. 2.4.

With increasing bias, a negative differential conductance (NDC) regime is seen in all panels. In order to understand the origin of the NDC, we first focus on the $U = 0$ results, since the calculation of conductance for $U = 0$ does not depend on the second-order approximation for the self-energy, and is hence exact. The non-interacting regime also exhibits NDC at high bias values as seen in the top panels and the bottom left panel. We confirm that the finiteness of the bandwidth of the hybridization is responsible for the NDC[55] since the wide, flat hybridization does not yield NDC. Additionally, the top right panel shows an intermediate bias regime where NDC is obtained at large $U$ values. In the strong coupling regime, reached by increasing $U$ and/or $\lambda$, the width of the central Kondo peak in the dot DOS, being proportional to $T_K$, shrinks exponentially. However, adiabatic continuity to

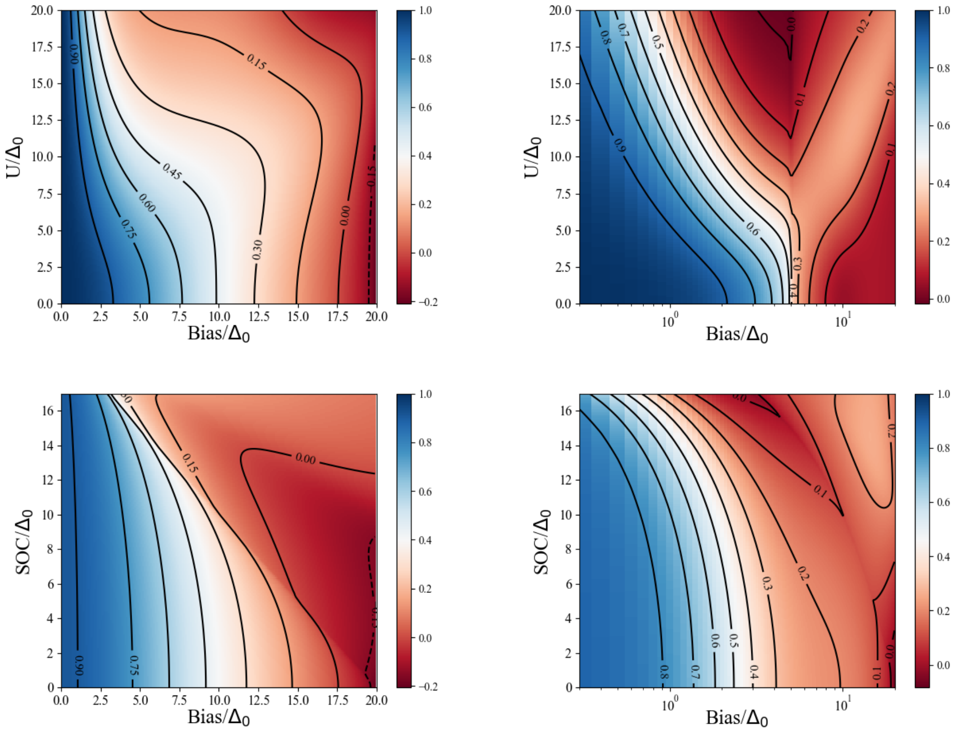

Figure 2.7: Variation of the differential conductance with interaction ($U$), spin-orbit coupling (SOC) and bias. The colours correspond to the values of the conductance $G = dJ/dV_{sd}$ as mentioned in the colour bar with certain values marked by the black contours. The dashed lines represent the negative differential resistance regime The top left and right panels correspond to varying $U$ and fixed SOC equal to zero and $15\Delta_0$ respectively. The bottom left and right panels correspond to varying SOC and fixed $U$ equal to zero and $15\Delta_0$ respectively. Note that the top and bottom right panels show the $x$-axis on the logarithmic scale for clarity since the linear response regime is highly compressed for large $U$ and/or SOC.

the non-interacting limit ensures that the Kondo peak has precisely the same form as the non-interacting dot DOS if the frequency is scaled as $\omega/Z_0\Delta_0$[56]. This fact implies that the system has an effective bandwidth of $Z_0\Delta_0$ in the strong coupling regime, and hence as the bias value crosses the linear response regime, an NDC regime may be obtained in parallel to the non-interacting regime. Since IPA is perturbative, and not accurate in strong coupling the NDC seen in strong coupling at intermediate bias values could be due to both the finite support of the hybridization and the approximation used for computing the self-energy.

The top left panel of fig. 2.7 shows that in the absence of SOC, the conductance decreases monotonically with increasing bias, and the linear response regime (over which the conductance is close to 1) shrinks with increasing interaction strength. The top right panel shows that in the presence of strong SOC ($15\Delta_0$), the conductance becomes highly non-monotonic, and a light band (for $U \gtrsim 10\Delta_0$) appears signifying a peak at a non-zero bias, that shifts to higher bias with increasing interaction strength. We observe that the bias value at which the peak occurs is almost the same as the interaction strength. Another interesting observation can be made from the bottom right panel of fig. 2.7, which shows the existence of a finite bias conductance peak for $\lambda \gtrsim 10\Delta_0$, whose position (on the bias-axis) is almost independent of the value of SOC. Thus, we see that the position of the finite bias peak correlates very well with the interaction strength, but is independent of $\lambda$, which suggests that the Hubbard bands and their increasing prominence with increasing $\lambda$ are giving rise to this peak. A physical basis for the emergence of this finite bias conductance peak in terms of the spectral functions and the hybridization functions may be constructed using the results of Sec. C-1.

As fig. 2.5 shows, an argument for the conductance peak at a bias value equal to interaction, is that the chemical potential of the left lead matches with one Hubbard band, while that of the right lead matches with the other, and hence the conductance is peaked due to a resonant situation when the SOC is large ($\gtrsim 10\Delta_0$), as the bottom right panel of fig. 2.7 shows. Indeed, the left bottom panel, for which $U = 0$, shows that the conductance decreases monotonically with increasing bias, while the bottom right panel shows a peak at bias around $15\Delta_0$ which is present only for large SOC ($\gtrsim 10\Delta_0$), but independent of the value of SOC. Thus, we find that, at $T = 0$, in addition to the zero bias peak, a finite bias peak arises in the presence of strong spin-orbit coupling, which is positioned at a bias roughly equal to the value of the interaction strength.

We now focus on finite temperature effects on conductance and also examine whether the IPA results conform to the universal Kondo scaling of the ZBC. We extend the bias to negative values, and show the conductance at

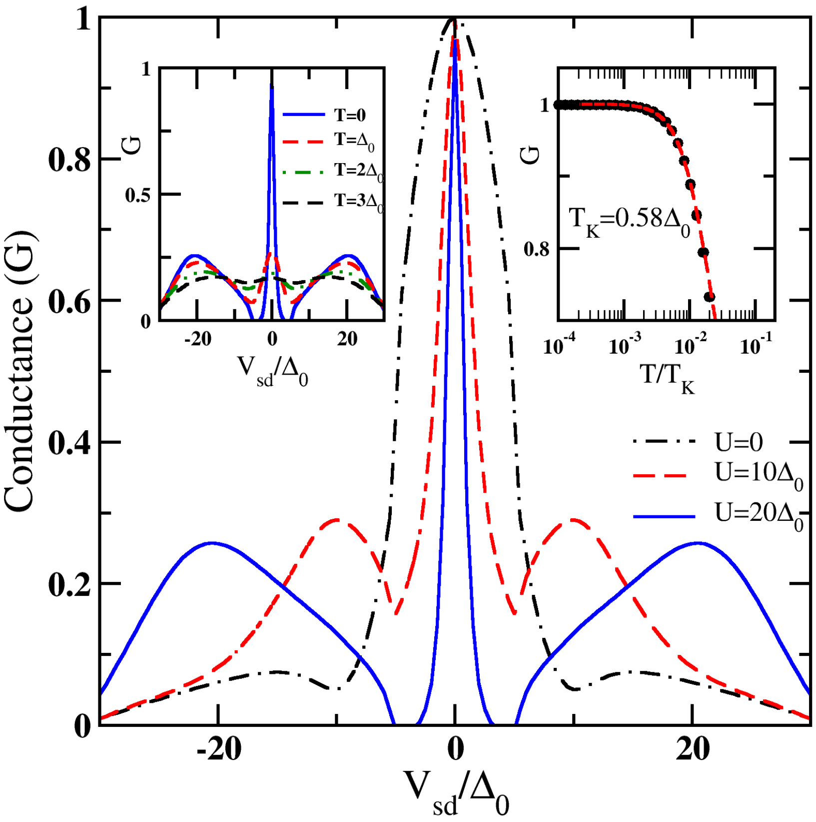

Figure 2.8: The main panel shows the $T = 0$ differential conductance in units of $G_0$ as a function of scaled bias ($V_{sd}/\Delta_0$) for three values of interaction strength, namely $U = 0$ (dot-dashed line), $10\Delta_0$ (dashed line), $20\Delta_0$ (solid line). The SOC is fixed at $\lambda = 15\Delta_0$ and a semi-elliptic hybridization function has been used in the calculations. The left inset shows $G$ *vs* $V_{sd}/\Delta_0$ for $U = 20\Delta_0$ at four different temperatures, mentioned as legends. The central peak is seen to melt with increasing temperature. The right inset shows the ZBC as a function of $T/T_K$; The black symbols represent IPA data, and the red dashed line represents a fit, $G(T) = G_0(1 + (2^{1/s} - 1)(T/T_K)^2)^{-s}$ with $s = 0.22$ and $T_K = 0.58\Delta_0$ as appropriate for universal Kondo behaviour

zero temperature and a fixed SOC of $\lambda = 15\Delta_0$ as a function of bias, for various $U$ values, and a semi-elliptic hybridization function, in the main panel of fig. 2.8. The conductance at $T = 0$ is seen to have a three-peak form consistent with the p-h symmetric regime, and the results of fig. 2.7. For the finite $U$ values, the locations of the side peaks correspond closely to the value of $U/\Delta_0$, while the zero bias peak is characteristic of the linear response regime. We can also see that the full width at half maximum (FWHM) of the central peak decreases sharply with increasing interaction, while the conductance at zero bias is pinned at unity. The width of the central peak is roughly proportional to the zero bias quasiparticle weight[57], which decreases exponentially (algebraically within IPA) with increasing $U/\Delta_0$. The left inset of fig. 2.8 shows the temperature dependence of the conductance for the largest $U/\Delta_0$ considered in the main panel. Interestingly, the central peak melts, and thus, at modest temperatures, we see a two-peak structure, which resembles the results of a recent experimental study[14]. However, the right inset shows that the conductance at zero bias decreases monotonically with increasing temperature in accordance with the universal Kondo behavior[1], while the 'double zero bias peak' feature seen in experiments[14] exhibits the opposite behaviour, namely an increase of $G$ with temperature. A rise in the ZBC is indeed observed at higher temperatures, but the rise is very modest and bears little comparison to experimental results[14]. Moreover, the finite bias peaks melt rapidly with increasing temperature (left inset, fig 2.8), leading to a broad featureless conductance. Such "spectral weight" transfer over large scales is indeed a characteristic of the weak/intermediate coupling regime. Hence, the finite bias conductance peak in the weak/intermediate coupling regime fails to explain the experimental results. As we will show below, the latter is best understood within the IPA framework from a strong correlation perspective.

### Strong correlation regime and comparison to experiments

As we noted earlier, the experimental results of Smith *et al.*[14] are in clear disagreement with our results from the low/intermediate correlation regime. Thus, in this subsection, we will study the system in the strong correlation regime. The temperature interval over which the resistivity shows universal behaviour when viewed on an absolute scale, i.e as $T/\Delta_0$ (and not as $T/T_K$) shrinks drastically in the strong interaction and strong spin-orbit coupling regime, because $T/\Delta_0 = (T/T_K)(T_K/\Delta_0)$, and the latter term is exponentially small in the strong coupling regime. In such a regime, a clear separation of scales happens in the conductivity as well as in the spectra. We show this in the top left panel of fig. 2.9, where the conductance is shown as a function

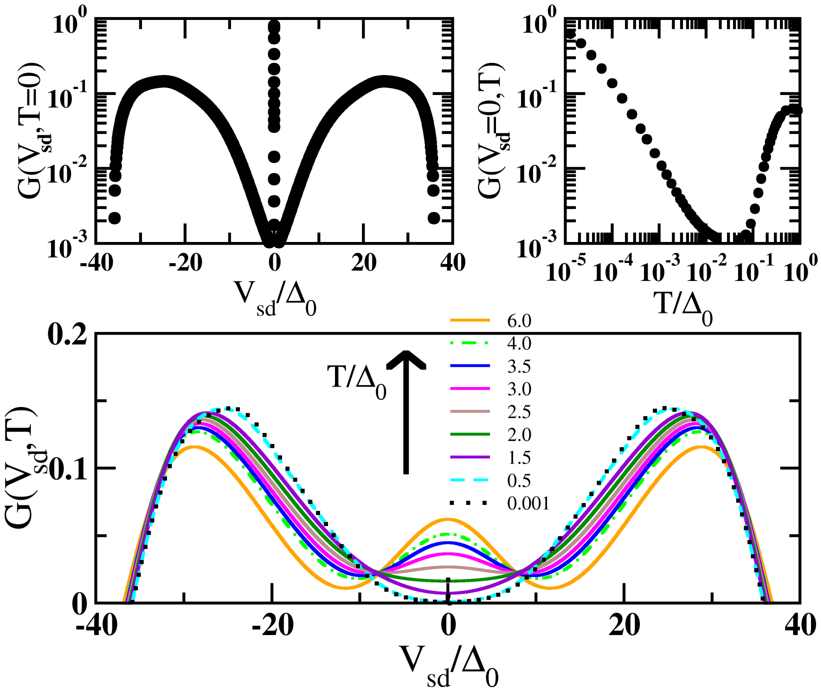

Figure 2.9: Scaled conductance, $G(V_{sd}, T)$ as a function of bias, $V_{sd}/\Delta_0$ for various temperatures, $T/\Delta_0$ indicated as legends in the main panel. The parameters (except for bias) are the same as those considered in fig. 2.6(c). The left inset shows the zero temperature conductance as a function of scaled bias, while the right inset shows the ZBC, $G(V_{sd} = 0, T)$ as a function of scaled temperature.

of bias, computed within IPA at $T = 0$ for $U = 20\Delta_0, \lambda = 18\Delta_0$, using the Gaussian form of hybridization.

The quasiparticle weight that determines the linear response regime, and the $U$ scale that determines the finite bias conductance peak show up as distinct features in the form of an extremely narrow zero bias peak (width $\sim Z_0\Delta_0 \sim 10^{-3}\Delta_0$), and broad, finite bias peaks. The top right panel shows that the ZBC decreases rapidly with increasing temperature, and reaches a value three orders of magnitude smaller than the $T = 0$ unitary limit at $T \sim 10^{-2}\Delta_0$. The ZBC follows the evolution of the dot spectral function and as fig. 2.6 shows, the melting of the Kondo peak manifests in the rapid decrease of the ZBC. However, as the temperature reaches non-universal values beyond $0.5\Delta_0$, the Hubbard bands become accessible, and the ZBC starts to rise again. The bottom panel shows the conductance as a function of bias for various temperatures in this rising ZBC regime. The two finite bias peaks are the only distinct features of the conductance in a wide temperature interval of $T \in (10^{-3}\Delta_0, 0.5\Delta_0)$. For $T \gtrsim 0.5\Delta_0$, consistent with the top right panel, the ZBC starts rising, filling in the gap between the finite bias peaks, and concomitantly the latter slightly diminishes in magnitude. An isosbestic point, commonly seen in many correlated systems, is visible around $V_{sd} \simeq 10\Delta_0$. In contrast to the results of the weak/intermediate coupling regime of the previous section, the finite bias peaks retain their form even at $T/\Delta_0 = 6.0$ as the bottom panel of fig. 2.8 shows, and this behaviour is characteristic of the strong coupling regime.

In a recent experiment by Smith *et al.*[14], the conductance through a point contact in an InGaAs/InAlAs heterostructure and a split-gate geometry was measured as a function of source-drain bias with varying in-plane and transverse magnetic fields. The highlight of this study was the tunability of the Kondo effect through the tuning of the Rashba spin-orbit coupling of the leads. The split-gate voltage, $V_{sg}$, was used to control the electron density, which in turn, determines the strength of the RSOC ($\lambda$). At a fixed temperature of about 25mK, a single zero bias peak was observed at low $\lambda$, while a 'double zero bias peak' was observed at high $\lambda$ (see fig1(i) of Smith *et al.*[14]).

The zero bias peak is known to be related to the equilibrium Kondo scale, and in the absence of a magnetic field, the zero bias peak must be present in the conductance at $T = 0$, no matter how strong the correlation is. But since the experiment is performed at a fixed and finite absolute temperature, the scenario becomes drastically different. As $\lambda$ is increased, the $T_K$ value decreases, so the ratio of $T/T_K$ increases exponentially. This implies that the system with low $\lambda$ experiences a low $T/T_K$ ratio, while the system with high $\lambda$ is at a very high $T/T_K$ ratio for a given $T$. We have shown infig. 2.9

that the central zero bias peak melts rapidly on a scale of $T_K$ at high $\lambda$, while the finite bias peaks retain their form. Thus, we conjecture that the experimental finding of a crossover from a single peak to a two-peak structure by increasing $\lambda$ is arising through a combined crossover of a weak to strong coupling (exponentially decreasing $T_K$) and from a low $T/T_K$ ratio to a high value of $T/T_K$ (due to a fixed $T$).

We consolidate this speculation in fig. 2.10, where the top two panels show the conductance as a function of bias at low $\lambda = 2\Delta_0$ (left panel) and high $\lambda = 18\Delta_0$ (right panel) computed within IPA at a fixed temperature of $T = 0.05\Delta_0$, and $U = 20\Delta_0$ for a Gaussian hybridization. We see that a single zero bias peak has transformed into a double peak structure. We emphasize that the single zero bias peak is a universal feature implying that its form and temperature dependence are determined by the Kondo scale, but the finite bias peaks are non-universal features whose position, and form are determined by non-universal parameters such as $V_{sd}, U$ and $\lambda$. The bottom panel shows the conductance for the same parameters as the top two panels, but with varying $\lambda$ marked as numbers. The conductance curves are shifted vertically by a constant number to provide clarity. The graph shows the gradual evolution of the single-peak structure into a two-peak structure. The dashed line marks the evolution of these finite bias peaks (marked by crosses).

Interestingly, the central peak is flanked by two satellite structures, which we identify visually (marked by stars). These peaks drift to higher $V_{sd}$ with increasing $\lambda$, and merge with the 'Hubbard peaks', and continue the blue shift for higher $\lambda$ values. Similar features are observed in the experimental results (see Fig. 4(c) of Smith *et al.* [14]).

Naturally, experimental results are far richer than what our simple model and the perturbative calculation reveal. However, the theoretical model used for explaining the experimental results[14] is exactly the same as the one used in the present work, and our results based on IPA may be viewed as complementary to those found by the quantum master equation approach.

## 2.4 Discussion and conclusions

We have investigated the interplay of electron-electron interactions, bias, and spin-orbit coupling on the conductance through an Anderson impurity, using a second-order Keldysh approach. We validated the method and our implementation through extensive benchmarks. The linear response regime and its relation with the equilibrium quasiparticle weight ($Z_0$) is explored, and the decrease of $Z_0$ with increasing spin-orbit coupling ($\lambda$), for finite bandwidth hybridization functions, is highlighted and discussed in detail. This

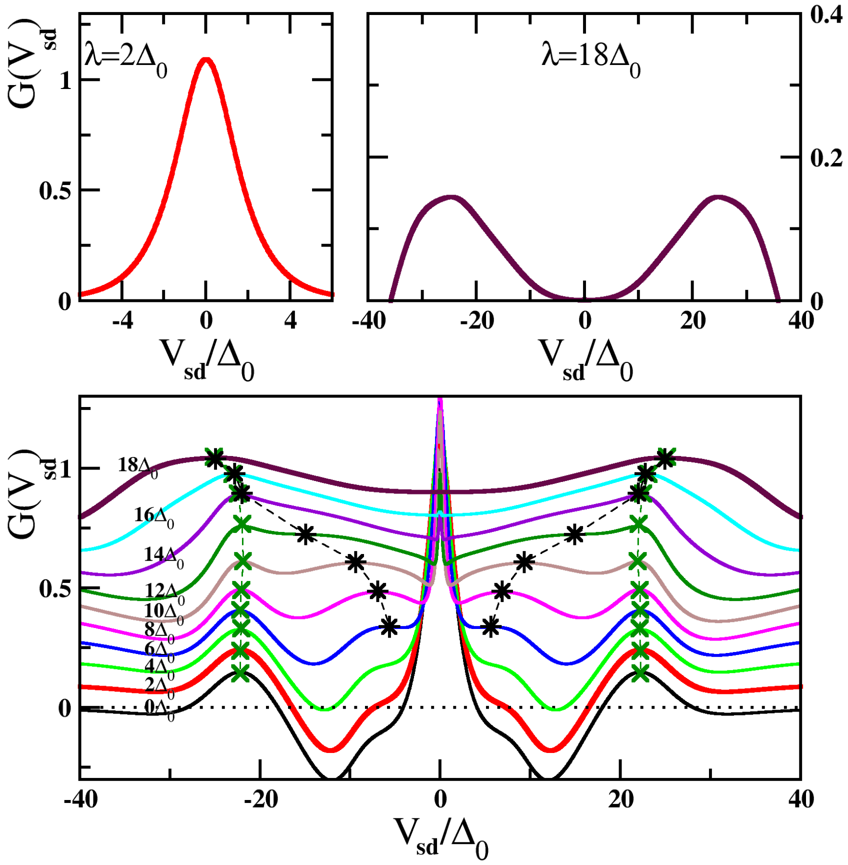

Figure 2.10: The conductance plotted as a function of $V_{sd}/\Delta_0$ for various values of SOC strengths as marked on the curves. The interaction and temperature are kept fixed at $U = 20\Delta_0, T = 0.05\Delta_0$ respectively. The crosses track the location of the $V_{sd} = \pm U$ peak, while the stars track a satellite feature of the zero bias peak. The left and right insets correspond to the low ($\lambda = 2\Delta_0$) and high ($\lambda = 18\Delta_0$) SOC strengths respectively. The insets show the different single and double peak conductance in these regimes.

decrease turns out to be crucial for explaining the experimental observation of a crossover of a single zero bias peak into a double peak structure with increasing $\lambda$. The quantum master equation approach[14], which was used for explaining the experimental results[14], while recovering the split peak structure, addresses the finite field effects. However, the dependence of the Kondo scale on $\lambda$ was not incorporated, and finite temperature effects have not been addressed, and these two aspects have been incorporated and investigated in detail in our work.

One of the inferences made from the experimental results[14] is that the Kondo scale increases with increasing $\lambda$. This inference directly contradicts our results, since in our study the Kondo scale is represented by $Z_0\Delta_0$ which has been found to decrease with increasing $\lambda$ (fig. 2.4 and hence deserves a discussion. We note that the $T_K$ is determined experimentally for the experimental system at high $\lambda$ by increasing the magnetic field (parallel to the SOC field), which induces Zeeman splitting of the spin-degenerate levels, until the double peak form of the conductance converges to a single zero bias peak structure, and then fitting the temperature dependence of the ZBC. It is well known from equilibrium studies that the quasiparticle weight increases monotonically with increasing magnetic field[58], so the determination of $T_K$ for the high magnetic field system is probably not representative of the $T_K$ for the zero-field system with the double peak conductance. In fact, for this system, if our results are any indication, then the $T_K$ is probably around the lower limit of the temperatures considered in the experiments. Increasing the magnetic field is akin to a crossover from strong to weak coupling regime, and hence is equivalent to decreasing spin-orbit coupling. And hence the merging of the double peak conductance to a single peak with increasing magnetic field may be viewed as decreasing $\lambda$ in fig. 2.9.

A 0.7 anomaly has been observed in the experimental results and we provide a brief discussion of this feature vis-a-vis our results. The 0.7 anomaly is seen as a plateau or shoulder in the conductivity when the gate voltage is varied. The origin of the 0.7 anomaly has been under intense study and has been attributed to the Kondo effect[45] and more recently to van Hove ridges[59;60]. While the Kondo and van Hove ridge physics apply to quantum dots and 1D nanowire models, it has been shown that the low energy physics of the two systems are identical[59]. In the present work, changing the gate voltage amounts to moving away from the p-h symmetric limit. The scope of the present chapter is limited to the p-h symmetric limit, and broad featureless hybridization functions (hence ruling out van-Hove singularities), hence even in principle, the present work does not have any bearing on the physics of the 0.7 anomaly.

While the IPA has been shown to work well in the parameter regime under consideration, it fails to capture many subtler aspects such as the exponential decrease of $Z_0$ with increasing interaction strength, which requires a method capable of capturing true strong coupling physics where spin fluctuations are incorporated non-perturbatively. The IPA has been generalized for finite magnetic fields[47] as well as for the p-h asymmetric case[47], incorporating which will yield fresh insights into magnetotransport measurements and the influence of valence fluctuations, and possibly the 0.7 zero bias anomaly.

# Bibliography

[1] D. Goldhaber-Gordon, J. Göres, M. A. Kastner, H. Shtrikman, D. Mahalu, and U. Meirav, Phys. Rev. Lett. **81**, 5225 (1998).

[2] S. M. Cronenwett, T. H. Oosterkamp, and L. P. Kouwenhoven, Science **281**, 540 (1998).

[3] S. J. Chorley, M. R. Galpin, F. W. Jayatilaka, C. G. Smith, D. E. Logan, and M. R. Buitelaar, Phys. Rev. Lett. **109**, 156804 (2012).

[4] W. Liang, M. P. Shores, M. Bockrath, J. R. Long, and H. Park, Nature **417**, 725 (2002).

[5] L. H. Yu and D. Natelson, Nano Letters **4**, 79 (2004).

[6] L. Grigorian, G. U. Sumanasekera, A. L. Loper, S. L. Fang, J. L. Allen, and P. C. Eklund, Phys. Rev. B **60**, R11309 (1999).

[7] J. Nygård, D. H. Cobden, and P. E. Lindelof, Nature **408**, 342 (2000).

[8] A. Eichler, R. Deblock, M. Weiss, C. Karrasch, V. Meden, C. Schönenberger, and H. Bouchiat, Phys. Rev. B **79**, 161407(R) (2009).

[9] E. A. Laird, F. Kuemmeth, G. A. Steele, K. Grove-Rasmussen, J. Nygård, K. Flensberg, and L. P. Kouwenhoven, Rev. Mod. Phys. **87**, 703 (2015).

[10] B. J. van Wees, H. van Houten, C. W. J. Beenakker, J. G. Williamson, L. P. Kouwenhoven, D. van der Marel, and C. T. Foxon, Phys. Rev. Lett. **60**, 848 (1988).

[11] K. J. Thomas, J. T. Nicholls, M. Y. Simmons, M. Pepper, D. R. Mace, and D. A. Ritchie, Phys. Rev. Lett. **77**, 135 (1996).

[12] B. Brun, F. Martins, S. Faniel, B. Hackens, G. Bachelier, A. Cavanna, C. Ulysse, A. Ouerghi, U. Gennser, D. Mailly, S. Huant, V. Bayot, M. Sanquer, and H. Sellier, Nature Communications **5**, 4290 (2014).

[13] S. Heedt, W. Prost, J. Schubert, D. Grützmacher, and T. Schäpers, Nano Letters **16**, 3116 (2016), pMID: 27104768.

[14] L. W. Smith, H.-B. Chen, C.-W. Chang, C.-W. Wu, S.-T. Lo, S.-H. Chao, I. Farrer, H. E. Beere, J. P. Griffiths, G. A. C. Jones, D. A. Ritchie, Y.-N. Chen, and T.-M. Chen, Phys. Rev. Lett. **128**, 027701 (2022).

[15] S. V. Aradhya and L. Venkataraman, Nature Nanotechnology **8**, 399 (2013).

[16] T. Kobayashi, S. Tsuruta, S. Sasaki, T. Fujisawa, Y. Tokura, and T. Akazaki, Phys. Rev. Lett. **104**, 036804 (2010).

[17] A. Tsvelick and P. Wiegmann, Advances in Physics **32**, 453 (1983).

[18] H. R. Krishna-murthy, J. W. Wilkins, and K. G. Wilson, Phys. Rev. B **21**, 1003 (1980).

[19] R. Bulla, T. A. Costi, and T. Pruschke, Rev. Mod. Phys. **80**, 395 (2008).

[20] F. B. Anders, Phys. Rev. Lett. **101**, 066804 (2008).

[21] F. B. Anders and A. Schiller, Phys. Rev. Lett. **95**, 196801 (2005).

[22] P. Fritsch and S. Kehrein, Phys. Rev. B **81**, 035113 (2010).

[23] E. L. Minarelli, J. B. Rigo, and A. K. Mitchell, arXiv preprint arXiv:2209.01208 (2022).

[24] N. S. Wingreen and Y. Meir, Phys. Rev. B **49**, 11040 (1994).

[25] T. Fujii and K. Ueda, Phys. Rev. B **68**, 155310 (2003).

[26] V. Lopes and E. V. Anda, Journal of Physics and Chemistry of Solids **128**, 188 (2019), spin-Orbit Coupled Materials.

[27] A. V. Joura, J. K. Freericks, and A. I. Lichtenstein, Phys. Rev. B **91**, 245153 (2015).

[28] P. Werner, T. Oka, M. Eckstein, and A. J. Millis, Phys. Rev. B **81**, 035108 (2010).

[29] M. Nuss, M. Ganahl, H. G. Evertz, E. Arrigoni, and W. von der Linden, Phys. Rev. B **88**, 045132 (2013).

[30] P. Mehta and N. Andrei, Phys. Rev. Lett. **96**, 216802 (2006).

[31] Y. Cheng, W. Hou, Y. Wang, Z. Li, J. Wei, and Y. Yan, New Journal of Physics **17**, 033009 (2015).

[32] A. Dorda, M. Nuss, W. von der Linden, and E. Arrigoni, Phys. Rev. B **89**, 165105 (2014).

[33] C. Fasth, A. Fuhrer, L. Samuelson, V. N. Golovach, and D. Loss, Phys. Rev. Lett. **98**, 266801 (2007).

[34] A. Zazunov, R. Egger, T. Jonckheere, and T. Martin, Phys. Rev. Lett. **103**, 147004 (2009).

[35] T. Tanttu, B. Hensen, K. W. Chan, C. H. Yang, W. W. Huang, M. Fogarty, F. Hudson, K. Itoh, D. Culcer, A. Laucht, A. Morello, and A. Dzurak, Phys. Rev. X **9**, 021028 (2019).

[36] L. Guo, Y. Yan, R. Xu, J. Li, and C. Zeng, Phys. Rev. Lett. **126**, 057701 (2021).

[37] T. Schäpers, J. Knobbe, and V. A. Guzenko, Phys. Rev. B **69**, 235323 (2004).

[38] M. Zarea, S. E. Ulloa, and N. Sandler, Phys. Rev. Lett. **108**, 046601 (2012).

[39] A. Wong, S. E. Ulloa, N. Sandler, and K. Ingersent, Phys. Rev. B **93**, 075148 (2016).

[40] R. Žitko and J. Bonča, Phys. Rev. B **84**, 193411 (2011).

[41] H.-F. Lü and Y. Guo, Phys. Rev. B **76**, 045120 (2007).

[42] S. Zhang, W. Gong, G. Wei, and A. Du, Journal of Applied Physics **109**, 023704 (2011).

[43] M. M. Gelabert, L. Serra, D. Sánchez, and R. López, Phys. Rev. B **81**, 165317 (2010).

[44] M. A. Topinka, B. J. LeRoy, S. E. J. Shaw, E. J. Heller, R. M. Westervelt, K. D. Maranowski, and A. C. Gossard, Science **289**, 2323 (2000).

[45] Y. Meir, K. Hirose, and N. S. Wingreen, Phys. Rev. Lett. **89**, 196802 (2002).

[46] M. J. Iqbal, R. Levy, E. J. Koop, J. B. Dekker, J. P. de Jong, J. H. M. van der Velde, D. Reuter, A. D. Wieck, R. Aguado, Y. Meir, and C. H. van der Wal, Nature **501**, 79 (2013).

[47] A. A. Aligia, Phys. Rev. B **74**, 155125 (2006).

[48] Y. Meir and N. S. Wingreen, Phys. Rev. Lett. **68**, 2512 (1992).

[49] A. C. Hewson, *The Kondo Problem to Heavy Fermions*, Cambridge Studies in Magnetism (Cambridge University Press, 1993).

[50] H. Kajueter and G. Kotliar, Phys. Rev. Lett. **77**, 131 (1996).

[51] H. Barman and N. S. Vidhyadhiraja, International Journal of Modern Physics B **25**, 2461 (2011).

[52] A. Georges, G. Kotliar, W. Krauth, and M. J. Rozenberg, Rev. Mod. Phys. **68**, 13 (1996).

[53] M. Grobis, I. G. Rau, R. M. Potok, H. Shtrikman, and D. Goldhaber-Gordon, Phys. Rev. Lett. **100**, 246601 (2008).

[54] L. P. Syaina and M. A. Majidi, Journal of Physics: Conference Series **1011**, 012072 (2018).

[55] S. A. Evlashin, M. A. Tarkhov, D. A. Chernodubov, A. V. Inyushkin, A. A. Pilevsky, P. V. Dyakonov, A. A. Pavlov, N. V. Suetin, I. S. Akhatov, and V. Perebeinos, Phys. Rev. Applied **15**, 054057 (2021).

[56] D. E. Logan, M. P. Eastwood, and M. A. Tusch, Journal of Physics: Condensed Matter **10**, 2673 (1998).

[57] A. V. Kretinin, H. Shtrikman, D. Goldhaber-Gordon, M. Hanl, A. Weichselbaum, J. von Delft, T. Costi, and D. Mahalu, Phys. Rev. B **84**, 245316 (2011).

[58] D. E. Logan and N. L. Dickens, Europhysics Letters (EPL) **54**, 227 (2001).

[59] F. Bauer, J. Heyder, E. Schubert, D. Borowsky, D. Taubert, B. Bruognolo, D. Schuh, W. Wegscheider, J. von Delft, and S. Ludwig, Nature **501**, 73 (2013).

[60] D. H. Schimmel, B. Bruognolo, and J. von Delft, Phys. Rev. Lett. **119**, 196401 (2017).

# Chapter 3

# Influence of valence fluctuations on conductance of a quantum dot coupled to chiral leads

## 3.1 Introduction

As we have seen in chapter 2, the steady state single impurity Anderson Model (SIAM) and the related class of models serve as a prototypical model to study the interplay between the local Coulomb interaction on the dot and the DC bias on the leads. While we considered only the particle-hole (p-h) symmetric limit in chapter 2, the more general case of p-h asymmetry can be accessed by varying the dot energy level, which can be experimentally realised by varying the gate-source voltage.

Valence fluctuations occur in strongly-correlated systems due to the interaction between the localized and conduction electrons leading to a mixed-valence regime where the valence configuration of the strongly-correlated (generally transition metal) atom fluctuates. The fluctuations occur in a regime when there is strong hybridisation between the lead and dot electronic levels and is generally seen in experiments with variation of the temperature or pressure[1;2]. However, the gate voltage also determines the valence fluctuation cost by changing the dot energy and subsequently determines whether the system is in the Kondo coupling or in the mixed valence regimes[3]. Going beyond the p-h symmetric limit via the gate voltage also allows access to different regimes like Coulomb blockade[4].

Out of equilibrium, varying the gate-source voltage allows the observation of phenomena like Kondo ridges in the conductance[5] and can also be used to indirectly control other parameters of the system like spin-orbit coupling[6].

In systems which can be modelled as multiple dots, other parameters like the long-range RKKY interaction can also be varied by the gate voltage[7]. Quantum point contacts, which can be modelled as quantum dots[8] also show interesting physics with the variation of the gate-source voltage including the well-studied 0.7 anomaly and the accompanying zero bias conductance peak[9].

In this chapter, we study the interplay between the spin-orbit coupling and other system parameters like the p-h asymmetry, onsite interaction and the DC bias. Spin-orbit coupling (SOC) is central in applications like topological materials, spintronics, etc. while also giving rise to interesting physics like the zero bias conductance peaks seen in chapter 2. SOC has been measured directly in two-atom quantum dots[10] among other experimental observations including an anomalous Josephson current[11]. The SOC has also been shown to be tunable using a magnetic field[12] and gate-voltage[6] and hence is tenable experimentally. The interplay of SOC with interactions has been well studied in equilibrium[13–15] and also out of equilibrium[16] (see chapter 2). Coming to the interplay between p-h asymmetry and SOC, while a few theoretical studies[17] exist in equilibrium, the interplay between the gate voltage and SOC has been well studied out of equilibrium experimentally[18–21].

The SIAM has been studied using various theoretical methods such as numerical renormalization group[22–25], non-crossing approximation[26], perturbative methods[27–29], quantum Monte Carlo methods[30], exact diagonalization methods[31], Bethe ansatz[32], hierarchical equation of motion[33] and master equation approaches[34], etc. While each method has its strengths and weakness, in this chapter, we use the interpolative approximation (IPA) proposed for the p-h symmetric case by A.A Aligia[35]. The method is based on the iterative perturbation theory (IPT) in equilibrium and similarly uses an ansatz for the retarded second-order self-energy by calculating two parameters using the atomic limit and the high frequency limits of the model. In equilibrium, the IPT is known to perform well in the mixed valence regime.

While the IPA has been applied to the p-h symmetric case[35], incorporating the p-h asymmetry and studying the effect of gate voltage requires that the Luttinger theorem (in zero bias and temperature) and the current continuity (in finite bias) are respected. Also, the 0.7 anomaly which is seen in experiments with QPCs has been modelled both in terms of the SIAM[8] and other models[9]. The 0.7 anomaly is seen most clearly in strong magnetic fields, but is thought to have signatures in the zero field limit too. As seen in chapter 2, the SOC has an effect of decreasing the equilibrium scale and also broadening the hybridisation between the leads and the dot. We investigate the effect of the SOC on both the spectral function and on the current. We also investigate whether there is any signature of the 0.7 anomaly in the case of the QD coupled to chiral leads and subsequently the effect of SOC on the same.

In this chapter, we first introduce the problem, followed by a discussion of the formalism. In the formalism section, we derive the IPA self-energies, the interacting Green's functions and the expression for the current. We also mention some numerical details involved in the calculation. The formalism is followed by the results where we begin by benchmarking the method and look at the effect of SOC and gate voltage in both equilibrium and on the current. Finally, we conclude with a summary of the chapter.

## 3.2 Formalism

In this chapter, we look at the effect of valence fluctuations on the steady-state DC bias transport of the SIAM coupled to leads with SOC. The valence fluctuations are induced by the means of a source-gate voltage, which can be modelled as the dot energy.

### 3.2.1 Hamiltonian

The Hamiltonian for the system can be written as

$$H = H_0 + H_{\mathrm{d}} + H_{\mathrm{SO}} + H_{\mathrm{hyb}}\,, \tag{3.1}$$

where, the conduction bands of the leads are represented by

$$H_0 = \sum_{\alpha\mathbf{k}\sigma} \epsilon_{\mathbf{k}} c^{\dagger}_{\alpha\mathbf{k}\sigma} c_{\alpha\mathbf{k}\sigma} \tag{3.2}$$

and the isolated quantum dot is given by

$$H_{\mathrm{d}} = \sum_{\sigma} (\epsilon_d) d^{\dagger}_{\sigma} d_{\sigma} + U n_{d\uparrow} n_{d\downarrow}. \tag{3.3}$$

The Rashba spin-orbit interaction in the two-dimensional conduction band may be described as

$$H_{\mathrm{SO}} = \sum_{\alpha\mathbf{k}} \lambda \psi^{\dagger}_{\alpha\mathbf{k}} (\mathbf{k} \times \vec{\sigma})_z \psi_{\alpha\mathbf{k}}\,, \tag{3.4}$$

where $\mathbf{k} = (k_x, k_y)$, and $\psi^{\dagger}_{\alpha\mathbf{k}} = (c^{\dagger}_{\alpha\mathbf{k},\sigma}\ c^{\dagger}_{\alpha\mathbf{k},\bar{\sigma}})$. Finally, the hybridization between the quantum dot and the conduction band is given by

$$H_{\mathrm{hyb}} = \sum_{\alpha\mathbf{k}\sigma} \left( V_{\mathbf{k}} c^{\dagger}_{\alpha\mathbf{k}\sigma} d_{\sigma} + \mathrm{h.c} \right)\,. \tag{3.5}$$

We can use the angular momentum expansion[13] (detailed in Appendix B) to write the effective Hamiltonian with the emergent chiral leads as

$$\begin{aligned} H &= \sum_{khm} \epsilon_{kh} (c_{kh}^{m+\frac{1}{2}})^\dagger c_{kh}^{m+\frac{1}{2}} \\ &+ \sum_{khm} \delta_{m,0} \tilde{V}_k \left( (c_{kh}^{m+\frac{1}{2}})^\dagger d_\uparrow + h (c_{kh}^{m-\frac{1}{2}})^\dagger d_\downarrow + \text{h.c} \right) \\ &+ H_{\text{d}} \,, \end{aligned} \tag{3.6}$$

where $h = \pm 1$ is an emergent chiral quantum number, and $j_m = m + h/2$ is the angular momentum quantum number.

### 3.2.2 Green's functions and self-energy

In order to study the system, we need to calculate the dot Green's functions and subsequently the observable quantities like current, etc. Since we are working in the non-equilibrium limit, the Keldysh Green's functions (details in Appendix A) need to be calculated. This can be done by evaluating the matrix Dyson equations

$$\begin{aligned} \boldsymbol{G} = \begin{pmatrix} 0 & G_d^a \\ G_d^r & 2G_d^< + G^r - G^a \end{pmatrix} &= \\ \begin{pmatrix} 0 & g_d^a \\ g_d^r & 2g_d^< + g^r - g^a \end{pmatrix} &+ \boldsymbol{g} \begin{pmatrix} \Sigma^r - \Sigma^a - 2\Sigma^< & \Sigma^r \\ \Sigma^a & 0 \end{pmatrix} \boldsymbol{G} \\ &= \boldsymbol{g} + \boldsymbol{g}\boldsymbol{\Sigma}\boldsymbol{G} \end{aligned} \tag{3.7}$$

Which can be written by using the relationship between the different Green's functions as the pair of equations

$$[G_d^r(\omega)]^{-1} = [g_d^r(\omega)]^{-1} - \Sigma^r(\omega) \,, \tag{3.8}$$

$$G_d^<(\omega) = |G_d^r(\omega)|^2 \left( \frac{g_d^<(\omega)}{|g_d^r(\omega)|^2} - \Sigma^<(\omega) \right) , \tag{3.9}$$

The free Green's functions can be calculated using the equation of motion approach and are given by

$$\begin{aligned} [g_{d\sigma}^r(\omega)]^{-1} &= \omega - \tilde{\mu}_0 - \sum_\alpha \Gamma_\alpha(\omega) \\ g_{d\sigma}^<(\omega) &= 2\imath |g_{d\sigma}^r(\omega)|^2 \sum_\alpha \Delta_\alpha(\omega) f(\omega - \mu_\alpha) \end{aligned} \tag{3.10}$$

where we have the hybridisation function (refer to appendix B for details)

$$\Gamma_\alpha(\omega) = V_0^2 \mathrm{H}\left[\omega^+ - \mu_\alpha - h\lambda\right] \tag{3.11}$$

where H is the Hilbert transformation defined as

$$\mathrm{H}[z] = \int d\epsilon \, \frac{\rho_0(\epsilon)}{z - \epsilon} \, . \tag{3.12}$$

for a Gaussian density of states $\rho_0$ and $\Delta_\alpha(\omega) = -\operatorname{Im}\{\Gamma_\alpha(\omega)\}$.

The effect of interaction enters through the self-energy $\Sigma^{r,<}(\omega)$ which in turn can be calculated using the interpolative approximation (detailed calculations are found in appendix B). The self energies are given by

$$\Sigma^r(\omega) = U\langle n_d \rangle + \Sigma^r_{int}(\omega) \tag{3.13}$$

$$\Sigma^<(\omega) = \Sigma^<_{int}(\omega) \tag{3.14}$$

Where we have $n_d$, the dot occupancy and $\Sigma^r_{int}$ is the retarded IPA self energy that can be calculated (see appendix B for details) using the ansatz

$$\Sigma^r_{int}(\omega) = \frac{A_1 \Sigma^{r2}(\omega)}{1 - A_2 \Sigma^{r2}(\omega)} \tag{3.15}$$

We have the coefficients $A_1$ and $A_2$ obtained by considering the atomic and high-frequency limits and given by

$$A_1 = \frac{\langle n_d \rangle (1 - \langle n_d \rangle)}{\langle n_d^0 \rangle (1 - \langle n_d^0 \rangle)} \tag{3.16}$$

$$A_2 = \frac{\tilde{\mu}_0 - \epsilon_d - (1 - \langle n_d \rangle) U}{U^2 \langle n_d^0 \rangle (1 - \langle n_d^0 \rangle)} \tag{3.17}$$

which when substituted give

$$\Sigma^r_{int}(\omega) = \frac{\langle n_d \rangle (1 - \langle n_d \rangle) \Sigma^{r2}(\omega)}{\langle n_d^0 \rangle (1 - \langle n_d^0 \rangle) + [\tilde{\mu}_0 - \epsilon_d - (1 - \langle n_d \rangle) U][\Sigma^{r2}(\omega)/U^2]} . \tag{3.18}$$

Similarly, the lesser than IPA self energy $\Sigma^<_{int}$ can be calculated using the ansatz

$$\Sigma^<_{int}(\omega) = \frac{\operatorname{Im} \Sigma^r_{int}(\omega)}{\operatorname{Im} \Sigma^{r2}(\omega)} \Sigma^{<2}(\omega) \tag{3.19}$$

The $\Sigma^{r2,<2}$ are the self energies corresponding to the second order of the perturbation theory in $U$ (details again in appendix B) and are given by the expressions

$$\Sigma^{r2}(\omega) = U^2 \int d\epsilon_1 d\epsilon_2 d\epsilon_3 \frac{\rho^0(\epsilon_1)\rho^0(\epsilon_2)\rho^0(\epsilon_3)}{\omega^+ + \epsilon_3 - \epsilon_2 - \epsilon_1} \times [\tilde{f}(-\epsilon_1)\tilde{f}(-\epsilon_2)\tilde{f}(\epsilon_3) + \tilde{f}(\epsilon_1)\tilde{f}(\epsilon_2)\tilde{f}(-\epsilon_3)] \tag{3.20}$$

and

$$\Sigma^{<2}(\omega) = -2\imath\pi U^2 \int d\epsilon_1 d\epsilon_2 \rho^0(\epsilon_1)\rho^0(\epsilon_2)\rho^0(\epsilon_1+\epsilon_2-\omega) \\ \times [\tilde{f}(\epsilon_1)\tilde{f}(\epsilon_2)\tilde{f}(\omega-\epsilon_1-\epsilon_2)] \quad (3.21)$$

with $\rho^0 = -\frac{1}{\pi}\,\mathrm{Im}\{g_d^r(\omega)\}$, the dot density of states and the weighted Fermi function $\tilde{f}(\omega) = \sum_\alpha \Delta_\alpha(\omega) f_\alpha(\omega) / \sum_\alpha \Delta_\alpha(\omega)$. The interacting Green's functions can be calculated from the Dyson equations (eq. (3.8)).

### 3.2.3 Current

The central quantity to be calculated in order to study transport is the current. This can be calculated by using the Meir-Wingreen formula[36]

$$j_\alpha = \frac{2e}{\hbar}\int \frac{d\omega}{2\pi}\,\mathrm{Re}\left\{ \sum_{(khj_m)(d\sigma)} \tilde{V}^2_{k\alpha}[G^r_{d\sigma}(\omega) g^<_{k\alpha hj_m}(\omega) + G^<_{d\sigma}(\omega) g^a_{k\alpha hj_m}(\omega)] \right\} \quad (3.22)$$

which can be simplified by writing in terms of the dot Green's functions and the hybridisation as

$$j_\alpha = \pm_\alpha \int_{-\infty}^{\infty} d\omega (2i\Delta_\alpha(\omega))\,[2if_\alpha\,\mathrm{Im}\{G^r_d(\omega)\} + G^<_d(\omega)] \quad (3.23)$$

where we have the ± signs for the left and right leads respectively. We have also set $e/\hbar = 1$ and defined $f_\alpha = f(\omega - \mu_\alpha)$ for convenience.

### 3.2.4 Numerical details

While at the outset it may seem that the IPA self-energy and subsequently the Green's functions involve a straight forward calculation, one should notice that the IPA self-energy depends on the dot occupation $n_d$, which is further calculated using the interacting Green's functions as

$$n_d = \frac{1}{\pi}\int d\omega\, G^<(\omega) \quad (3.24)$$

Thus, we need to self consistently evaluate $n_d$ and the self-energy. This can be achieved by tuning $\tilde{\mu}_0$ while keeping the dot energy $\epsilon_d$ fixed.

Apart from the self-consistency, we also require adiabatic continuity to the Fermi liquid and hence require that the Luttinger theorem holds. This requires that the Luttinger integral

$$I_L = \mathrm{Im}\int_{-\infty}^{0} \frac{d\Sigma^r(\omega)}{d\omega} G^r_d(\omega) = 0 \quad (3.25)$$

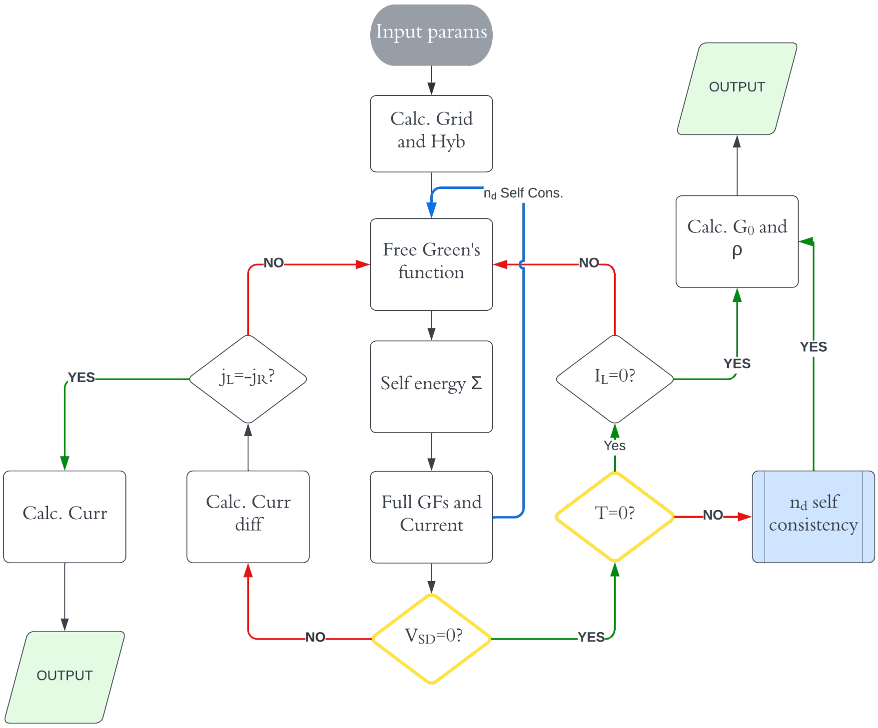

Figure 3.1: Flowchart for the calculations of ssIPA in the p-h asymmetric case with the constraints indicated depending on the parameters of calculation

In the zero temperature, equilibrium limit, the $\tilde{\mu}_0$ is varied while keeping the self-consistently derived $n_d$ constant in order to satisfy $I_L = 0$. The Luttinger theorem no longer holds away from these limits and the constraint of $I_L = 0$ is relaxed.

Since we are considering a closed system, conservation of charge is a necessary condition and leads to another constraint in the finite bias case. In the finite bias case, we require in addition to the self-consistency, the conservation of charge, via the current continuity equation $j_L = -j_R$. This constraint is again satisfied by varying $\tilde{\mu}_0$ while keeping the self-consistent $n_d$ fixed. The steps involved in calculation for all the calculation parameters are shown in the flowchart fig. 3.1.

The calculation of the $\tilde{\mu}_0$ subject to the constraints above is not always guaranteed to be numerically stable and we calculate the results for parameters where the discrepancy is less than a suitable tolerance.

## 3.3 Results

Now that we have derived the equations and described the numerical details of implementing the steady-state IPA, we can take a look at some of the results. By choosing a reasonable tolerance in evaluating the constraints, we are able to study the system in a wide range of parameters including access to the $V_{sd} = 0$ limit.

### 3.3.1 Benchmarks

Before we can investigate the interplay between $U, \lambda, V_{sd}$ and $\epsilon_d$, we need to benchmark the method away from p-h symmetry. This can be done by looking at the variation of the zero bias conductance with the scaled dot energy $\epsilon_d/U$ for various values of temperature, keeping the SOC strength $\lambda = 0$. These calculations are then compared to the NRG results of Izumida et al.[37] where we find nice qualitative agreement. The zero bias conductance is calculated using the expression[37]

$$G_0 = \frac{2e^2}{h} \int d\omega \left( \frac{-\partial f}{\partial \omega} \right) \pi \rho_d(\omega) \Delta_0 \tag{3.26}$$

Where $f(\omega)$ is the Fermi function. We plot the variation of the zero bias conductance with the dot energy $\epsilon_d/U$ using a Gaussian DOS for $U = 20\Delta_0, \lambda = 0$ in fig. 3.2 for various temperature values as indicated in the legend. We not only see a good qualitative agreement with the NRG results, but also see the appearance of isosbestic points near $G_0 \sim 0.65$ close to the $\epsilon_d = -U, 0$ values. The value of $G_0 \sim 0.65$ could indicate the origin to be related to the 0.7 anomaly reported in experiments with quantum point contacts, which also have the same low-energy Hamiltonian[38]. In all our calculations, we consider $\Delta_0 = 0.1, U = 20\Delta_0$ and the Gaussian DOS unless specified.

### 3.3.2 Equilibrium

Before going to the case of finite bias, we need to ascertain the effects of an interplay between the p-h asymmetry and the spin-orbit coupling $\lambda$. We look at the effects of $\lambda$ and temperature $T$ on the spectral function for various values of $\epsilon_d$.

We plot the spectral function in fig. 3.3 in each panel for different parameter ranges as mentioned in the caption. We begin with the zero temperature and SOC case in the top-left panel to ascertain the behaviour of the spectral function with $\epsilon_d$. We calculate the spectral function for $U = 20\Delta_0$ (constant

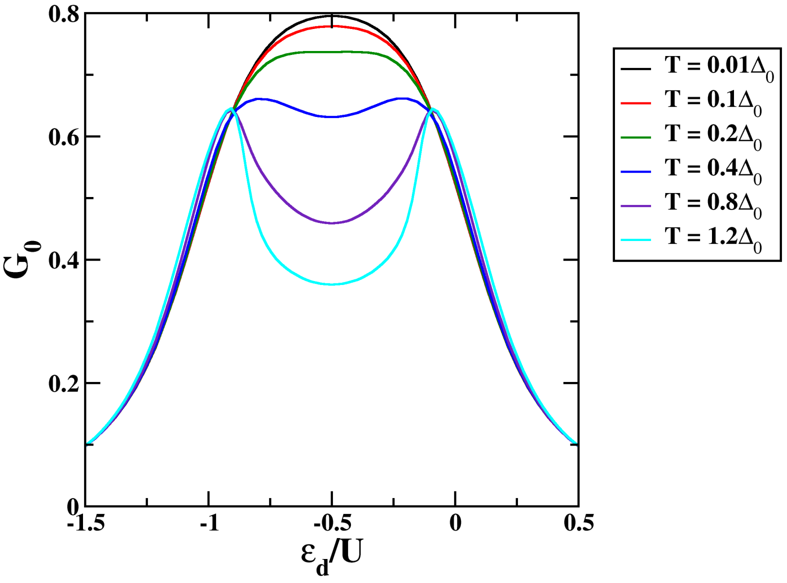

Figure 3.2: The zero bias conductance calculated using eq. (3.26) as a function of the scaled dot-energy $\epsilon_d/U$ for various values of temperature as indicated. The method benchmarks well with the NRG calculations of Izumida et al.[37].We also notice isosbestic points around $G_0 \sim 0.65$ which could be an indication of the 0.7 anomaly reported in experiments.

for all calculations presented) and see the appearance of the central Kondo peak and the Hubbard bands in the p-h symmetric case. Changing the $\epsilon_d$, results in a spectral weight transfer away from the $\omega = 0$ value. We see in the top-right panel that the finite temperature has an effect of the reducing the $\omega = 0$ peak, much like we see in chapter 2. The SOC too reprises its role in reducing the equilibrium scale and reducing the width of the central peak as can be seen in the bottom-left panel. The SOC also has an effect on the effective bandwidth. The combined effects of SOC and temperature can be seen to broaden the peaks along with diminishing the sidebands as seen for all values of $\epsilon_d$ in the bottom-right panel.

The zero bias conductance calculations show the clear effect of temperature and can be re-calculated in the presence of finite SOC to further study the interplay. We plot the zero bias conductance for $\lambda = 5\Delta_0$ in fig. 3.4 for various values of temperature. It is immediately apparent that the SOC has an effect of enhancing the effect of temperature and the appearance of the double peak happens at a lower temperature. This can be explained by the fact that the SOC sharpens the Kondo peak, i.e. reduces $T_K$, the universal scale. Since the temperature should always be compared to $T_K$, we see that increasing SOC has a net effect of increasing the effective temperature.

### 3.3.3 Current

Turning on the bias $V_{sd}$ on the leads and going out of equilibrium, we study the effects of SOC, p-h asymmetry and temperature on the IV characteristics. We plot the current through the left lead in fig. 3.5 for different values of $\epsilon_d/U$ for the range of SOC strengths $\lambda$ and temperatures $T$ as considered in fig. 3.3. Plotting the current for the $\lambda = 0, T = 0$ case, we see that the p-h symmetric limit has an oscillatory behaviour, while the IV curves corresponding to the deeply p-h asymmetric values of $\epsilon_d = -1.5U, 0.5U$ are mostly positive. It is also noteworthy that the $\epsilon_d = -U$ curve does not show any oscillation, while the $\epsilon_d = 0$ curve does. This clearly indicates a preferred direction of p-h asymmetry. Since we are looking at only the current through the left lead, this might be effect of $\mu_L$ on the hybridisation due to the finite Gaussian DOS. In the top-right panel, we see that the temperature does not have a significant effect on the general behaviour, but does affect the linear response regime, at least in the p-h symmetric case. Coming to the bottom-left panel, we see that the SOC broadens the effective hybridisation, and the oscillations are pushed beyond the $V_{sd}$ values considered here. The bottom-right panel shows the combined effect of SOC and temperature lead to a broadening of the effective hybridisation and a smoothening of the IV curve.

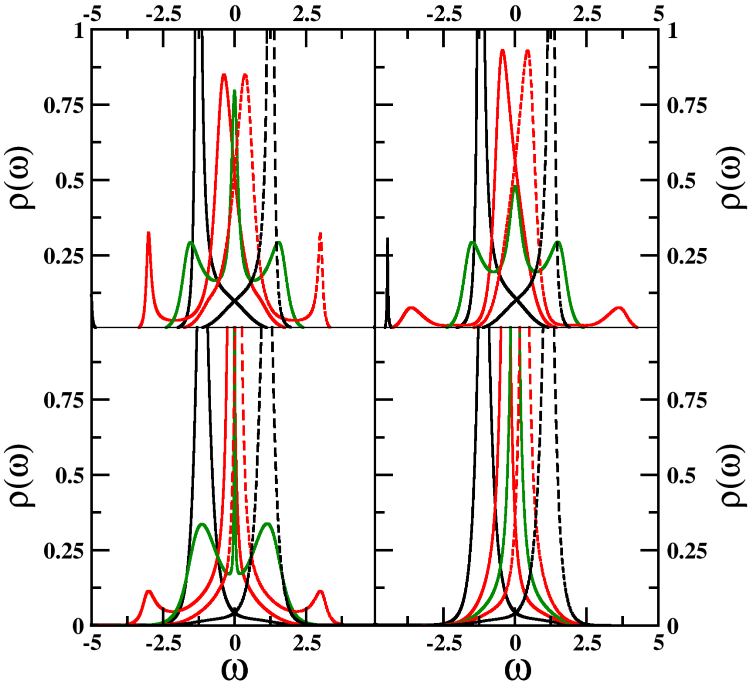

Figure 3.3: In each of the panels, we plot the spectral function $\rho(\omega)$ as a function of frequency $\omega$ for various values of $\epsilon_d/U$. The black solid line in all the panels corresponds to $\epsilon_d = -1.5U$, while the black dashed line corresponds to $\epsilon_d = 0.5U$. Similarly, the red solid and dashed lines correspond to $\epsilon_d = -U$ and $\epsilon_d = 0$ respectively. The green solid line corresponds to the p-h symmetric limit with $\epsilon_d = -U/2$. The panels correspond to different values of $\lambda$ and $T$, starting with the $\lambda = 0, T = 0$ case on the top-left panel. The top-right panel corresponds to $\lambda = 0, T = 0.1\Delta_0$, the bottom-left panel corresponds to $\lambda = 10\Delta_0, T = 0$ while the bottom right panels looks at the combined effects with $\lambda = 10\Delta_0, T = 0.1\Delta_0$

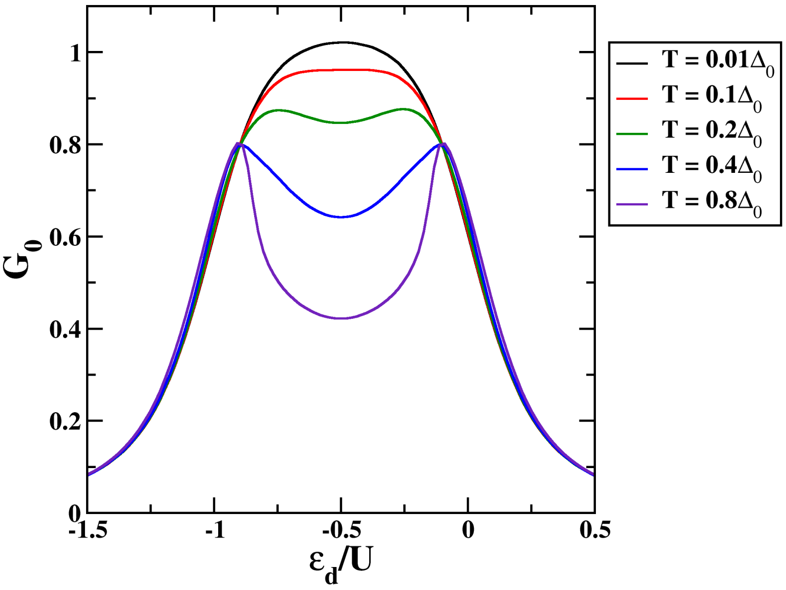

Figure 3.4: The zero bias conductance plotted as a function of $\epsilon_d/U$ in the presence of SOC ($\lambda = 5\Delta_0$) shows the persistence of the isosbestic point for various temperature values. The SOC has an effect of enhancing the effect of temperature due to the corresponding reduction of the universal scale as seen in chapter 2.

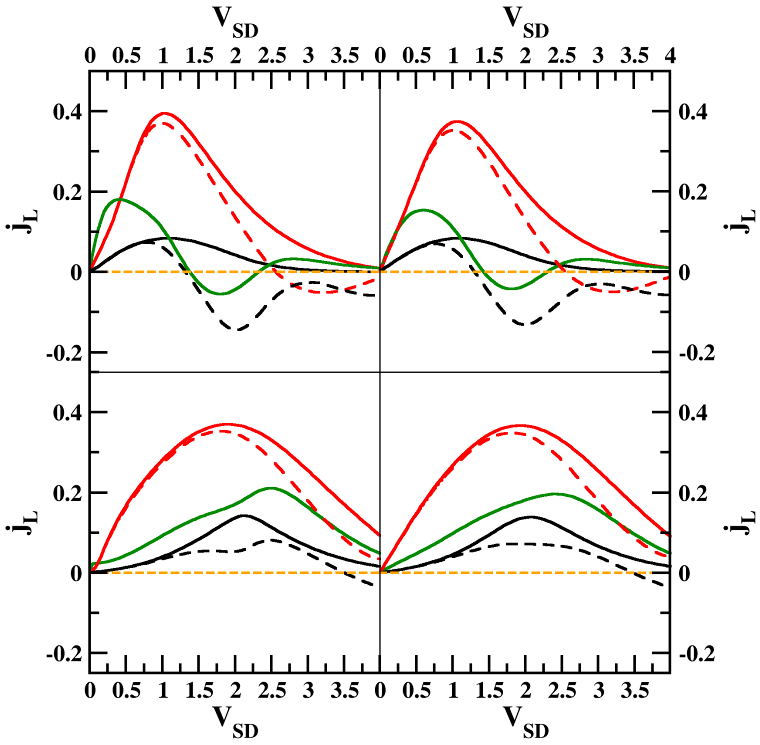

Figure 3.5: The current through the left lead $j_L$ plotted as a function of the $V_{sd}$ for various values of $\epsilon_d/U$ calculated for different parameters in each panel. The colour and line-styles correspond to the same $\epsilon_d/U$ as in fig. 3.3 and the panels correspond to the same $\lambda$ and $T$ values considered. We see that the current is enhanced and positive only away from p-h symmetry and an oscillatory behaviour is seen for the p-h symmetric curve. The temperature has an effect on the linear response, while the SOC broadens the current curve due to the increased effective bandwidth.

## 3.4 Summary

In this chapter, we have implemented the steady-state interpolative approximation to study the interplay between the valence fluctuations and SOC in DC transport through a quantum dot. The method has been benchmarked in the equilibrium case with earlier results[37] and we see a good agreement. While the calculation of $\tilde{\mu}_0$ is not numerically stable for all parameter ranges, we have been able to work with a wide range of parameters including the zero bias, finite temperature and a large range of $\epsilon_d$ values.

In this chapter, we focus on mainly investigating the interplay between the SOC and the p-h asymmetry. In equilibrium, we see that the effect of SOC in reducing the equilibrium scale lead to a larger effective temperature as evidenced by the effect on the zero bias conductance for various values of $\epsilon_d/U$. The reduction in the scale is also seen directly as the narrowing of the Kondo peak in the spectral function.

Out of equilibrium, we see that the current through the lead has an oscillatory behaviour and the emergence of negative current for the p-h symmetric and the moderately low p-h asymmetric cases. The SOC has an effect of increasing the effective bandwidth and thereby increasing the range of $V_{sd}$ where the current is positive for every value of $\epsilon_d/U$ considered.

Coming to the 0.7 anomaly, we see that the zero bias conductance shows an isosbestic point very close to the value of 0.7 and could be a signature of the same. Since we have not considered the magnetic field, this cannot be substantiated and needs a systematic study of the same. Such a systematic study in the presence of the magnetic field is a future direction which will be investigated.

# Bibliography

[1] Z. X. Yin, X. Du, W. Z. Cao, J. Jiang, C. Chen, S. R. Duan, J. S. Zhou, X. Gu, R. Z. Xu, Q. Q. Zhang, W. X. Zhao, Y. D. Li, Y.-f. Yang, H. F. Yang, A. J. Liang, Z. K. Liu, H. Yao, Y. P. Qi, Y. L. Chen, and L. X. Yang, Phys. Rev. B **105**, 245106 (2022).

[2] S. Dash, T. Morita, K. Kurokawa, Y. Matsuzawa, N. L. Saini, N. Yamamoto, J. Kajitani, R. Higashinaka, T. D. Matsuda, Y. Aoki, and T. Mizokawa, Phys. Rev. B **98**, 144501 (2018).

[3] S. Kirchner, L. Zhu, Q. Si, and D. Natelson, Proceedings of the National Academy of Sciences **102**, 18824 (2005).

[4] L. P. Kouwenhoven, D. G. Austing, and S. Tarucha, Reports on Progress in Physics **64**, 701 (2001).

[5] J. Nygård, D. H. Cobden, and P. E. Lindelof, Nature **408**, 342 (2000).

[6] L. W. Smith, H.-B. Chen, C.-W. Chang, C.-W. Wu, S.-T. Lo, S.-H. Chao, I. Farrer, H. E. Beere, J. P. Griffiths, G. A. C. Jones, D. A. Ritchie, Y.-N. Chen, and T.-M. Chen, Phys. Rev. Lett. **128**, 027701 (2022).

[7] Q. Yang, L. Wang, Z. Zhou, L. Wang, Y. Zhang, S. Zhao, G. Dong, Y. Cheng, T. Min, Z. Hu, W. Chen, K. Xia, and M. Liu, Nature Communications **9**, 991 (2018).

[8] Y. Meir, K. Hirose, and N. S. Wingreen, Phys. Rev. Lett. **89**, 196802 (2002).

[9] F. Bauer, J. Heyder, E. Schubert, D. Borowsky, D. Taubert, B. Bruognolo, D. Schuh, W. Wegscheider, J. von Delft, and S. Ludwig, Nature **501**, 73 (2013).

[10] C. Fasth, A. Fuhrer, L. Samuelson, V. N. Golovach, and D. Loss, Phys. Rev. Lett. **98**, 266801 (2007).

[11] A. Zazunov, R. Egger, T. Jonckheere, and T. Martin, Phys. Rev. Lett. **103**, 147004 (2009).

[12] T. Tanttu, B. Hensen, K. W. Chan, C. H. Yang, W. W. Huang, M. Fogarty, F. Hudson, K. Itoh, D. Culcer, A. Laucht, A. Morello, and A. Dzurak, Phys. Rev. X **9**, 021028 (2019).

[13] M. Zarea, S. E. Ulloa, and N. Sandler, Phys. Rev. Lett. **108**, 046601 (2012).

[14] A. Wong, S. E. Ulloa, N. Sandler, and K. Ingersent, Phys. Rev. B **93**, 075148 (2016).

[15] R. Žitko and J. Bonča, Phys. Rev. B **84**, 193411 (2011).

[16] A. Mirmira and N. S. Vidhyadhiraja, Phys. Rev. B **107**, 085107 (2023).

[17] G. R. de Sousa, J. F. Silva, and E. Vernek, Phys. Rev. B **94**, 125115 (2016).

[18] J. Nitta, T. Akazaki, H. Takayanagi, and T. Enoki, Phys. Rev. Lett. **78**, 1335 (1997).

[19] J. B. Miller, D. M. Zumbühl, C. M. Marcus, Y. B. Lyanda-Geller, D. Goldhaber-Gordon, K. Campman, and A. C. Gossard, Phys. Rev. Lett. **90**, 076807 (2003).

[20] A. D. Caviglia, M. Gabay, S. Gariglio, N. Reyren, C. Cancellieri, and J.-M. Triscone, Phys. Rev. Lett. **104**, 126803 (2010).

[21] S. Grap, S. Andergassen, J. Paaske, and V. Meden, Phys. Rev. B **83**, 115115 (2011).

[22] F. B. Anders, Phys. Rev. Lett. **101**, 066804 (2008).

[23] F. B. Anders and A. Schiller, Phys. Rev. Lett. **95**, 196801 (2005).

[24] P. Fritsch and S. Kehrein, Phys. Rev. B **81**, 035113 (2010).

[25] E. L. Minarelli, J. B. Rigo, and A. K. Mitchell, arXiv preprint arXiv:2209.01208 (2022).

[26] N. S. Wingreen and Y. Meir, Phys. Rev. B **49**, 11040 (1994).

[27] T. Fujii and K. Ueda, Phys. Rev. B **68**, 155310 (2003).

[28] V. Lopes and E. V. Anda, Journal of Physics and Chemistry of Solids **128**, 188 (2019), spin-Orbit Coupled Materials.

[29] A. V. Joura, J. K. Freericks, and A. I. Lichtenstein, Phys. Rev. B **91**, 245153 (2015).

[30] P. Werner, T. Oka, M. Eckstein, and A. J. Millis, Phys. Rev. B **81**, 035108 (2010).

[31] M. Nuss, M. Ganahl, H. G. Evertz, E. Arrigoni, and W. von der Linden, Phys. Rev. B **88**, 045132 (2013).

[32] P. Mehta and N. Andrei, Phys. Rev. Lett. **96**, 216802 (2006).

[33] Y. Cheng, W. Hou, Y. Wang, Z. Li, J. Wei, and Y. Yan, New Journal of Physics **17**, 033009 (2015).

[34] A. Dorda, M. Nuss, W. von der Linden, and E. Arrigoni, Phys. Rev. B **89**, 165105 (2014).

[35] A. A. Aligia, Phys. Rev. B **74**, 155125 (2006).

[36] Y. Meir and N. S. Wingreen, Phys. Rev. Lett. **68**, 2512 (1992).

[37] W. Izumida, O. Sakai, and S. Suzuki, Journal of the Physical Society of Japan **70**, 1045 (2001).

[38] F. Bauer, J. Heyder, E. Schubert, D. Borowsky, D. Taubert, B. Bruognolo, D. Schuh, W. Wegscheider, J. von Delft, and S. Ludwig, Nature **501**, 73 (2013).

# Chapter 4

# A non-perturbative Local Moment Approach for systems out of equilibrium

## 4.1 Introduction

As we have seen earlier, the solution of the Single Impurity Anderson Model (SIAM) is important both as a paradigmatic benchmark for any method and also in using the method as an impurity solver for Dynamical Mean Field Theory (DMFT) based calculations. In this regard, the Local Moment Approach (LMA) has been a very successful method in equilibrium and has been applied to a wide variety of systems like the SIAM[1], the Gapped Anderson Model[2], Periodic Anderson Model[3;4], Bilayer models[5], etc. The success of the LMA is in no small part due to the explicit inclusion of the local moment via the Unrestricted Hartree-Fock (UHF) Green's functions. The regular and well-known deficiencies of the UHF are circumvented in the LMA by considering a two self-energy picture followed by a restoration of the symmetry[1]. This allows the LMA to be applied to solve systems with a wide range of interaction and coupling strengths, unlike the slave particle approaches, which rely on $U \rightarrow \infty$ and the $1/N$ approaches, which rely on $N \rightarrow \infty$ limits and cannot be accurately applied to a spin-$\frac{1}{2}$ ($N = 2$) and finite U scenarios.

Nonequilibrium quantum phenomena have been studied using a wide variety of approaches like Keldysh perturbation theory[6;7], Quantum Monte Carlo methods[8], Renormalization group methods[9], Equation of Motion techniques[10], Exact diagonalization based approaches[11], Master equation based approaches[12], etc. Experiments have measured transport quantities like current, differential conductance, etc. in systems with various parameters and found universal behaviour in the low bias linear response regime[13;14]. But for large bias values beyond from the linear response regime, the universality is seen to break down and can lead to the emergence of non-universal features. Even though there are quite a few theoretical methods, each suffers from certain shortcomings that limit the scope of application. A few examples of this would be the sign problem in the Quantum Monte-Carlo-based approaches, the limited system size practically accessible with exact diagonalisation-based methods and the unsystematic truncation of the hierarchy of equations of motion in the equation of motion-based techniques. This has resulted in consensus regarding many phenomena like the fate of the Kondo effect still not being established out of equilibrium. Capturing the subtler aspects of universality, like an exponentially small Kondo scale, is impossible with Keldysh perturbation theory-based methods, and a non-perturbative approach is required. Keeping all these factors in mind, the generalization of the LMA to the nonequilibrium scenario, as we have done in this chapter, is indeed a much-needed and fruitful endeavour.

The LMA has been applied with great success in equilibrium, in particular by its excellent agreement with exact methods like Bethe ansatz and NRG. The LMA has been known to capture accurately the strong-coupling behaviour both at and away from particle-hole symmetry. It has also been used to explain the universal features at finite temperature. It is not only an accurate method, but is also computationally inexpensive compared to its counterparts like the CTQMC, DMRG or Exact Diagonalization. Thus, it is a great candidate for generalization to nonequilibrium.

The LMA is generalized to non-equilibrium by recasting Green's functions and the self-energies in terms of the Keldysh contour times and subsequently using the Langreth rules to work with real-time quantities. We obtain general time-dependent expressions for the aforementioned functions and then restrict ourselves to the steady state scenario where we can use the Fourier transform to express these quantities in terms of $\omega$. As a demonstration, we consider the SIAM in the infinitely wide flat band limit where we can show analytically that the expressions reduce to the equilibrium counterparts when the bias is set to zero and the corresponding $U \to \infty$ asymptotes for the self-energy and the equilibrium scale $\omega_m$. The results from our calculations can be compared both to well-known equilibrium benchmarks and results from other non-equilibrium techniques applied on the SIAM. In equilibrium, the NRG results and earlier work with the LMA serve as sanity checks, while the zero bias finite temperature conductance and the corresponding empirically derived form serve as a good benchmark to look at universality[14]. It is well known that the Kondo temperature, which is proportional to the location of the polarization peak ($\omega_m$) is the equilibrium scale and universality is seen to hold even for large values of temperature ($T \sim 100\omega_m$)[15]. The role of $\omega_m$ out of equilibrium and the extent of universality are important questions we answer.

Mesoscopic transport has been well studied and continues to have sustained interest[16–18]. In this regard, the IV (current-voltage) diagrams and the differential conductance are also interesting quantities that are obtained from the generalized LMA. Unlike methods like CTQMC, the steady-state LMA can be easily applied to both the zero and finite temperature regimes and allows us to look at the effect of temperature on the transport quantities like the current and differential conductance.

In this chapter, we have derived the formalism for the steady-state LMA followed by analytical expressions in the case of equilibrium. This is followed by a detailed explanation of the numerical implementation followed by the results and their discussion. We conclude with the summary and conclusions of the chapter.

## 4.2 Formalism

As we have seen, the Single Impurity Anderson Model (SIAM) is a paradigm that is the ideal starting place to generalize the LMA to out-of-equilibrium. The SIAM connected to leads with a DC bias is given by the following Hamiltonian:

$$H = \epsilon_d \, d^\dagger_\sigma d_\sigma + U n_\uparrow n_\downarrow + \sum_{k\sigma,\alpha} \left( \epsilon_{k,\alpha} c^\dagger_{k\sigma,\alpha} c_{k\sigma,\alpha} + V_{k\alpha} d^\dagger_\sigma c_{k\sigma,\alpha} + V^*_{k\alpha} c^\dagger_{k\sigma,\alpha} d_\sigma \right) \quad (4.1)$$

where $d^\dagger_\sigma\,(d_\sigma)$ are the creation(annihilation) operators on the impurity site. $n_{\uparrow(\downarrow)} = d^\dagger_{\uparrow(\downarrow)} d_{\uparrow(\downarrow)}$ is the number operator. $c^\dagger_{k\sigma,\alpha}\,(c_{k\sigma,\alpha})$ are the corresponding operators for the noninteracting baths. $\alpha \in \{L, R\}$, where $L$, $R$ denote the left and the right baths, which are set at the chemical potentials $\mu_L$ and $\mu_R$, respectively, and have a temperature $T$. $\epsilon_{k,\alpha}$ are the bath dispersions and $V_{k\alpha}$ denote the hybridisation between the baths and the impurity. To be able to simplify the calculations and to derive analytical results, we consider the limit where $\epsilon_{k,\alpha} = \epsilon$ and $V_{k,\alpha} = V$, which correspond to the flat band and $k$-independent coupling.

The generalization of the LMA to non-equilibrium involves the following steps: derivation of the unrestricted Hartree-Fock Green's functions, constructing and evaluating the bare polarization diagrams using the UHF Green's functions, using the random phase approximation to derive the full polarization and calculating the $<, R$ self energies in terms of the polarization and UHF Green's functions. Since the LMA consists of two self-energies, the restoration of symmetry between these has to be done in equilibrium. The details of these individual steps follows.

### 4.2.1 Unrestricted Hartree Fock Approximation

The LMA is built on the unrestricted Hartree-Fock (UHF) Approximation which includes the local moment explicitly and allows us to later dynamically couple the single-particle processes to the underlying low-energy spin fluctuations. Since the UHF approximation is a mean-field approximation for the interaction term, we can begin by writing the mean-field approximation explicitly as

$$H = \epsilon_d \, d_\sigma^\dagger d_\sigma + U \sum_\sigma (n_\sigma \langle n_{\bar{\sigma}} \rangle) + \sum_{k\sigma,\alpha} \left( \epsilon_{k,\alpha} c_{k\sigma,\alpha}^\dagger c_{k\sigma,\alpha} + V_{k\alpha} d_\sigma^\dagger c_{k\sigma,\alpha} + V_{k\alpha}^* c_{k\sigma,\alpha}^\dagger d_\sigma \right) \tag{4.2}$$

where the $\langle n \rangle$ is the expectation value of the number operator in the ground state. The local moment($M$) and the occupation($n$) on the dot can be calculated using the expressions

$$\begin{aligned} M &= |\langle n_\uparrow \rangle - \langle n_\downarrow \rangle| \\ n &= \langle n_\uparrow \rangle + \langle n_\downarrow \rangle \end{aligned} \tag{4.3}$$

Using these definitions, we can write the interaction term as

$$U \sum_\sigma (n_\sigma \langle n_{\bar{\sigma}} \rangle) = \sum_\sigma \frac{U}{2}(n - \sigma M) \tag{4.4}$$

The corresponding Green's functions can be calculated using the Dyson equation

$$\mathcal{G}(z, z') = \mathcal{G}_0(z, z') + \int_{\mathcal{C}} \mathcal{G}_0(z, \bar{z}) \Sigma(\bar{z}) \mathcal{G}(\bar{z}, z') d\bar{z} \tag{4.5}$$

Where $\mathcal{G}(z, z')$ is the interacting Green's function, $\mathcal{G}_0(z, z')$ is the non-interacting Green's function and $\Sigma(\bar{z})$ is the self-energy. The indices $z, z', \bar{z}$ correspond to times on $\mathcal{C}$, the Keldysh contour. The essential feature of the UHF is the appearance of two degenerate solutions for the impurity moment namely $M = \pm|M|$, which we indicate with $A, B$ respectively to get

$$G^0 = \frac{1}{2}[\mathcal{G}_{A\sigma} + \mathcal{G}_{B\sigma}] \tag{4.6}$$

The UHF approximation is an approximation for the self-energy and for the particle-hole symmetric case, the dot energy level $\epsilon_d = -\frac{U}{2}$, and $n = 1$. This leads to the cancellation of the first term in eq (4.4) which gives the required self-energy contribution

$$\Sigma^0_{A\sigma} = \frac{-\sigma U}{2} M = -\Sigma^0_{B\sigma} \tag{4.7}$$

Which we can see is independent of time and hence a static approximation. We can now use the Langreth rules (see §1 for the derivation) to go from the Keldysh contour to real time. Since we choose to work in the steady-state regime, only $t - t'$ the time difference is relevant and allows us to use the Fourier transform to obtain

$$\begin{aligned} \mathcal{G}^R_{A\sigma}(\omega) &= \frac{1}{\omega^+ + \frac{\sigma U M}{2} + \Gamma(\omega)} \\ \mathcal{G}^<_{A\sigma}(\omega) &= 2i\mathrm{Im}\left[\Gamma(\omega)\right] \left\{ \frac{f(\omega - \mu_L) + f(\omega - \mu_R)}{2} \right\} |\mathcal{G}^R_{A\sigma}(\omega)|^2 \end{aligned} \tag{4.8}$$

Where $\Gamma(\omega)$ is the hybridisation function and $f(\omega - \mu_\alpha)$ is the Fermi function. Corresponding equations can also be written for the $B$-solution. The hybridisation function can be calculated as $\Gamma = \sum_\alpha \Gamma_\alpha$, with the individual lead hybridisations being given by

$$\Gamma_\alpha(\omega) = \sum_k \frac{|V_k|^2}{\omega^+ - \epsilon_{k\alpha}} \tag{4.9}$$

We can define a weighted Fermi function $\tilde{f}(\omega) = \left\{ \frac{\Delta_L f(\omega-\mu_L) + \Delta_R f(\omega-\mu_R)}{\Delta_L + \Delta_R} \right\}$, where $\Delta_\alpha = -\mathrm{Im}\{\Gamma_\alpha\}$ and the spectral function $\rho_\sigma = -\frac{1}{\pi}\mathrm{Im}\{\mathcal{G}^R_{A\sigma}(\omega)\}$ to write the following

$$\begin{aligned} \mathrm{Im}\{\mathcal{G}^R_{A\sigma(\omega)}\} &= -\pi\rho_\sigma(\omega) \\ \mathrm{Im}\{\mathcal{G}^A_{A\sigma(\omega)}\} &= \pi\rho_\sigma(\omega) \\ \mathcal{G}^<_{A\sigma(\omega)} &= 2\pi i \rho_\sigma(\omega)\tilde{f}(\omega) \\ \mathcal{G}^>_{A\sigma(\omega)} &= -2\pi i \rho_\sigma(\omega)\left(1 - \tilde{f}(\omega)\right) \end{aligned} \tag{4.10}$$

In the subsequent sections of this chapter, we restrict ourselves to the infinite flat-band case and a $k$-independent coupling to the dot to get

$$\Gamma_\alpha(\omega) = -\frac{i\Delta_0}{2}. \tag{4.11}$$

While in equilibrium the UHF recovers the noninteracting ($U = 0$) and atomic ($\Delta_0 = 0$) limits, the Fermi liquid behaviour is violated and no corresponding Kondo resonance is captured. While this is a serious deficiency, one can circumvent this issue is by dynamically coupling the single-particle processes to the low-frequency spin fluctuations.

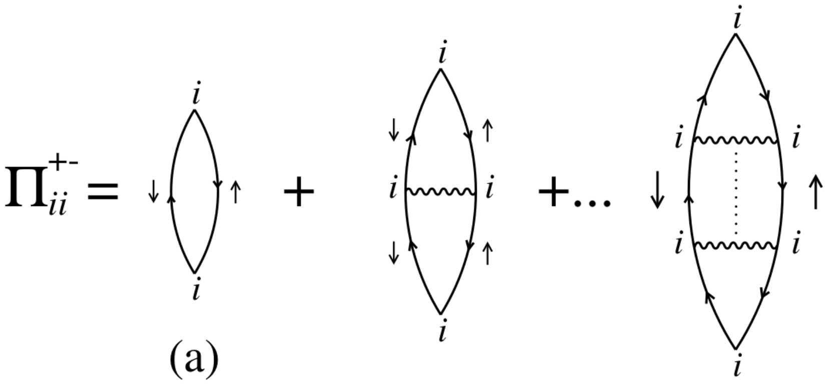

Figure 4.1: The particle-hole ladder diagrams denoting the polarization $\Pi_{+-}$ with bare propagators denoted by solid lines and the interaction denoted by the squiggly lines. The time increases vertically

### 4.2.2 Polarization

The transverse spin fluctuations can be considered by calculating the corresponding polarization propagators

$$\begin{aligned}\Pi^{+-}(z,z') &= i\langle T[S^+(z)S^-(z')]\rangle \\ \Pi^{-+}(z,z') &= i\langle T[S^-(z)S^+(z')]\rangle\end{aligned} \tag{4.12}$$

Where we have dropped the $A/B$ labels for convenience and use the expression for the $A$ solution unless specified. The propagators can be calculated by performing the ladder sum of the interactions as shown in figure 4.1

#### Zeroth Order

The zeroth order polarization bubble in figure 4.1 can be calculated using the expression

$$^0\Pi_{+-}(z,z') = i\mathcal{G}_\downarrow(z,z')\mathcal{G}_\uparrow(z',z). \tag{4.13}$$

We can now go from the Keldysh contour to the real time by making use of the Langreth rules corresponding to the product to get the real time components

$$\begin{aligned}{}^0\Pi^{R/A}_{+-}(t,t') &= i\mathcal{G}^{R/A}_\downarrow(t,t')\mathcal{G}^<_\uparrow(t',t) + i\mathcal{G}^<_\downarrow(t,t')\mathcal{G}^{A/R}_\uparrow(t',t) \\ {}^0\Pi^<_{+-}(t,t') &= i\mathcal{G}^<_\downarrow(t,t')\mathcal{G}^>_\uparrow(t',t)\end{aligned} \tag{4.14}$$

Like before, we restrict ourselves to the steady-state, which allows us to use the Fourier transform $g(\omega) = 1/2\pi \int d(t-t')e^{i\omega(t-t')}g(t-t')$ to get

$$\begin{aligned} {}^0\Pi^{R/A}_{+-}(\omega) &= i\int \tfrac{d\epsilon}{2\pi}\left[\mathcal{G}^<_\downarrow(\epsilon)\mathcal{G}^{R/A}_\uparrow(\epsilon-\omega) + \mathcal{G}^{A/R}_\downarrow(\epsilon)\mathcal{G}^<_\uparrow(\epsilon-\omega)\right] \\ {}^0\Pi^<_{+-}(\omega) &= i\int \tfrac{d\epsilon}{2\pi}\left[\mathcal{G}^<_\downarrow(\epsilon)\mathcal{G}^>_\uparrow(\epsilon-\omega)\right] \end{aligned} \tag{4.15}$$

While the convolutions above can be directly calculated, it is better for numerical implementation to express the polarization in terms of the spectral function $\rho_\sigma = -\frac{1}{\pi}\operatorname{Im}\{\mathcal{G}^R_\sigma(\omega)\}$. This can be achieved by using the spectral representation for the retarded and advanced Green's function as given below

$$\mathcal{G}^{R/A}_\sigma(\epsilon) = \int \frac{d\epsilon'\rho_\sigma(\epsilon')}{\epsilon^\pm - \epsilon'}. \tag{4.16}$$

Using the spectral representation and substituting the corresponding frequencies, we get the expressions

$$\begin{aligned} {}^0\Pi^{R/A}_{+-}(\omega) = \int \tfrac{d\epsilon}{2\pi}\Bigg[&(i\mathcal{G}^<_\downarrow(\epsilon))\left(\int \frac{d\epsilon'\rho_\uparrow(\epsilon')}{\epsilon^\pm - \omega - \epsilon'}\right) \\ &+\left(\int \frac{d\epsilon'\rho_\downarrow(\epsilon')}{\epsilon^\mp - \epsilon'}\right)(i\mathcal{G}^<_\uparrow(\epsilon-\omega))\Bigg] \end{aligned} \tag{4.17}$$

and

$$ {}^0\Pi^<_{+-}(\omega) = i\int \tfrac{d\epsilon}{2\pi}\{i\mathcal{G}^<_\downarrow(\epsilon)\}\{-i\mathcal{G}^>_\uparrow(\epsilon-\omega)\} \tag{4.18}$$

where we have used the fact that $G^{\lessgtr}$ are purely imaginary.

While we have now represented the convolutions in terms of the spectral function and other real functions like $iG^<_\sigma(\epsilon)$, the integral in eqn (4.16) and subsequently in the polarization cannot be directly implemented and needs to be simplified. This can be done by using the Sokhotski–Plemelj theorem

$$\int \frac{d\epsilon'\rho_\sigma(\epsilon')}{\epsilon^\pm - \epsilon'} = \mathcal{P}\int \frac{d\epsilon'\rho_\sigma(\epsilon')}{\epsilon - \epsilon'} \pm i\pi\rho(\epsilon) \tag{4.19}$$

where $\mathcal{P}$ stands for the Cauchy Principal Value. Then we require only the imaginary parts of ${}^0\Pi^{r/<}_{+-}(\omega)$, which are given by

$$\operatorname{Im}\{{}^0\Pi^R_{+-}(\omega)\} = -\int \tfrac{d\epsilon}{2}\left[\left(\operatorname{Im}\{\mathcal{G}^<_\downarrow(\epsilon)\}\right)\rho_\uparrow(\epsilon-\omega) - \rho_\downarrow(\epsilon)\left(\operatorname{Im}\{\mathcal{G}^<_\uparrow(\epsilon-\omega)\}\right)\right] \tag{4.20}$$

and

$$\mathrm{Im}\big\{{}^0\Pi^<_{+-}(\omega)\big\} = -\int \tfrac{d\epsilon}{2\pi}\,\mathrm{Im}\big\{\mathcal{G}^<_\downarrow(\epsilon)\big\}\,\mathrm{Im}\big\{\mathcal{G}^>_\uparrow(\epsilon-\omega)\big\} \tag{4.21}$$

These expressions can now be expressed only in terms of real functions by using the equations (4.10) and substituting the expressions for the lesser than components to get

$$\mathrm{Im}\big\{{}^0\Pi^R_{+-}(\omega)\big\} = \pi\int d\epsilon\,\Big[\rho_\downarrow(\epsilon)\tilde{f}(\epsilon)\rho_\uparrow(\epsilon-\omega) - \rho_\downarrow(\epsilon)\rho_\uparrow(\epsilon-\omega)(1-\tilde{f}(\epsilon-\omega))\Big] \tag{4.22}$$

and

$$\mathrm{Im}\big\{{}^0\Pi^<_{+-}(\omega)\big\} = 2\pi\int d\epsilon\rho_\downarrow(\epsilon)\tilde{f}(\epsilon)\rho_\uparrow(\epsilon-\omega)\,\Big(1-\tilde{f}(\epsilon-\omega)\Big) \tag{4.23}$$

**Hard-core Boson constraint**

We see in the eqn (4.23) the appearance of the product $\tilde{f}(\epsilon)[1-\tilde{f}(\epsilon-\omega)]$. This product is responsible for carrying the information about the occupation of the dot in the self energy. We can now simplify this product using the expressions

$$\begin{aligned} 1-\tilde{f}(\epsilon) &= \frac{(1-f_L(\epsilon))+(1-f_R(\epsilon))}{2} \\ 1-f_L(\epsilon) &= \frac{1}{e^{\beta(-\epsilon+\mu_L)}+1} \end{aligned} \tag{4.24}$$

Where we have used $f_\alpha(\epsilon) = f(\epsilon-\mu_\alpha)$ and the definition of the Fermi function in terms of $\beta = 1/k_BT$, the inverse temperature. If we now work in the bias range where the particle-hole symmetry is conserved, i.e. $\mu_L = -\mu_R = \mu$, we get

$$\begin{aligned} 1-f_L(\epsilon) &= \frac{1}{e^{\beta(-\epsilon-\mu_R)}+1} &&= f_R(-\epsilon) \\ 1-\tilde{f}(\epsilon) &= \frac{f_R(-\epsilon)+f_L(-\epsilon)}{2} &&= \tilde{f}(-\epsilon) \end{aligned} \tag{4.25}$$

Using this identity, we can now simplify the product of Fermi functions in eqn (4.23), as follows

$$\begin{aligned} \tilde{f}(\epsilon)[1-\tilde{f}(\epsilon-\omega)] &= \tilde{f}(\epsilon)\tilde{f}(-\epsilon+\omega) \\ &= \frac{1}{4}\left[f_L(\epsilon)+f_R(\epsilon)\right]\left[f_L(-\epsilon+\omega)+f_R(-\epsilon+\omega)\right] \end{aligned} \tag{4.26}$$

Which gives rise to four terms

$$\begin{aligned} I &: f_L(\epsilon)f_L(-\epsilon+\omega) \\ II &: f_R(\epsilon)f_R(-\epsilon+\omega) \\ III &: f_L(\epsilon)f_R(-\epsilon+\omega) \\ IV &: f_R(\epsilon)f_L(-\epsilon+\omega) \end{aligned} \tag{4.27}$$

Now, let us consider the $I$st term. We can use the definition of the Fermi functions to write

$$\begin{aligned} f_L(\epsilon)f_L(-\epsilon+\omega) &= \frac{1}{e^{\beta(\epsilon-\mu)}+1}\frac{1}{e^{\beta(-\epsilon+\omega-\mu)}+1} \\ &= \frac{e^{\beta(\epsilon-\omega+\mu)}}{\left(e^{\beta(\epsilon-\mu)}+1\right)\left(e^{\beta(\epsilon-\omega+\mu)}+1\right)} \end{aligned} \tag{4.28}$$

The product can now be simplified using partial fractions to get

$$\begin{aligned} f_L(\epsilon)f_L(-\epsilon+\omega) &= \frac{e^{\beta(\epsilon-\omega+\mu)}}{e^{\beta(\epsilon+\mu)}-e^{\beta(\epsilon-\mu)}}\left[\frac{1}{e^{\beta(\epsilon-\mu)}+1}-\frac{1}{e^{\beta(\epsilon-\omega+\mu)}+1}\right] \\ &= \frac{e^{\beta(-\omega+\mu)}}{e^{\beta(-\omega+\mu)}-e^{\beta(-\mu)}}[f_L(\epsilon)-f_R(\epsilon-\omega)] \\ &= \frac{1}{1-e^{\beta(-2\mu+\omega)}}[f_L(\epsilon)-f_R(\epsilon-\omega)] \\ &= -n_B(\omega-2\mu)[f_L(\epsilon)-f_R(\epsilon-\omega)] \end{aligned} \tag{4.29}$$

Where we have the Bose function $n_B(\omega-2\mu) = \frac{1}{e^{\beta(\omega-2\mu)}-1}$ . Also, using $2\mu = V_{sd}$, the source-drain bias, we have

$$I : f_L(\epsilon)f_L(-\epsilon+\omega) = -n_B(\omega-V_{sd})[f_L(\epsilon)-f_R(\epsilon-\omega)] \tag{4.30}$$

Carrying out a similar exercise for the other terms yields

$$\begin{aligned} II &: -n_B(\omega+V_{sd})[f_R(\epsilon)-f_L(\epsilon-\omega)] \\ III &: -n_B(\omega)[f_L(\epsilon)-f_L(\epsilon-\omega)] \\ IV &: -n_B(\omega)[f_R(\epsilon)-f_R(\epsilon-\omega)] \end{aligned} \tag{4.31}$$

Thus the product in eqn (4.23) reads

$$\begin{aligned} \tilde{f}(\epsilon)[1-\tilde{f}(\epsilon-\omega)] = -\frac{1}{4}\Big[&n_B(\omega-V_{sd})[f_L(\epsilon)-f_R(\epsilon-\omega)] \\ &+ n_B(\omega+V_{sd})[f_R(\epsilon)-f_L(\epsilon-\omega)] \\ &+ 2n_B(\omega)[\tilde{f}(\epsilon)-\tilde{f}(\epsilon-\omega)]\Big] \end{aligned} \tag{4.32}$$

The Bose functions arising in the expressions above correspond to a spin-flip when an electron with spin $\sigma$ hops into and out of the impurity site resulting in an electron with spin $\bar{\sigma}$ correspondingly hopping off or into the impurity site. Since the spin-flip occurs as a result of Fermion hopping, the number of spin-flips at a given energy is limited by the electronic occupation of the impurity site at that energy. Hence, the spin-flips are hard-core Bosons. This implies that while at zero temperature, the expressions in eqn (4.23) can be directly used to compute the polarization, at finite temperature, the Bose function needs to be treated carefully.

At finite temperature, if one uses the eqn (4.32) directly, the Bose function corresponds to free Bosons, which allow the possibility of an infinite number of spin-flips and hence have to be replaced with the physically correct hard-core Bosons. This can be done by replacing the finite temperature Bose function with its zero temperature counterpart, i.e. $n_B(\omega) \to -\Theta(-\omega)$. This constraint though physically motivated is not being derived diagrammatically and is hence an assumption of the method. Not imposing such a constraint results in incorrect results even in equilibrium. Thus we have the corrected expression

$$\begin{aligned}\mathrm{Im}\big\{{}^0\Pi^<_{+-}(\omega)\big\} = \frac{\pi}{2}\int d\epsilon \rho_\downarrow(\epsilon)\rho_\uparrow(\epsilon-\omega)\Big[\Theta(-\omega+V_{sd})[f_L(\epsilon)-f_R(\epsilon-\omega)] \\ +\Theta(-\omega-V_{sd})[f_R(\epsilon)-f_L(\epsilon-\omega)] \\ +2\Theta(-\omega)[\tilde{f}(\epsilon)-\tilde{f}(\epsilon-\omega)]\Big]\end{aligned} \tag{4.33}$$

The expressions eqs. (4.22) and (4.23) are convolutions of real functions and subsequently can be calculated easily using either the Fast Fourier Transform (in case of a uniform grid) or explicit multiplication (in case of a nonuniform grid). The real parts of the polarization can be found using the Kramers-Kronig Transformation

$$\mathrm{Re}\{\chi(\omega)\} = \frac{1}{\pi}\int \frac{\mathrm{Im}\{\chi(\epsilon)\}}{\epsilon-\omega}d\epsilon \tag{4.34}$$

Thus the zeroth order bubble of the Polarization can be calculated as

$$\begin{aligned}{}^0\Pi^R_{+-}(\omega) &= \mathrm{Re}\big\{{}^0\Pi^R_{+-}(\omega)\big\} + i\,\mathrm{Im}\big\{{}^0\Pi^R_{+-}(\omega)\big\} \\ {}^0\Pi^<_{+-}(\omega) &= i\,\mathrm{Im}\big\{{}^0\Pi^<_{+-}(\omega)\big\}\end{aligned} \tag{4.35}$$

Since we considered only the $A$ solution, we need a way to calculate the corresponding zeroth order propagators for the $B$ solution. While this can be done by repeating the entire calculation, we can use the symmetry of $A, B$ solutions[1] to write

$${}^0\Pi^{R/<}_{A+-}(\omega) = {}^0\Pi^{R/<}_{B-+}(\omega) \tag{4.36}$$

We can also look at the form of the polarization ( eq. (4.13)) and notice that by a change of variables that

$$ {}^{0}\Pi^{R/<}_{A+-}(\omega) = {}^{0}\Pi^{R/<}_{A-+}(-\omega) \tag{4.37}$$

### Full Polarization - Random Phase Approximation

The LMA involves considering the spin fluctuation via the polarization propagators which have a form as seen in fig. 4.1, these diagrams can be mathematically expressed as

$$\Pi_{+-}(z,z') = \mathcal{G}_{\downarrow}(z,z')\mathcal{G}_{\uparrow}(z',z) + \int d\bar{z}\mathcal{G}(z,\bar{z})U(\bar{z})\mathcal{G}(\bar{z},z') + \cdots \tag{4.38}$$

The form of the diagrams allows us to calculate the propagators to all orders by performing the ladder sum. The corresponding Dyson equation for this reads as

$$\Pi_{+-}(z,z') = {}^{0}\Pi_{+-}(z,z') + \int d\bar{z}^{0}\Pi_{+-}(z,\bar{z})U\Pi_{+-}(\bar{z},z') \tag{4.39}$$

Where we have used eq. (4.13) and the fact that $U(\bar{z}) = U$. We once again apply the Langreth rules to go from the Keldysh contour times to the real times. This gives us the components

$$\begin{aligned} \Pi^{R/A}_{+-}(t,t') &= {}^{0}\Pi^{R/A}_{+-}(t,t') + \int dt_1{}^{0}\Pi^{R/A}_{+-}(t,t_1)U\Pi^{R/A}_{+-}(t_1,t') \\ \Pi^{<}_{+-}(t,t') &= {}^{0}\Pi^{<}_{+-}(t,t') + \int dt_1{}^{0}\Pi^{R}_{+-}(t,t_1)U\Pi^{<}_{+-}(t_1,t') \\ &\quad + \int dt_1{}^{0}\Pi^{<}_{+-}(t,t_1)U\Pi^{A}_{+-}(t_1,t') \end{aligned} \tag{4.40}$$

We first consider the retarded component. We now again restrict ourselves to the steady state which allows us to apply a Fourier transform as shown below

$$\Pi^{R}_{+-}(\omega) = {}^{0}\Pi^{R}_{+-}(\omega) + U\int dt_1 e^{-i\omega_1(t-t_1)0}\Pi^{R}_{+-}(t-t_1)e^{-i\omega_2(t_1-t')}\Pi^{R}_{+-}(t_1-t') \tag{4.41}$$

The integral over the intermediate time can be simplified by using the identity $\int dte^{i(\omega_1-\omega_2)t} = \delta(\omega_1-\omega_2)$ to get

$$\Pi^{R}_{+-}(\omega) =^{0} \Pi^{R}_{+-}(\omega) + U^{0}\Pi^{R}_{+-}(\omega)\Pi^{R}_{+-}(\omega) \tag{4.42}$$

Which we see is of the Random Phase Approximation (RPA) form and can be written as

$$\Pi^R_{+-}(\omega) = \frac{{}^0\Pi^R_{+-}(\omega)}{1 - U^0\Pi^R_{+-}(\omega)} \tag{4.43}$$

Now we turn to the lesser-than component in eqn (4.40) which is given by

$$\Pi^<_{+-}(t,t') = {}^0\Pi^<_{+-}(t,t') + \int dt_1 {}^0\Pi^R_{+-}(t,t_1)U\Pi^<_{+-}(t_1,t') \\ + \int dt_1 {}^0\Pi^<_{+-}(t,t_1)U\Pi^A_{+-}(t_1,t') \tag{4.44}$$

Again using the steady state condition, we can apply the Fourier transform as shown below

$$\Pi^<_{+-}(\omega) = {}^0\Pi^<_{+-}(\omega) + U\int dt_1 e^{-i\omega_1(t-t_1)0}\Pi^R_{+-}(t-t_1)e^{-i\omega_2(t_1-t')}\Pi^<_{+-}(t_1-t') \\ + U\int dt_1 e^{-i\omega_1(t-t_1)0}\Pi^<_{+-}(t-t_1)e^{-i\omega_2(t_1-t')}\Pi^A_{+-}(t_1-t') \tag{4.45}$$

This can once again be simplified using the identity $\int dt e^{i(\omega_1-\omega_2)t} = \delta(\omega_1-\omega_2)$ to get

$$\Pi^<_{+-}(\omega) =^0 \Pi^<_{+-}(\omega) + U^0\Pi^R_{+-}(\omega)\Pi^<_{+-}(\omega) + U^0\Pi^<_{+-}(\omega)\Pi^A_{+-}(\omega) \tag{4.46}$$

In order to simplify this, we need the expression for $\Pi^A_{+-}(\omega)$. This can be obtained without explicit calculation by comparing the Dyson equation (eqn (4.40)) for the advanced and retarded components and noticing that they have an identical structure. This allows us to write

$$\Pi^<_{+-}(\omega) =^0 \Pi^<_{+-}(\omega) + U^0\Pi^R_{+-}(\omega)\Pi^<_{+-}(\omega) + U^0\Pi^<_{+-}(\omega)\frac{{}^0\Pi^A_{+-}(\omega)}{1 - U^0\Pi^A_{+-}(\omega)} \tag{4.47}$$

which upon rearrangement of the terms gives

$$[1 - U^0\Pi^R_{+-}(\omega)]\Pi^<_{+-}(\omega) = \frac{{}^0\Pi^<_{+-}(\omega)[1 - U^0\Pi^A_{+-}(\omega)] + U^0\Pi^<_{+-}(\omega){}^0\Pi^A_{+-}(\omega)}{1 - U^0\Pi^A_{+-}(\omega)}. \tag{4.48}$$

This can be further simplified as

$$\Pi^<_{+-}(\omega) = \frac{{}^0\Pi^<_{+-}(\omega)}{[1 - U^0\Pi^R_{+-}(\omega)][1 - U^0\Pi^A_{+-}(\omega)]} \tag{4.49}$$

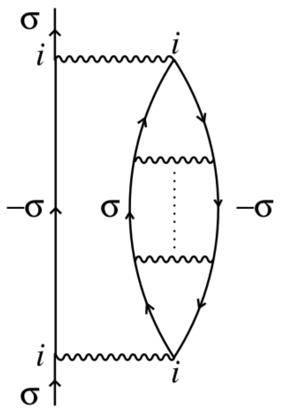

Figure 4.2: The self-energy approximation of LMA. The solid lines are the UHF propagators, with the spin-flip explicitly seen and the form consisting of the UHF propagators along with the polarization bubble. The time increases vertically

Thus we have the required components of the full polarization

$$\begin{aligned}\Pi^R_{+-}(\omega) &= \frac{{}^0\Pi^R_{+-}(\omega)}{1 - U\,{}^0\Pi^R_{+-}(\omega)} \\ \Pi^<_{+-}(\omega) &= \frac{{}^0\Pi^<_{+-}(\omega)}{[1 - U\,{}^0\Pi^R_{+-}(\omega)][1 - U\,{}^0\Pi^A_{+-}(\omega)]}\end{aligned} \tag{4.50}$$

Once again we considered only the $A$ solution for ease of notation, but the $B$ solution can also be calculated from this as the full polarization also has the same symmetry expressed in eqn (4.36).

### 4.2.3 Self-Energy

The most crucial aspect of any many-body theory for solving the impurity problem is the self-energy. The self-energy approximation of the LMA is based on the fact that the dynamical spin-flip scattering as calculated using the polarization propagators is essential to capture Kondo physics and is considered by taking the self-energy to be the diagram in figure 4.2.

The self-energy can be expressed mathematically as

$$\Sigma_{A\sigma}(z, z') = iU^2 \mathcal{G}_{A\bar{\sigma}}(z, z')\Pi_{A\bar{\sigma}\sigma}(z', z) \tag{4.51}$$

In order to simplify the notation, we again drop the $A$ label and without loss of generality consider only the $\sigma =\uparrow$ case. We can use the Langreth rules to go from the times on the Keldysh contour to real times to get the components

$$\begin{aligned}\Sigma^R_\uparrow(t,t') &= iU^2\left[\mathcal{G}^R_\downarrow(t,t')\Pi^<_{+-}(t',t) + \mathcal{G}^<_\downarrow(t',t)\Pi^A_{+-}(t',t)\right]\\ \Sigma^<_\sigma(t,t') &= iU^2\mathcal{G}^<_\downarrow(t,t')\Pi^>_{+-}(t',t)\end{aligned} \tag{4.52}$$

Restricting ourselves to the steady state case, we can use the Fourier transform $g(\omega) = 1/2\pi\int d(t-t')e^{i\omega(t-t')}g(t-t')$ to get

$$\begin{aligned}\Sigma^R_\uparrow(\omega) &= iU^2\int\tfrac{d\epsilon}{2\pi}\left[\mathcal{G}^R_\downarrow(\epsilon)\Pi^<_{+-}(\epsilon-\omega) + \mathcal{G}^<_\downarrow(\epsilon)\Pi^A_{+-}(\epsilon-\omega)\right]\\ \Sigma^<_\uparrow(\omega) &= iU^2\int\tfrac{d\epsilon}{2\pi}\mathcal{G}^<_\downarrow(\epsilon)\Pi^>_{+-}(\epsilon-\omega)\end{aligned} \tag{4.53}$$

Similar to the calculation for the zeroth order polarization, we express the Green's functions in terms of the spectral function $\rho(\omega)$ using the spectral representation (eqn (4.16)) and use the expressions eqn (4.10) to get the imaginary parts of the self-energy which read

$$\begin{aligned}\operatorname{Im}\left\{\Sigma^R_\uparrow(\omega)\right\} &= -U^2\int d\epsilon\Big[\frac{1}{2}\rho_\downarrow(\epsilon)\operatorname{Im}\left\{\Pi^<_{+-}(\epsilon-\omega)\right\}\\ &\qquad + \rho_\downarrow(\epsilon)\tilde{f}(\epsilon)\operatorname{Im}\left\{\Pi^R_{+-}(\epsilon-\omega)\right\}\Big]\\ \operatorname{Im}\left\{\Sigma^<_\uparrow(\omega)\right\} &= -U^2\int d\epsilon\rho_\downarrow(\epsilon)\tilde{f}(\epsilon)\operatorname{Im}\left\{\Pi^>_{+-}(\epsilon-\omega)\right\}\end{aligned} \tag{4.54}$$

Where we have used $\operatorname{Im}\left\{\Pi^A_{+-}(\omega)\right\} = -\operatorname{Im}\left\{\Pi^R_{+-}(\omega)\right\}$. While eqn (4.54) is useful for calculations, we can also perform a change of variables to get

$$\begin{aligned}\operatorname{Im}\left\{\Sigma^R_\uparrow(\omega)\right\} &= -U^2\int d\omega_1\Big[\frac{1}{2}\operatorname{Im}\left\{\Pi^<_{+-}(\omega_1)\right\}\rho_\downarrow(\omega+\omega_1)\\ &\qquad + \operatorname{Im}\left\{\Pi^R_{+-}(\omega_1)\right\}\rho_\downarrow(\omega+\omega_1)\tilde{f}(\omega+\omega_1)\Big]\\ \operatorname{Im}\left\{\Sigma^<_\uparrow(\omega)\right\} &= -U^2\int d\omega_1\operatorname{Im}\left\{\Pi^<_{+-}(\omega_1)\right\}\rho_\downarrow(\omega+\omega_1)\left(1-\tilde{f}(\omega+\omega_1)\right)\end{aligned} \tag{4.55}$$

We now once again have the expressions in terms of convolutions of real functions and can be evaluated either using FFT or explicit multiplication as the grid may require. The corresponding real parts can be found using the Kramers-Kronig Transform (eqn (4.34)) to give the full self-energy

$$\Sigma^r_\uparrow(\omega) = \operatorname{Re}\left\{\Sigma^r_\uparrow(\omega)\right\} + i\operatorname{Im}\left\{\Sigma^r_\uparrow(\omega)\right\} \tag{4.56}$$

$$\Sigma^<_\uparrow(\omega) = i\operatorname{Im}\left\{\Sigma^<_\uparrow(\omega)\right\} \tag{4.57}$$

The two labels $A, B$ and the corresponding self energies $\Sigma_{A/B}$ form the basis of the Local Moment Approach. The expression for $\Sigma_B$ can be obtained by using the symmetry[1] given by

$$\Sigma_{A\sigma}(\omega) = \Sigma_{B\bar{\sigma}}(\omega) \tag{4.58}$$

which further allows us to obtain the self-energy for $\bar{\sigma}$ without explicit calculation using

$$\Sigma_{A\sigma}(\omega) = -\Sigma^{*}_{A\bar{\sigma}}(-\omega). \tag{4.59}$$

### 4.2.4 Symmetry Restoration

While we have described how the spin-flip dynamics are included in the LMA via the polarization and the self-energy approximation, the major difference with LMA when compared to other methods is the concept of symmetry restoration. As has been seen, the UHF approximation could capture the noninteracting and atomic limits, but failed to capture Fermi liquid behaviour. Since this is the deficiency we want to circumvent, the obvious question which arises is: Under what conditions does the self-energy $\Sigma(\omega)$ as $\omega \to 0$ give rise to Fermi liquid behaviour? Or in other words, what is the condition required for $\Sigma(\omega) \xrightarrow{\omega\to 0} \mathcal{O}(\omega^2)$?

This can be seen by looking at the full self-energy including both the UHF and the self-energy approximations to be given by the expression

$$\begin{aligned}\tilde{\Sigma}_{A\sigma}(\omega) &= \Sigma^{0}_{A\sigma}(\omega) + \Sigma_{A\sigma}(\omega)\\ \tilde{\Sigma}_{A\sigma}(\omega) &= -\frac{\sigma}{2}UM + \Sigma_{A\sigma}(\omega)\end{aligned} \tag{4.60}$$

Where again the symmetries in eqn (4.36) apply. The condition for adiabatic continuity to the non-interacting picture is given by the pinning of the $\omega = 0$ spectrum or equivalently the Friedel sum rule. As we can see from eqn (4.10) and the corresponding Dyson equations for the self-energy, this corresponds to

$$\tilde{\Sigma}_{A\sigma}(\omega = 0) = 0 \tag{4.61}$$

Which using the symmetries and dropping the $A$ label reduces to

$$\tilde{\Sigma}_{\uparrow}(\omega = 0) = \tilde{\Sigma}_{\downarrow}(\omega = 0) = 0 \tag{4.62}$$

As can be seen in eqn (4.54) (and from discussions in[1]), the imaginary parts of the self-energy components vanish at the Fermi level i.e. $\mathrm{Im}\{\Sigma^{R}\}(\omega = 0) = 0$, the condition needs to be only satisfied by the real part of the self-energy, i.e.

$$\mathrm{Re}\{\Sigma^{R}_{\sigma}(\omega = 0)\} = \frac{\sigma}{2}UM \tag{4.63}$$

which corresponds to

$$\mathrm{Re}\big\{\Sigma_{\uparrow}^{R}(\omega=0)-\Sigma_{\downarrow}^{R}(\omega=0)\big\}=UM \tag{4.64}$$

In practice, the satisfaction of the condition is ensured by self-consistently varying $U$ for a fixed $UM$ beginning with a guess value close to the $U$ determined from the RPA form of the polarization.

While the symmetry restoration is necessary in the equilibrium scenario, in case of nonequilibrium, the picture completely changes. Since the concept of a ground state is no longer well defined and the system is not restricted to the equilibrium ground state, the requirement for a Fermi-liquid picture is relaxed. This is also seen in the fact that the Luttinger theorem arising from the Friedel sum rule no longer holds. This is also the case for finite temperature and the symmetry restoration is valid only in zero temperature. Thus, when we consider a non-zero bias and temperature, we satisfy the symmetry restoration only for zero bias and temperature and use the thus calculated value of $U$ to perform the finite bias and temperature calculations.

#### Spin Flip scale

Apart from the recovery of the Fermi-liquid physics, another important aspect of the symmetry restoration is the emergence of a low energy spin-flip scale $\omega_m$. As has been shown[19], if one considers only the UHF approximation, self-consistently solving for the moment leads to a $\omega = 0$ pole in the polarization $\Pi_{+-}^{R}$. This physically corresponds to the fact that the UHF solution is degenerate and has a zero energy cost for a spin flip. Since this is valid only in the atomic limit, the zero energy spin flip is not correct for the case of the Fermi-liquid regime where there is an adiabatic continuation to the non-interacting limit. Since the local moment is determined self-consistently while performing the symmetry restoration, the corresponding $\mathrm{Im}\big\{\Pi_{+-}^{R}\big\}(\omega)$ does not have a pole at $\omega = 0$, but in fact at a small finite value $\omega_m$. This scale has been shown to be proportional to the Kondo scale and subsequently, the quasiparticle weight which is the universal scale in equilibrium.

### 4.2.5 Transport quantities

One of the most interesting aspects of out-of-equilibrium systems is transport. In the subsequent discussion, we restrict ourselves to the steady-state infinitely-wide flat-band case of the SIAM and calculate expressions for current and differential conductance. Before we calculate the current, we need to calculate the interacting dot Green's function using the Dyson equations

$$\begin{aligned} G^R &= G_0^R + G_0^R \Sigma^R G^R \\ G^< &= G^R \Sigma^< G^A \end{aligned} \tag{4.65}$$

In the steady state case, using the Fourier transform and the expressions for the self-energy and UHF Green's functions, we get

$$\begin{aligned} G_\sigma^{R/A}(\omega) &= \frac{1}{\omega^\pm + \frac{\sigma UM}{2} + \Gamma(\omega) - \Sigma_\sigma^{R/A}(\omega)} \\ G_\sigma^<(\omega) &= G_\sigma^R(\omega)\Sigma_\sigma^<(\omega)G_\sigma^A(\omega). \end{aligned} \tag{4.66}$$

### Current

The current through the lead $\alpha$ into the central dot can be calculated using the Meir-Wingreen formula[16;20] using the interacting Green's function as

$$j_{\alpha\sigma} = \frac{ie}{h}\int d\omega \Delta_\alpha(\omega)[2if(\omega-\mu_\alpha)\,\mathrm{Im}\, G_\sigma^R(\omega) + G_\sigma^<(\omega)] \tag{4.67}$$

In steady-state, charge conservation will lead to the condition $j_L = -j_R$. Further, we can use the infinitely-wide flat band limit ($\Delta_\alpha = -\,\mathrm{Im}\{\Gamma_\alpha\} = \Delta_0/2$) and symmetrise the current ($j = \sum_\sigma \frac{j_{L\sigma}-j_{R\sigma}}{2}$), to get

$$j = -\Delta_0 \int d\omega \, [f(\omega-\mu_L) - f(\omega-\mu_R)]\,\mathrm{Im}\Big\{\tilde{G}^R(\omega)\Big\} \tag{4.68}$$

where we have defined $\tilde{G}^R(\omega) = \frac{1}{2}[G_\uparrow^R(\omega) + G_\downarrow^R(\omega)]$ and set $\frac{e}{h} = 1$.

### Conductance

The differential conductance $G$ is straight-forward to calculate once we have obtained the current using

$$G = \frac{dj}{dV_{sd}} \tag{4.69}$$

Where $V_{sd} = \mu_L - \mu_R$, is the source-drain bias.

## 4.3 Analytical Expressions

As we have described in the earlier section, while the LMA expressions we have derived hold for the case of the SIAM with an arbitrary lead density of states, it is instructive to consider the case of the infinitely-wide flat band limit. This not only simplifies the calculations of quantities like the current but also allows us to analytically calculate expressions for the polarization and self-energy.

### 4.3.1 Recovery of equilibrium

We see from the formalism, that the self-energy approximation is built on the polarization and hence the first set of expressions we would like to derive would be the zero bias limit of the polarization and show that we can recover the equilibrium expressions by simply putting $V_{sd} = \mu_\alpha = 0$. This serves as a sanity check and also allows for clearly identifying various limits of the quantities in question.

By looking at the form of the full polarization in eqn (4.50), we see that it is sufficient to show the recovery of equilibrium for the zeroth order term since the bias enters implicitly only through ${}^0\Pi^{R/<}_{+-}(\omega)$. Moreover, as we have seen earlier, we can use the Kramers-Kronig Transform ( eq. (4.34)) to obtain the real part of the polarization and hence need to consider only the imaginary components

$$\begin{aligned}\mathrm{Im}\big\{{}^0\Pi^R_{+-}(\omega)\big\} &= \pi \int d\epsilon \left[\rho_\downarrow(\epsilon)\tilde{f}(\epsilon)\rho_\uparrow(\epsilon-\omega) - \rho_\downarrow(\omega)\rho_\uparrow(\epsilon-\omega)(1-\tilde{f}(\epsilon-\omega))\right] \\ \mathrm{Im}\big\{{}^0\Pi^<_{+-}(\omega)\big\} &= 2\pi \int d\epsilon\rho_\downarrow(\epsilon)\left(1-\tilde{f}(\epsilon)\right)\rho_\uparrow(\epsilon-\omega)\tilde{f}(\epsilon-\omega)\end{aligned} \tag{4.70}$$

Where we recall that $\rho(\epsilon) = -\frac{1}{\pi}\,\mathrm{Im}\big\{\mathcal{G}^R_\sigma(\epsilon)\big\}$ and $\tilde{f}(\omega) = \left\{\frac{\Delta_L f(\omega-\mu_L)+\Delta_R f(\omega-\mu_R)}{\Delta_L+\Delta_R}\right\}$ . In order to recover equilibrium, let us consider $V_{sd} = \mu_\alpha = 0$ and the infinitely-wide flat band case. The weighted Fermi-function then reduces to $\tilde{f}(\omega) = f(\omega)$ and allows us to simplify the expression for the retarded component of the zeroth order polarization as

$$\mathrm{Im}\big\{{}^0\Pi^R_{+-}(\omega)\big\} = \pi \int d\epsilon \left[\rho_\downarrow(\epsilon)f(\epsilon)\rho_\uparrow(\epsilon-\omega) - \rho_\downarrow(\epsilon)\rho_\uparrow(\epsilon-\omega)(1-f(\epsilon-\omega))\right] \tag{4.71}$$

If we additionally consider the case of zero temperature, then the Fermi functions can be replaced with the corresponding Heaviside functions, i.e. $f(\omega) = \Theta(-\omega)$. This allows us to write

$$\begin{aligned}\mathrm{Im}\big\{{}^0\Pi^R_{+-}(\omega)\big\} = \pi &\int d\epsilon \left[\rho_\downarrow(\epsilon)\Theta(-\epsilon)\rho_\uparrow(\epsilon-\omega)\right] \\ &- \pi \int d\epsilon \left[\rho_\downarrow(\omega)\rho_\uparrow(\epsilon-\omega)(\Theta(\epsilon-\omega))\right]\end{aligned} \tag{4.72}$$

where we have used the fact that $1 - f(\omega) = f(-\omega)$ and split the integral. Using properties of the Heaviside function, we can now write the limits of integration explicitly as

$$\frac{1}{\pi}\,\mathrm{Im}\big\{{}^{0}\Pi^{R}_{+-}(\omega)\big\} = \Theta(\omega)\int_{0}^{|\omega|} d\epsilon\,[\rho_{\downarrow}(\epsilon)\rho_{\uparrow}(\epsilon-\omega)] \\ -\Theta(-\omega)\int_{-|\omega|}^{0} d\epsilon\,[\rho_{\downarrow}(\omega)\rho_{\uparrow}(\epsilon-\omega)] \quad (4.73)$$

In order to compare this expression to the equilibrium result, we notice the relation between the time-ordered and retarded Green's functions in equilibrium is $G^{T}(\omega) = sgn(\omega)G^{R}(\omega)$, where $sgn$ is the sign function. We can use this to rewrite the expression for the imaginary part as

$$\frac{1}{\pi}\,\mathrm{Im}\big\{{}^{0}\Pi^{T}_{+-}(\omega)\big\} = +\Theta(\omega)\int_{0}^{|\omega|} d\epsilon\,[\rho_{\downarrow}(\epsilon)\rho_{\uparrow}(\epsilon-\omega)] \\ +\Theta(-\omega)\int_{-|\omega|}^{0} d\epsilon\,[\rho_{\downarrow}(\omega)\rho_{\uparrow}(\epsilon-\omega)] \quad (4.74)$$

Which we see is precisely the expression (2.23a) derived by D. Logan et al.[1]. Coming to the lesser-than component, we see that

$$\mathrm{Im}\big\{{}^{0}\Pi^{<}_{+-}(\omega)\big\} = 2\pi\int d\epsilon\rho_{\downarrow}(\epsilon)\left(1-\tilde{f}(\epsilon)\right)\rho_{\uparrow}(\epsilon-\omega)\tilde{f}(\epsilon-\omega) \quad (4.75)$$

reduces upon substituting the Heaviside functions and using the identity $1 - f(\omega) = f(-\omega)$ to

$$\mathrm{Im}\big\{{}^{0}\Pi^{<}_{+-}(\omega)\big\} = 2\pi\int d\epsilon\rho_{\downarrow}(\epsilon)\Theta(\epsilon)\rho_{\uparrow}(\epsilon-\omega)\Theta(-\epsilon+\omega) \quad (4.76)$$

which becomes

$$\mathrm{Im}\big\{{}^{0}\Pi^{<}_{+-}(\omega)\big\} = 2\pi\int_{0}^{|\omega|} d\epsilon\rho_{\downarrow}(\epsilon)\rho_{\uparrow}(\epsilon-\omega). \quad (4.77)$$

We also notice that in the expression for self-energy eqn (4.51), replacing the contour-ordered components with the time-ordered components and subsequently performing the Fourier transform gives

$$\Sigma^{T}_{A\sigma}(\omega) = \frac{U^{2}}{2\pi i}\int d\epsilon\mathcal{G}_{A\sigma}(\epsilon)\Pi_{A\bar{\sigma}\sigma}(\epsilon+\omega) \quad (4.78)$$

which is precisely the expression (3.10) derived in D. Logan et al.[1]. Thus we can see that the generalised LMA formalism reduces exactly to the equilibrium expressions when we consider $V_{sd} = 0$. This is in addition to the LMA being able to recover the atomic limit exactly in equilibrium and speaks to the robustness of the method.

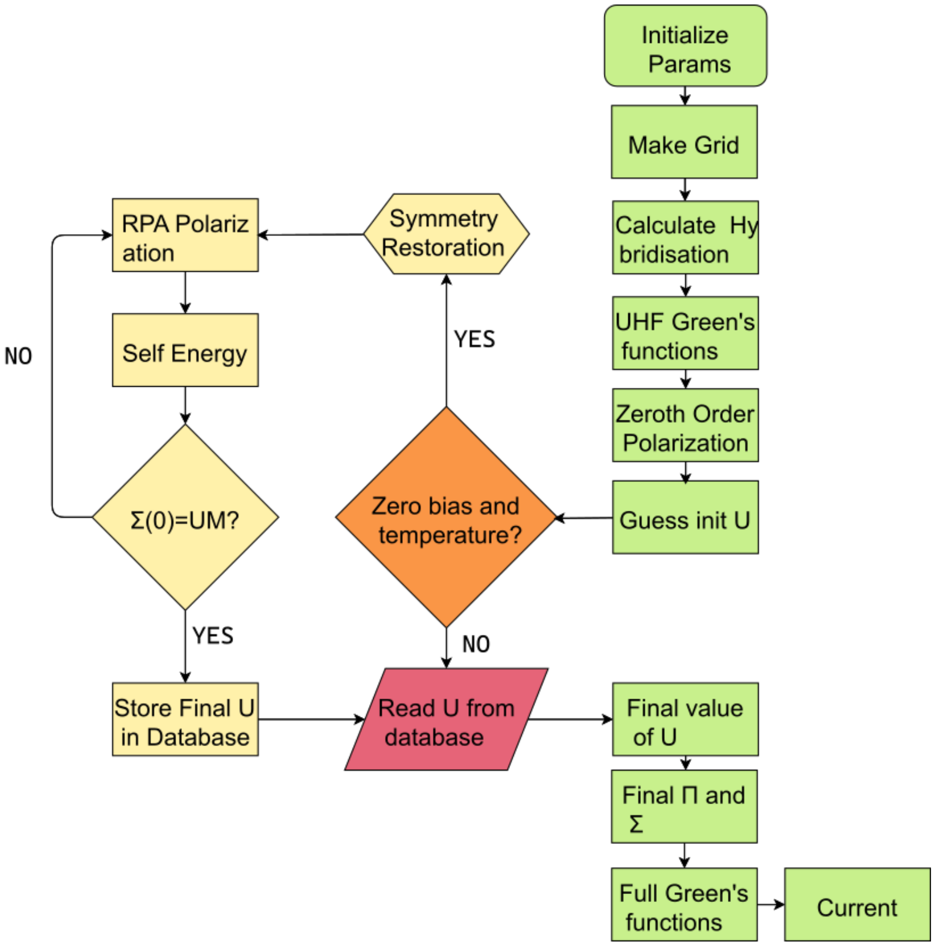

Figure 4.3: Flowchart describing the various steps involved in the LMA calculation. The processes in green deal with the main branch of calculations while the ones in yellow and red deal with the symmetry restoration

## 4.4 Numerical Implementation

Now that we have discussed the formalism, we move on to the question of numerical implementation. The sequence of calculations and the self-consistency loop are described in the flowchart in figure 4.3.

### 4.4.1 $UM$ as the input parameter

While the interaction strength $U$ is a system parameter, it is computationally more optimal to consider the product $UM$ as an initialization parameter. This choice is motivated by the fact that $U$ enters only the full polarization (eqn (4.50)) and the self-energy (eqn (4.56)) and necessitates us to recalculate only these quantities in the self-consistency for symmetry restoration. This allows us to solve for the roots of the symmetry restoration condition by varying $U$ and we obtain a final value upon satisfying the condition. This is then further used to calculate the interacting Green's functions and subsequently the current.

### 4.4.2 Non-uniform Grid

The first significant choice one must make while implementing the LMA equations is the choice of the grid. While considerations like the extent of the grid are obviously important, the choice of the grid spacing is crucial. As we have seen, the symmetry restoration gives rise to a new equilibrium scale $\omega_m$, which is defined as the location of the pole in $\text{Im}\left\{\Pi^R_{+-}(\omega)\right\}$ and a large density of points ($d\omega \sim 10^{-5}$) are required near $\omega \sim \omega_m$ to properly capture the scale. One of the major advantages of LMA is the ability to accurately capture the Fermi-liquid behaviour, which crucially relies on comparing values at $\omega = 0$. This again necessitates a very large density ($d\omega \sim 10^{-10}$) of points near zero to accurately capture the exponentially narrow Kondo resonance accurately. While these are theoretically feasible to be achieved by considering a uniform grid of very fine spacing, it is practically more feasible to work with a locally refined grid with the required characteristics.

The non-uniform grid of our choice can be described completely by a set of seven parameters viz. $\epsilon_0, \omega_{\text{fine}}, \epsilon_2, \epsilon_3, \epsilon_4, \epsilon_{\text{box}}, \omega_{\text{max}}$. The most straightforward among these is $\omega_{\text{max}}$ which gives us the extent of the grid. The grid is generated in such a way that the frequencies near zero have the maximal density with $d\omega(\omega = 0) = \epsilon_0$. The grid is generated using the GP

$$\omega_n = k\omega_{n-1} = k^{(n-1)}\epsilon_0 \tag{4.79}$$

Where $k = 1 + \frac{\epsilon_2}{\omega_{\text{fine}}}$ is determined by the extent $\omega_{\text{fine}}$ of the fine grid and $\epsilon_2$, the largest spacing in the fine part of the grid. While these parameters ensure that the grid is very dense near $\omega = 0$, we still need to account for the density required at $\omega_m$.

This is done by inserting a 'box' in the grid for $\omega \in [\frac{\omega_m}{10}, 3\omega_m]$. This corresponds to fixing the grid density to be $\epsilon_3$ if the value of $\omega_m > \omega_{\text{fine}}$ or the value $d\omega(\omega = \frac{\omega_m}{10})$ if otherwise. Whichever the choice, the corresponding density of points is represented by $\epsilon_{\text{box}}$.

After inserting the box and considering the fine grid, there is no necessity to have a large density of points all the way to $\omega_{\text{max}}$, thus we consider a coarse grid from $\omega = \max(\omega_{\text{fine}}, 3\omega_m)$ to the full extent $\omega = \omega_{\text{max}}$. The corresponding density of points of this coarse grid is represented by $\epsilon_4$. All these features can be seen when the density of points is plotted against the frequency as shown in figure 4.4.

### 4.4.3 Convolution

We see from the expressions for ${}^0\Pi_{+-}(\omega)$ and $\Sigma_\sigma(\omega)$, we need to calculate the imaginary parts using convolutions, which are defined as

$$(f \star g)(\omega) = \int d\epsilon f(\epsilon) g(\epsilon - \omega) \tag{4.80}$$

In the case of the uniform grid, one can use the Convolution theorem which allows evaluation by means of the Fourier transform. But in our case, we need to calculate the convolution on a locally refined grid and have to resort to explicit multiplication. A point to be noted here is the fact that while the Fourier transform exists for a non-uniform grid, the corresponding inverse transform is not defined in a straightforward way and the evaluation of that would require some non-trivial approximations.

In order to calculate the convolution, we notice that $\epsilon - \omega$ may lie outside the range $\epsilon \in [-\omega_{\max}, \omega_{\max}]$ and one either needs to pad the arrays to be of size $[-2\omega_{\max}, 2\omega_{max}]$ or restrict the integral to values $\epsilon \in [\epsilon_{\min}, \epsilon_{\max}]$ for every value of $\omega$ such that

$$\begin{aligned} \epsilon_{\min} &= \max(\omega - \omega_{\max}, -\omega_{\max}) \\ \epsilon_{\max} &= \min(\omega + \omega_{\max}, \omega_{\max}) \end{aligned} \tag{4.81}$$

Another thing to notice is that since the grid is finite, $\epsilon - \omega$ need not lie on a point of the grid for all values of $\epsilon, \omega$. Thus, this requires us to construct a new grid to include all such points i.e. $\bar{\omega}_{ij} = \epsilon_i - \omega_j$. This necessitates us to interpolate the function $g(\epsilon - \omega)$ for these values, which we achieve by linear interpolation. A similar set of arguments and hence a similar solution is also required to implement the Kronig-Kramers Transform which is implemented by considering an interlacing grid $\bar{\omega}_j = \frac{1}{2}(\omega_j + \omega_{j-1})$.

### 4.4.4 Root Solver

The crucial condition for LMA in equilibrium is that of symmetry restoration. We do the symmetry restoration by self-consistently calculating the expressions for $\Pi_{+-}(\omega)$ and $\Sigma_\sigma(\omega)$ starting from a guess value of $U$. The $U_{\text{guess}}$ is chosen to be slightly less than the value of $U_{\text{crit}} = 1/\operatorname{Re}\left\{{}^0\Pi^R_{+-}(\omega = 0)\right\}$. The

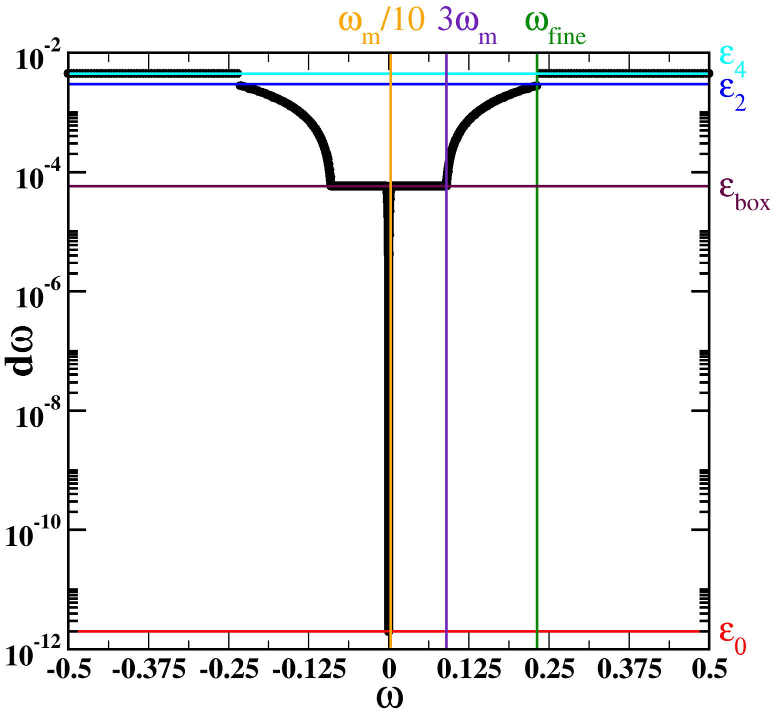

Figure 4.4: The grid spacing $d\omega$ plotted vs the frequency $\omega$ for a typical LMA calculation $(UM = 6, V_{sd} = 0)$. The parameters $\epsilon_0, \epsilon_2, \epsilon_4, \omega_{\text{fine}}$ are marked with corresponding colours. Since the spin-flip scale for this calculation was $\omega_m = 0.03$ which is lesser than the extent of the fine grid $\omega_{\text{fine}} = 0.231$, the box spacing $\epsilon_{\text{box}}$ is determined by the spacing $d\omega(\omega = \omega_m/10) = 5.8341 \times 10^{-5}$ and not by $\epsilon_3$. The coarse grid spacing $\epsilon_4$ is also marked. Only the values of frequency in the vicinity of $\omega \in [-0.5, 0.5]$ are considered in order to see the different grid parameters clearly. Hence, $\omega_{\text{max}} = 45$ is out of these bounds and is not represented in the figure.

symmetry restoration is carried on via a root solver which finds the root of the condition

$$\mathrm{Re}\{\Sigma_\uparrow(0)\} - \mathrm{Re}\{\Sigma_\downarrow(0)\} - UM = 0 \tag{4.82}$$

In our implementation, we first calculate the difference for $U_{\mathrm{guess}}$ and an initial step size $\Delta U$. This allows us to ascertain the direction of root finding and allows us to come to a coarse solution using bisection. This is further refined using linear interpolation to obtain the symmetry-restored value of $U$ for a given tolerance.

## 4.5 Results and discussion

We begin with extensive benchmarking with equilibrium results in both zero and finite temperature limits. Since the method is novel, we need to compare the accuracy and the limits of the method with other methods and the LMA in equilibrium.

### 4.5.1 Zero temperature benchmarks

The polarization which takes into account the spin fluctuations is compared with the results from equilibrium LMA[21] by plotting the imaginary part as a function of frequency. In the main plot of the top panel of Fig. 4.5, we plot the imaginary part of the RPA polarization $\Pi^R_{+-}(\omega)$ for $UM = 12$ as a function of frequency and plot the imaginary part of the zeroth order polarization $\Pi^0_{+-}(\omega)$ in the inset. In the bottom panel, we have Fig 2 from Logan et al.(1998)[21] for comparison, where they have considered $\tilde{U} = \frac{U}{\pi\Delta_0} = 4$ and $\tilde{\omega} = \frac{\omega}{\Delta_0}$. Since we have considered $\Delta_0 = 1$ here, the corresponding $U = 4\pi \sim 12$. We see that the polarization matches very well with the equilibrium results.

Since the retarded self-energy $\Sigma^R(\omega)$ (eqn (4.54)) has both the $\Pi^{R,<}$ contributions, it needs to be compared to the equilibrium case where it is evaluated using only the $\Pi^{+-}$ polarization[21]. In order to do this, we use the equilibrium code developed in the group earlier[5] and plot the real and imaginary retarded self-energy $\Sigma^R_\uparrow$ for $UM = 12$ in Fig. 4.6. We see a one-to-one matching with the $\Sigma^R$ obtained from this method and earlier calculations.

### 4.5.2 Finite temperature benchmarks

In finite temperature, the hardcore Boson constraint becomes relevant and needs to be benchmarked with earlier calculations. We do this by calculating

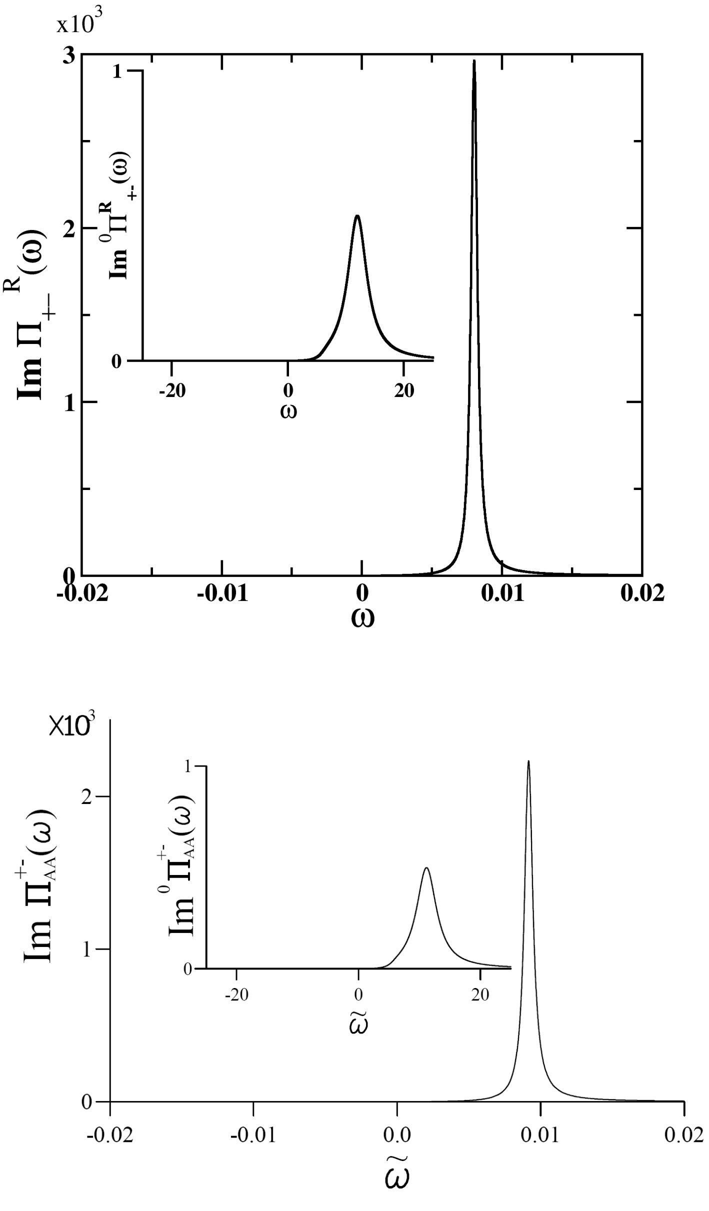

Figure 4.5: Comparison of the polarization for the equilibrium. The top panel is calculated from the code, the bottom panel is taken from Fig. 2 of Logan et al (1998).[21]. The $UM = 12$ for our calculation while the paper uses $\tilde{U} = U/\pi\Delta_0 = 4$. Since we have taken $\Delta_0 = 1$, the corresponding value of $U = 4\pi$ and $\tilde{\omega} = \omega/\Delta_0 = \omega$. The inset shows the corresponding imaginary part of the zeroth order polarization.

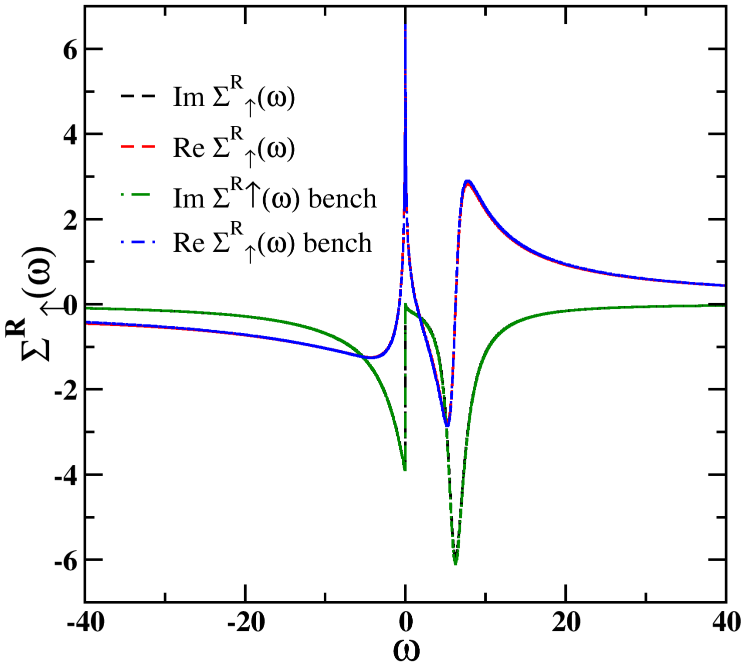

Figure 4.6: Real and Imaginary Parts of self-energy benchmarked with the equilibrium flat band LMA code for $UM = 12$ with $\Delta_0 = 1$ at zero temperature.

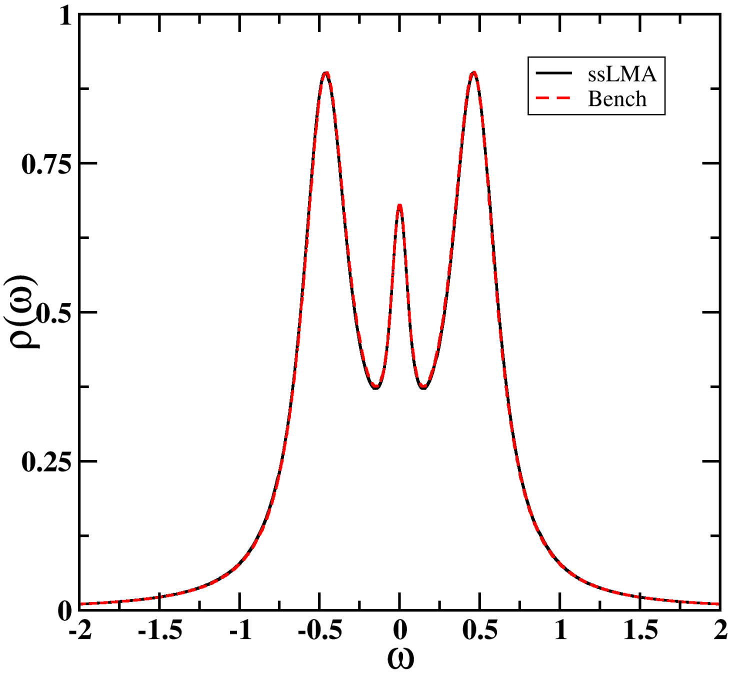

Figure 4.7: The spectral function $\rho(\omega)$ as a function of $\omega$ for $UM = 5\Delta_0$ and $T = 10\omega_m$ plotted in black. The red line is the benchmark obtained from earlier implementations of the equilibrium LMA.

the spectral function $\rho(\omega) = -\frac{1}{\pi}\,\mathrm{Im}\left\{\tilde{G}^R\right\}$ for $UM = 5\Delta_0$ and $T = 10\omega_m$ case and comparing it to calculations from earlier implementations. We use $\Delta_0 = 1$ and plot the $\rho$ as a function of $\omega$ in Fig. 4.7 and see excellent agreement with the benchmark obtained from earlier implementation.

We now look at the effect of temperature in equilibrium and benchmark with the results obtained by Logan et al. (2002)[15]. We look at the scaled spectral function $\pi\Delta_0\rho(\omega;T)$ as a function of the scaled frequency $\omega/\omega_m$ for various values of temperature. We plot the results for $UM = 20\Delta_0$ in Fig. 4.8 for $\Delta_0 = 0.1$ and temperatures $T \in [0, 100\omega_m]$. In order to look at the variation of the Kondo peak, we look at the zoomed-in range of $\omega/\omega_m \in [-50, 50]$. Comparing Fig 4.8 with Fig. 5 of Logan et al. (2002)[15], we see good agreement.

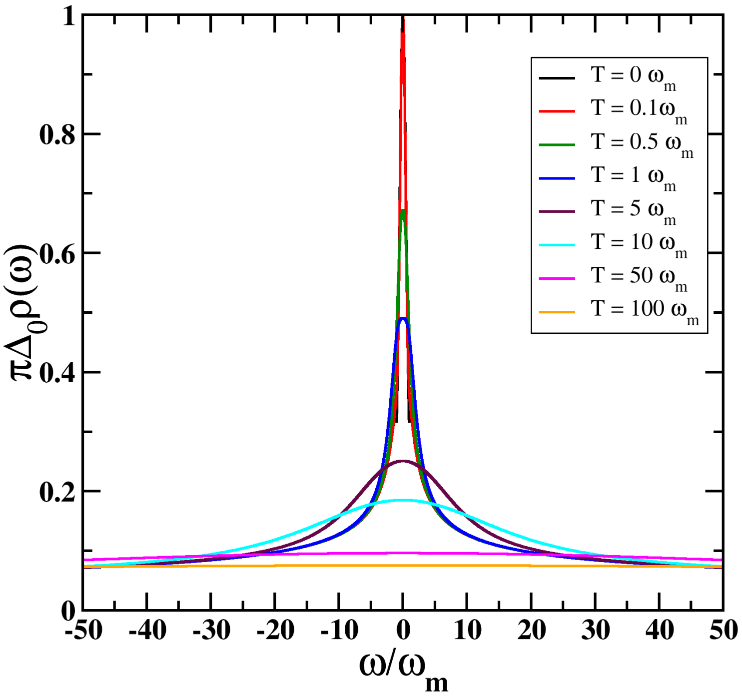

Figure 4.8: The scaled spectral function $\pi\Delta_0\rho(\omega;T)$ plotted as a function of the scaled frequency $\omega/\omega_m$ for different values of temperature as indicated in the legend. The figure shows the variation of the central Kondo peak and hence is plotted only for $\omega/\omega_m \in [-50, 50]$. The calculations were carried out for $UM = 20\Delta_0$, with $\Delta_0 = 0.1$ and $V_{sd} = 0$

### 4.5.3 Transport

A central quantity of interest in transport across the system is the current. We look at the zero temperature limit and consider the weak-intermediate coupling ($UM < 10\Delta_0$) and the strong coupling ($UM > 10\Delta_0$) regimes. In Fig. 4.9, we plot the $j - V_{sd}$ (IV) curves for both the weak-intermediate coupling regime (top panel) and the strong coupling regime (bottom panel). Since we are working in the infinitely wide flat band limit, we see that the IV curves saturate to a finite value for all values of $UM$. The weak-intermediate coupling regime shows IV behaviour similar to the results from ssIPA (Fig. 2.2), while we see a non-universal satellite feature appear in the strong coupling regime. This satellite feature is not seen in other methods and could be a shortcoming of the ssLMA method. The strong coupling regime is characterised by very low values of $\omega_m$ and the satellite feature could be due to the same. Since we find excellent agreement for equilibrium results, a detailed look at the diagrams considered to construct the ssLMA might be needed.

Looking at the effect of $V_{sd}$ on the spectral function, we see that there is a re-entrant behaviour of the peaks with increasing $V_{sd}$. We plot the spectral function $\rho(\omega)$ as a function of $\omega$ for $UM = 5$ and $V_{sd} \in [0, 50]$ in Fig. 4.10 and see that the central peak vanishes around $V_{sd} = 0.5$ and re-emerges at $V_{sd} = 50$. The sidebands which correspond to the $\omega = \pm UM$ in the zero bias case move out with increasing $V_{sd}$ up to $V_{sd} = 0.5$ before re-entering at larger values.

### 4.5.4 Universality

Another aspect which is captured by the LMA in equilibrium is universality. We start by looking at the case of zero bias and zero temperature and see that there is an emergent universality in the scaled spectral function $\pi\Delta_0\rho(\omega)$ as a function of the scaled frequency $\omega/\omega_m$ for values of $UM > 12\Delta_0$. The onset of universality defines the strong coupling regime and agrees well with earlier results. In Fig. 4.11, we plot the scaled spectral function $\pi\Delta_0\rho(\omega)$ for various values of $UM \in [10\Delta_0, 20\Delta_0]$ at zero temperature and bias with $\Delta_0 = 0.1$. We show the behaviour for $\omega \in [-150\omega_m, 150\omega_m]$ which zooms in on the central peak and we see the collapse for values of $UM > 12\Delta_0$.

Next, we look at the variation of the zero bias conductance with temperature and see the emergence of universal behaviour when the temperature is scaled with $\omega_m$. We plot the conductance $G(T)/G(0)$ as a function of scaled temperature $T/\omega_m$ for various strong coupling values of $UM$ in Fig. 4.12. The universal collapse can be observed up to $T \sim 20\omega_m$ for all curves with higher values of $UM$ showing universality for even larger values of $T$. We

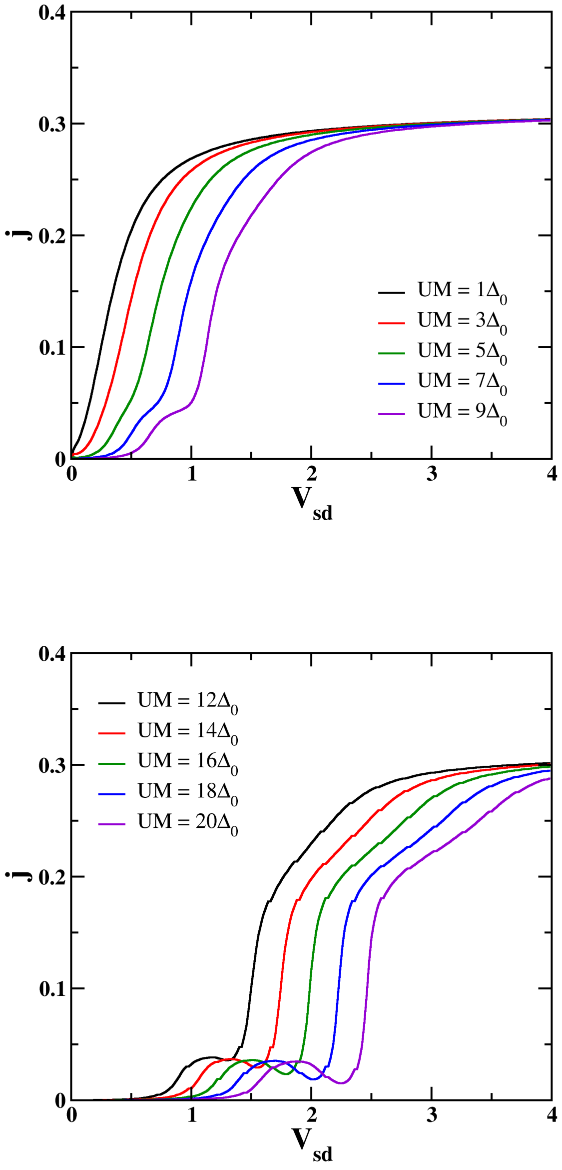

Figure 4.9: Zero temperature IV curves for various values of $UM$ in weak-intermediate coupling (*Top panel*) and strong coupling (*Bottom panel*) regimes as indicated in the legends. We see that the curves saturate for both regimes as seen from results from other methods, while there is a satellite feature emerging in the strong coupling regime.

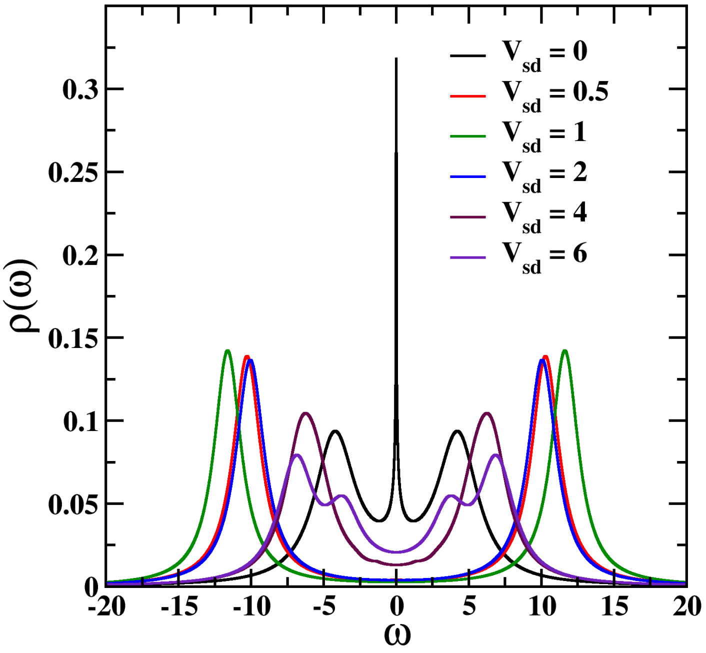

Figure 4.10: The spectral function $\rho(\omega)$ plotted vs $\omega$ for various values of $V_{sd}$ as indicated in the legend. The calculations were performed for $UM = 5\Delta_0$ and $\Delta_0 = 1$. The rentrant behaviour of the sidebands can be seen for $V_{sd} > 1$

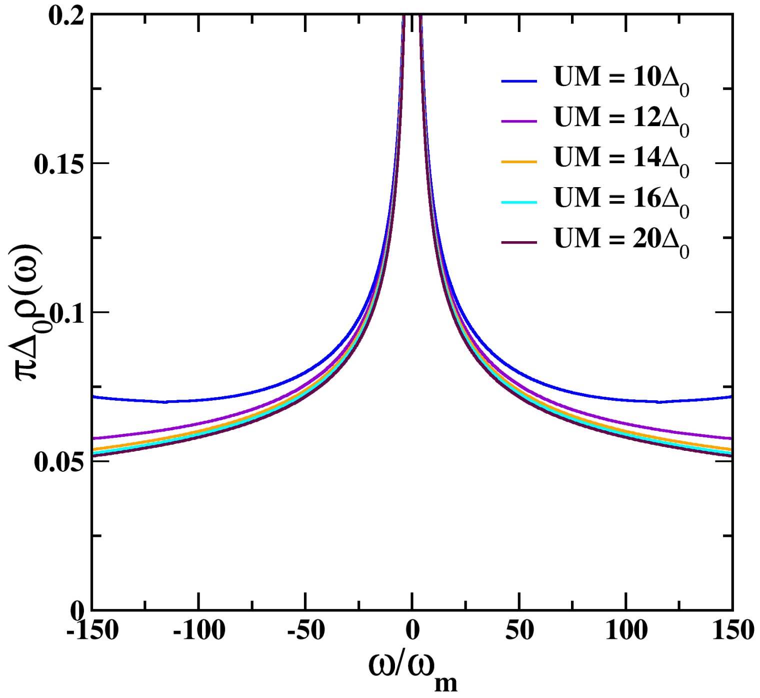

Figure 4.11: The zero temperature scaled spectral function $\pi\Delta_0\rho(\omega)$ plotted as a function of the scaled frequency $\omega/\omega_m$ in the zoomed in region $\omega \in [-150\omega_m, 150\omega_m]$ for various values of $UM$ as indicated in the legend. The collapse of the curves for $UM > 12\Delta_0$ shows universality and serves as the marker for strong coupling. We have used $\Delta_0 = 0.1, V_{sd} = 0$ for the calculations.

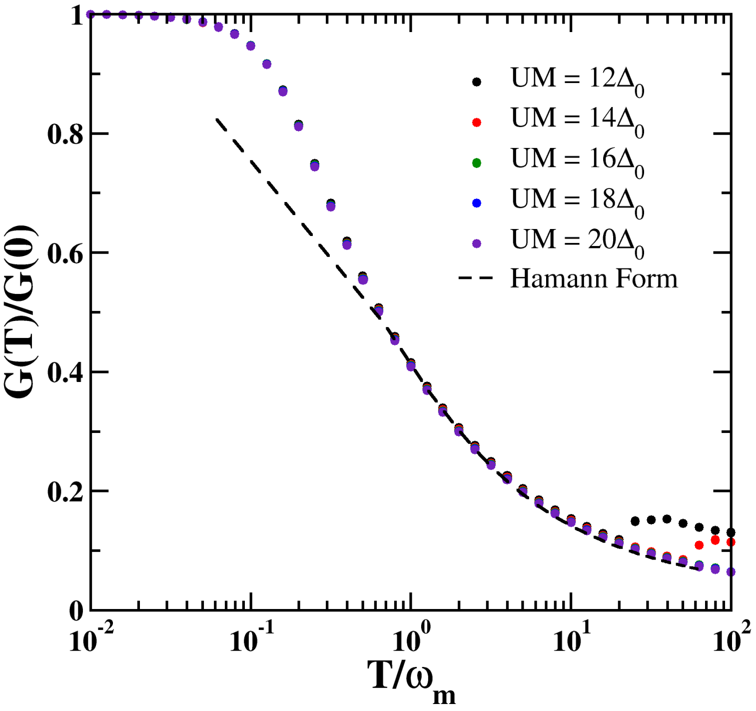

Figure 4.12: The zero-bias conductance plotted for different values of $UM$ in the strong coupling regime showing a universal behaviour with scaled temperature $T/\omega_m$. The dashed line corresponds to the Hamann form[22] of the conductance eqn. (4.83). The results agree well with Fig. 8 of Logan et al. (2002)[15]

plot the Hamann approximation[22] of the conductance given by

$$\frac{G(T)}{G(0)} = \frac{1}{2}\left\{1 - \frac{\ln(T/T_K)}{\left[\ln(T/T_K)^2 + \frac{3\pi^2}{4}\right]^{\frac{1}{2}}}\right\} \tag{4.83}$$

We have used the fact that $T_K$, the Kondo temperature is proportional to $\omega_m$ in order to compare our results. We see a good agreement between our calculations Fig. 4.12 and Fig. 8 of Logan et al. (2002)[15].

Finally, we look at the linear response regime and plot the scaled current $j/\omega_m$ as a function of scaled bias $V_{sd}/\omega_m$ for various values for $UM$ and see that the $\omega_m$, which is the universal scale in the equilibrium case controls the extent of the linear response regime. In Fig. 4.13, we see that the curves for

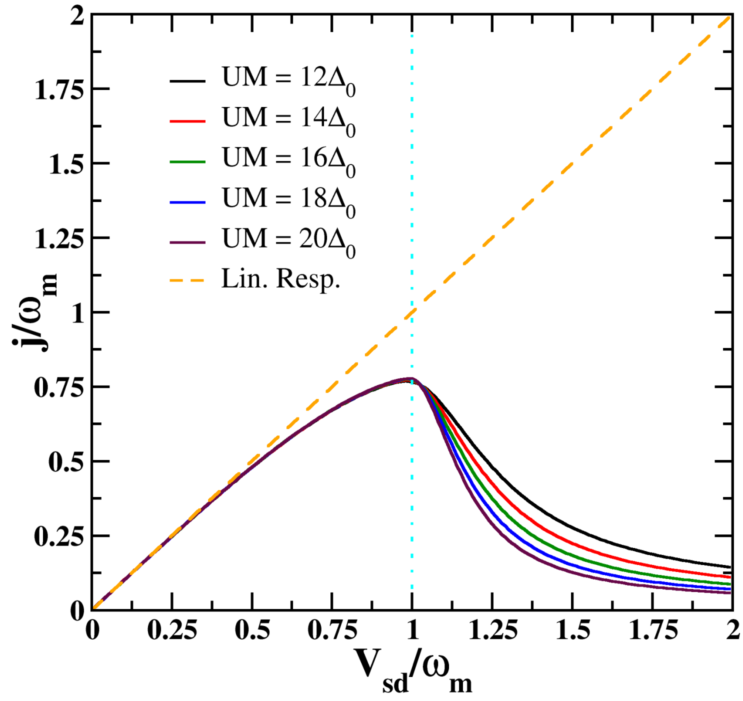

Figure 4.13: Scaled IV curve showing linear response regime and an emergent isosbestic point at $V_{sd} = \omega_m$. The equilibrium scale $\omega_m$ controls the extent of the linear response regime.

different values of $UM$ collapse up to $V_{sd} = 0.5\omega_m$ with the linear response. The curves are still universal even beyond $V_{sd} = 0.5\omega_m$ while being non-linear up to $V_{sd} = \omega_m$ followed by an isosbestic point where they break off into non-universal curves. The breaking off subsequent to $V_{sd} = \omega_m$ leads to the satellite feature in the IV curves and subsequently the NDR regime.

## 4.6 Summary and conclusions

In this chapter, we have derived the steady state Local Moment Approach (ssLMA) and applied it to study the quantum dot connected to lead with DC bias. We work in the infinitely wide flat band limit and calculate the polarization, self-energy, full Green's functions and subsequently the observables like spectral function and current. We also see that we can analytically recover the equilibrium results when $V_{sd} = 0$.

The method has been benchmarked extensively with equilibrium in both the zero and finite temperature limits and shows excellent agreement. We also have looked at the transport quantities and see the IV characteristics are captured well for the weak-intermediate coupling regime, while a satellite feature appears in the strong coupling regime. The spectral function shows a re-entrant behaviour of the sidebands and a re-emergence of the central peak with increasing bias. The method is able to capture the universal behaviour and shows that the spin-flip scale ($\omega_m$) is the universal scale in equilibrium and controls the extent of the linear response regime out of equilibrium. We see that the zero bias and zero temperature curves collapse when scaled with $\omega_m$ which defines the strong coupling regime. We also see that the zero bias conductance follows a universal behaviour for large temperatures (even up to $T \sim 100\omega_m$) and compares well with earlier results. In the nonequilibrium case, we see a universal linear response of the scaled IV curves up to a $V_{sd} \sim 0.5\omega_m$ followed by a non-linear universal curve up to $V_{sd} \sim \omega_m$. This is followed by an isosbestic point and subsequent breaking off of the scaled IV curves for different $UM$ values and is responsible for the satellite feature in IV curves.

The satellite feature in the IV curves in the strong coupling regime is not seen in other methods and could be a shortcoming of the method. As extensive benchmarks show, the satellite feature is not a numerical/implementation fault and needs a deeper analysis of the physics, including a systematic look at the diagrams considered. This is an open question and will be considered in the future.

# Bibliography

[1] D. E. Logan, M. P. Eastwood, and M. A. Tusch, Journal of Physics: Condensed Matter **10**, 2673 (1998).

[2] M. R. Galpin and D. E. Logan, The European Physical Journal B **62**, 129 (2008).

[3] V. E. Smith, D. E. Logan, and H. R. Krishnamurthy, The European Physical Journal B - Condensed Matter and Complex Systems **32**, 49 (2003).

[4] N. S. Vidhyadhiraja, V. E. Smith, D. E. Logan, and H. R. Krishnamurthy, Journal of Physics: Condensed Matter **15**, 4045 (2003).

[5] S. Sen and N. S. Vidhyadhiraja, Phys. Rev. B **93**, 155136 (2016).

[6] T. Fujii and K. Ueda, Phys. Rev. B **68**, 155310 (2003).

[7] A. A. Aligia, Phys. Rev. B **74**, 155125 (2006).

[8] L. Mühlbacher and E. Rabani, Phys. Rev. Lett. **100**, 176403 (2008).

[9] F. B. Anders and A. Schiller, Phys. Rev. Lett. **95**, 196801 (2005).

[10] R. Härtle, G. Cohen, D. R. Reichman, and A. J. Millis, Phys. Rev. B **88**, 235426 (2013).

[11] M. Nuss, M. Ganahl, H. G. Evertz, E. Arrigoni, and W. von der Linden, Phys. Rev. B **88**, 045132 (2013).

[12] E. Arrigoni, M. Knap, and W. von der Linden, Phys. Rev. Lett. **110**, 086403 (2013).

[13] D. Goldhaber-Gordon, J. Göres, M. A. Kastner, H. Shtrikman, D. Mahalu, and U. Meirav, Phys. Rev. Lett. **81**, 5225 (1998).

[14] M. Grobis, I. G. Rau, R. M. Potok, H. Shtrikman, and D. Goldhaber-Gordon, Phys. Rev. Lett. **100**, 246601 (2008).

[15] D. E. Logan and N. L. Dickens, Journal of Physics: Condensed Matter **14**, 3605 (2002).

[16] H. Haug, A.-P. Jauho, *et al.*, *Quantum kinetics in transport and optics of semiconductors*, Vol. 2 (Springer, 2008).

[17] G. Stefanucci and R. van Leeuwen, *Nonequilibrium Many-Body Theory of Quantum Systems: A Modern Introduction* (Cambridge University Press, 2013).

[18] D. Sánchez and M. Moskalets, Entropy **22** (2020), 10.3390/e22090977.

[19] N. S. Vidhyadhiraja and D. E. Logan, The European Physical Journal B - Condensed Matter and Complex Systems **39**, 313 (2004).

[20] Y. Meir and N. S. Wingreen, Phys. Rev. Lett. **68**, 2512 (1992).

[21] D. E. Logan, M. P. Eastwood, and M. A. Tusch, Journal of Physics: Condensed Matter **10**, 2673 (1998).

[22] D. R. Hamann, Phys. Rev. **158**, 570 (1967).

# Chapter 5

# Piecewise constant driving protocols in the Kitaev chain

## 5.1 Introduction

The Kitaev chain[1], a 1D tight-binding model with p-wave superconducting pairing, has been the subject of much attention due to it being capable of hosting Majorana Zero Modes(MZMs). These MZMs in addition to being interesting for the fundamental physics aspects like non-Abelian statistics, also have potential applications as qubits in fault-tolerant computation[2]. The MZMs appear in the ends of a Kitaev chain and their presence/absence is associated with a $\mathbb{Z}_2$ topological index called the parity. The Kitaev chain has not only been studied extensively as a theoretical model[3–7], but has also received experimental attention[8–15]. The Kitaev chain can also be shown to map to the well-studied transverse field Ising model (TFIM) via the means of a Jordan-Wigner transformation and the topological phases can be characterised using the coefficients of the corresponding TFIM.

Systems driven out of equilibrium by periodic driving have been known to exhibit a great number of emergent phenomena like topology[16–20], time crystals[21–23], artificial gauge fields[24;25], emergent metastable states[26;27], nonequilibrium quantum phase transitions[28–31], etc.. The Floquet theory based on the Floquet theorem, the counterpart of the Bloch theorem for time coupled with High Frequency Expansion (HFE) has been used to study a wide variety of systems under a large number of driving protocols. Experimental techniques like ultrafast spectroscopy and optical lattice techniques have allowed for the realisation of many theoretical proposals. In fact, recent years have seen the field of Floquet Engineering emerge[32], where one can construct a driving protocol to obtain desired emergent Hamiltonians and corresponding states. While a majority of the work on periodically driven systems has been through the use of Floquet theory as described above, the HFE used in the same is also the weakest link due to the requirement of the driving frequency to be the largest energy scale in the system. While there has been the simultaneous development of other approaches like Renormalization Group methods and Keldysh based methods which circumvent this problem, they suffer from their own shortcomings either in the truncation of terms in the effective Hamiltonian or in computational expense.

Coming to periodic driving in the Kitaev chain, Thakurathi et al[18] have shown that by applying periodic $\delta$-function kicks through the chemical potential, the Floquet Hamiltonians of the driven Kitaev chain and the corresponding TFIM show the emergence of topology even when the initial parameters correspond to the topologically trivial phase. They have seen that this emergence can be characterised by both the winding number calculated from the Floquet Hamiltonian for the TFIM as well as the number of Floquet MZMs arising in the edges of the Kitaev chain. They also see that there is a maximum frequency of driving above which no topology change is observed, while the winding number increases for lower frequencies. The Floquet MZMs are very sensitive to the periodicity of the driving protocol and even an infinitesimally small aperiodicity leads to their destruction[33]. In this chapter, we benchmark the method in case of the square wave driving and investigate the effects of square wave driving in various phases.

Electrical noise is ubiquitous in experiments measuring transport quantities. It is seen to be of many types like thermal noise, shot noise, 1/f noise, etc. While a host of empirical and theoretical proposals have looked at the origin of electrical noise, a larger number of studies have looked at the effect of noise on various emergent properties. For example, studies of noise in periodically driven systems have looked at both randomness in the frequency as well as the amplitude of the driving and studied the effect of noise on emergent properties like topology, metastable states, etc. The noise in periodically driven systems has been studied using a number of approaches like the Floquet scattering theory, transfer matrix method, master equation approach etc., some of which allow for the calculation of exact solutions. In the case of the Kitaev chain, an exact solution has been worked out when temporal noise is present in the chemical potential, hopping or pairing terms[34]. In this chapter, we will use the Transfer Matrix method (by D. Nghiem and R. Joynt[35]) to study various piecewise constant driving protocols. The Transfer Matrix method allows the calculation of the time evolution operator as a product of transfer matrices corresponding to each constant piece in the driving protocol. The method allows for exact solutions and has been applied to study telegraphic noise[36]. The effect of the noise on the emergence of topology when driving needs a detailed investigation. This is done by the calculation of the disorder averaged transfer matrices and looking at the effect of the disorder on the topology via the rate function.

Apart from periodic driving, a common way of achieving non-equilibrium is through quenches. In case of the Kitaev chain in particular, studies involving quenching to and across the boundaries of topological and trivial phases have seen that the survival probability of the MZMs decay when quenched across the boundary but have a periodic re-emergence when quenched to the boundary values[37]. Systems when quenched and allowed to evolve with time, display the possibility of having dynamical quantum phase transitions (DQPTs) where physical quantities become nonanalytic as a function of time. These DQPTs are not driven by conventional control parameters like temperature, pressure, etc., but occur just due to the evolution in time. The central quantity for characterising these DQPTs is the Loschmidt echo, which has been well studied both in theory and experiments. The DQPTs are signalled by nonanalyticites in the Loschmidt echo and have been both proposed theoretically and observed experimentally in optical lattice systems. The emergence of these DQPTs in the TFIM following a quench across topologically invariant phases has been studied in detail with attention paid to both the dynamical order parameters and scaling and universality of these phase transitions[29]. The time at which these DQPTs arise and the mechanism of how the associated topology change needs to be studied in detail. The calculation of the critical time and the corresponding gap closing serve as an explanation for the change in topology.

In this chapter, we use the transfer matrix method to look at three driving protocols - square wave periodic, piecewise constant noise in the chemical potential and quenches across various parameter regimes. We begin with the Hamiltonian and derive the ground state and the different phases of the model. This is followed by the derivation of the transfer matrices for the square wave, noise and quench cases. The descriptions of the Loschmidt echo and Dynamical quantum phase transitions follow. In the following section, subsequent to benchmarking, we present the results for all the three protocols. Finally, we conclude with a summary of the chapter.

## 5.2 Model Hamiltonian

Let's consider the Hamiltonian of the Kitaev chain

$$H = \sum_{n=1}^{N-1}[\gamma(f_n^\dagger f_{n+1} + f_{n+1}^\dagger f_n) + \Delta(f_n f_{n+1} + f_{n+1}^\dagger f_n^\dagger)] - \sum_{n=1}^{N}\mu(2f_n^\dagger f_n - 1) \quad (5.1)$$

Where the $\gamma$ is the hopping term, $\Delta$ is the pairing term and $\mu$ is the chemical potential. If we take the periodic boundary condition $f_{N+1} = f_1$, then we can write

$$H = \sum_{n=1}^{N}[\gamma(f_n^\dagger f_{n+1} + f_{n+1}^\dagger f_n) + \Delta(f_n f_{n+1} + f_{n+1}^\dagger f_n^\dagger)] - \mu(2f_n^\dagger f_n - 1) \quad (5.2)$$

We can now perform the Fourier transform into $k$-space with $k \in [-\pi, \pi]$ and step-size $\frac{2\pi}{N}$, the notation we use for the Fourier transform is

$$f_n = \frac{1}{\sqrt{N}} \sum_{k=-\pi}^{\pi} f_k e^{-\imath kn} \quad (5.3)$$

In order to simplify notation, we represent $\sum_{k=-\pi}^{\pi} \equiv \sum_k$. We can now define

$$\Delta_k = -\imath\Delta\sin(k) \quad (5.4)$$

$$\epsilon_k = [\gamma\cos(k) - \mu] \quad (5.5)$$

Subsequent to this definition, the Hamiltonian reads

$$H = \sum_k \left\{\epsilon_k(f_k^\dagger f_k + f_{-k}^\dagger f_{-k}) - \Delta_k^* f_{-k} f_k - \Delta_k f_k^\dagger f_{-k}^\dagger + \mu\right\} \quad (5.6)$$

With this, the hopping term and chemical potential term become

$$H_{\text{hopping}} = 2\gamma\sum_k \cos(k) f_k^\dagger f_k \quad (5.7)$$

$$H_{\text{chem pot}} = -\mu\sum_k (2f_k^\dagger f_k - 1) \quad (5.8)$$

while the pairing term becomes

$$H_{\text{pairing}} = \Delta\sum_{k=-\pi}^{\pi} f_k f_{-k} e^{\imath k} + f_{-k}^\dagger f_k^\dagger e^{-\imath k} \quad (5.9)$$

We can split the summation $\sum_{k=-\pi}^{\pi} = \sum_{k=-\pi}^{0} + \sum_{k=0}^{\pi}$. Using a dummy index, we find that

$$H_{\text{pairing}} = 2\imath\Delta \sum_{k=0}^{\pi} \sin(k)[f_k f_{-k} + f_{-k}^\dagger f_k^\dagger] \tag{5.10}$$

Now we note that $\sin(-k) = -\sin(k)$ and also that the operators pick up a $-$ve sign when $k \to -k$, thus the product is an even function and we can use $\sum_{k=0}^{\pi} = \frac{1}{2}\sum_{k=-\pi}^{\pi}$ to write

$$H_{\text{pairing}} = \imath\Delta \sum_{k=-\pi}^{\pi} \sin(k)[f_k f_{-k} - f_{-k}^\dagger f_k^\dagger] \tag{5.11}$$

Thus we can write the full Hamiltonian as

$$H = \sum_k \left\{ 2[\gamma\cos(k) - \mu] f_k^\dagger f_k + \imath\Delta\sin(k)[f_k^\dagger f_{-k}^\dagger - f_{-k} f_k] + \mu \right\} \tag{5.12}$$

### 5.2.1 Bogulibov transformation

We can rewrite the Hamiltonian using the spinor notation as

$$H = \sum_k \Psi^\dagger(\epsilon_k \sigma_z + \Delta_k \sigma_x)\Psi \tag{5.13}$$

$\sigma_i$ the Pauli matrices, and the spinor $\Psi = \begin{pmatrix} f_k \\ f_{-k} \end{pmatrix}$. Which we can see is off-diagonal and is inconvenient for calculating the eigenstates and eigenvalues. We can diagonalize the Hamiltonian using the Bogoliubov transformation as in Jishi (Pg 305). We can do this by making the following substitutions

$$\Delta_k = -\imath\Delta\sin(k) \tag{5.14}$$

$$\epsilon_k = [\gamma\cos(k) - \mu] \tag{5.15}$$

under these substitutions, the Hamiltonian in eqn (5.12) becomes

$$H = \sum_k \left\{ \epsilon_k(f_k^\dagger f_k + f_{-k}^\dagger f_{-k}) - \Delta_k^* f_{-k} f_k - \Delta_k f_k^\dagger f_{-k}^\dagger + \mu \right\} \tag{5.16}$$

The Hamiltonian in Jishi considers spinful fermions. Since we are working with spinless fermions, we have suppressed the spin index using $\sum_{k\sigma} \epsilon_k f_k^\dagger f_k =$

$\frac{1}{2}\sum_k(\epsilon_k f_k^\dagger f_k + \epsilon_{-k} f_{-k}^\dagger f_{-k})$. This allows us to perform the Bogoliubov transformation given by

$$f_k = u_k^*\gamma_k + v_k\gamma_{-k}^\dagger \quad f_{-k} = u_k^*\gamma_{-k} - v_k\gamma_k^\dagger \tag{5.17}$$
$$f_k^\dagger = u_k\gamma_k^\dagger + v_k^*\gamma_{-k} \quad f_{-k}^\dagger = u_k\gamma_{-k}^\dagger - v_k^*\gamma_k \tag{5.18}$$

Here the $\gamma_k^{(\dagger)}$ annihilates(creates) a Bogoliubovon and we have $|u_k|^2+|v_k|^2 = 1$. Substituting these expressions in the Hamiltonian, we can look at the kinetic energy term given by

$$\begin{aligned}\sum_k \epsilon_k(f_k^\dagger f_k + f_k^\dagger f_{-k}) = \sum_k \epsilon_k\Big(&[|u_k|^2 - |v_k|^2]\{\gamma_k^\dagger\gamma_k + \gamma_{-k}^\dagger\gamma_{-k}\} \\ &+ 2u_kv_k\gamma_k^\dagger\gamma_{-k}^\dagger + 2u_k^*v_k^*\gamma_{-k}\gamma_k\Big)\end{aligned} \tag{5.19}$$

and the pairing term in the Hamiltonian given by

$$\begin{aligned}-\Delta_k f_k^\dagger f_{-k}^\dagger &= -\Delta_k u_k^2\gamma_k^\dagger\gamma_{-k}^\dagger + \Delta_k u_k v_k^*\gamma_k^\dagger\gamma_k \\ &+ \Delta_k u_k v_k^*\gamma_{-k}^\dagger\gamma_{-k} + \Delta_k(v_k^*)^2\gamma_{-k}\gamma_k \\ -\Delta_k^* f_{-k} f_k &= -\Delta_k^*(u_k^*)^2\gamma_{-k}\gamma_k + \Delta_k^* u_k^* v_k\gamma_k^\dagger\gamma_k \\ &+ \Delta_k^* u_k^* v_k\gamma_{-k}^\dagger\gamma_{-k} + \Delta_k^* v_k^2\gamma_k^\dagger\gamma_{-k}^\dagger\end{aligned} \tag{5.20}$$

Combining these, we can write

$$\begin{aligned}H = \sum_k \Big\{&[\epsilon_k(|u_k|^2 - |v_k|^2) + \Delta_k u_k v_k^* + \Delta^* u_k^* v_k](\gamma_k^\dagger\gamma_k + \gamma_{-k}^\dagger\gamma_{-k}) \\ &+ \big([2\epsilon_k u_k v_k - \Delta_k u_k^2 + \Delta_k^* v_k^2]\gamma_k^\dagger\gamma_{-k}^\dagger + h.c\big)\Big\}\end{aligned} \tag{5.21}$$

We use the fact that the Bogoliubov transformation diagonalizes the Hamiltonian, i.e.

$$2\epsilon_k u_k v_k - \Delta_k u_k^2 + \Delta_k^* v_k^2 = 0 \tag{5.22}$$

In order to solve this, we will consider $u_k = |u_k|e^{\imath\theta_k}; v_k = |v_k|e^{\imath\phi_k}; \Delta_k = |\Delta_k|e^{2\imath\delta_k}$. This reduces the equation to

$$2\epsilon_k|u_kv_k|e^{\imath(\theta_k+\phi_k)} - |\Delta_k||u_k|^2e^{2\imath(\theta_k+\delta_k)} + |\Delta_k||v_k|^2e^{2\imath(\phi_k-\delta_k)} = 0 \tag{5.23}$$

If we choose $\theta_k = -\phi_k = -\delta_k$ and using the constraint $|u_k|^2+|v_k|^2 = 1$, we find

$$|u_k|^2 = \frac{1}{2}\Big[1 + \frac{\epsilon_k}{\sqrt{\epsilon_k^2 + |\Delta_k|^2}}\Big] \tag{5.24}$$
$$|v_k|^2 = \frac{1}{2}\Big[1 - \frac{\epsilon_k}{\sqrt{\epsilon_k^2 + |\Delta_k|^2}}\Big] \tag{5.25}$$

If we recall, we had

$$\Delta_k = -\imath\Delta\sin(k) \tag{5.26}$$

$$\epsilon_k = [\gamma\cos(k) - \mu] \tag{5.27}$$

We can choose $\Delta = |\Delta|e^{\imath\frac{\pi}{2}}$, so that $\Delta_k$ is real. If we consider $\epsilon_k$ also real, then we have $\theta_k = 0$, which will give us the diagonal Hamiltonian

$$H = \sum_k E_k(\gamma_k^\dagger\gamma_k + \gamma_{-k}^\dagger\gamma_{-k}) + \underbrace{\sum_k(2\epsilon_k v_k^2 - \Delta_k u_k v_k + \mu)}_{\text{numerical factor}} \tag{5.28}$$

Where we have $E_k = \sqrt{\epsilon_k^2 + |\Delta_k|^2}$ and the numerical factor which corresponds to the ground state energy.

## 5.3 Ground state

The ground state of the Hamiltonian is a vacuum of Bogoliubovons. Thus we have

$$\gamma_k|\Psi_0\rangle = \gamma_{-k}|\Psi_0\rangle = 0 \tag{5.29}$$

Hence we can use this to construct a ground state as

$$|\Psi_0\rangle = \prod_k \gamma_k\gamma_{-k}|0\rangle \tag{5.30}$$

Where $|0\rangle$ is the electron vacuum state. The G.S. in terms of the electron creation operators becomes

$$|\Psi_0\rangle = \prod_k(u_k + v_k f_k^\dagger f_{-k}^\dagger)|0\rangle \tag{5.31}$$

Calculating the Ground state energy using the Schrodinger equation $H|\Psi_0\rangle = \varepsilon_0|\Psi_0\rangle$, we get only the numerical factor

$$\varepsilon_0 = \sum_k\{2\epsilon_k v_k^2 - 2\Delta_k u_k v_k + \mu\} \tag{5.32}$$

## 5.4 Topology and phase diagram

Let us consider the Hamiltonian of the Kitaev chain (eqn(5.12)) given by

$$H = \sum_k \Big\{2[\gamma\cos(k) - \mu]f_k^\dagger f_k + \imath\Delta\sin(k)[f_k^\dagger f_{-k}^\dagger - f_{-k}f_k] + \mu\Big\} \tag{5.33}$$

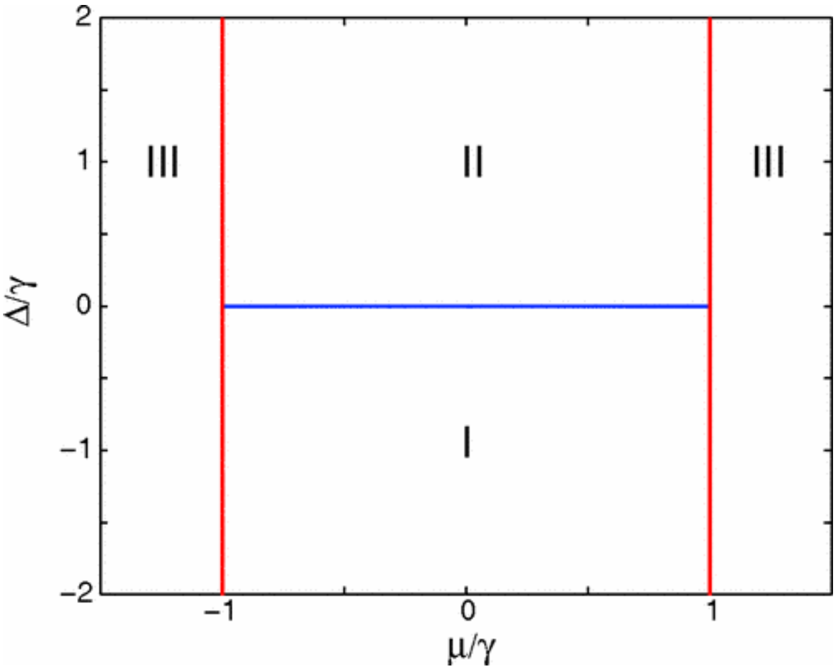

Figure 5.1: Phase diagram of the model with the phases I,II,III marked. Taken from Thakurathi et al.[18]

We see that the Hamiltonian can be diagonalised (eqn (5.28)) and has a dispersion given by

$$E_k = \sqrt{\epsilon_k^2 + |\Delta_k|^2} = \sqrt{(\gamma\cos(k) - \mu)^2 + \Delta^2\sin^2(k)} \tag{5.34}$$

where we have substituted the expressions for $\epsilon_k$ and $\Delta_k$ from eqn (5.4). We can now consider the two-dimensional parameter space defined by $\mu/\gamma$ and $\Delta/\gamma$. We see that there are two routes to having a zero crossing of the $E_k$ in this parameter space. The first is if we consider the case of the $k = 0/\pi$ momentum, we can see that $E_k$ has a gap closing for the lines $\mu/\gamma = \pm 1$. On the other hand, if we consider $\Delta/\gamma = 0$, we can see that the gap closes for the momentum $k = \cos^{-1}(-\mu/\gamma)$. These zero crossings give rise to three distinct phases and can be represented as in the phase diagram Fig 5.1.

While we have explained the zero crossing lines, we actually see that the phases they demarcate, viz. phases I,II, and III in the phase diagram, are actually different topological phases. In order to see this, we work with the Majorana basis. This can be achieved by writing the Hamiltonian in terms of the Majorana operators given by

$$\begin{aligned} a_{2n-1} &= f_n^\dagger + f_n \\ a_{2n} &= i(f_n - f_n^\dagger). \end{aligned} \tag{5.35}$$

We see that these Majorana operators are Hermitian and satisfy $a_{2n}^2 = a_{2n-1}^2 = 1$ and $\{a_j, a_k\} = 2\delta_{jk}$. This allows us to write the Hamiltonian in eqn (5.1) as

$$H = i\sum_{n=1}^{N-1}\left(J_x a_{2n}a_{2n+1} - J_y a_{2n-1}a_{2n+2}\right) + i\sum_{n=1}^{N}\mu a_{2n-1}a_{2n} \tag{5.36}$$

with $J_x = \frac{1}{2}(\gamma - \Delta)$ and $J_y = \frac{1}{2}(\gamma + \Delta)$. We can see that the Kitaev chain in the Majorana representation can have either intra-site or inter-site pairing of the Majoranas and leads to either a topologically trivial phase with all Majoranas paired up within their sites or a topologically non-trivial phase with Majoranas in the bulk paired up across the sites leaving two unpaired Majorana modes on either end. The labels $J_{x,y}$ are chosen since they correspond to the TFIM which can be seen when we perform the Jordan-Wigner transformation given by

$$\begin{aligned} a_{2n-1} &= \left(\prod_{j=1}^{n-1}\sigma_j^z\right)\sigma_n^x \\ a_{2n} &= \left(\prod_{j=1}^{n-1}\sigma_j^z\right)\sigma_n^y \end{aligned} \tag{5.37}$$

where $\sigma^{x,y,z}$ are the Pauli matrices. Applying the transformation to the Hamiltonian, we get

$$H = -\sum_{n=1}^{N-1}\left(J_x\sigma_n^x\sigma_{n+1}^x + J_y\sigma_n^y\sigma_{n+1}^y\right) - \sum_{n=1}^{N}\mu\sigma_n^z. \tag{5.38}$$

Coming back to the phase diagram fig 5.1, if we consider an open chain with an even number of sites, we see that in phase I, i.e. $\Delta/\gamma < 0; -1 < \mu/\gamma < 1$, the $a_{2N}$ mode is uncoupled on the right and the $a_1$ mode is uncoupled on the left. This also corresponds to the case of $\sigma^x$ long-range ferromagnetic order in the TFIM. Phase II, i.e. $\Delta/\gamma > 0; -1 < \mu/\gamma < 1$, has the $a_{2N-1}$ mode and the $a_2$ modes uncoupled on the right and left respectively while corresponding to the $\sigma^y$ long-range ferromagnetic order in the TFIM. Phase III, i.e. $|\mu/\gamma| > 1$, is a topologically trivial phase with no unbound Majorana modes and corresponds to a paramagnetic phase of the TFIM with no spin order.

While we have described the topological order in terms of the Majorana modes, another useful approach would be to look at the bulk Hamiltonian (eqn (5.12)) and define a topological invariant. This can be achieved by representing the Hamiltonian in terms of the Pauli matrices as

$$H = a_{2k}\sigma^y + a_{3k}\sigma^z \tag{5.39}$$

Where we have two $k$-dependent functions given by $a_{2k} = 2(\gamma \cos k - \mu)$ and $a_{3k} = 2\Delta \sin k$ in this case. While $a_{2/3k}$ are known for the Hamiltonian in consideration, they can also be generalised for other Hamiltonians of the same form. This allows us to define the vector $\vec{V_k} = a_{2k}\hat{y} + a_{3k}\hat{z}$ and the angle $\phi_k = \tan^{-1}\frac{a_2k}{a_3k}$.

The winding number $W$ can then be calculated using the integral

$$W = \frac{1}{2\pi}\oint_C \frac{\mathrm{d}\phi_\mathrm{k}}{\mathrm{dk}}dk. \tag{5.40}$$

We can verify that this is indeed the winding number by using the Cauchy's integral formula and constructing a function $z(a_2k, a_3k)$ which has a pole at the origin. We can think of an integral

$$I = \int_C \frac{f(z)}{z - z_0}dz \tag{5.41}$$

Where $f(z)$ is analytic and the integrand has a pole at $z_0$, i.e. the problem of finding the winding number of the coefficients of the effective Hamiltonian can be mapped onto this by considering

$$\begin{aligned} z &= a_{2k} + \imath a_{3k} \\ dz &= \Big(\frac{\partial a_{2k}}{\partial k} + \imath\frac{\partial a_{3k}}{\partial k}\Big)dk \\ f(z) &= 1; \quad z_0 = 0 \end{aligned}$$

By using the Cauchy's integral formula, the integral is given by $f(z_0)$, which is

$$I = \frac{1}{2\pi\imath}\int_{-\pi}^{\pi} dk\frac{(\partial_k a_{2k} + \imath\partial_k a_{3k})}{a_{2k} + \imath a_{3k}} \tag{5.42}$$

Since the $z$ is a construct, we can simplify the calculation by taking $z = re^{\imath\phi}$, which gives

$$I = \frac{1}{2\pi\imath}\int_{-\pi}^{\pi} dk\frac{\partial}{\partial_k}\big[ln(|a_{2k} + \imath a_{3k}|) + \imath\phi_k\big] \tag{5.43}$$

From which we can verify that $I$ is indeed the winding number with $\phi_k = \tan^{-1}(\frac{a_{2k}}{a_{3k}})$. We see that $W = 0/1$ in each of the phases and becomes undefined on the phase boundaries. This allows us to define the winding number as a $\mathbb{Z}$ topological invariant and will be calculated as the primary means of ascertaining the topology in the calculations that follow.

## 5.5 Time evolution

In order to look at the time evolution of the system, we need to calculate the evolution operator

$$U(t,0) = \exp(-\imath Ht) = \exp\left(-\imath t \sum_k E_k[\gamma_k^\dagger \gamma_k + \gamma_{-k}^\dagger \gamma_{-k}]\right) \exp(-\imath \varepsilon_0 t) \quad (5.44)$$

The ground state energy part will give rise to a phase when acted upon the initial state. Suppressing this term, we can use the algebraic properties of the Bogoliubov operators (i.e. $\gamma^2 = 0$) to write

$$\begin{aligned} U(t,0) = \prod_k \, [1 + \underbrace{\gamma_k^\dagger \gamma_k (e^{-\imath E_k t} - 1)}_{I} + \underbrace{\gamma_{-k}^\dagger \gamma_{-k} (e^{-\imath E_k t} - 1)}_{II} \\ + \underbrace{\gamma_k^\dagger \gamma_k \gamma_{-k}^\dagger \gamma_{-k} (e^{-\imath E_k t} - 1)^2}_{III} \,] \end{aligned} \quad (5.45)$$

Since we are looking at piece-wise constant noise, we can consider the Hamiltonian to be independent of time in each piece and look at the evolution of the wavefunction from one piece (index (0)) to the next (index (1)). In this way, we can break up the entire time evolution into pieces and track the evolution of the wave function. Looking at the form of the evolution operator, we see that the BCS ground state wave function is an eigenstate of the evolution operator. If we go back to the fermionic operator notation and put $\alpha_k = (e^{-\imath E_k t} - 1)$, we can see that the three parts of the evolution operator become

$$\begin{aligned} I =& \ \alpha_k(|u_k|^2 f_k^\dagger f_k + |v_k|^2 - |v_k|^2 f_{-k}^\dagger f_{-k} - u_k^* v_k f_k^\dagger f_{-k}^\dagger - u_k v_k^* f_{-k} f_k) && (5.46) \\ II =& \ \alpha_k(|u_k|^2 f_{-k}^\dagger f_{-k} + |v_k|^2 - |v_k|^2 f_k^\dagger f_k - u_k^* v_k f_k^\dagger f_{-k}^\dagger - u_k v_k^* f_{-k} f_k) && (5.47) \\ III =& \ \alpha_k^2(f_k^\dagger f_k f_{-k}^\dagger f_{-k} - u_k^* v_k f_k^\dagger f_{-k}^\dagger - u_k v_k^* f_{-k} f_k && (5.48) \\ & + |v_k|^2[1 - f_{-k}^\dagger f_{-k} - f_k^\dagger f_k]) \end{aligned}$$

Let us consider the action of this evolution operator on the ground state. The details of the piece-wise evolution are hidden in the $u_k, v_k$ and hence also in $\alpha_k$. Hence, we use the labels (0/1) to differentiate the parameters of the initial state and the evolution operator which takes it to the next step.

Thus, the action of the three parts on the BCS ground state is given by

$$I|\Psi_0\rangle = \alpha_k^{(1)}\big[\big(u_k^{(0)}|v_k^{(1)}|^2 - u_k^{(1)}v_k^{*(1)}v_k^{(0)}\big) + \big(|u_k^{(1)}|^2 v_k^{(0)} - u_k^{*(1)}v_k^{(1)}u_k^{(0)}\big) f_k^\dagger f_{-k}^\dagger\big]|0\rangle \tag{5.49}$$

$$II|\Psi_0\rangle = \alpha_k^{(1)}\big[\big(u_k^{(0)}|v_k^{(1)}|^2 - u_k^{(1)}v_k^{*(1)}v_k^{(0)}\big) + \big(|u_k^{(1)}|^2 v_k^{(0)} - u_k^{*(1)}v_k^{(1)}u_k^{(0)}\big) f_k^\dagger f_{-k}^\dagger\big]|0\rangle \tag{5.50}$$

$$III|\Psi_0\rangle = (\alpha_k^{(1)})^2\big[\big(u_k^{(0)}|v_k^{(1)}|^2 - u_k^{(1)}v_k^{*(1)}v_k^{(0)}\big) + \big(|u_k^{(1)}|^2 v_k^{(0)} - u_k^{*(1)}v_k^{(1)}u_k^{(0)}\big) f_k^\dagger f_{-k}^\dagger\big]|0\rangle \tag{5.51}$$

From the form of the resultant state, we can see that if (0) = (1), i.e. evolution of the initial state with the initial Hamiltonian, is the same state with a phase factor. We also notice that the BCS ground state form is retained at any arbitrary step of the evolution. Combining all the terms, the state reads

$$\begin{aligned}|\Psi_1\rangle = \prod_k \Bigg\{ &\Big[u_k^{(0)} + \big(u_k^{(0)}|v_k^{(1)}|^2 - u_k^{(1)}v_k^{*(1)}v_k^{(0)}\big)\big(2\alpha_k^{(1)} + (\alpha_k^{(1)})^2\big)\Big] \\ &+ \Big[v_k^{(0)} + \big(|u_k^{(1)}|^2 v_k^{(0)} - u_k^{*(1)}v_k^{(1)}u_k^{(0)}\big)\big(2\alpha_k^{(1)} + (\alpha_k^{(1)})^2\big)\Big] f_k^\dagger f_{-k}^\dagger \Bigg\} e^{-\imath\varepsilon_0^{(1)}t}|0\rangle\end{aligned} \tag{5.52}$$

Which we can see can be written as a BCS wavefunction with renormalized values $|\Psi_1\rangle = \prod_k (A_k + B_k f_k^\dagger f_{-k}^\dagger)|0\rangle$, where

$$A_k = e^{-\imath\varepsilon_0^{(1)}t}\Big[u_k^{(0)} + \big(u_k^{(0)}|v_k^{(1)}|^2 - u_k^{(1)}v_k^{*(1)}v_k^{(0)}\big)\big(2\alpha_k^{(1)} + (\alpha_k^{(1)})^2\big)\Big] \tag{5.53}$$

$$B_k = e^{-\imath\varepsilon_0^{(1)}t}\Big[v_k^{(0)} + \big(|u_k^{(1)}|^2 v_k^{(0)} - u_k^{*(1)}v_k^{(1)}u_k^{(0)}\big)\big(2\alpha_k^{(1)} + (\alpha_k^{(1)})^2\big)\Big] \tag{5.54}$$

This can be expressed in the matrix form as

$$\begin{pmatrix} A_k \\ B_k \end{pmatrix} = e^{-\imath\varepsilon_0^{(1)}t} \underbrace{\begin{pmatrix} 1 + \beta(|v_k^{(1)}|^2) & -\beta u_k^{(1)}v_k^{*(1)} \\ -\beta u_k^{*(1)}v_k^{(1)} & 1 + \beta(|u_k^{(1)}|^2) \end{pmatrix}}_{\mathcal{T}_k(g_1;t-t_0)} \begin{pmatrix} u_k^{(0)} \\ v_k^{(0)} \end{pmatrix} \tag{5.55}$$

Where we have defined $\beta_k = (2\alpha_k^{(1)} + [\alpha_k^{(1)}]^2)$ with $\alpha_k^{(1)} = e^{-\imath E_k^{(1)}(t-t_0)} - 1$.

The transfer matrix $\mathcal{T}_k(g;t)$ depends on the parameters $g \equiv (\mu, \gamma, \Delta)$ through the corresponding $u_k, v_k, E_k$ and evolves the wavefunction from $t_0$ to $t$ through $\beta_k(g,t)$ to get the state at $t$ to be $\begin{pmatrix} A_k(t) \\ B_k(t) \end{pmatrix} = \chi_k(t)$. We can now generalise to an arbitrary number of pieces of time evolution and can write state for the $m^{th}$ piece of the time evolution as

$$\chi_k(m\tau + t_0) = e^{-\imath \sum_{i=1}^{m} \varepsilon_0^{(i)} \tau} \prod_{i=1}^{m} \big(\mathcal{T}_k(g_i, \tau)\big) \chi_k(t_0) \tag{5.56}$$

### 5.5.1 Square Wave

Let us now calculate the transfer matrix and the time-evolved state for various driving protocols. We begin with the case of the square wave driving where the parameters $g := (\gamma, \mu, \Delta)$ are oscillating between two values in each of the time steps $\tau$.

The time evolution operator for each period of the square wave (with periodicity $2\tau$) is given by

$$\mathcal{T}_k(g_1, g_2; 2\tau) = \mathcal{T}_k(g_2; \tau)\mathcal{T}_k(g_1, \tau) \tag{5.57}$$

where the transfer matrices $\mathcal{T}_k$ depend on the parameters of the evolution $g$. We can use the piecewise constant nature of the driving, whereby the transfer matrix for each piece can be written trivially as

$$\mathcal{T}_k(g; t) = \exp\{[-\imath H(g)t]\} \tag{5.58}$$

Thus, we can write the entire time evolution as a product of these individual pieces as

$$\chi_k(m\tau + t_0) = e^{-\imath \frac{m}{2}(\varepsilon_0^{(1)} + \varepsilon_0^{(0)})\tau} \big(\mathcal{T}_k(\tau)\big)^m \chi_k(t_0) \tag{5.59}$$

We can simplify this further by expanding

$$\mathcal{T}_k(g; t) = \mathbb{1} + \beta_k(g; t) S_k(g) \tag{5.60}$$

where,

$$S_k(g) = \begin{pmatrix} (|v_k(g)|^2) & -u_k(g)v_k^*(g) \\ -u_k^*(g)v_k(g) & (|u_k(g)|^2) \end{pmatrix} \tag{5.61}$$

If we consider the case where $u_k, v_k$ are real, then we have

$$S_k(g) = \frac{1}{2E_k} \begin{pmatrix} E_k - \epsilon_k & -\Delta_k \\ -\Delta_k & E_k + \epsilon_k \end{pmatrix} = \frac{1}{2E_k}[E_k \mathbb{1} - \epsilon_k \sigma_z - \Delta_k \sigma_x] \tag{5.62}$$

where we can notice by the structure of the matrix, that $S_k(g)^2 = S_k(g)$. Thus we write

$$\mathcal{T}_k(g; t) = (\mathbb{1} + \beta_k(g; t) S_k(g)) = e^{-2\imath E_k S_k(g) t} \tag{5.63}$$

This can be expressed in terms of the Pauli matrices as

$$\mathcal{T}_k(g;t) = e^{-\imath[E_k\mathbb{1} - \epsilon_k\sigma_z - \Delta_k\sigma_x]t} = e^{-\imath E_k t} e^{\imath \vec{X}_k \cdot \vec{\sigma} t} \tag{5.64}$$

Where $\vec{X}_k = (\Delta_k, 0, \epsilon_k)$. The full transfer matrix is given by $\mathcal{T}(g;t) = \bigotimes_k \mathcal{T}_k(g;t)$, where we have used the fact that the various $k$ dependent terms are independent. This reads

$$\mathcal{T}(g;t) = \begin{pmatrix} \mathcal{T}_{k_1}(g;t) & & \\ & \ddots & \\ & & \mathcal{T}_{k_N}(g;t) \end{pmatrix} \tag{5.65}$$

The time-evolved wavefunction can be written as

$$|\Psi(t)\rangle = \begin{pmatrix} \Psi_{k_1}(t) \\ \Psi_{k_2}(t) \\ \vdots \\ \Psi_{k_N}(t) \end{pmatrix} \tag{5.66}$$

which using the transfer matrix gives

$$|\Psi(t)\rangle = \mathcal{T}(g_N; t_N - t_{N-1})\mathcal{T}(g_{N-1}; t_{N-1} - t_{N-2}) \dots \mathcal{T}(g_1; t_1 - t_0)|\Psi(t_0)\rangle \tag{5.67}$$

### 5.5.2 Noise

In the case of the piece-wise constant noise, the parameter set $g$ are uncorrelated random numbers drawn from a probability distribution $\mathcal{P}(g)$. This allows us to calculate each instance of the driving as a product of transfer matrices,

$$\mathcal{T}(t_N) = \mathcal{T}(g_N; t_N - t_{N-1}) \times \mathcal{T}(g_{N-1}; t_{N-1} - t_{N-2}) \dots \mathcal{T}(g_1; t_1 - t_0). \tag{5.68}$$

These individual instances need to be averaged over disorder by considering the probability distribution $\mathcal{P}(g)$. Thus the disorder-averaged wavefunction is given by

$$\begin{aligned} \overline{|\Psi(t)\rangle} = \int \Big(\prod_{i=1}^{N} dg_i \mathcal{P}(g_i)\Big)\mathcal{T}(g_N; t_N - t_{N-1}) \\ \times \mathcal{T}(g_{N-1}; t_{N-1} - t_{N-2}) \dots \mathcal{T}(g_1; t_1 - t_0)|\Psi(t_0)\rangle. \end{aligned} \tag{5.69}$$

Since the $g_i$ are independent in each step, we have

$$\overline{|\Psi(t)\rangle} = \int dg_N \mathcal{T}(g_N; \Delta t_N)\mathcal{P}(g_N) \int dg_{N-1}\mathcal{T}(g_{N-1}; \Delta t_{N-1})\mathcal{P}(g_{N-1}) \\ \times \ldots \int dg_1 \mathcal{T}(g_1; \Delta t_1)\mathcal{P}(g_1)|\Psi(t_0)\rangle \quad (5.70)$$

which can be written as

$$\overline{|\Psi(t)\rangle} = \overline{\mathcal{T}}(\Delta t_N)\overline{\mathcal{T}}(\Delta t_{N-1}) \ldots \overline{\mathcal{T}}(\Delta t_1)|\Psi(t_0)\rangle \quad (5.71)$$

Using the independence of the $k$-dependent terms, the full transfer matrix under disorder averaging becomes

$$\overline{\mathcal{T}}(t) = \begin{pmatrix} \overline{\mathcal{T}}_{k_1}(t) & & \\ & \ddots & \\ & & \overline{\mathcal{T}}_{k_N}(t) \end{pmatrix} \quad (5.72)$$

Where we have for each $k$, the disorder averaged transfer matrix $\overline{\mathcal{T}}_k(t) = \int dg \mathcal{P}(g)\mathcal{T}_k(g;t)$.

### 5.5.3 Quench

We have calculated the transfer matrix for multiple pieces in the earlier sections and we now come to the simple case of a quench from a set of parameters $g_1$ to $g_2$ and continued time evolution with the set $g_2$. The transfer matrix is given by

$$\mathcal{T}_k(g_1, g_2; t) = \mathcal{T}_k(g_2; t)\mathcal{T}_k(g_1, \tau) \quad (5.73)$$

This product can be explicitly calculated as follows by writing the transfer matrix as

$$\mathcal{T}_k(g; t) = e^{-\imath E_k(g)t} e^{\imath \vec{X}_k(g)\cdot\vec{\sigma}t} \quad (5.74)$$

In this expression, we see that the $e^{-\imath E_k t}$ part commutes and can be easily calculated. To calculate the $\sigma$ part, we make use of the multiplication identity of Pauli vectors,

$$e^{\imath a\hat{n}\cdot\vec{\sigma}} e^{\imath b\hat{m}\cdot\vec{\sigma}} = e^{\imath c\hat{p}\cdot\vec{\sigma}} \quad (5.75)$$

where,

$$\begin{aligned} \cos c &= \cos a \cos b - (\hat{n}\cdot\hat{m}) \sin a \sin b \\ \hat{p} &= \frac{1}{\sin c}\left[\hat{n} \sin a \cos b + \hat{m} \cos a \sin b - \hat{n} \times \hat{m} \sin a \sin b\right] \end{aligned} \quad (5.76)$$

By using this identity, we can calculate

$$\tilde{\mathcal{T}}_k(g_2, g_1; t+\tau) = e^{-\imath(E_k(g_2)t + E_k(g_1)\tau)} e^{\imath t \vec{X}_k(g_2)\cdot\vec{\sigma}} e^{\imath\tau\vec{X}_k(g_1)\cdot\vec{\sigma}} \tag{5.77}$$

This gives us for the magnitude part,

$$\begin{aligned}\cos c_k = {} & \cos(E_k(g_2)t)\cos(E_k(g_1)\tau) - \\ & \hat{X}_k(g_2)\cdot\hat{X}_k(g_1)\sin(E_k(g_2)t)\sin(E_k(g_1)\tau)\end{aligned} \tag{5.78}$$

with

$$\hat{X}_k(g_2)\cdot\hat{X}_k(g_1) = \frac{\Delta_k(g_2)\Delta_k(g_1) + \epsilon_k(g_2)\epsilon_k(g_1)}{E_k(g_2)E_k(g_1)} \tag{5.79}$$

and the direction is given by the unit vector

$$\hat{p_k}\cdot\vec{\sigma} = \frac{1}{\sin c}[\alpha_{1k}\sigma_x + \alpha_{2k}\sigma_y + \alpha_{3k}\sigma_z] \tag{5.80}$$

with

$$\begin{aligned}\alpha_{1k} &= \frac{\Delta_k(g_2)}{E_k(g_2)}\sin(E_k(g_2)t)\cos(E_k(g_1)\tau) + \frac{\Delta_k(g_1)}{E_k(g_1)}\cos(E_k(g_2)t)\sin(E_k(g_1)\tau) \\ \alpha_{2k} &= -\left[\frac{\Delta_k(g_2)\epsilon_k(g_1) - \epsilon_k(g_2)\Delta_k(g_1)}{E_k(g_2)E_k(g_1)}\right]\sin(E_k(g_2)t)\sin(E_k(g_1)\tau) \\ \alpha_{3k} &= -\frac{\epsilon_k(g_2)}{E_k(g_2)}\sin(E_k(g_2)t)\cos(E_k(g_1)\tau) - \frac{\epsilon_k(g_1)}{E_k(g_1)}\cos(E_k(g_2)t)\sin(E_k(g_1)\tau).\end{aligned}$$

Thus we can write the effective Hamiltonian $H_{eff}$, which is defined by $\mathcal{T}_k(g;t) = e^{\imath H_{eff}(t)}$ as

$$H_{eff} = \sum_{i=1}^{3} a_{ik}\sigma_i \tag{5.81}$$

With $a_i = \frac{c_k}{\sin(c_k)}\alpha_k$. We also know that given an exponential of a Pauli vector, we can write

$$\tilde{\mathcal{T}}_k = e^{\imath c_k \hat{p_k}\cdot\vec{\sigma}} = \cos(c_k)\mathbb{1} + \imath\sin(c_k)\hat{p_k}\cdot\vec{\sigma} \tag{5.82}$$

By using the algebra of the Pauli matrices and calculating the trace of the matrices, we have

$$Tr(\mathbb{1}\tilde{\mathcal{T}}_k) = 2\cos(c_k) \tag{5.83}$$

$$Tr(\sigma_i\tilde{\mathcal{T}}_k) = 2\imath\sin(c_k)\hat{p}_{ik} \tag{5.84}$$

Thus we can write the effective Hamiltonian as

$$H_{eff} = c_k\hat{p}_{ik}\cdot\vec{\sigma} \tag{5.85}$$

Which gives

$$a_{ik} = \frac{c_k}{2\imath\sin c_k}Tr(\sigma_i\tilde{\mathcal{T}}_k). \tag{5.86}$$

### Eigenvectors of the effective Hamiltonian

We can calculate the time-dependent effective Hamiltonian by using the transfer matrix:

$$\mathcal{T}_k(g;t) = e^{\imath H_{eff}(t)}. \tag{5.87}$$

We can evaluate this using the expression for the transfer matrix and the properties of the Pauli vector. Using these we write

$$H_{eff}(t) = a_{1k}(t)\sigma_x + a_{2k}(t)\sigma_y + a_{3k}(t)\sigma_z. \tag{5.88}$$

We can look at the winding of the coefficients $a_{ik}$ and look at the time at which the topological transitions occur. We plot the minimum eigenvalue and the winding number as a function of time in Fig. 5.2 and see that some of the transitions also occur along with the zero level crossings of the effective Hamiltonian. The signature of these transitions is also seen in the discontinuous change in the sign of the $a_{3k}$ coefficient for $k = 0, \pm\pi$. The eigenvalues of the effective Hamiltonian are given by $\varepsilon = \pm\sqrt{\sum_{i=1}^{3} a_{ik}^2}$ and the corresponding eigenvectors are

$$|\varphi_k^+\rangle = \frac{1}{\sqrt{2\varepsilon(a_{3k}+\varepsilon)}}\begin{pmatrix} a_{3k}+\varepsilon \\ a_{1k}+\imath a_{2k} \end{pmatrix} \tag{5.89}$$

$$|\varphi_k^-\rangle = \frac{1}{\sqrt{2\varepsilon(a_{3k}+\varepsilon)}}\begin{pmatrix} -a_{1k}+\imath a_{2k} \\ a_{3k}+\varepsilon \end{pmatrix} \tag{5.90}$$

Since we can calculate the evolution of the states by operating the transfer matrix on the initial state, we can track the overlap of the time-evolved state with the corresponding eigenvectors of the instantaneous effective Hamiltonian for all times. i.e

$$c_k^+ = \langle\psi_k(t)|\varphi_k^+(t)\rangle \quad c_k^- = \langle\psi_k(t)|\varphi_k^-(t)\rangle \tag{5.91}$$

We see that there are three important $k$-points viz. $k = 0, \pm\pi$. Tracking the changes of the overlaps of these points with time provides us with a signature for the topological transition. We plot the overlap of the time-evolved state with the eigenvectors for each value of the momentum in Fig. 5.3 and see that the overlap has no zero crossings in the trivial case, but has multiple zero crossings when the winding number is non-zero. We now look more closely at the nature of the topological transitions. These topological transitions involve a discontinuous change in the overlap for either the $k = 0$ or $k = \pm\pi$. We can see the two transitions happen with different time scales. We plot the overlap of the time-evolved state in both the topological and trivial cases for all values of the momentum $k$ in Fig. 5.4. We see that the transitions are driven by either a sharp change in the overlap of the $k = \pm\pi$ or the $k = 0$ states.

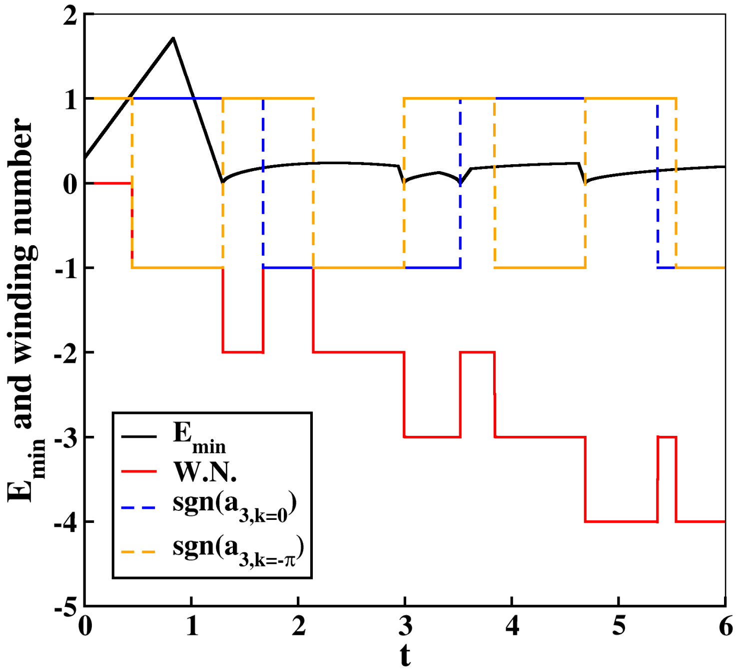

Figure 5.2: The change in winding number as a function of time. We can see that the transitions occur when $a_{3k=0,\pm\pi}$ changes sign. Also plotted is the minimum value of the eigenvalue for each time point. We can see that some transitions are accompanied by zero level crossings.

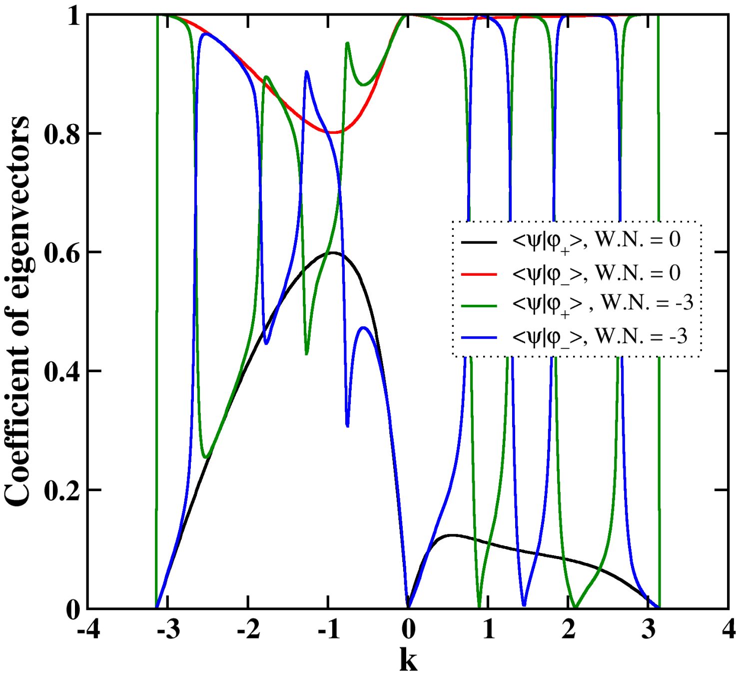

Figure 5.3: Overlap of the time evolved state with $|\varphi^{\pm}\rangle$ for different winding numbers

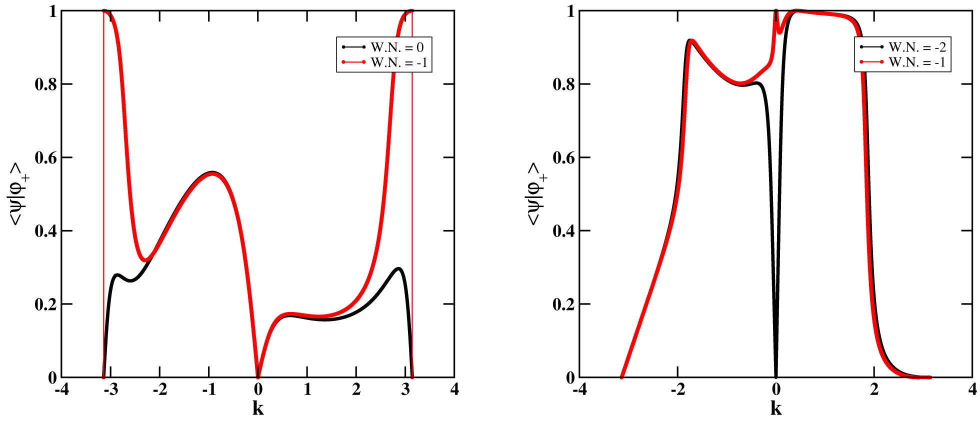

Figure 5.4: *Left panel:* A topological transition driven by the change in the overlap of the $k = \pm\pi$ states. *Right panel:* The transition is driven by the change in the overlap of the $k = 0$ state.

## 5.6 Loschmidt Echo

In order to look at the effect of driving, we need to consider the difference between the initial and time-evolved wavefunctions. This can be done by considering the Loschmidt echo as a function of time, which is defined as the overlap between the initial and time-evolved step. That is

$$\mathcal{L}(t) = |\langle\Psi(t)|\Psi_0\rangle|^2 \tag{5.92}$$

In the case of the piecewise constant time evolution, we can consider the overlap of the initial state and the state after the first piece of time evolution $|\Psi_1\rangle$. The Loschmidt amplitude can be calculated by noting that $|\Psi_1\rangle = \prod_k (A_k + B_k f_k^\dagger f_{-k}^\dagger)|0\rangle$, thus the terms are

$$\begin{aligned}\langle\Psi_1|\Psi_0\rangle = \prod_k \Big[&\langle 0|(A_k^* u_k^{(0)})|0\rangle + \langle 0|(B_k^* u_k^{(0)}) f_{-k} f_k|0\rangle \\ &+ \langle 0|(A_k^* v_k^{(0)}) f_k^\dagger f_{-k}^\dagger|0\rangle + \langle 0|(B_k^* v_k^{(0)} f_k f_k^\dagger f_{-k} f_{-k}^\dagger)|0\rangle\Big]\end{aligned} \tag{5.93}$$

Applying the fermionic creation and annihilation operators to the vacuum state $|0\rangle$, we are left with

$$\langle\Psi_1|\Psi_0\rangle = \prod_k \left[\langle 0|(A_k^* u_k^{(0)})|0\rangle + \langle 0|(B_k^* v_k^{(0)}|0\rangle\right] \tag{5.94}$$

In terms of the Bogulibov parameters $u_k, v_k$, this works out to be

$$\langle\Psi_1|\Psi_0\rangle = \prod_k \{1 + [2\alpha_k^{*(1)} + (\alpha_k^{*(1)})^2][|u_k^{(0)}|^2|v_k^{(1)}|^2 + |v_k^{(0)}|^2|u_k^{(1)}|^2 - u_k^{*(1)}u_k^{(0)}v_k^{(1)}v_k^{*(0)} - u_k^{(1)}u_k^{*(0)}v_k^{*(1)}v_k^{(0)}]\} \tag{5.95}$$

If we put $[2\alpha_k^{(1)} + (\alpha_k^{(1)})^2] = \beta_k$, we can calculate

$$\mathcal{L}_1 = |\langle\Psi_1|\Psi_0\rangle|^2 = \prod_k \Big\{ \big[1 + \beta_k^*(|u_k^{(0)}|^2|v_k^{(1)}|^2 + |v_k^{(0)}|^2|u_k^{(1)}|^2 - u_k^{*(1)}u_k^{(0)}v_k^{(1)}v_k^{*(0)} - u_k^{(1)}u_k^{*(0)}v_k^{*(1)}v_k^{(0)})\big]\big[1 + \beta_k(|u_k^{(0)}|^2|v_k^{(1)}|^2 + |v_k^{(0)}|^2|u_k^{(1)}|^2 - u_k^{*(1)}u_k^{(0)}v_k^{(1)}v_k^{*(0)} - u_k^{(1)}u_k^{*(0)}v_k^{*(1)}v_k^{(0)})\big]\Big\} \tag{5.96}$$

Which simplifies to

$$\mathcal{L}_1 = |\langle\Psi_1|\Psi_0\rangle|^2 = \prod_k \Big\{1 + (\beta_k + \beta_k^*)\big[|u_k^{(0)}|^2|v)_k^{(1)}|^2 + |v_k^{(0)}|^2|u_k^{(1)}|^2 - u_k^{*(1)}u_k^{(0)}v_k^{(1)}v_k^{*(0)} - u_k^{(1)}u_k^{*(0)}v_k^{*(1)}v_k^{(0)}\big] + |\beta_k|^2\big[|u_k^{(0)}|^2|v_k^{(1)}|^2 + |v_k^{(0)}|^2|u_k^{(1)}|^2 - u_k^{*(1)}u_k^{(0)}v_k^{(1)}v_k^{*(0)} - u_k^{(1)}u_k^{*(0)}v_k^{*(1)}v_k^{(0)}\big]^2\Big\} \tag{5.97}$$

Since the time dependence is now restricted to $\beta_k$, the time evolution of the Loschmidt Echo $\mathcal{L}(t)$ can be easily calculated given the $u_k^{(0/1)}, v_k^{(0/1)}$ in both pieces. This procedure can also be applied to other piecewise constant driving protocols with a corresponding calculation. The Loschmidt echo is also the Majorana survival probability[37] and allows us to ascertain the fate of the Majorana end modes when time evolution occurs in each of the phases.

## 5.7 Dynamical quantum phase transitions

In equilibrium, phase transitions are known to be accompanied by the non-analytic behaviour of the free-energy when the control parameter is varied. In particular, quantum phase transitions are those where the control parameter is independent of temperature and the transition can be observed even at absolute zero. Extending this definition into non-equilibrium, one can look at the dynamical quantum phase transition (DQPT) where the phase transition is characterised by a non-analyticity when the system is evolved in time[29].

In non-equilibrium, the concept of free-energy is no longer applicable and hence cannot be the quantity which has the non-analyticity. We know that the partition function in terms of the free-energy is given by

$$Z = e^{-\beta F} \tag{5.98}$$

where $\beta = 1/k_B T$ and $F$ is the Free energy. Following Heyl[29], we define the Loschmidt amplitude

$$\mathcal{G}(t) = \langle \Psi_0 | \Psi(t) \rangle = \langle \Psi_0 | e^{-iHt} | \Psi_0 \rangle \tag{5.99}$$

This Loschmidt amplitude is formally similar to the partition function (for a detailed discussion see §2.5 of[29]) with a particular dependence on the number of degrees of freedom $N$ in the large $N$ limit that can be expressed as

$$\mathcal{G}(t) = e^{-Ng(t)} \tag{5.100}$$

where $g(t)$ is the associated rate function. This can be rewritten as

$$g(t) = -\lim_{N\to\infty} \frac{1}{N} \log[\mathcal{G}(t)]. \tag{5.101}$$

A corresponding rate function can also be calculated for the Loschmidt echo $\mathcal{L}(t)$ as

$$\lambda(t) = -\lim_{N\to\infty} \frac{1}{N} \log[\mathcal{L}(t)] \tag{5.102}$$

As mentioned above, the signature of a DQPT is the non-analyticity of the rate function. This occurs when the time-evolved wavefunction becomes orthogonal to the initial wavefunction, i.e $\langle \psi(0) | \psi(t) \rangle = 0$.

This condition, for a time-independent Hamiltonian, such as in a quench problem, is equivalent to $\mathcal{G}(t) = \langle \psi(0) | e^{-iHt} | \psi(0) \rangle = 0$. Since we have found the time evolution operator and the time-evolved wavefunction, we can find the condition(s) for the vanishing of the Loschmidt amplitude ($\mathcal{G}(t)$).

$$\begin{aligned} \mathcal{G}(t) &= \prod_k \begin{pmatrix} u_k^{(0)} & v_k^{(0)} \end{pmatrix} \begin{pmatrix} 1 + \beta_k(t) |v_k^{(0)}|^2 & -\beta_k(t) u_k^{(1)} v_k^{(1)} \\ -\beta_k(t) u_k^{(1)} v_k^{(1)} & 1 + \beta_k(t) |u_k^{(0)}|^2 \end{pmatrix} \begin{pmatrix} u_k^{(0)} \\ v_k^{(0)} \end{pmatrix} \\ &= \prod_k \left[ 1 + \left( e^{-2iE_k t} - 1 \right) \left( u_k^{(0)} v_k^{(1)} - u_k^{(1)} v_k^{(0)} \right)^2 \right] \end{aligned} \tag{5.103}$$

The condition for the Loschmidt amplitude to vanish is that any one of the terms in the product should vanish. Since $\beta_k(t)$ is the only term that can change sign, and the other terms are real and positive-definite, a sub-condition is that $\beta_k(t)$ is real and negative. This implies

$$2E_{k_c} t_c = (2n+1)\pi \tag{5.104}$$

for which $\beta_{k_c}(t_c) = -2$. Simultaneously,

$$\left(u_{k_c}^{(0)} v_{k_c}^{(1)} - u_{k_c}^{(1)} v_{k_c}^{(0)}\right)^2 = \frac{1}{2} \tag{5.105}$$

should also be satisfied. These two conditions yield a specific combination of momentum and time i.e. $(k_c, t_c)$, for a specific quench from $g_0$ to $g_1$. The above condition for $k_c$ yields

$$\frac{\epsilon_{k_c}^{(0)}}{\Delta_{k_c}^{(0)}} = \frac{\Delta_{k_c}^{(1)}}{\epsilon_{k_c}^{(1)}}. \tag{5.106}$$

Another way of arriving at this would be to use the transfer matrix. We know that $\mathcal{G}(t)$ vanishes for $(k_c, t_c)$ when the initial and final states become orthogonal. We can write this condition as,

$$\langle \Psi_{k_c}(t_0) | \Psi_{k_c}(t_c) \rangle = \langle \Psi_{k_c}(t_0) | \mathcal{T}(g; t_c) \Psi_{k_c}(0) \rangle = 0 \tag{5.107}$$

Since $\beta_{k_c}(t_c)$ part of the transfer matrix only contributes to the global phase, the orthogonality comes from the $e^{\imath \vec{X}_k \cdot \vec{\sigma} t}$ ,which in terms of the $u_k, v_k$ read

$$\begin{pmatrix} u_{k_c}^{(0)} & v_{k_c}^{(0)} \end{pmatrix} \hat{X}_{k_c} \cdot \vec{\sigma} \begin{pmatrix} u_{k_c}^{(0)} \\ v_{k_c}^{(0)} \end{pmatrix} = 0 \tag{5.108}$$

Where by substituting, we can see

$$\begin{pmatrix} u_{k_c}^{(0)} & v_{k_c}^{(0)} \end{pmatrix} \left(\frac{\Delta_{k_c}^{(1)}}{E_{k_c}^{(1)}} \sigma_x + \frac{\epsilon_{k_c}^{(1)}}{E_{k_c}^{(1)}} \sigma_z\right) \begin{pmatrix} u_{k_c}^{(0)} \\ v_{k_c}^{(0)} \end{pmatrix} = 0 \tag{5.109}$$

Which can be simplified to give

$$\Delta_{k_c}^{(1)} \Delta_{k_c}^{(0)} + \epsilon_{k_c}^{(1)} \epsilon_{k_c}^{(0)} = 0 \tag{5.110}$$

Substituting $\epsilon_k = -(\gamma \cos(k) - \mu)$ and $\Delta_k = \Delta \sin(k)$, we get the following equation for $k_c$:

$$(\gamma_0 \gamma_1 - \Delta_0 \Delta_1) \cos^2(k_c) - (\gamma_0 \mu_1 + \gamma_1 \mu_0) \cos(k_c) + (\mu_0 \mu_1 + \Delta_0 \Delta_1) = 0. \tag{5.111}$$

Thus we can work out the momentum which would be responsible for the non-analyticity at the critical time $t_c$. Furthermore, we see that these $k_c$ correspond to either $k = 0$ or the $k = \pm\pi$ states where the gap closes at $t_c$.

## 5.8 Results

Now that we have elaborated on the method, we come to the results. We will first benchmark the method against other methods and known results. We follow that by calculations of the rate function for three driving protocols viz. the square wave, noise and quench.

### 5.8.1 Benchmarks

In order to verify the calculations, we first look at the winding number. As given above, we calculate the winding number using the integral (eqn (5.40))

$$W = \frac{1}{2\pi} \oint_C \frac{\mathrm{d}\phi_{\mathrm{k}}}{\mathrm{dk}} dk. \tag{5.112}$$

We can see that this expression is indeed correct and works in the time evolved case by looking at the variation of the $a_{2/3k}$ when quenched from phase III to phase II and looking at whether there is any winding around the origin. This is seen in Fig. 5.5, where the $a_{2/3k}$ are plotted in the initial phase ($\gamma = \delta = 1, \mu_0 = 3.0$) on the left and the value post quench, at $t = t_c$ into phase II ($\gamma = \delta = 1, \mu_0 = 0.0$) is plotted on the right.

Coming to the case of the square wave driving protocol, we see that the winding number changes in all the three phases, but has a minimum time period required to observe such a change. We evolve the system in phase III ($\gamma = \delta = 1, \mu = 2.0$) and plot in Fig. 5.6 the dependence of the winding number on the frequency of the square wave. We see that there is a maximum frequency above which there is no winding, while low frequency driving leads to larger winding numbers. This is consistent with the results of Thakurathi et al.[18] in case of periodic $\delta$-function kicks.

Another benchmark is the observation of dynamical quantum phase transitions (DQPTs) when the system is quenched from one phase to the other. We look at the quench from phase II to III in particular from $\gamma = \delta = 1, \mu_0 = 0$ to $\gamma = \delta = 1, \mu_1 = 3.0$. In Fig. 5.7 we plot the rate function $g(t) = -\frac{1}{N}\log[\mathcal{G}(t)]$ with the time and see that there appear nonanalyticities. We scale the time with $t_c$ the critical time and show the behaviour over a few multiples of $t_c$ in the main panel and an extended period of time in the inset

### 5.8.2 Square Wave

Coming to the calculations using the transfer matrix method, we start with the case of periodic driving. In this protocol, we consider without loss of

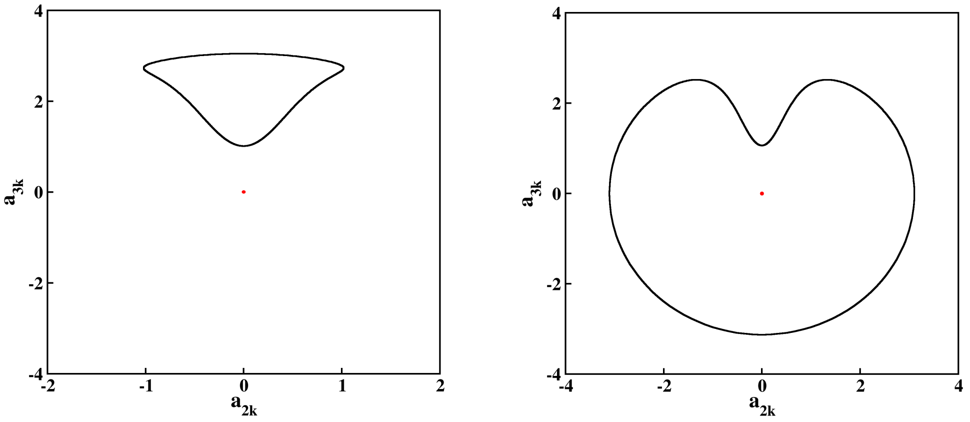

Figure 5.5: The Hamiltonian coefficients $a_{2k}, a_{3k}$ plotted for a system quenched from phase III to phase II. The left panel shows the initial parameters and the right panel corresponds to the final parameters post the quench and evolution up to t=$t_c$. The red dot indicates the origin and as can be seen, the $a_{2/3k}$ get modified to wind around the origin post the quench.

generality, only the variation of the chemical potential between the two fixed values.

We first look at the square wave driving where the parameters of both the pieces lies within the same topological phase of the system. We plot the rate function $g(t) = -\frac{1}{N}\log[\mathcal{G}(t)]$ as a function of time within both the topologically interesting and trivial phases. In particular, in the topological phase, we consider the parameters to be $\gamma = \Delta = 1$ and the chemical potential fluctuates between the values $\mu_0 = 0.5$ and $\mu_1 = 0.6$ which corresponds to phase II of the phase diagram (Fig. 5.1). Since the phase is topological, we see the presence of the dynamical quantum phase transitions (DQPTs) as evidenced by the non-analyticities in the rate function plotted in the left panel of Fig. 5.8. On the right panel, we look at the topologically trivial phase, in particular corresponding to the parameters $\gamma = \Delta = 1$ and the chemical potentials $\mu_0 = 3.0, \mu_1 = 3.1$. This shows no non-analyticities as expected within phase III.

Next, we look at the case where the chemical potential values lie on two sides of the phase boundary between phases II and III. In particular, we look at both the cases where the initial Hamiltonian corresponds to phase II and III, while the other set of parameters belongs to phases III and II correspondingly. We again plot the rate function as a function of time in

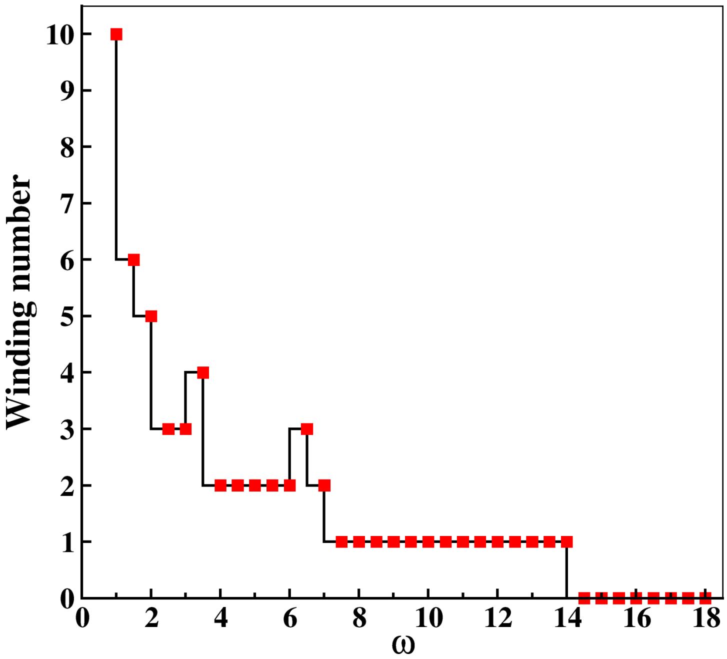

Figure 5.6: The winding number for the square wave drive within phase III plotted as a function of the driving frequency. We see a maximum frequency above which there is no winding and lower frequencies give rise to larger winding.

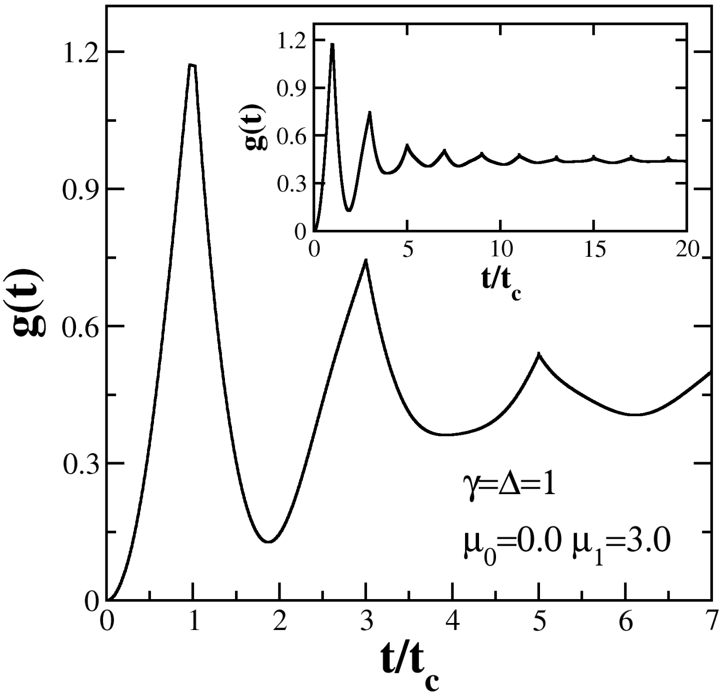

Figure 5.7: The rate function $g(t)$ plotted as a function of the scaled time $t/t_c$. The main panel shows the time evolution of $g(t)$ up to $t = 7t_c$, while the inset shows the evolution for a longer range. We clearly see the non-analytic behaviour occurring at odd multiples of $t_c$. The details of the quench are mentioned in the legend.

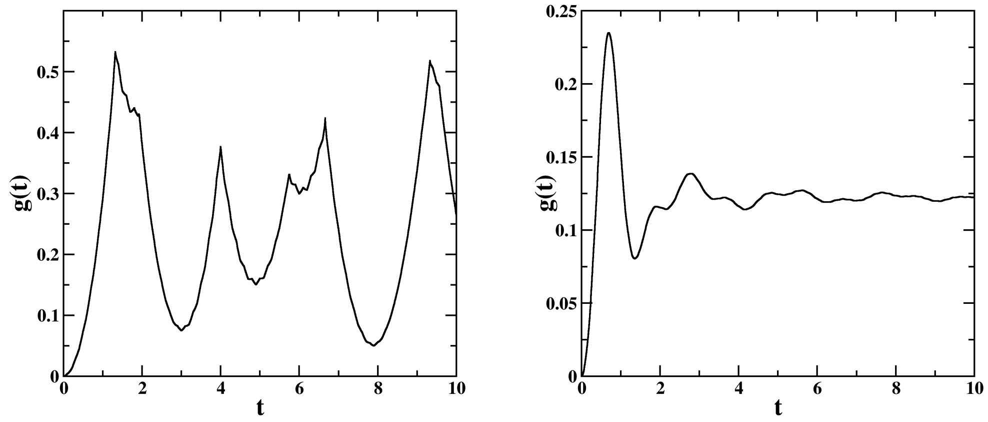

Figure 5.8: Rate function plotted as a function of time for square wave driving in phase II ($\gamma = \delta = 1; \mu = 0.5$) and phase III ($\gamma = \delta = 1; \mu = 3.0$) on the left panel and right panels respectively. The left panel shows non-analyticites in the topological phase while the right panel corresponding to the trivial does not.

Fig. 5.9 with the initial phase being II in the left panel and III in the right panel. Particularly, left panel corresponds to $\gamma = \Delta = 1$ with $\mu_0 = 0.5$ and $\mu_1 = 3.0$, while the right panel corresponds to $\gamma = \Delta = 1$ with $\mu_0 = 3.0$ and $\mu_1 = 0.5$. We We see that DQPTs are modified significantly and are present in the case where the initial phase is the topological phase while the other case does not show DQPTs. Both cases show smaller features and do not have smooth lines as seen in the within the phase results.

### 5.8.3 Noise

The transfer matrix method was proposed[35] in order to study the effect of noise in the transverse field Ising model and allows for an exact calculation of the resulting time-evolved state. We use this method in our case to look at the piecewise constant noise where the chemical potential is selected from the uniform random distribution $[-W, W]$, where $W$ is the half-width. We look at the rate function in a similar manner to the square wave driving case and consider both cases where $W$ is chosen such that the parameters all fall within a single topological phase and the case where some values can lie on the other side of the phase boundary.

We begin with the case where the $W$ is chosen such that the parameters

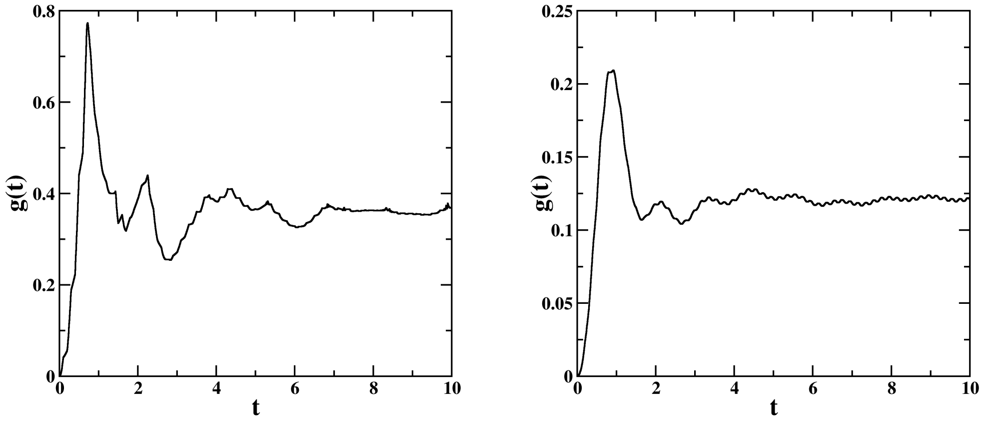

Figure 5.9: Rate function plotted as a function of time for square wave driving from phase II to III ($\gamma = \delta = 1; \mu_0 = 0.5, \mu_1 = 3.0$) and phase III to II ($\gamma = \delta = 1; \mu_0 = 3.0, \mu_1 = 0.5$) in the left and right panels respectively. The DQPTs are present in the left panel while not present in the right panel.

lie in the topological phase corresponding to $\gamma = \Delta = 1$ and the mean value of the chemical potential is $\mu = 0.5$. Starting from this initial condition, the subsequent values are chosen such that $\mu_1 = \mu_0 + w$, where $w$ is randomly chosen from $[-0.1, 0.1]$. This is done for 1000 disorder configurations and subsequently, the disorder averaged transfer matrix is calculated. The time evolved state is calculated using this transfer matrix and is used to calculate the rate function. The rate function as a function of time is plotted in the left panel of Fig. 5.10. A similar exercise is carried out for the topologically trivial phase with $\gamma = \Delta = 1$, $\mu_0 = 3.0$ and $w \in [-0.1, 0.1]$. The rate function for this case is plotted on the right panel of Fig. 5.10. We see that in the case of disorder, the unitary nature of the operator is no longer maintained and leads to the normalization no longer being unity. This is manifested in the decaying trend of the rate function as time increases. Coming to the non-analyticities, we see non-analytic behaviour in the case of the topological phase, while any such features are absent in the trivial phase. While these non-analyticities arise from the same $t_c$, characterisation of them as DQPTs (and associated geometric phase) may be more complicated due to the loss of normalization.

We repeat the same procedure mentioned above for the case where the noise window is broad enough to allow for the chemical potentials to lie on either side of a phase boundary. In the left panel of Fig. 5.11, we consider

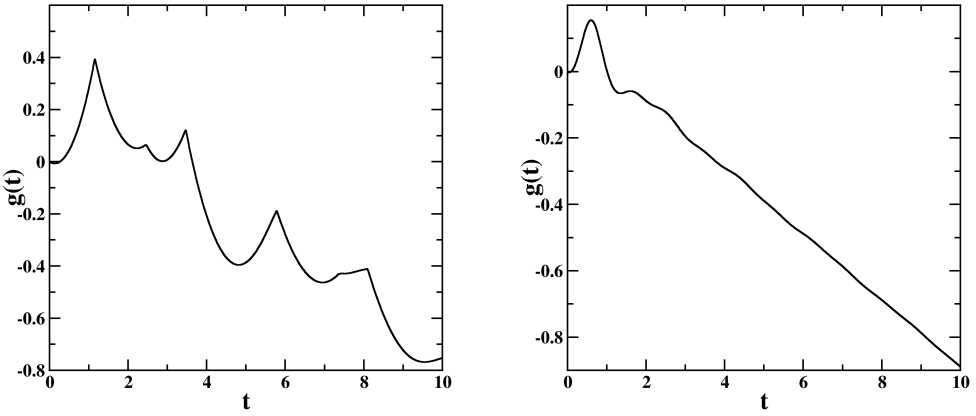

Figure 5.10: Rate function plotted as a function of time for random noise picked from a box distribution $w \in [-0.1, 0.1]$ with the chemical potential becoming $\mu_1 = \mu_0 + w$ in phase II ($\gamma = \delta = 1; \mu = 0.5$) and phase III ($\gamma = \delta = 1; \mu = 3.0$) respectively. We see a decaying trend corresponding to the loss of normalization and the presence of non-analyticities only in the left panel.

the mean chemical potential to be in phase II, i.e. $\mu_0 = 0.5$ and picked the value of the random number $w$ from a larger range $[-1, 1]$. In the right panel of Fig. 5.11, we consider the mean potential to lie in phase III and again pick $w \in [-1, 1]$. We see that the normalization is lost as expected and the rate function shows a decaying trend. The non-analytic behaviour is restricted only to the case where the mean chemical potential lies in phase II, while the other case shows almost a linear decay of the rate function with time.

In order to look at the effect of the size of the box distribution within the same phase, we consider the case where the mean chemical potential is $\mu_0 = 0.5$ and look at the rate function for various values of $W$ ranging from 0.1-0.5. We plot the rate function in Fig. 5.12 and find no difference in the different values, at least for the parameter range considered. This shows the significance of the mean chemical potential in determining the general characteristics of the rate function.

### 5.8.4 Quench

Since both the square wave and noise protocols can be thought to be made up of multiple pieces of a quench followed by time evolution, it would be

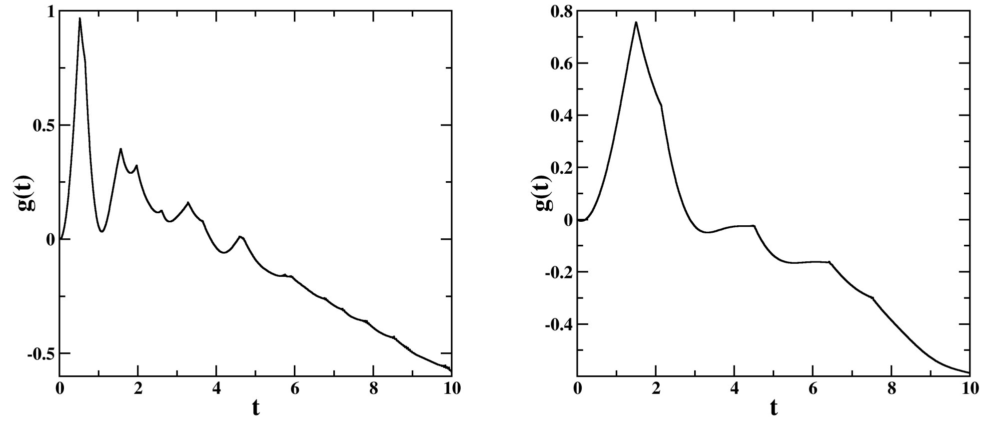

Figure 5.11: Rate function plotted as a function of time when the noise is applied post a quench across the phase boundary. The random noise is picked from a box distribution $w \in [-1, 1]$ with the chemical potential becoming $\mu_2 = \mu_1 + w$ in phase II ($\gamma = \delta = 1; \mu_0 = 0.5, \mu_1 = 3.0$) and phase III ($\gamma = \delta = 1; \mu_0 = 3.0, \mu_1 = 0.5$) respectively. The loss of normalization leads to a decaying value of $g(t)$ and see non-analyticities only in the left panel.

interesting to look at the effects on the system when the Hamiltonian is quenched from one set of parameters to another followed by time evolution. As earlier, we restrict ourselves without loss of generality to $\gamma = \Delta = 1$ and look at quenches both within a topological phase and across the phase transition boundary.

Let's start with the case where the parameters are chosen such that the system is in the same topological phase post the quench. We plot the rate function for the quench within the topological phase II, i.e. $\gamma = \Delta = 1$ and $\mu_0 = 0.5, \mu_1 = 0.8$ in the left panel of Fig. 5.13 and the rate function for quench within the trivial phase III corresponding to $\gamma = \Delta = 1$ and $\mu_0 = 3.0, \mu_1 = 3.3$ in the right panel of Fig. 5.13. We see that the DQPTs arise only in quench within the topological phase and the right panel shows smooth variation with no non-analyticities. We next move on to the case where the quench is across the phase boundary and consider both the quenches from the topological phase II to the trivial phase III and vice versa. Keeping $\gamma = \Delta = 1$ fixed, we consider in the left panel of Fig. 5.14, a quench from $\mu_0 = 0.5$, in phase II to $\mu_1 = 3.0$ corresponding to phase III. In the right panel of Fig. 5.14, we consider the opposite case with $\mu_0 = 3.0$ and $\mu_1 = 0.5$. We find the occurrence of DQPTs in both cases, though corresponding to

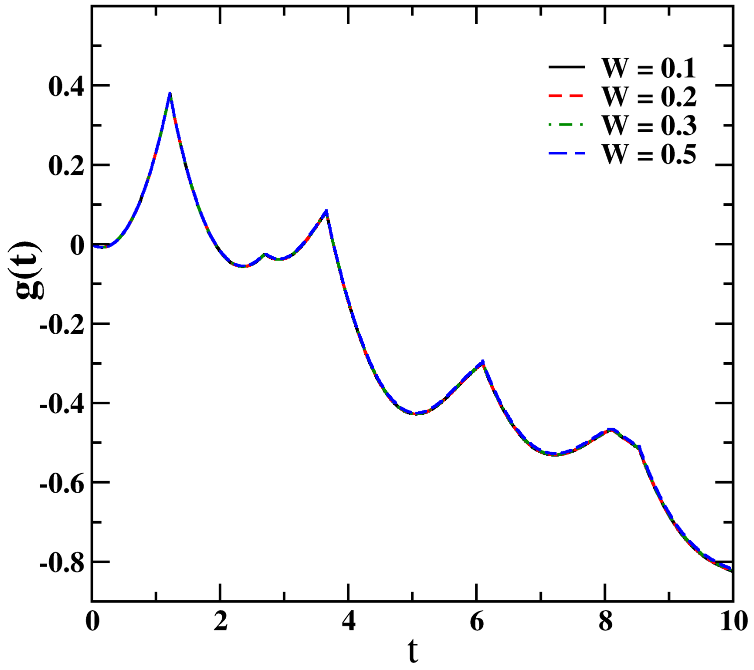

Figure 5.12: The dependence of the rate function on the magnitude of the noise picked from a uniform distribution $w \in [-W, W]$ for a system within phase II ($\gamma = \delta = 1; \mu = 0.5$). We see no dependence of the positions of the DQPTs for the different values of $W$ as indicated in the legend.

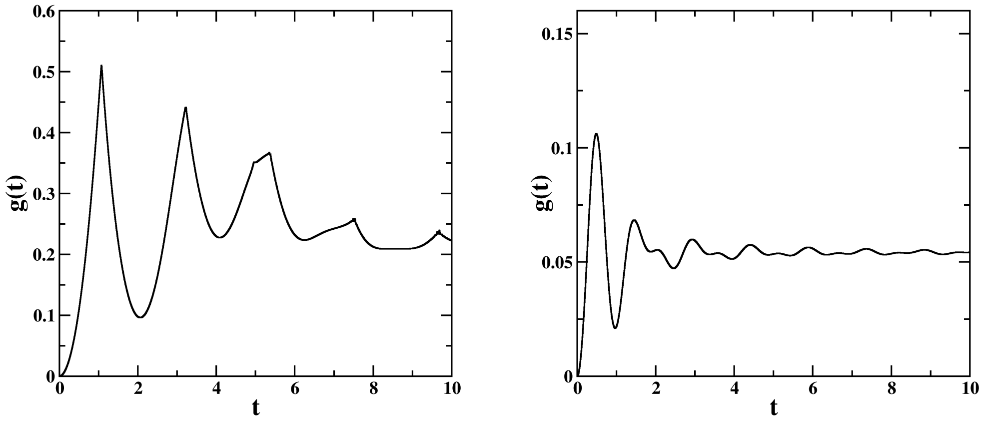

Figure 5.13: Rate function plotted as a function of time for a quench within phase II ($\gamma = \delta = 1; \mu_0 = 0.5, \mu_1 = 0.8$) and phase III ($\gamma = \delta = 1; \mu_0 = 3.0, \mu_1 = 3.3$) in the left and right panels respectively. We see the DQPTs only in the left panel corresponding to phase II.

different critical times.

Thus we have taken a broad look at the time evolution using three different protocols both within and across topological phases.

## 5.9 Summary

In this chapter, we have elucidated the transfer matrix method proposed by D. Nghiem and R. Joynt[35] and applied it to obtain the exact solutions for the Kitaev chain subject to three different driving protocols. We have also looked at the dynamical quantum phase transitions proposed by M. Heyl[29] in various parts of the topological phase diagram under all the three driving protocols. We have analytically derived the expressions for the critical times $t_c$ and also the transfer matrices for each of the three protocols. We begin by benchmarking the method with known results of M. Thakurathi et al.[18] and that of M. Heyl[29] and verify that the method is valid for the square wave and quench results respectively.

We further go on to study systematically the effect of driving in both within and across the topological phase diagram and look at the behaviour of the rate function as a function of time. We see that in all the three protocols, at least in the parameter regimes considered, that the DQPTs

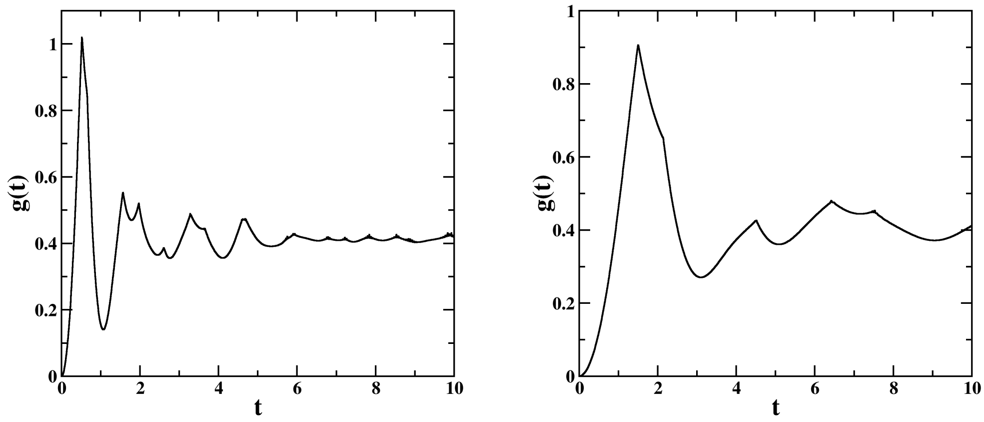

Figure 5.14: Rate function plotted as a function of time for a quench from phase II to III ($\gamma = \delta = 1; \mu_0 = 0.5, \mu_1 = 3.0$) and phase III to II ($\gamma = \delta = 1; \mu_0 = 3.0, \mu_1 = 0.5$) in the left and right panels respectively. We see DQPTs arising in both cases with differing critical times.

occur only when the topological phase (phase II in this case) is involved in the time evolution.

In the case of the noise, we see that the normalization of the wavefunction is no longer conserved due to the non-unitary nature of the transfer matrix and hence see a decaying rate function. Further, we see that the width of the disorder window $W$ does not have any effect on the position and behaviour of the DQPTs and hence we see that the noise does not play a role in determining the nature of the DQPTs.

In the case of quenches across the phase boundary, we see DQPTs arising in both quenches from and to the topological phase, though with differing critical times. These critical times correspond to either a $k = \pm\pi$ or $k = 0$ gap closing and subsequently correspond to either a decrease or increase in the winding number respectively.

# Bibliography

[1] A. Y. Kitaev, Physics-Uspekhi **44**, 131 (2001).

[2] S. D. Sarma, M. Freedman, and C. Nayak, npj Quantum Information **1**, 15001 (2015).

[3] L. Fu and C. L. Kane, Phys. Rev. Lett. **100**, 096407 (2008).

[4] R. M. Lutchyn, J. D. Sau, and S. Das Sarma, Phys. Rev. Lett. **105**, 077001 (2010).

[5] L. Jiang, T. Kitagawa, J. Alicea, A. R. Akhmerov, D. Pekker, G. Refael, J. I. Cirac, E. Demler, M. D. Lukin, and P. Zoller, Phys. Rev. Lett. **106**, 220402 (2011).

[6] J. D. Sau and S. D. Sarma, Nature Communications **3**, 964 (2012).

[7] J. Alicea, Reports on Progress in Physics **75**, 076501 (2012).

[8] V. Mourik, K. Zuo, S. M. Frolov, S. R. Plissard, E. P. A. M. Bakkers, and L. P. Kouwenhoven, Science **336**, 1003 (2012).

[9] H. Zhang, D. E. Liu, M. Wimmer, and L. P. Kouwenhoven, Nature Communications **10**, 5128 (2019).

[10] R. M. Lutchyn, E. P. A. M. Bakkers, L. P. Kouwenhoven, P. Krogstrup, C. M. Marcus, and Y. Oreg, Nature Reviews Materials **3**, 52 (2018).

[11] A. Das, Y. Ronen, Y. Most, Y. Oreg, M. Heiblum, and H. Shtrikman, Nature Physics **8**, 887 (2012).

[12] C. Beenakker, Annual Review of Condensed Matter Physics **4**, 113 (2013).

[13] S. Nadj-Perge, I. K. Drozdov, J. Li, H. Chen, S. Jeon, J. Seo, A. H. MacDonald, B. A. Bernevig, and A. Yazdani, Science **346**, 602 (2014).

[14] M. T. Deng, C. L. Yu, G. Y. Huang, M. Larsson, P. Caroff, and H. Q. Xu, Nano Letters **12**, 6414 (2012).

[15] K. Flensberg, F. von Oppen, and A. Stern, Nature Reviews Materials **6**, 944 (2021).

[16] T. Kitagawa, E. Berg, M. Rudner, and E. Demler, Phys. Rev. B **82**, 235114 (2010).

[17] N. H. Lindner, G. Refael, and V. Galitski, Nature Physics **7**, 490 (2011).

[18] M. Thakurathi, A. A. Patel, D. Sen, and A. Dutta, Phys. Rev. B **88**, 155133 (2013).

[19] R. Seshadri, A. Dutta, and D. Sen, Phys. Rev. B **100**, 115403 (2019).

[20] Y. Peng, Phys. Rev. Res. **2**, 013124 (2020).

[21] D. V. Else, B. Bauer, and C. Nayak, Phys. Rev. Lett. **117**, 090402 (2016).

[22] N. Y. Yao, A. C. Potter, I.-D. Potirniche, and A. Vishwanath, Phys. Rev. Lett. **118**, 030401 (2017).

[23] B. Huang, Y.-H. Wu, and W. V. Liu, Phys. Rev. Lett. **120**, 110603 (2018).

[24] C. Weitenberg and J. Simonet, Nature Physics **17**, 1342 (2021).

[25] M. Aidelsburger, S. Nascimbene, and N. Goldman, Comptes Rendus Physique **19**, 394 (2018), quantum simulation / Simulation quantique.

[26] T. Shirai, S. Todo, and S. Miyashita, Phys. Rev. A **101**, 013809 (2020).

[27] A. Castro, U. D. Giovannini, S. A. Sato, H. Hübener, and A. Rubio, New Journal of Physics **25**, 043023 (2023).

[28] V. M. Bastidas, C. Emary, G. Schaller, and T. Brandes, Phys. Rev. A **86**, 063627 (2012).

[29] M. Heyl, Reports on Progress in Physics **81**, 054001 (2018).

[30] B. Zhou, C. Yang, and S. Chen, Phys. Rev. B **100**, 184313 (2019).

[31] R. Hamazaki, Nature Communications **12**, 5108 (2021).

[32] T. Oka and S. Kitamura, Annual Review of Condensed Matter Physics **10**, 387 (2019).

[33] S. Maity, U. Bhattacharya, and A. Dutta, Phys. Rev. B **98**, 064305 (2018).

[34] Y. Hu, Z. Cai, M. A. Baranov, and P. Zoller, Phys. Rev. B **92**, 165118 (2015).

[35] D. Nghiem and R. Joynt, Phys. Rev. A **73**, 032333 (2006).

[36] B. Cheng, Q.-H. Wang, and R. Joynt, Phys. Rev. A **78**, 022313 (2008).

[37] A. Rajak and A. Dutta, Phys. Rev. E **89**, 042125 (2014).

# Chapter 6

# Mapping a periodically driven quantum dot to a time-dependent Kondo model: a projector method approach

## 6.1 Introduction

In many condensed matter systems, one often sees that the low energy degrees of freedom are most dominant in understanding the physics of the system. Hence, it is much more fruitful to consider only the low-energy degrees of freedom and systematically eliminate the higher-energy degrees of freedom. While a simple ultraviolet cutoff may be the most straightforward way of doing that, better methods exist whereby the Hilbert space is reduced while including most of the high-energy contributions. In this regard, two broad categories of slave particle approaches and renormalization group approaches form the most studied methods. The slave particle methods[1–5] involve projecting out the higher energy fluctuations via the introduction of auxiliary degrees of freedom by means of the slave particles and corresponding constraints. The renormalization group approaches[6–14] on the other hand seek to integrate out the effect of the higher energy fluctuations and arrive at an underlying scale invariant effective Hamiltonian.

A large body of research exists on studying interacting systems using renormalization methods. Starting from the initial efforts in renormalization[7] and Poor man's scaling[6] to modern methods like the numerical renormalization group (NRG)[11;15], density-matrix renormalization group (DMRG)[10], functional renormalization group (FRG)[13], flow equation approach[12], unitary renormalization group (URG)[14], etc. While a host of these methods have been successfully applied to various interacting systems, a simple but effective method to arrive at an effective low-energy Hamiltonian is the Schrieffer-Wolff Transformation (SWT)[16]. The SWT involves elimination of the higher energy degrees of freedom by choosing a generator such that the effective Hamiltonian is first order in interaction. While there are systematic ways of choosing the generator for certain models[17], the generator for a general system still needs to be chosen via an ansatz. This shortcoming of the SWT is overcome by the Projection Operator Method (POM) elaborated by Hewson[18] (not to be confused with the similarly named method by Nakajima and Zwanzig), where the projection to the singly occupied subspace is done explicitly via the projection operators, and no generator is needed. Both the SWT and POM have been successfully applied in equilibrium to study multiple systems, and more pertinent to our interest, the single impurity Anderson model (SIAM) which has the Kondo impurity model as the effective low energy Hamiltonian.

Coming to nonequilibrium, multiple renormalization methods like NRG, FRG, Flow equations, etc. have been generalized and applied to both systems in steady states and to study transient dynamics. In the case of periodic driving, multiple experimental and theoretical studies have been conducted on systems which exhibit exotic phenomena like time crystals[19–21], artificial gauge fields[22;23], emergent topology[24–28], etc. The Floquet theorem[29], which is the time-analogue of the Bloch theorem, not only allows for the calculation of the time evolution operator in terms of a periodic function, but also allows for the calculation of an effective time-independent Hamiltonian whose eigenstates form the basis for the extended Hilbert space. This Floquet Hamiltonian approach which can be calculated using a transformation to a rotating frame along with the perturbative High Frequency Expansion (HFE) has been successfully applied to multiple systems and driving protocols[30]. The Floquet theory has also been used to derive the SWT for periodically driven systems[31] and some groups have claimed that the effective Hamiltonian can be a 2-Channel Kondo model[32].

The interest in these systems is not merely theoretical, but can also be used as a template for constructing quantum computing devices where more efficient calculations can be carried out via the exchange interaction[33]. The SWT and the time-dependent projection operator method (TDPOM) can be used to study systems where the exchange coupling can be tuned by means of a time-dependent bias.

The projection operator Method (POM) as mentioned earlier, provides a systematic alternative to the SWT and bypasses the need for an ansatz to calculate the generator. In this regard, we apply the POM on the time-dependent many-body Schrödinger equation and derive an effective Hamiltonian in the singly-occupied subspace. The SIAM subjected to sinusoidal driving has been studied in the $U = \infty$ limit using the TDSWT[32] and an emergent two-channel Kondo Hamiltonian has been found. The nature of the Kondo effect both in the finite and $U = \infty$ limits when subject to sinusoidal driving is a question answered in this chapter. The possibility of tuning the Kondo coupling via driving is also studied for an example case. In this chapter, subsequent to the introduction, we derive the general expressions for the time-dependent POM followed by an application to the sinusoidally driven SIAM. The effective Kondo Hamiltonian is derived for both the sine and cosine driving terms, followed by a comparison with the TDSWT. This is followed by the time dependent Kondo coupling for a specific value of driving parameters. Finally, we conclude with the summary of the chapter.

## 6.2 Formalism

The time-dependent projection operators can be obtained by considering the time-dependent Schrödinger equation and projecting the Hamiltonian into its constituent subspaces.

### 6.2.1 General preliminaries

We begin with the time-dependent Schrödinger equation given by

$$H(t)\psi(t) = \imath\partial_t\psi(t) \tag{6.1}$$

which can be written in the matrix form as

$$\begin{bmatrix} H_{00} & H_{01} & H_{02} \\ H_{10} & H_{11} & H_{12} \\ H_{20} & H_{21} & H_{22} \end{bmatrix} \begin{bmatrix} \psi_0 \\ \psi_1 \\ \psi_2 \end{bmatrix} = \begin{bmatrix} \imath\partial_t\psi_0 \\ \imath\partial_t\psi_1 \\ \imath\partial_t\psi_2 \end{bmatrix} \tag{6.2}$$

Where we have $H_{nn'} = \mathcal{P}_n H(t) \mathcal{P}_{n'}$ with $\mathcal{P}_m$ being the projection operator to the $m$-occupied subspace. In order to simplify further calculations, we also set $H_{02} = H_{20} = 0$ which corresponds to ignoring simultaneous two-particle excitations. This gives us the set of equations

$$\begin{aligned} H_{00}\psi_0 + H_{01}\psi_1 &= \imath\partial_t\psi_0 \\ H_{10}\psi_0 + H_{11}\psi_1 + H_{12}\psi_2 &= \imath\partial_t\psi_1 \\ H_{21}\psi_1 + H_{22}\psi_2 &= \imath\partial_t\psi_2 \end{aligned} \tag{6.3}$$

Eliminating $\psi_0$ and $\psi_2$ we have

$$[H_{11} + H_{10}(\imath\partial_t - H_{00})^{-1}H_{01} + H_{12}(\imath\partial_t - H_{22})^{-1}H_{21}]\psi_1 = \imath\partial_t\psi_1 \tag{6.4}$$

This expression is valid for any general time-dependent Hamiltonian $H(t)$. While the term $H_{11}$ can be easily evaluated, the second and third terms, i.e. terms of the form $B^\dagger(\imath\partial_t - A)^{-1}B$ need to be evaluated more carefully.

### Fourier Series decomposition

In order to simplify the terms of the form $B^\dagger(\imath\partial_t - A)^{-1}B$, we make use of the Fourier decomposition of $B$. This is given by

$$B(t) = \sum_n e^{-\imath n\Omega t}B^{(n)} \tag{6.5}$$

where the Fourier components $B^{(n)}$ are given by

$$B^{(n)} = \frac{1}{T}\int_0^T dt e^{\imath n\Omega t}B(t) \tag{6.6}$$

and $T = \frac{2\pi}{\Omega}$. We now denote $X = (\imath\partial_t - A)^{-1}B$ and construct an ansatz of the form

$$X = -A^{-1}B^{(0)} + \sum_{n\neq 0}(n\Omega - A)^{-1}e^{-\imath n\Omega t}B^{(n)} \tag{6.7}$$

This ansatz can be verified as follows

$$\begin{aligned} B &= (\imath\partial_t - A)X \\ &= (\imath\partial_t - A)(-A^{-1}B^{(0)} + \sum_{n\neq 0}(n\Omega - A)^{-1}e^{-\imath n\Omega t}B^{(n)}) \\ &= B^{(0)} + \sum_{n\neq 0} e^{-\imath n\Omega}B^{(n)} = B \end{aligned} \tag{6.8}$$

Therefore, using the ansatz to calculate the cross terms we have,

$$B^\dagger(\imath\partial_t - A)^{-1}B = -B^\dagger A^{-1}B^{(0)} + \sum_{n\neq 0} B^\dagger(n\Omega - A)^{-1}e^{-\imath n\Omega t}B^{(n)} \tag{6.9}$$

In order to simplify the term $B^\dagger(n\Omega - A)^{-1}B$, we use the identity

$$\frac{1}{n\Omega - A}B^{(n)} = B^{(n)}\frac{1}{n\Omega - A - b} \tag{6.10}$$

where $b$ can be obtained by evaluating the commutator $[A, B^{(n)}] = bB^{(n)}$. Now, using the identity in the Fourier decomposition of $B^\dagger$ Eq. (6.5) we have

$$\begin{aligned} B^\dagger(\imath\partial_t - A)^{-1}B = -\sum_m e^{-\imath m\Omega t}(B^\dagger)^{(m)}A^{-1}B^{(0)} \\ + \sum_{n,m} e^{-\imath(m+n)\Omega t}(B^\dagger)^{(m)}(B^{(n)})\frac{1}{n\Omega - A - b} \end{aligned} \tag{6.11}$$

Also we have $A^{-1}B^{(0)} = B^{(0)}\frac{1}{A+b}$, whereby equation (6.11) becomes

$$B^\dagger(\imath\partial_t - A)^{-1}B = \sum_{n,m} e^{-\imath(m+n)\Omega t}(B^\dagger)^{(m)}(B^{(n)})\frac{1}{n\Omega - A - b} \tag{6.12}$$

Thus we have a closed-form expression for evaluating all the projections of the Hamiltonian.

### 6.2.2 Application to the Single Impurity Anderson Model

We now apply this formalism to the driven Single impurity Anderson model (SIAM) given by the Hamiltonian

$$H_{\text{lead}} = \sum_{k\alpha\sigma} \epsilon_{k\alpha} c^\dagger_{k\alpha\sigma} c_{k\alpha\sigma} \tag{6.13}$$

$$H_{\text{dot}} = U n_{d\uparrow} n_{d\downarrow} + \sum_\sigma \epsilon_d n_{d\sigma} \tag{6.14}$$

$$H_{\text{hyb}} = v \sum_{k\alpha\sigma} (c^\dagger_{k\alpha\sigma} d_\sigma + h.c.) \tag{6.15}$$

$$H_{\text{dr}}(t) = -\Delta_0 \sin(\Omega t)(\sum_{k\sigma} n_{kL\sigma} - \sum_{k\sigma} n_{kR\sigma}) \tag{6.16}$$

where $c^{(\dagger)}_{k\alpha\sigma}$ are the annihilation (creation) operators of the $\alpha = L, R$ leads connected to an interacting ($U$) dot $\epsilon_d$ via the hybridisation term $H_{\text{hyb}}$ and the driving term $H_{\text{dr}}$ corresponds to a sinusoidal AC bias on the left and right leads. In order to eliminate the driving term, we use a canonical transformation $\tilde{H}(t) = U^\dagger(H(t) - \imath\partial_t)U$ given by

$$\begin{aligned} U &= \exp\left(-\imath \int H_{\text{dr}}(t)dt\right) \\ &= \exp\left(-\imath\eta\cos(\Omega t)\sum_{k\sigma} n_{kL\sigma}\right)\exp\left(\imath\eta\cos(\Omega t)\sum_{k\sigma} n_{kR\sigma}\right) \end{aligned} \tag{6.17}$$

where $\eta = \frac{\Delta_0}{\Omega}$. Applying the canonical transformation to the full Hamiltonian, we can see that only the hybridisation term is modified and the new term is given by

$$\tilde{H}_{\text{hyb}}(t) = v \sum_{k\alpha\sigma} (e^{\pm_\alpha \imath\phi(t)} c^\dagger_{k\alpha\sigma} d_\sigma + h.c.) \tag{6.18}$$

where $\phi(t) = \eta \cos(\Omega t)$ and $\pm_\alpha$ is positive/negative for $\alpha = L/R$ respectively.

### Projection Operator method

We now apply the Projection operator for this Hamiltonian in order to get the effective Hamiltonian. We split the Hamiltonian into

$$H(t) = H_0 + \tilde{H}_{\text{hyb}}(t) \tag{6.19}$$

and calculate the projections. The projection operators are given by

$$\begin{aligned} \mathcal{P}_0 &= (1 - n_{d\uparrow})(1 - n_{d\downarrow}) \\ \mathcal{P}_1 &= n_{d\uparrow} + n_{d\downarrow} - 2n_{d\uparrow}n_{d\downarrow} \\ \mathcal{P}_2 &= n_{d\uparrow}n_{d\downarrow} \end{aligned} \tag{6.20}$$

Applying these projection operators on $H(t)$, we get the necessary projections. The diagonal terms are given by

$$\begin{aligned} H_{11} &= H_{\text{lead}}\mathcal{P}_1 + \epsilon_d \mathcal{P}_1 \\ H_{00} &= H_{\text{lead}}\mathcal{P}_0 \\ H_{22} &= H_{\text{lead}}\mathcal{P}_2 + (U + 2\epsilon_d)\mathcal{P}_2 \end{aligned} \tag{6.21}$$

and the off-diagonal terms are given by

$$H_{01} = H^\dagger_{10} = v \sum_{k\alpha\sigma} e^{\pm_\alpha \imath\phi(t)} c^\dagger_{k\alpha\sigma} d_\sigma (1 - n_{d\bar{\sigma}}) \tag{6.22}$$

$$H_{21} = H^\dagger_{12} = v \sum_{k\alpha\sigma} e^{\mp_\alpha \imath\phi(t)} d^\dagger_\sigma c_{k\alpha\sigma} n_{d\bar{\sigma}} \tag{6.23}$$

We can see that only the off-diagonal terms are time-dependent and hence we need to calculate only their Fourier decomposition. This can be done by considering the Jacobi-Anger expansion

$$e^{\imath\phi(t)} = \sum_{n=-\infty}^{\infty} (\imath)^n \mathcal{J}_n(\eta) e^{\imath n\Omega t} \tag{6.24}$$

where $\mathcal{J}_n(\eta)$ are the Bessel functions of the first kind. The Fourier decomposition gives

$$H_{01} = H_{01}^{(0)} + \sum_n H_{01}^{(n)} e^{-\imath n\Omega t} \tag{6.25}$$

$$H_{21} = H_{21}^{(0)} + \sum_n H_{21}^{(n)} e^{-\imath n\Omega t} \tag{6.26}$$

where the Fourier components are given by

$$\begin{aligned}
H_{01}^{(0)} &= v\mathcal{J}_0(\eta)\sum_{k\alpha\sigma} c_{k\alpha\sigma}^{\dagger} d_\sigma(1-n_{d\bar{\sigma}})\\
H_{01}^{(n)} &= (-1)^n(\imath)^n v\mathcal{J}_{-n}(\eta)\sum_{k\sigma}[c_{kL\sigma}^{\dagger} d_\sigma(1-n_{d\bar{\sigma}}) + (-1)^n c_{kR\sigma}^{\dagger} d_\sigma(1-n_{d\bar{\sigma}})]\\
H_{21}^{(0)} &= v\mathcal{J}_0(\eta)\sum_{k\alpha\sigma} d_\sigma^{\dagger} c_{k\alpha\sigma} n_{d\bar{\sigma}}\\
H_{21}^{(n)} &= (\imath)^n v\mathcal{J}_{-n}(\eta)\sum_{k\sigma}[d_\sigma^{\dagger} c_{kL\sigma} n_{d\bar{\sigma}} + (-1)^n d_\sigma^{\dagger} c_{kR\sigma} n_{d\bar{\sigma}}]
\end{aligned} \tag{6.27}$$

Before attempting to calculate the terms of the form $(\imath\partial_t - A)^{-1}B$, we need to find the commutator $[A, B^{(n)}]$.

If we consider the terms only of the form $[A, B^{(n)}] = bB^{(n)} : b \in \mathbb{C}$, we can evaluate the commutators as

$$\begin{aligned}
[H_{00}, H_{01}^{(n)}] = (-1)^n(\imath)^n v\mathcal{J}_{-n}(\eta)\sum_{k\sigma}[&\epsilon_{kL} c_{kL\sigma}^{\dagger} d_\sigma(1-n_{d\bar{\sigma}})\\
&+ (-1)^n \epsilon_{kR} c_{kR\sigma}^{\dagger} d_\sigma(1-n_{d\bar{\sigma}})]
\end{aligned} \tag{6.28}$$

and

$$[H_{22}, H_{21}^{(n)}] = (U+2\epsilon_d)(\imath)^n v\mathcal{J}_{-n}(\eta)\sum_{k\sigma}[d_\sigma^{\dagger} c_{kL\sigma} n_{d\bar{\sigma}} + (-1)^n d_\sigma^{\dagger} c_{kR\sigma} n_{d\bar{\sigma}}] \tag{6.29}$$

By considering only the terms of form $[A, B^n] = bB^{(n)}$, we ignore the terms that are of the form

$$\begin{aligned}
[H_{00}, H_{01}^{(n)}] = (-1)^n(\imath)^n v\mathcal{J}_{-n}(\eta)\sum_{k\alpha\sigma}[&\epsilon_{kL} c_{k'\alpha\sigma}^{\dagger} c_{k'\alpha\sigma} c_{kL\sigma}^{\dagger} d_\sigma(1-n_{d\bar{\sigma}})\\
&+ (-1)^n \epsilon_{kR} c_{k'\alpha\sigma}^{\dagger} c_{k'\alpha\sigma} c_{kR\sigma}^{\dagger} d_\sigma(1-n_{d\bar{\sigma}})]
\end{aligned} \tag{6.30}$$

and

$$\begin{aligned}
[H_{22}, H_{21}^{(n)}] = (U+2\epsilon_d)(\imath)^n v\mathcal{J}_{-n}(\eta)\sum_{kk'\alpha\sigma}[&c_{k'\alpha\sigma}^{\dagger} c_{k'\alpha\sigma} d_\sigma^{\dagger} c_{kL\sigma} n_{d\bar{\sigma}}\\
&+ (-1)^n c_{k'\alpha\sigma}^{\dagger} c_{k'\alpha\sigma} d_\sigma^{\dagger} c_{kR\sigma} n_{d\bar{\sigma}}]
\end{aligned} \tag{6.31}$$

Where $k' \neq k$. We can now calculate $\sum_{n,m} e^{-\imath(m+n)\Omega t}(B^\dagger)^{(m)}(B^{(n)})\frac{1}{n\Omega - A - b}$.If we take both the leads to have $\epsilon_{kL} = \epsilon_{kR} = \epsilon_k$, and noting that $B^\dagger = (B^0)^\dagger + \sum_m (B^{(m)})^\dagger e^{-\imath m\Omega t}$, we get

$$\begin{aligned}\sum_{n,m} H_{10}^{(m)} H_{01}^{(n)} \frac{e^{-\imath(n-m)\Omega t}}{n\Omega - H_{00} - \epsilon_k} &= v^2 \sum_{n,m} \frac{e^{-\imath(n-m)\Omega t}}{n\Omega - H_{00} - \epsilon_k} (\imath)^{n+m} \\ \times \mathcal{J}_{-n}(\eta)\mathcal{J}_{-m}(\eta) \sum_{kk'\sigma\sigma'} &\Big\{ d_\sigma^\dagger (1 - n_{d\bar{\sigma}'}) \big[ (-1)^n c_{kL\sigma} c_{k'L\sigma'}^\dagger + c_{kL\sigma} c_{k'R\sigma'}^\dagger \\ &+ (-1)^{n+m} c_{kR\sigma} c_{k'L\sigma'}^\dagger + (-1)^m c_{kR\sigma} c_{k'R\sigma'}^\dagger \big] (1 - n_{d\bar{\sigma}}) d_{\sigma'} \Big\} \end{aligned} \tag{6.32}$$

and

$$\begin{aligned}\sum_{n,m} H_{12}^{(m)} H_{21}^{(n)} \frac{e^{-\imath(n-m)\Omega t}}{n\Omega - H_{22} - U - 2\epsilon_d} &= v^2 \sum_{n,m} \frac{e^{-\imath(n-m)\Omega t}}{n\Omega - H_{22} - U - 2\epsilon_d} (\imath)^{n+m} \\ \times (-1)^m \mathcal{J}_{-n}(\eta)\mathcal{J}_{-m}(\eta) \sum_{kk'\sigma\sigma'} &\Big\{ \big[ c_{kL\sigma}^\dagger d_\sigma n_{d\bar{\sigma}'} n_{d\bar{\sigma}} d_{\sigma'}^\dagger c_{k'L\sigma'} \\ + (-1)^n c_{kL\sigma}^\dagger d_\sigma n_{d\bar{\sigma}'} n_{d\bar{\sigma}} d_{\sigma'}^\dagger c_{k'R\sigma'} &+ (-1)^m c_{kR\sigma}^\dagger d_\sigma n_{d\bar{\sigma}'} n_{d\bar{\sigma}} d_{\sigma'}^\dagger c_{k'L\sigma'} \\ &+ (-1)^{m+n} c_{kR\sigma}^\dagger d_\sigma n_{d\bar{\sigma}'} n_{d\bar{\sigma}} d_{\sigma'}^\dagger c_{k'R\sigma'} \big] \Big\} \end{aligned} \tag{6.33}$$

In order to simplify further, we can use the expression

$$\frac{1}{n\Omega - H_0 - b} = \frac{1}{n\Omega - b} \Big( 1 - \frac{H_0}{n\Omega - b} \Big)^{-1} \tag{6.34}$$

and considering only terms to order $v^2$ (Notice $H_0 \sim \mathcal{O}(v)$), we can ignore the $\frac{H_0}{n\Omega - b}$ term.

### Basis change

Instead of writing the terms in terms of the lead operators $c_{L,R}^{(\dagger)}$, it is more convenient to work with a new basis given by

$$b_{k(e/o)\sigma} = \frac{1}{\sqrt{2}} (c_{kL\sigma} \pm_{e/o} c_{kR\sigma}) \tag{6.35}$$

In this basis, the terms read

$$H_{11} = H_{\text{lead}} \mathcal{P}_1 + \epsilon_d \mathcal{P}_1 \tag{6.36}$$

The $\mathcal{O}(v^2)$ terms read

$$\begin{aligned}
\sum_{n,m} H_{10}^{(m)} H_{01}^{(n)} \frac{e^{-\imath(n-m)\Omega t}}{n\Omega - \epsilon_k} &= v^2 \sum_{n,m} \frac{e^{-\imath(n-m)\Omega t}}{n\Omega - \epsilon_k} (\imath)^{n+m} \\
&\times \mathcal{J}_{-n}(\eta)\mathcal{J}_{-m}(\eta) \sum_{kk'\sigma\sigma'} \Big\{ d_\sigma^\dagger (1 - n_{d\bar{\sigma}'})(1 - n_{d\bar{\sigma}}) d_{\sigma'} \big[ \\
&\quad b_{ke\sigma} b_{k'e\sigma'}^\dagger \{(-1)^n + 1 + (-1)^{n+m} + (-1)^m\} \\
&\quad + b_{ke\sigma} b_{k'o\sigma'}^\dagger \{(-1)^n - 1 + (-1)^{n+m} - (-1)^m\} \\
&\quad + b_{ko\sigma} b_{k'e\sigma'}^\dagger \{(-1)^n + 1 - (-1)^{n+m} - (-1)^m\} \\
&\qquad + b_{ko\sigma} b_{k'o\sigma'}^\dagger \{(-1)^n - 1 - (-1)^{n+m} + (-1)^m\} \big] \Big\} \qquad (6.37)
\end{aligned}$$

and

$$\begin{aligned}
\sum_{n,m} H_{12}^{(m)} H_{21}^{(n)} \frac{e^{-\imath(n-m)\Omega t}}{n\Omega - U - 2\epsilon_d} &= v^2 \sum_{n,m} \frac{e^{-\imath(n-m)\Omega t}}{n\Omega - U - 2\epsilon_d} (\imath)^{n+m} \\
&\times \mathcal{J}_{-n}(\eta)\mathcal{J}_{-m}(\eta) \sum_{kk'\sigma\sigma'} \Big\{ d_\sigma n_{d\bar{\sigma}'} n_{d\bar{\sigma}} d_{\sigma'}^\dagger \big[ \\
&\quad b_{ke\sigma}^\dagger b_{k'e\sigma'} \{1 + (-1)^n + (-1)^m + (-1)^{m+n}\} \\
&\quad + b_{ke\sigma}^\dagger b_{k'o\sigma'} \{1 - (-1)^n + (-1)^m - (-1)^{m+n}\} \\
&\quad + b_{ko\sigma}^\dagger b_{k'e\sigma'} \{-1 - (-1)^n + (-1)^m + (-1)^{m+n}\} \\
&\qquad + b_{ko\sigma}^\dagger b_{k'o\sigma'} \{-1 + (-1)^n + (-1)^m - (-1)^{m+n}\} \big] \Big\} \qquad (6.38)
\end{aligned}$$

Now the indices $m, n$ can take both even and odd values. This gives us four cases. In equation (6.37) only one $bb^\dagger$ term survives in each combination of $n, m$ being odd or even. The terms are tabulated below

| $n$ | $m$ | $\beta\beta'$ | Term |
|---|---|---|---|
| even | even | $ee$ | $4b_{ke\sigma}b_{k'e\sigma'}^\dagger$ |
| even | odd | $oe$ | $-4b_{ko\sigma}b_{k'e\sigma'}^\dagger$ |
| odd | even | $eo$ | $4b_{ke\sigma}b_{k'o\sigma'}^\dagger$ |
| odd | odd | $oo$ | $-4b_{ko\sigma}b_{k'o\sigma'}^\dagger$ |

Table 6.1: The signs of the $H_{10}H_{01}$ terms

In the case of equation (6.38) we have only one $b^\dagger b$ term surviving as well. The terms are

| $n$ | $m$ | $\beta\beta'$ | Term |
|---|---|---|---|
| even | even | $ee$ | $4b^\dagger_{ke\sigma}b_{k'e\sigma'}$ |
| even | odd | $oe$ | $4b^\dagger_{ko\sigma}b_{k'e\sigma'}$ |
| odd | even | $eo$ | $-4b^\dagger_{ke\sigma}b_{k'o\sigma'}$ |
| odd | odd | $oo$ | $-4b^\dagger_{ko\sigma}b_{k'o\sigma'}$ |

Table 6.2: The signs of the $H_{12}H_{21}$ terms

We can see that $(\imath)^{n+m}$ is imaginary for $n, m$ not both odd or even (mixing terms) and is real otherwise. If we denote the surviving term by the index $\beta = e, o$ , we can write equations (6.37) and (6.38) compactly as

$$\sum_{n,m} H_{10}^{(m)} H_{01}^{(n)} \frac{e^{-\imath(n-m)\Omega t}}{n\Omega - \epsilon_k} = \sum_{\substack{kk'\sigma\sigma' \\ \beta\beta'}} \mathbb{J}_1^{\beta\beta'} \left\{ d^\dagger_\sigma (1 - n_{d\bar{\sigma}'})(1 - n_{d\bar{\sigma}}) d_{\sigma'} b_{k\beta\sigma} b^\dagger_{k'\beta'\sigma'} \right\} \tag{6.39}$$

where $\mathbb{J}_1^{\beta\beta'} = \pm_1^{\beta\beta'} 4v^2 \sum_{n,m} \frac{e^{-\imath(n-m)\Omega t}}{n\Omega - \epsilon_k} (\imath)^{n+m} \mathcal{J}_n(\eta) \mathcal{J}_m(\eta)$, and

$$\sum_{n,m} H_{12}^{(m)} H_{21}^{(n)} \frac{e^{-\imath(n-m)\Omega t}}{n\Omega - U - 2\epsilon_d} = \sum_{\substack{kk'\sigma\sigma' \\ \beta\beta'}} \mathbb{J}_2^{\beta\beta'} \left\{ d_\sigma n_{d\bar{\sigma}'} n_{d\bar{\sigma}} d^\dagger_{\sigma'} b^\dagger_{k\beta\sigma} b_{k'\beta'\sigma'} \right\} \tag{6.40}$$

where $\mathbb{J}_2^{\beta\beta'} = \pm_2^{\beta\beta'} 4v^2 \sum_{n,m} \frac{e^{-\imath(n-m)\Omega t}}{n\Omega - U - 2\epsilon_d} (\imath)^{n+m} \mathcal{J}_n(\eta) \mathcal{J}_m(\eta)$.

### Effective Hamiltonian

Now that we have evaluated each of the components, we can put them together to find the effective Hamiltonian from equation (6.4). The individual terms are given in equations (6.21), (6.39), (6.40) and read

$$\begin{aligned} H_{11} &= H_{\text{lead}} \mathcal{P}_1 + \epsilon_d \mathcal{P}_1 \\ \sum_{n,m} H_{10}^{(m)} H_{01}^{(n)} \frac{e^{-\imath(n-m)\Omega t}}{n\Omega - \epsilon_k} &= \sum_{\substack{kk'\sigma\sigma' \\ \beta,\beta'=e,o}} \mathbb{J}_1^{\beta\beta'} \left\{ d^\dagger_\sigma (1 - n_{d\bar{\sigma}'})(1 - n_{d\bar{\sigma}}) d_{\sigma'} b_{k\beta\sigma} b^\dagger_{k'\beta'\sigma'} \right\} \\ \sum_{n,m} H_{12}^{(m)} H_{21}^{(n)} \frac{e^{-\imath(n-m)\Omega t}}{n\Omega - U - 2\epsilon_d} &= \sum_{\substack{kk'\sigma\sigma' \\ \beta,\beta'=e,o}} \mathbb{J}_2^{\beta\beta'} \left\{ d_\sigma n_{d\bar{\sigma}'} n_{d\bar{\sigma}} d^\dagger_{\sigma'} b^\dagger_{k\beta\sigma} b_{k'\beta'\sigma'} \right\} \end{aligned} \tag{6.41}$$

Since we want to evaluate the effective Hamiltonian in the singly occupied subspace, we have

$$n_{d\uparrow} + n_{d\downarrow} = 1 \tag{6.42}$$

$$n_{d\uparrow} n_{d\downarrow} = 0 \tag{6.43}$$

Substituting these in the terms gives rise to the effective Hamiltonian

$$\begin{aligned} H_{\text{eff}} = H_{\text{lead}} + \epsilon_d + \sum_{k\beta} \mathbb{J}_1^{\beta\beta} + \sum_{\substack{kk'\\ \beta\beta'\\ \sigma}} \Big\{ \big( - \mathbb{J}_1^{\beta\beta'} n_{d\sigma} + \mathbb{J}_2^{\beta'\beta} n_{d\bar{\sigma}} \big) b^{\dagger}_{k'\beta'\sigma} b_{k\beta\sigma} \\ - \big( \mathbb{J}_1^{\beta\beta'} + \mathbb{J}_2^{\beta'\beta} \big) d^{\dagger}_{\sigma} d_{\bar{\sigma}} b^{\dagger}_{k'\beta'\bar{\sigma}} b_{k\beta\sigma} \Big\} \end{aligned} \tag{6.44}$$

Ignoring the numerical factors $\epsilon_d + \sum_{k\beta} \mathbb{J}_1^{\beta\beta}$, we get

$$H_{\text{eff}} = H_{\text{lead}} + \sum_{\substack{kk'\\ \beta\beta'\\ \sigma}} \Big\{ \big( - \mathbb{J}_1^{\beta\beta'} n_{d\sigma} + \mathbb{J}_2^{\beta'\beta} n_{d\bar{\sigma}} \big) b^{\dagger}_{k'\beta'\sigma} b_{k\beta\sigma} - \big( \mathbb{J}_1^{\beta\beta'} + \mathbb{J}_2^{\beta'\beta} \big) d^{\dagger}_{\sigma} d_{\bar{\sigma}} b^{\dagger}_{k'\beta'\bar{\sigma}} b_{k\beta\sigma} \Big\} \tag{6.45}$$

In equilibrium, we know that the low energy effective Hamiltonian of the SIAM considered in eqn (6.13) is the Kondo model. If we compare our effective Hamiltonian (eqn (6.45)) to a Kondo Hamiltonian of the form

$$H_K = H_{\text{lead}} + \sum_{\substack{kk'\\ \beta\beta'}} \Big\{ J^z_{\substack{kk'\\ \beta\beta'}} S^z s^z_{\substack{kk'\\ \beta\beta'}} + J^+_{\substack{kk'\\ \beta\beta'}} S^+ s^-_{\substack{kk'\\ \beta\beta'}} + J^-_{\substack{kk'\\ \beta\beta'}} S^- s^+_{\substack{kk'\\ \beta\beta'}} \Big\}, \tag{6.46}$$

we can make a direct comparison of terms for the $H_{\text{lead}}$ and the $S^{\pm}$ terms to get

$$J^+_{\substack{kk'\\ \beta\beta'}} = J^-_{\substack{kk'\\ \beta\beta'}} = -(\mathbb{J}_1^{\beta\beta'} + \mathbb{J}_2^{\beta'\beta}) \tag{6.47}$$

To simplify the $\big( - \mathbb{J}_1^{\beta\beta'} n_{d\sigma} + \mathbb{J}_2^{\beta'\beta} n_{d\bar{\sigma}} \big) b^{\dagger}_{k'\beta'\sigma} b_{k\beta\sigma}$ term, we can use

$$n_{d\sigma} = \frac{1 \pm_{\sigma} S^z}{2} \tag{6.48}$$

$$b^{\dagger}_{k'\beta'\sigma} b_{k\beta\sigma} = \frac{1}{2} (n^{\beta'\beta}_{kk'} \pm_{\sigma} s^z_{\substack{kk'\\ \beta'\beta}}) \tag{6.49}$$

where $n_{kk'}^{\beta'\beta} = \sum_\sigma b^\dagger_{k'\beta'\sigma} b_{k\beta\sigma}$ and $s^z_{\substack{kk'\\ \beta'\beta}} = b^\dagger_{k'\beta'\uparrow} b_{k\beta\uparrow} - b^\dagger_{k'\beta'\downarrow} b_{k\beta\downarrow}$. This gives

$$\sum_{\substack{kk'\\ \beta\beta'\\ \sigma}} \big( - \mathbb{J}_1^{\beta\beta'} n_{d\sigma} + \mathbb{J}_2^{\beta'\beta} n_{d\bar{\sigma}} \big) b^\dagger_{k'\beta'\sigma} b_{k\beta\sigma}$$

$$= \frac{1}{4} \sum_{\substack{kk'\\ \beta\beta'\\ \sigma}} \Big( - \mathbb{J}_1^{\beta\beta'} [1 \pm_\sigma S^z][n_{kk'}^{\beta'\beta} \pm_\sigma s^z_{\substack{kk'\\ \beta'\beta}}] + \mathbb{J}_2^{\beta'\beta} [1 \mp_\sigma S^z][n_{kk'}^{\beta'\beta} \pm_\sigma s^z_{\substack{kk'\\ \beta'\beta}}] \Big) \tag{6.50}$$

Which gives us

$$\sum_{\substack{kk'\\ \beta\beta'\\ \sigma}} \big( - \mathbb{J}_1^{\beta\beta'} n_{d\sigma} + \mathbb{J}_2^{\beta'\beta} n_{d\bar{\sigma}} \big) b^\dagger_{k'\beta'\sigma} b_{k\beta\sigma}$$

$$= \frac{1}{4} \sum_{\substack{kk'\\ \beta\beta'\\ \sigma}} \Big( (-\mathbb{J}_1^{\beta\beta'} + \mathbb{J}_2^{\beta'\beta}) n_{kk'}^{\beta'\beta} + (-\mathbb{J}_1^{\beta\beta'} - \mathbb{J}_2^{\beta'\beta}) S^z s^z_{\substack{kk'\\ \beta'\beta}} + () \cancelto{0}{\sum_\sigma \pm_\sigma} \Big) \tag{6.51}$$

The $\sum_{\substack{kk'\\ \beta\beta'\\ \sigma}} (-\mathbb{J}_1^{\beta\beta'} + \mathbb{J}_2^{\beta'\beta}) n_{kk'}^{\beta'\beta}$ term is a potential scattering term and we can ignore it. Then we have

$$\sum_{\substack{kk'\\ \beta\beta'\\ \sigma}} \big( - \mathbb{J}_1^{\beta\beta'} n_{d\sigma} + \mathbb{J}_2^{\beta'\beta} n_{d\bar{\sigma}} \big) b^\dagger_{k'\beta'\sigma} b_{k\beta\sigma} = -\frac{1}{4} \sum_{\substack{kk'\\ \beta\beta'\\ \sigma}} (\mathbb{J}_1^{\beta\beta'} + \mathbb{J}_2^{\beta'\beta}) S^z s^z_{\substack{kk'\\ \beta'\beta}} \tag{6.52}$$

Thus from equations (6.47) and (6.52) we have

$$J(\eta, t) = J^z_{\substack{kk'\\ \beta\beta'}} = J^\pm_{\substack{kk'\\ \beta\beta'}} = -(\mathbb{J}_1^{\beta\beta'} + \mathbb{J}_2^{\beta'\beta}) \tag{6.53}$$

Thus the effective Hamiltonian in (6.46) is of the form

$$H_K = H_{\text{lead}} + \sum_{\substack{kk'\\ \beta\beta'}} J(\eta, t) \mathbf{S} \cdot \mathbf{s}_{\substack{kk'\\ \beta\beta'}} \tag{6.54}$$

From the expressions for $\mathbb{J}_{1/2}$, we can calculate

$$J(\eta, t) = -(\mathbb{J}_1^{\beta\beta'} + \mathbb{J}_2^{\beta'\beta}) = -4v^2 \sum_{n,m} e^{-\imath(n-m)\Omega t} \imath^{n+m} \mathcal{J}_m(\eta) \mathcal{J}_n(\eta)$$

$$\times \Big[ \frac{\pm_1^{\beta\beta'}}{n\Omega - \epsilon_k} + \frac{\pm_2^{\beta'\beta}}{n\Omega - U - 2\epsilon_d} \Big] \tag{6.55}$$

Where we have for $\beta, \beta' = e, o$

$$\pm_1^{\beta\beta'} = \begin{pmatrix} + & + \\ - & - \end{pmatrix} \tag{6.56}$$

$$\pm_2^{\beta\beta'} = \begin{pmatrix} + & - \\ + & - \end{pmatrix} \tag{6.57}$$

Therefore we can see that we have

$$J(\eta, t) = -(\mathbb{J}_1^{\beta\beta'} + \mathbb{J}_2^{\beta'\beta}) = \mp 4v^2 \sum_{n,m} e^{-\imath(n-m)\Omega t} \imath^{n+m} \mathcal{J}_m(\eta) \mathcal{J}_n(\eta) \times \left[ \frac{1}{n\Omega - \epsilon_k} + \frac{1}{n\Omega - U - 2\epsilon_d} \right] \tag{6.58}$$

Where we have $-$ for the $\beta\beta' = ee, eo$ and $+$ for the $\beta\beta' = oo, oe$ cases respectively. The indices $m, n$ take odd or even values in the case of each $\beta\beta' = e, o$ according to the tables 6.1 and 6.2.

We now notice that since the mixing terms $eo, oe$ are not always zero, the two reservoirs are connected and form a single channel. Thus, the effective Kondo Hamiltonian is the single-channel Kondo model.

## 6.3 Results and Discussion

As mentioned earlier, the effective Kondo Hamiltonian obtained using the time-dependent projection operator method (TDPOM) is a single-channel Kondo model due to the presence of mixing terms. The time-dependent Schrieffer-Wolff transformation (TDSWT) used by M. Eckstein et al.[32], does not capture these mixing terms at the $v^2$ order correctly, leading to a false identification of the effective Hamiltonian with a two-channel Kondo model.

### 6.3.1 $U = \infty$ Limit

In the $U = \infty$ limit, the exchange coupling terms $J_{e/o}$ derived from the TDSWT read

$$J_{e/o}(\eta, \Omega) = 4v^2 \sum_{l\,\mathrm{even(odd)}} \frac{\mathcal{J}_{|l|}(\eta)^2}{|\epsilon_f| + l\Omega} \tag{6.59}$$

where $\epsilon_f$ is the dot energy ($\epsilon_d$ in our case).

In the TDSWT, the exchange coupling $J_o$ corresponds to the ferromagnetic case when $\Omega > |\epsilon_f|$ since for each $|l|$, the negative term $\mathcal{J}_{|l|}^2/(|\epsilon_f| - l\Omega)$ is greater in magnitude than the positive term $\mathcal{J}_{|l|}^2/(|\epsilon_f| + l\Omega)$. This corresponds to the competition between a ferromagnetic channel ($o$) and an

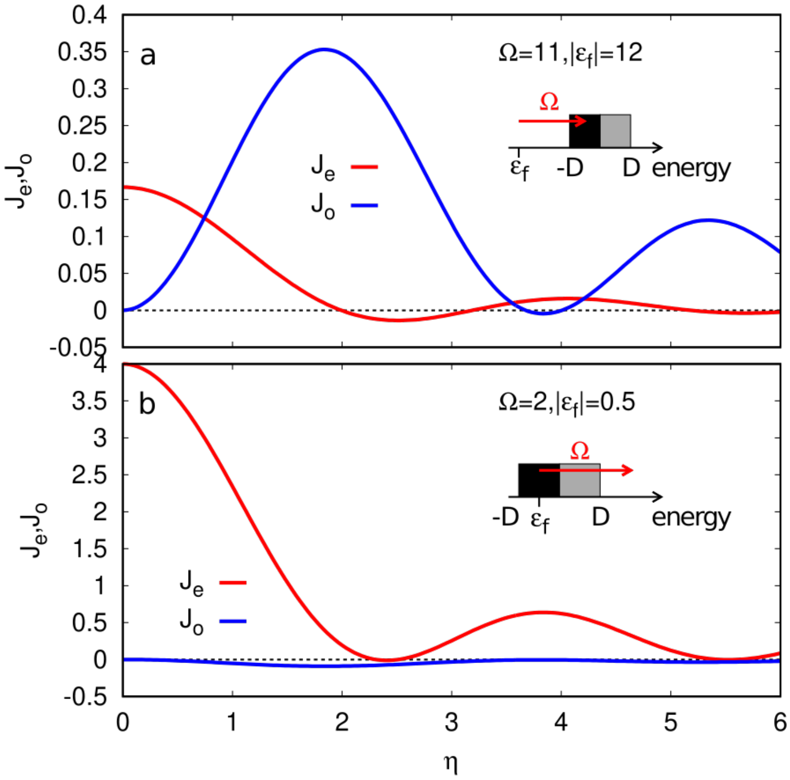

Figure 6.1: The exchange interaction $J_{e/o}$ from TDSWT plotted as a function of $\eta = \frac{\Omega}{\Delta_0}$ for the antiferromagnetic case $\Omega < |\epsilon_f|$ in panel **a** and the ferromagnetic case $\Omega > |\epsilon_f|$ in panel **b** for the frequency $\Omega$ and $\epsilon_f$ as mentioned in the legend. Taken from M. Eckstein et al.[32].

antiferromagnetic channel ($e$). On the other hand, by similar arguments, it can be seen that $J_o$ corresponds to the antiferromagnetic case when $\Omega < |\epsilon_f|$ and hence both the $e/o$ channels are antiferromagnetic. This can be seen in Fig. 6.1 taken from M. Eckstein et al.[32], where the exchange couplings $J_{e/o}$ are plotted as a function of $\eta = \frac{\Omega}{\Delta_0}$ for the antiferromagnetic case in panel a and the ferromagnetic case in panel b.

In the same $U = \infty$ limit, the Kondo coupling calculated from TDPOM, i.e. eqn (6.58) reads

$$J(\eta, t) = \mp 4v^2 \sum_{n,m} e^{-\imath(n-m)\Omega t} \imath^{n+m} \mathcal{J}_m(\eta)\mathcal{J}_n(\eta) \left[\frac{1}{n\Omega - \epsilon_k}\right] \tag{6.60}$$

Where we have $-$ for the $\beta\beta' = ee, eo$ and $+$ for the $\beta\beta' = oo, oe$ cases respectively. The indices $m, n$ take odd or even values in the case of each

$\beta\beta' = e, o$ according to the tables 6.1 and 6.2. We see that the coupling has a similar form to that obtained from TDSWT (eqn (6.59)), in addition to having non-zero mixing terms $eo, oe$ and also the possibility of taking imaginary values depending on $\imath^{m+n}$.

### 6.3.2 Cosine driving

One thing to note is that the imaginary coupling does not arise in the case when the driving term is given by

$$H_{dr} = \Delta_0 \cos(\Omega t)\big(\sum_{k\sigma} n_{kL\sigma} - n_{kR\sigma}\big) \tag{6.61}$$

due to the corresponding $\phi(t) = \eta \sin(\Omega t)$ and the Jacobi-Anger expansion reading

$$e^{\imath\phi(t)} = \sum_{n=-\infty}^{\infty} \mathcal{J}_n(\eta) e^{\imath n\Omega t} \tag{6.62}$$

We can derive the exchange coupling following the same line of arguments as in the case of sine driving to get

$$\begin{aligned} J(\eta, t) = -4v^2 \sum_{n,m} e^{-\imath(n-m)\Omega t} \mathcal{J}_m(\eta)\mathcal{J}_n(\eta) \\ \times \left[\frac{1}{n\Omega - \epsilon_k} \pm \frac{1}{n\Omega - U - 2\epsilon_d}\right] \end{aligned} \tag{6.63}$$

Where we have + for the $\beta\beta' = ee, oe$ and $-$ for the $\beta\beta' = oo, eo$ cases respectively. The indices $m, n$ take odd or even values in the case of each $\beta\beta' = e, o$ according to the table 6.3 given below.

| $n$ | $m$ | $\beta\beta'$ |
|---|---|---|
| even | even | $ee$ |
| even | odd | $eo$ |
| odd | even | $oe$ |
| odd | odd | $oo$ |

Table 6.3: The values taken by the indices $m, n$ for $\beta\beta'$ with cosine driving

In the limit $U = \infty$, the second term in eqn (6.58) becomes zero and hence we have

$$J(\eta, t) = -4v^2 \sum_{n,m} e^{-\imath(n-m)\Omega t} \mathcal{J}_m(\eta)\mathcal{J}_n(\eta) \left[\frac{1}{n\Omega - \epsilon_k}\right] \tag{6.64}$$

Where we again note that the mixing terms $eo, oe$ do not become zero and hence continue to give rise to a single-channel Kondo effect.

### 6.3.3 Time-averaging

Also note that in the TDSWT method, due to the periodic nature of the driving, the time-dependence was removed by considering the time-averaged exchange coupling $J(\eta) = \frac{1}{T}\int_0^T dt J(\eta, T)$, in order to obtain the Floquet exchange coupling and subsequently the time-independent Hamiltonian. Since this is a further approximation and involves only keeping $\mathcal{O}(\Omega^{-1})$ terms, we can choose to retain the full time-dependent exchange coupling obtained from the TDPOM.

Calculating the time-averaged $J(\eta)$ allows us to compare the results obtained from TDPOM and TDSWT. Integrating $J(\eta, t)$ from eqn (6.60) over one time period, we get

$$J(\eta) = \frac{\mp 4v^2}{T} \sum_{n,m} \imath^{n+m} \mathcal{J}_m(\eta) \mathcal{J}_n(\eta) \left[\frac{1}{n\Omega - \epsilon_k}\right] \int_0^T dt e^{-\imath(n-m)\Omega t} \tag{6.65}$$

If we consider $\Omega$ to be a very large energy scale of the system, i.e. tractable to the Floquet formalism, we can use the identity $\frac{1}{T}\int dt e^{-\imath(n-m)\Omega t} = \delta_{n,m}$, to get

$$\begin{aligned} J_e(\eta) &= -4v^2 \sum_{n\,\text{even}} \mathcal{J}_n^2(\eta) \left[\frac{1}{n\Omega - \epsilon_k}\right] \\ J_o(\eta) &= -4v^2 \sum_{n\,\text{odd}} \mathcal{J}_n^2(\eta) \left[\frac{1}{n\Omega - \epsilon_k}\right] \end{aligned} \tag{6.66}$$

Using the Bessel function identity $\mathcal{J}_{-n}(\eta) = (-1)^n \mathcal{J}_n(\eta)$, we can write

$$J_{e/o} = -4v^2 \sum_{\substack{n=0 \\ n\,\text{even/odd}}}^{\infty} \mathcal{J}_n(\eta) \left[\frac{1}{n\Omega - \epsilon_k} - \frac{1}{n\Omega + \epsilon_k}\right] \tag{6.67}$$

In the time-averaged case, the $eo, oe$ terms are no longer present and thus we get a two-channel Kondo model and the expression eqn (6.67) recovers the TDSWT results. We plot the $J_{e/o}$ in the antiferromagnetic and ferromagnetic cases in the top and bottom panels of Fig. 6.2 for the values of $\Omega$ and $\epsilon_k$ as indicated in the legend. The value of $v = 0.5, \Delta_0 = 1$ was fixed for both cases

But it bears reiterating that the $J_{eo/oe}$ terms are not present in the expression for the exchange coupling, eqn (6.67), only because of the time-averaging. This is equivalent to keeping only the $\mathcal{O}(\Omega^{-1})$ terms in the effective Hamiltonian. In general, the $J(\eta, t)$ will have non-zero mixing terms and cannot be thought to give rise to an effective two-channel Kondo Hamiltonian.

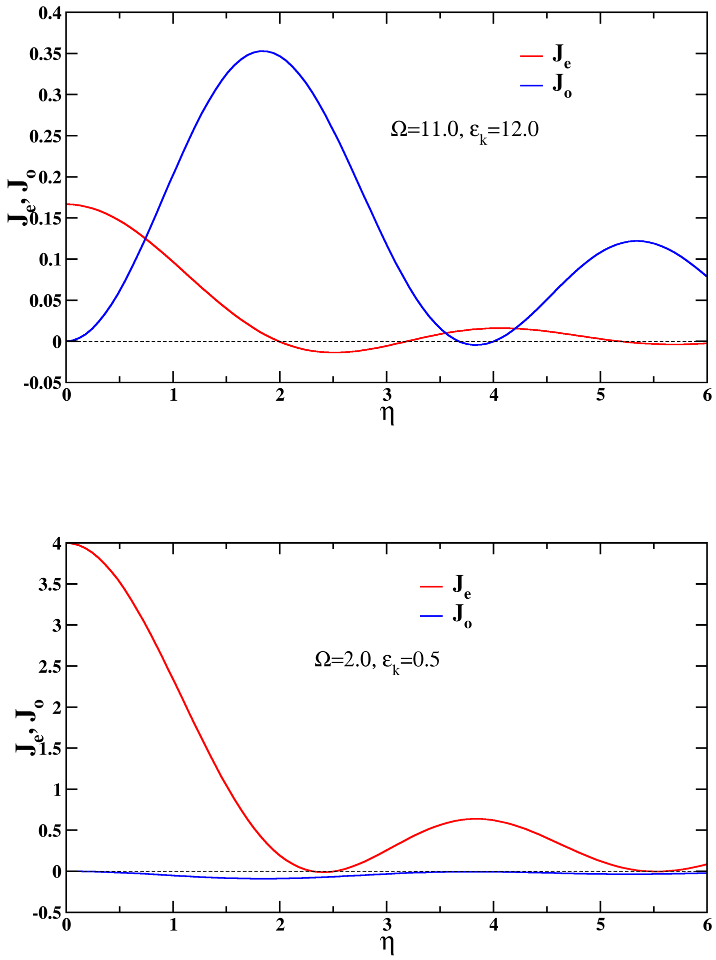

Figure 6.2: The time averaged exchange coupling for the $e, o$ channels plotted as a function of $\eta$. The top panel corresponds to the antiferromagnetic case with $\Omega = 11 < \epsilon_k = 12$ and the bottom panel corresponds to the ferromagnetic case with $\Omega = 2 > \epsilon_k = 0.5$. The hybridisation $v = 0.5$ and amplitude of drive $\Delta_0 = 1$ for both panels. Comparing to Fig.6.1, one can see that the TDSWT results are recovered.

| k | $\mathcal{J}_0(\eta)$ | $\mathcal{J}_1(\eta)$ | $\mathcal{J}_2(\eta)$ | $\mathcal{J}_3(\eta)$ | $\mathcal{J}_4(\eta)$ | $\mathcal{J}_5(\eta)$ |
|---|---|---|---|---|---|---|
| 1 | 2.4048 | 3.8317 | 5.1356 | 6.3802 | 7.5883 | 8.7715 |
| 2 | 5.5201 | 7.0156 | 8.4172 | 9.7610 | 11.0647 | 12.3386 |
| 3 | 8.6537 | 10.1735 | 11.6198 | 13.0152 | 14.3725 | 15.7002 |
| 4 | 11.7915 | 13.3237 | 14.7960 | 16.2235 | 17.6160 | 18.9801 |
| 5 | 14.9309 | 16.4706 | 17.9598 | 19.4094 | 20.8269 | 22.2178 |

Table 6.4: The first five roots of the Bessel functions $\mathcal{J}_{0\cdots5}(\eta)$. Taken from Wolfram MathWorld.

### 6.3.4 Bessel roots

Another angle of approach to making sense of the exchange coupling is to tune $\eta$ such that $\mathcal{J}_n(\eta) = 0$ for at least some $n$ (low order) and look at the effect on the dynamics $J(t)$. The first few roots $j_{n,k}$ of the Bessel functions $\mathcal{J}_n(\eta)$ are given in Table 6.4.

Let us consider the case where we fix $\eta = 2.4048$, which is the first zero of $\mathcal{J}_0(\eta)$ and look at the time evolution of the various components of $J(\eta = 2.4048, t)$. Since only $\mathcal{J}_0(\eta)$ goes to zero at $\eta = 2.4048$, the higher $m, n$ terms are still present and contribute to all the $ee, eo, oe, oo$ components.

Considering the sine driving protocol, we evaluate $J(t)$ for the parameter set $v = 0.5, \Delta_0 = 1, \Omega = 11, \epsilon_k = 12, U = 8, \epsilon_d = -U/2$. Plotting the different components in Fig. 6.3 as a function of time for the first five periods of the drive allows us to notice that the $ee, eo$ components are the most dominant and oscillate in sign. The $oe, oo$ components are almost an order of magnitude smaller and are negative at all times.

## 6.4 Summary

We have derived the time-dependent projection operator method for a general time-dependent driving using the time-dependent Schrödinger equation and also applied it to the specific case of the sinusoidally driven single impurity Anderson model. While the method involves dropping terms not of the form $[A, B^{(n)}] = bB^{(n)}$ and also the terms of $\mathcal{O}(v^3)$ and higher, the method is able to capture all the terms at $v^2$ order.

This allows us to see that the two emergent channels $e, o$ are not independent in all cases and in fact form a single channel via the mixing terms $J_{oe,eo}$. This is in contrast to the TDSWT results[32] which are obtained post a time averaging, which corresponds to the Floquet expansion keeping up

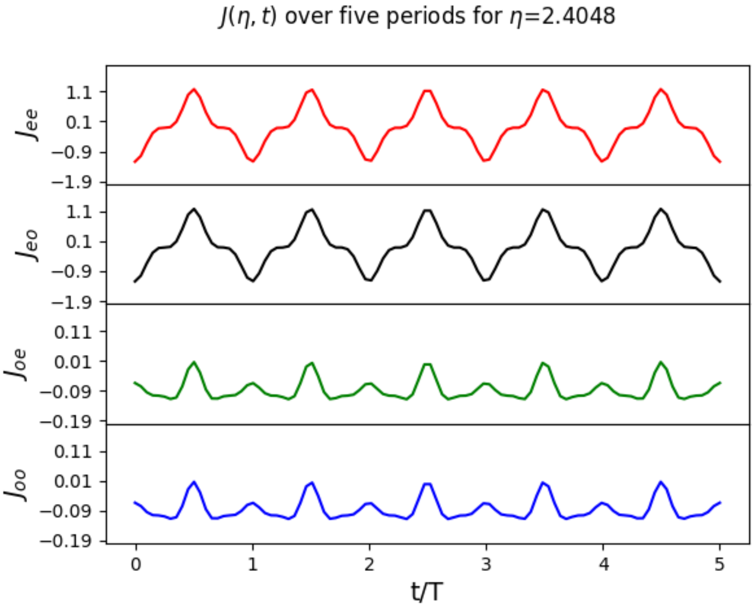

Figure 6.3: Time dependence of the exchange coupling $J(\eta = 2.4048, t)$ plotted for the first five periods. The components from top to bottom are $ee, eo, oe, oo$ respectively. We see that the $ee, eo$ terms are almost an order of magnitude more dominant compared to the $oe, oo$ terms. The calculation was performed for the parameters $v = 0.5, \Delta_0 = 1, \Omega = 11, \epsilon_k = 12, U = 8, \epsilon_d = -U/2$

to $\mathcal{O}(\Omega^{-1})$ terms. Performing a similar time averaging, we are able to recover the TDSWT results analytically starting from the general expression for $J(\eta, t)$.

The TDPOM allows us to go further and look at the full time dependence of the exchange coupling and we look at one example case where we choose $\eta$ such that it is the first zero of the Bessel function $\mathcal{J}_0(\eta)$. In this case, we see that the $ee, eo$ components are the most dominant and change sign through the evolution. Fine tuning such a response might be useful for both engineering materials similar to Floquet engineering[34] and also possibly in quantum computing via the exchange interaction[33].

# Bibliography

[1] P. Coleman, Phys. Rev. B **29**, 3035 (1984).

[2] G. Kotliar and A. E. Ruckenstein, Phys. Rev. Lett. **57**, 1362 (1986).

[3] S. Florens and A. Georges, Phys. Rev. B **70**, 035114 (2004).

[4] L. de'Medici, A. Georges, and S. Biermann, Phys. Rev. B **72**, 205124 (2005).

[5] A. B. Georgescu and S. Ismail-Beigi, Phys. Rev. B **92**, 235117 (2015).

[6] P. W. Anderson, Journal of Physics C: Solid State Physics **3**, 2436 (1970).

[7] K. G. Wilson, Rev. Mod. Phys. **47**, 773 (1975).

[8] H. R. Krishna-murthy, J. W. Wilkins, and K. G. Wilson, Phys. Rev. B **21**, 1003 (1980).

[9] R. Shankar, Rev. Mod. Phys. **66**, 129 (1994).

[10] U. Schollwöck, Rev. Mod. Phys. **77**, 259 (2005).

[11] R. Bulla, T. A. Costi, and T. Pruschke, Rev. Mod. Phys. **80**, 395 (2008).

[12] S. Kehrein, *The flow equation approach to many-particle systems*, Vol. 217 (Springer, 2007).

[13] W. Metzner, M. Salmhofer, C. Honerkamp, V. Meden, and K. Schönhammer, Rev. Mod. Phys. **84**, 299 (2012).

[14] A. Mukherjee and S. Lal, Nuclear Physics B **960**, 115170 (2020).

[15] H. R. Krishna-murthy, J. W. Wilkins, and K. G. Wilson, Phys. Rev. B **21**, 1003 (1980).

[16] J. R. Schrieffer and P. A. Wolff, Phys. Rev. **149**, 491 (1966).

[17] R. U. Haq and K. Singh, "A systematic method for schrieffer-wolff transformation and its generalizations," (2020), arXiv:2004.06534 [cond-mat.str-el] .

[18] A. C. Hewson, *The Kondo problem to heavy fermions*, Vol. 2 (Cambridge university press, 1997).

[19] D. V. Else, B. Bauer, and C. Nayak, Phys. Rev. Lett. **117**, 090402 (2016).

[20] N. Y. Yao, A. C. Potter, I.-D. Potirniche, and A. Vishwanath, Phys. Rev. Lett. **118**, 030401 (2017).

[21] B. Huang, Y.-H. Wu, and W. V. Liu, Phys. Rev. Lett. **120**, 110603 (2018).

[22] C. Weitenberg and J. Simonet, Nature Physics **17**, 1342 (2021).

[23] M. Aidelsburger, S. Nascimbene, and N. Goldman, Comptes Rendus Physique **19**, 394 (2018), quantum simulation / Simulation quantique.

[24] T. Kitagawa, E. Berg, M. Rudner, and E. Demler, Phys. Rev. B **82**, 235114 (2010).

[25] N. H. Lindner, G. Refael, and V. Galitski, Nature Physics **7**, 490 (2011).

[26] M. Thakurathi, A. A. Patel, D. Sen, and A. Dutta, Phys. Rev. B **88**, 155133 (2013).

[27] R. Seshadri, A. Dutta, and D. Sen, Phys. Rev. B **100**, 115403 (2019).

[28] Y. Peng, Phys. Rev. Res. **2**, 013124 (2020).

[29] G. Floquet, in *Annales scientifiques de l'École normale supérieure*, Vol. 12 (1883) pp. 47–88.

[30] M. Bukov, L. D'Alessio, and A. Polkovnikov, Advances in Physics **64**, 139 (2015).

[31] M. Bukov, M. Kolodrubetz, and A. Polkovnikov, Phys. Rev. Lett. **116**, 125301 (2016).

[32] M. Eckstein and P. Werner, "Two-channel kondo physics in a periodically driven single-impurity anderson model," (2017), arXiv:1704.02300 [cond-mat.str-el] .

[33] D. P. DiVincenzo, D. Bacon, J. Kempe, G. Burkard, and K. B. Whaley, Nature **408**, 339 (2000).

[34] T. Oka and S. Kitamura, Annual Review of Condensed Matter Physics **10**, 387 (2019).

# Chapter 7

# Summary and conclusions

In this thesis, we have considered both steady-state and time-dependent methods to study quantum many-body systems out of equilibrium.

In chapters 2 and 3 we have applied the Keldysh second order perturbation theory and steady-state interpolative approximation to study the effects of spin-orbit coupling (SOC) on the transport through a quantum dot connected to leads with SOC. We consider the particle-hole symmetric limit in chapter 2 and see that the Kondo scale decreases with an increase in the SOC strength and can explain the experimental finding of the split zero bias conductance peak. We also see that the linear response regime is determined by the equilibrium scale.

In chapter 3, we introduce a gate voltage in the model, which allows us to study the effect of SOC away from particle-hole symmetry. We find that the zero-bias conductance has isosbestic points around $G_0 \sim 0.65$ and also see the effects of a reduced equilibrium scale and broadening of the effective hybridisation in the presence of SOC. The KPT2 and IPA introduced in chapters 2 and 3 are effective and efficient impurity solvers and may be clubbed directly with dynamical mean field theory in order to access systems in higher dimensions.

While, we dealt with the application of existing methods in chapters 2 and 3, we derive a new method in chapter 4 by generalizing the local moment approach to the nonequilibrium case. Subsequent to rigorous benchmarking, we see that the method is able to capture the transport in the weak-intermediate coupling well and also capture the persistence of universality. While we see the emergence of a satellite feature in the strong coupling regime, a detailed study into the diagrams involved in the method may shed light on the origin and possible ways to take into account any physics not captured by a straightforward generalization as done in chapter 4

In chapter 5, we derive analytically an exact solution for the time evolution of a Kitaev chain subject to piecwise constant driving using the transfer matrix method. We are able to account for the changing topology and emergent Majorana zero modes with time evolution by deriving the critical time scale for a gap closing. We also are able to study the emergence of dynamical quantum phase transitions and the effect of noise. The transfer matrix method applied allows us to exactly solve for the time-dependent states of the Kitaev chain when subject to piecewise constant driving. This can be quite easily modified to study systems like the SSH model, which are in the same class as the Kitaev chain. The emergence of higher order topological invariants can also be studied with such a treatment.

In chapter 6, we have derived a time-dependent generalization of the projection operator method and have applied it to the sinusoidally driven single impurity Anderson model to obtain the effective low-energy Kondo model. The method, much like its equilibrium counterpart does not need any ansatz for the generator and is able to capture the mixing terms which the time-dependent Schrieffer-Wolff transformation misses. The time-dependent projection operator method (TDPOM) allows us to calculate the time-dependent effective low-energy Hamiltonians starting from the corresponding microscopic Hamiltonians. The TDPOM needs to be paired with another method in order to solve the time-dependent effective Hamiltonian. While some methods do exist in this regard, there is a great need for accurate and inexpensive methods which can solve the time-dependent problem.

In conclusion, the field of non-equilibrium quantum many-body systems is a treasure trove of novel physics and the growing interest in such systems is a testament to the possibilities that can be accessed. With increasing interest in the physics, the development of methods to study such systems is paramount and this thesis seeks to develop and apply a collection of methods, both numerical and analytic to study both steady-state and time-dependent quantum many-body systems.

# Appendix A

# A brief introduction to Keldysh field theory

In this chapter we will review the Keldysh[1] field theoretic formalism and hope to provide a concise introduction to the concepts needed for working out the methods in chapters 2 to 4.

## A.1 Preliminaries

Consider a time-dependent Hamiltonian of the form

$$\mathcal{H}(t) = H_0 + V + H_{\text{ext}}(t) = H_0 + H'(t) \tag{A.1}$$

Where $H_0$ corresponds to the non-interacting, $V$ to the interaction and $H_{\text{ext}}(t)$ to the time-dependent parts respectively.

### A.1.1 Schrödinger picture

The Schrödinger picture of quantum mechanics posits the time dependence in the state $|\psi_S(t)\rangle$ which evolves according to the time-dependent Schrödinger equation (TDSE)

$$i\hbar\frac{\partial}{\partial t}|\psi_S(t)\rangle = \mathcal{H}(t)|\psi_S(t)\rangle \tag{A.2}$$

while the operators corresponding to the observable quantities do not have an explicit time dependence.

The evolution of the state from an initial time $t_0$ can be calculated by the means of an evolution operator

$$|\psi_S(t)\rangle = U(t, t_0)|\psi_S(t_0)\rangle \tag{A.3}$$

where the evolution operator also satisfies the TDSE

$$i\hbar\frac{\partial}{\partial t}U(t,t_0) = \mathcal{H}(t)U(t,t_0) \tag{A.4}$$

This equation can be solved by converting it into the integral form and iteratively breaking up the time evolution (refer to[2;3] for details) to get

$$U(t,t_0) = T\exp\left[\left(\frac{-i}{\hbar}\int_{t_0}^{t}dt'\mathcal{H}(t')\right)\right] \tag{A.5}$$

where $T$ is the time ordering operator. This is for 'forward' time evolution when $t > t_0$, while the 'backward' time evolution i.e. $t < t_0$ has the time ordering replaced by the anti-time ordering $\tilde{T}$ operator. It can be seen that the evolution operator has the following properties

$$\begin{aligned} U(t,t) &= \mathbb{1} \\ U^{\dagger}(t,t_0) = U^{-1}(t,t_0) &= U(t_0,t) \\ U(t,t'')U(t'',t') &= U(t,t') \end{aligned} \tag{A.6}$$

The operators in the Schrodinger picture is time independent and the expectation value of an observable is given by

$$\langle\hat{O}\rangle(t) = \langle\psi_S(t)|\hat{O}_S|\psi_S(t)\rangle \tag{A.7}$$

where $\hat{O}_S$ is the operator in the Schrödinger picture.

### A.1.2 Heisenberg picture

Another picture of quantum mechanics is the Heisenberg picture, where the time dependence is in the operators corresponding to the observables of the system $\hat{O}$, while the state is time independent. Since the two pictures refer to the same system, we can see that the operators in the Heisenberg picture $\hat{O}_H(t)$ are related to the Schrödinger picture by

$$\hat{O}_H(t) = U^{\dagger}(t,t_0)\hat{O}_S U(t,t_0) \tag{A.8}$$

The equation of motion for the operators follow from the Heisenberg equation

$$i\hbar\frac{d}{dt}\hat{O}(t) = [\hat{O}(t),\hat{\mathcal{H}}(t)] \tag{A.9}$$

where $\hat{\mathcal{H}}(t) = U^{\dagger}(t,t_0)\mathcal{H}(t)U(t,t_0)$. Another useful observation is that the operators at equal times follow the same commutation relations as that of the original (Schrödinger picture) operators, i.e. $[\hat{A}(t), \hat{B}(t)] = [A, B]$. The states in the Heisenberg picture are time independent and hence the expectation value of an observable is

$$\langle \hat{O} \rangle (t) = \langle \psi_H | \hat{O}_H(t) | \psi_H \rangle \tag{A.10}$$

Or more generally in terms of the density matrix

$$\langle \hat{O} \rangle (t) = \mathrm{Tr}\Big[\rho_H \hat{O}(t)\Big] = \mathrm{Tr}\Big[\rho_0 \hat{O}(t)\Big] \tag{A.11}$$

### A.1.3 Interaction picture

We can also look at separating the non-interacting and interacting parts in the Hamiltonian $\mathcal{H}(t)$ in order to aid calculation. This leads to the interaction picture, which is intermediate between the Schrödinger and Heisenberg pictures and has

$$\begin{aligned} |\psi_I(t)\rangle &= \exp(iH_0(t-t_0)/\hbar)|\psi_S(t)\rangle \\ O(t) &= \exp(iH_0(t-t_0)/\hbar)\hat{O}(t)\exp(-iH_0(t-t_0)/\hbar) \end{aligned} \tag{A.12}$$

Where we have dropped the ˆ to differentiate between the Heisenberg and interaction picture operators. The time-dependent state and operators each follow their corresponding TDSE and Heisenberg equations

$$\begin{aligned} i\hbar\frac{\partial}{\partial t}|\psi_I(t)\rangle &= H'(t)|\psi_I(t)\rangle \\ i\hbar\frac{d}{dt}O(t) &= [O(t), H_0] \end{aligned} \tag{A.13}$$

The evolution operator is now replaced by the scattering matrix defined by $H'(t)$ instead of the $\mathcal{H}(t)$ in the evolution operator. This can be written as

$$S(t, t_0) = \begin{cases} T\exp\Big[\Big(\frac{-i}{\hbar}\int_{t_0}^{t} dt' H'(t')\Big)\Big] & \text{if} \quad t > t_0 \\ \tilde{T}\exp\Big[\Big(\frac{-i}{\hbar}\int_{t_0}^{t} dt' H'(t')\Big)\Big] & \text{if} \quad t < t_0 \end{cases} \tag{A.14}$$

holding the corresponding identities as eqn (A.6) and

$$\begin{aligned} |\psi_I(t)\rangle &= S(t, t_0)|\psi_I(t_0)\rangle \\ \hat{O}(t) &= S^\dagger(t, t_0)O(t)S(t, t_0) \end{aligned} \tag{A.15}$$

### A.1.4 Equilibrium

Consider the time dependent perturbation $H_{\text{ext}}$ to be applied at $t = 0$, i.e. $H_{\text{ext}} = h(t)\Theta(t)$. The real time causal Green's function can be defined as

$$G(1,1') = -i\langle T[\psi_H(1)\psi_H^\dagger(1')] \tag{A.16}$$

where $T$ is the time-ordering operator, $\psi_H(1)$ is the field operator and $\langle\cdots\rangle$ corresponds to the grand canonical average. Switching to the interaction picture, we can write

$$\begin{aligned} T[\psi_H(1)\psi_H^\dagger(1')] = {} & \Theta(t-t')S^\dagger(t,t_0)\psi(1)S(t,t')\psi^\dagger(1')S(t,t_0) \\ & \pm \Theta(t'-t)S^\dagger(t',t_0)\psi^\dagger(1')S(t',t)\psi(1)S(t,t_0) \end{aligned} \tag{A.17}$$

where the ± correspond to Bosonic or Fermionic systems respectively. We can use the properties of the scattering matrix to write the Green's function

$$G(1,1') = -i\langle S(t_0,t_m)T[S(t_m,t_0)\psi(1)\psi^\dagger(1')]\rangle \tag{A.18}$$

where $t_m = max(t,t')$ and by expanding identity as $S(t_m,\infty)S(\infty,t_m) = 1$, we can write

$$G(1,1') = -i\langle S(t_0,\infty)T[S(\infty,t_0)\psi(1)\psi^\dagger(1')]\rangle \tag{A.19}$$

Now if we consider the equilibrium case, i.e. $H_{\text{ext}} = 0$, the ensemble average in eqn (A.19) reduces to an average over the interacting ground state.

$$G(1,1') = -i\langle\psi_{0_H}|S(t_0,\infty)T[S(\infty,t_0)\psi(1)\psi^\dagger(1')]|\psi_{0_H}\rangle \tag{A.20}$$

In order to obtain the expression in terms of the non-interacting ground state, let us consider an adiabatically switching on and off of the interaction term, i.e.

$$V(t) = e^{-\epsilon|t-t_0|}V \tag{A.21}$$

where $\epsilon$ is a infinitesimally small number. This means that the ground state evolves adiabatically slowly to the interacting ground state

$$|\psi_{0_H}\rangle = |\psi_{0_I}(t_0)\rangle = S_\epsilon(t_0,-\infty)|\psi_{0_I}(-\infty)\rangle \tag{A.22}$$

where $S_\epsilon$ is the scattering matrix determined using $V(t)$ and we get

$$G(1,1') = -i\langle\psi_{0_I}(\infty)|T[S_\epsilon(\infty,-\infty)T[S(\infty,t_0)\psi(1)\psi^\dagger(1')]|\psi_{0_I}(-\infty)\rangle \tag{A.23}$$

Since both $|\psi_{0_I}(-\infty)\rangle$ and $|\psi_{0_I}(\infty) = S_\epsilon(\infty, -\infty)|\psi_{0_I}(-\infty)$ are ground states of the non-interacting, non-degenerate $H_0$, they should differ by at most a phase factor $e^{i\phi}$. Rewriting $|\Phi_0\rangle = |\psi_{0_I}(-\infty)\rangle$ allows us to write, after taking the limit $\epsilon \to 0$ (ensured by Gell-Mann Low theorem),

$$iG(1,1') = \frac{\langle \Phi_0 | T[S(\infty, -\infty)\psi(1)\psi^\dagger(1')] | \Phi_0 \rangle}{\langle \Phi_0 | S(\infty, -\infty) | \Phi_0 \rangle} \tag{A.24}$$

which is directly recognisable as allowing for a perturbation expansion through the application of Wick's theorem. The perturbation theory crucial relies on the fact that the ground state is non-degenerate and consequently states in the remote past and future coincide. This assumption breaks down in non-equilibrium where the $t = \infty$ state can be entirely different from the ground state at $t = -\infty$. Thus, we need a new method of arriving at the perturbative expansion.

## A.2 Schwinger-Keldysh Contour

As we have seen earlier, Wick's theorem and a perturbative expansion cannot be written in a straight forward way for nonequilibrium systems. This can be remedied by defining the evolution operator and Green's functions on the Schwinger-Keldysh[1] contour.

The Schwinger-Keldysh contour is motivated by the observation that the expression for the expectation value of the evolution operator can be written as

$$\begin{aligned}\langle O(t) \rangle = \langle \Psi_0 | \tilde{T} \left\{ \exp\left[ -i \int_t^{t_0} dt' H'(t') \right] \right\} O(t) \\ \times T \left\{ \exp\left[ -i \int_{t_0}^{t} dt' H'(t') \right] \right\} |\Psi_0\rangle\end{aligned} \tag{A.25}$$

where we have set $\hbar = 1$ and defined $|\Psi_0\rangle = |\psi_I(t_0)\rangle$. Expanding the exponentials in powers of the Hamiltonian $H'(t')$,we see that a generic expansion consists of terms like

$$\tilde{T}\left\{H'(t_1)H'(t_2)\cdots H'(t_n)\right\} O(t) T\left\{H'(t'_1)H'(t'_2)\cdots H'(t'_m)\right\} \tag{A.26}$$

where we have all $\{t_i\}$ and $\{t'_j\}$ lie between $t_0, t$. This motivates the definition of the Keldysh contour

$$\gamma \equiv \underbrace{(t_0, t)}_{\gamma_+} \oplus \underbrace{(t, t_0)}_{\gamma_-} \tag{A.27}$$

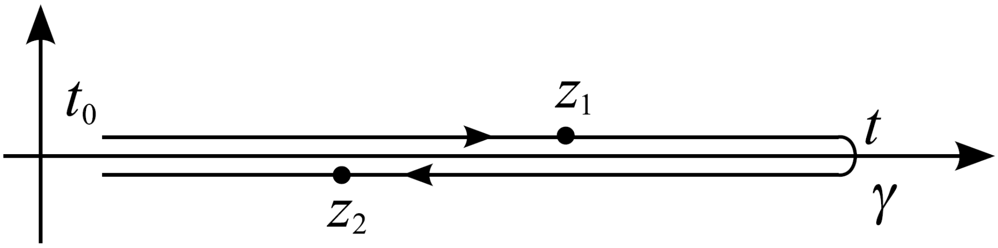

Figure A.1: The Schwinger-Keldysh contour $\gamma$ with the forward branch running from $t_0 \to t$ and the backward branch $t \to t_0$. Taken from G. Stefanucci and R. van Leeuwen's book[3]

which consists of two branches: the forward branch $\gamma_-$ which goes from $t_0$ to $t$ and the backward branch $\gamma_+$ which goes from $t$ to $t_0$. A generic point $z \in \gamma$ can lie on either branch and can assume a value between $t_0$ and $t$. This is illustrated in Fig. A.1 with two possible times $z_1, z_2$ on branches $\mp$ indicated. The operators at times on the contour can be written as

$$O(z') \equiv \begin{cases} O_-(t') & \text{if } z' = t'_- \in \gamma_- \\ O_+(t') & \text{if } z' = t'_+ \in \gamma_+ \end{cases} \tag{A.28}$$

Now that we have constructed the contour, we can define a contour ordering $\mathcal{T}$ such that $\mathcal{T}$ acts as a chronological time ordering on $\gamma_-$ and anti-chronological time ordering on $\gamma_+$. This also allows us to consider products of operators on the branches

$$\mathcal{T}[A(z_1)B(z_2)] = \begin{cases} T[A_-(t_1)B_-(t_2)] & \text{if } z_1 = t_{1-} \text{ and } z_2 = t_{2-} \\ A_-(t_1)B_+(t_2) & \text{if } z_1 = t_{1-} \text{ and } z_2 = t_{2+} \\ A_+(t_1)B_-(t_2) & \text{if } z_1 = t_{1+} \text{ and } z_2 = t_{2-} \\ \tilde{T}[A_+(t_1)B_+(t_2)] & \text{if } z_1 = t_{1+} \text{ and } z_2 = t_{2+} \end{cases} \tag{A.29}$$

While in general, the operators can have $O_+ \neq O_-$, for our purposes, we consider only the operators which are equal in both branches, and they equal the corresponding real-time argument. We can extend this to the case of definite integrals on the contour and the details can be found in G. Stefanucci and R. van Leeuwen's book[3]. The contour as it has been defined has a dependence on $t$, which does not allow for universal calculation. We can have a universal contour by extending $t \to \infty$.

Thus with this, we can now define the contour ordered Green's function

$$\mathcal{G}(z_1, z_2) = -i\langle \mathcal{T}[\psi(z_1)\psi^\dagger(z_2)]\rangle \tag{A.30}$$

which can be represented in terms of the grand canonical partition function as

$$\mathcal{G}(z_1, z_2) = \frac{-i\,\mathrm{Tr}\big[e^{-\beta(H-\mu N)}\mathcal{T}\{\psi(z_1)\psi^\dagger(z_2)\}\big]}{\mathrm{Tr}\big[e^{-\beta(H-\mu N)}\big]} \tag{A.31}$$

where $H = H_0 + V$ is the time independent interacting Hamiltonian. Using the expressions for the contour time ordering (eqn (A.29)) we have

$$\mathcal{G}[z_1, z_2] = \begin{cases} G^T(t_1, t_2) & \text{if } z_1 = t_{1-} \text{ and } z_2 = t_{2-} \\ G^<(t_1, t_2) & \text{if } z_1 = t_{1-} \text{ and } z_2 = t_{2+} \\ G^>(t_1, t_2) & \text{if } z_1 = t_{1+} \text{ and } z_2 = t_{2-} \\ G^{\tilde{T}}(t_1, t_2) & \text{if } z_1 = t_{1+} \text{ and } z_2 = t_{2+} \end{cases} \tag{A.32}$$

where we recall that the $<, >$ Green's functions are defined as

$$\begin{aligned} G^<(t, t') &= \mp\langle\psi^\dagger(t')\psi(t)\rangle \\ G^>(t, t') &= -i\langle\psi(t)\psi^\dagger(t')\rangle \end{aligned} \tag{A.33}$$

Since we have

$$\begin{aligned} G^T(t, t') &= -i\Theta(t - t')\langle\psi(t)\psi^\dagger(t')\rangle \mp i\Theta(t' - t)\langle\psi^\dagger(t')\psi(t)\rangle \\ G^{\tilde{T}}(t, t') &= -i\Theta(t' - t)\langle\psi(t)\psi^\dagger(t')\rangle \mp i\Theta(t - t')\langle\psi^\dagger(t')\psi(t)\rangle \end{aligned} \tag{A.34}$$

We see that $G^<(t, t') + G^>(t, t') = G^T(t, t') + G^{\tilde{T}}(t, t')$. Thus, only three out of the four Green's functions are independent. We can also define the retarded and advanced Green's functions

$$\begin{aligned} G^R(t, t') &= -i\Theta(t - t')\langle[\psi(t), \psi^\dagger(t')]_\mp\rangle = \Theta(t - t')[G^>(t, t') - G^<(t, t')] \\ G^A(t, t') &= i\Theta(t' - t)\langle[\psi(t), \psi^\dagger(t')]_\mp\rangle = \Theta(t - t')[-G^>(t, t') + G^<(t, t')] \end{aligned} \tag{A.35}$$

Switching to the Schwinger-Keldysh contour allows us to calculate the perturbation theory using Wick's theorem (see G. Stefanucci et al.[3] for details) and hence allow us to formulate many-body perturbation theory based methods. Another aspect is the introduction of the imaginary time Kadanoff-Baym[4] contour ($t_0 \in \gamma_-$ to $t_0 - i\beta$), which allows one to start from the non-interacting Green's functions and build in the interactions (see R. Jishi[2] and

G. Stefanucci's[3] books for a detailed treatment). The Gell-Mann Low theorem allows for an adiabatic switching on of the interaction, and hence we can consider the case where $t_0 \to -\infty$ and drop the imaginary time piece of the contour. This is the Keldysh contour and is defined to run from $(-\infty, \infty)$ in both directions.

Using this, the perturbation expansion of the contour ordered Green's functions can be written in the form of a Dyson equation given by

$$\begin{aligned} \mathcal{G}(z_1, z_2) = \mathcal{G}^0(z_1, z_2) &+ \int_\gamma dz' \mathcal{G}^0(z_1, z') U_{\text{ext}}(z') \mathcal{G}(z', z_2) \\ &+ \int_\gamma dz' \int_\gamma dz'' \mathcal{G}^0(z, z') \Sigma^*(z', z'') \mathcal{G}(z'', z_2) \end{aligned} \tag{A.36}$$

where $U_{\text{ext}}$ is the external potential giving rise to the time-dependent perturbation and $\Sigma^*$ is the self energy resulting from $V$, the interactions. We can write the Dyson equation in a compact notation as

$$\mathcal{G} = \mathcal{G}^0 + \mathcal{G}^0 U \mathcal{G} + \mathcal{G}^0 \Sigma^* \mathcal{G} \tag{A.37}$$

## A.3 Real time Green's functions

While we have seen the expansion for the contour ordered Green's function, it is imperative to calculate the real time Green's functions based on which other observables can be derived. An impediment to straightforward calculation of them are the convolutions like $\int dz' G_0(z_1, z') G_0(z', z_2)$ and the product terms like $G_0(z_1, z_2) G_0(z_2, z_1)$.

In order to handle such terms, we need to convert the contour integrals and the products into their real-time counterparts. These can be accomplished by using the Langreth rules[5] detailed below.

Consider a convolution of the form

$$C(z, z') = \int_\gamma A(z, z'') B(z'', z') dz'' \tag{A.38}$$

where $A, B, C$ are general operators on the Keldysh contour. We can look at the $<$ component

$$C^<(t, t') = C(t \in \gamma_-, t' \in \gamma_+) = \int_\gamma A(t \in \gamma_-, z'') B(z'', t' \in \gamma_+) dz'' \tag{A.39}$$

Since $z''$ can lie on either branch, we split the integral over the whole contour into two parts. Using the Keldysh contour and denoting $t \in \gamma_\pm = t_\pm$, we have

$$C^<(t,t') = \int_{-\infty}^{\infty} d(\tau_-)A(t_-,\tau_-)B(\tau_-,t'_+) + \int_{\infty}^{-\infty} d(\tau_+)A(t_-,\tau_+)B(\tau_+,t'_+) \tag{A.40}$$

Using the expressions eqn (A.29), we have

$$C^<(t,t') = \int_{-\infty}^{\infty} [A^T(t,\tau)B^<(\tau,t') - A^<(t,\tau)B^{\tilde{T}}(\tau,t')] \tag{A.41}$$

We can use the relations $A^T = A^< + A^R$ and $B^{\tilde{T}} = B^< - B^A$ to write

$$C^<(t,t') = \int_{-\infty}^{\infty} [A^R(t,\tau)B^<(\tau,t') - A^<(t,\tau)B^A(\tau,t')] \tag{A.42}$$

Similarly we have an expression for $C^>(t,t')$. Using the fact that $C^R(t,t') = \theta(t-t')[C^>(t,t') - C^<(t,t')]$ we can write the expression for $C^R(t,t')$ as

$$C^R(t,t') = \int_{-\infty}^{\infty} A^R(t,\tau)B^R(\tau,t')d\tau \tag{A.43}$$

and a similar expression for $C^A(t,t')$.

The product terms $C(z,z') = A(z,z')B(z',z)$ can be calculated using a similar approach and are given by

$$\begin{aligned} C^<(t,t') &= A^<(t,t')B^>(t',t) \\ C^>(t,t') &= A^>(t,t')B^<(t',t) \\ C^R(t,t') &= A^R(t,t')B^<(t',t) + A^<(t,t')B^A(t',t) \\ C^A(t,t') &= A^A(t,t')B^<(t',t) + A^<(t,t')B^R(t',t) \end{aligned} \tag{A.44}$$

Thus we can use the Langreth rules, which are collated in the Table A.1, to solve for the convolution and product terms in the perturbation series.

## A.4 Steady state Resonant Level Model

We now apply the Keldysh formalism introduced above to the case of the resonant level model with DC bias across the leads in the steady state as a pedagogical example. The Hamiltonian is given by

$$H = H_L + H_D + H_{\text{hyb}} \tag{A.45}$$

Table A.1: The Langreth rules

| Definition | $c(z,z') = \int_\gamma d\bar{z} a(z,\bar{z}) b(\bar{z},z')$ | $c(z,z') = a(z,z') b(z',z)$ |
|---|---|---|
| $k^>(t,t') = k(t_+,t_-)$ | $c^> = a^> b^A + a^R b^>$ | $c^> = a^> b^<$ |
| $k^<(t,t') = k(t_-,t_+)$ | $c^< = a^< b^A + a^R b^<$ | $c^< = a^< b^>$ |
| $k^R(t,t') = \theta(t-t')[k^>(t,t') - k^<(t,t')]$ | $c^R = a^R b^R$ | $c^R = a^R b^< + a^< b^A$ |
| $k^A(t,t') = -\theta(t'-t)[k^>(t,t') - k^<(t,t')]$ | $c^A = a^A b^A$ | $c^A = a^A b^< + a^< b^R$ |

where $H_L$ is the Hamiltonian of the leads, $H_D$ is the dot Hamiltonian and $H_{\text{hyb}}$ is the hybridisation term. These are given by

$$\begin{aligned} H_L &= \sum_{k\alpha=L,R,\sigma} \epsilon_{k\alpha\sigma} c^\dagger_{k\alpha\sigma} c_{k\alpha\sigma} \\ H_D &= \sum_\sigma \epsilon_d d^\dagger_\sigma d_\sigma \\ H_{\text{hyb}} &= \sum_{k\alpha\sigma} V_{k\alpha\sigma} c^\dagger_{k\alpha\sigma} d_\sigma + h.c. \end{aligned} \tag{A.46}$$

The expression for current from the left lead into the dot is given by

$$I_L = -e \left\langle \frac{dN_L}{dt} \right\rangle = \frac{ie}{\hbar} [N_L, H] \tag{A.47}$$

Since $N_L$ commutes with all the terms except $H_{\text{hyb}}$, we can calculate the commutator to write

$$I_L(t) = \frac{ie}{\hbar} \sum_{k\sigma} \Big[ V_{kL} n_{L\sigma} \langle c^\dagger_{kL\sigma}(t) d_\sigma(t) \rangle - h.c. \Big] \tag{A.48}$$

This can be simplified by defining the mixed Green's functions

$$\begin{aligned} G^<_{d,kL}(t,t';\sigma) &= i \langle c^\dagger_{kL\sigma}(t') d_\sigma(t) \rangle \\ G^<_{kL,d}(t,t';\sigma) &= i \langle d^\dagger_\sigma(t') c_{kL\sigma}(t) \rangle \end{aligned} \tag{A.49}$$

Substituting and simplifying allows us to write the expression for the current as

$$I_L = \frac{2e}{\hbar} \operatorname{Re} \Big[ \sum_{k\sigma} V_{kL} G^<_{d,kL}(t,t;\sigma) \Big] \tag{A.50}$$

In order to calculate the mixed Green's functions, we first calculate the contour Green's function $\mathcal{G}_{d,kL}(z,z';\sigma)$. This gives a Dyson like expression for the mixed Green's functions

$$\mathcal{G}_{d,kL}(z,z';\sigma) = \frac{1}{\hbar}\int_{\gamma} dz''\mathcal{G}_{d\sigma}(z,z'')V^{*}_{kL\sigma}\mathcal{G}^{0}_{kL\sigma}(z'',z') \tag{A.51}$$

where we have

$$\begin{aligned} \mathcal{G}^{0}_{kL\sigma}(z,z') &= -i\langle\mathcal{T}[c_{kL\sigma}(z)c^{\dagger}_{kL\sigma}(z')]\rangle \\ \mathcal{G}_{d\sigma}(z,z') &= -i\langle\mathcal{T}[d_{\sigma}(z)d^{\dagger}_{\sigma}(z')]\rangle \end{aligned} \tag{A.52}$$

We now apply the Langreth rules to get the mixed Green's function required to calculate the current

$$\begin{aligned} G^{<}_{d,kL}(t,t';\sigma) = \frac{1}{\hbar}\int_{-\infty}^{\infty} dt''[&G^{R}_{d\sigma}(t,t')G^{0<}_{kL\sigma}(t'',t') \\ &+ G^{<}_{d\sigma}(t,t'')G^{0A}_{kL\sigma}(t'',t')]V^{*}_{kL} \end{aligned} \tag{A.53}$$

Since we are looking at the steady-state case, the Green's functions depend only on the time difference and we can apply the Fourier transform

$$G^{()}_{()}(t,t') = G^{()}_{()}(t-t') = \frac{1}{2\pi}\int_{-\infty}^{\infty} d\omega G^{()}_{()}(\omega)e^{-i\omega(t-t')} \tag{A.54}$$

for the various terms. Using the relation $\int_{-\infty}^{\infty} dte^{i(\omega-\omega')t} = 2\pi\delta(\omega-\omega')$ and substituting the expression for $G^{<}_{d,kL}(\omega)$ in the eqn (A.50), we get

$$I_L = \frac{e^2}{\pi\hbar^2}\int_{-\infty}^{\infty} d\omega\,\mathrm{Re}\left\{\sum_{kL\sigma}|V_{kL}|^2[G^{R}_{d\sigma}(\omega)G^{0<}_{kL\sigma}(\omega) + G^{<}_{d\sigma}(\omega)G^{0A}_{kL\sigma}(\omega)]\right\} \tag{A.55}$$

The lead Green's functions are given by

$$\begin{aligned} G^{0<}_{kL\sigma}(\omega) &= 2\pi i f_L(\omega)\delta(\omega-\epsilon_{kL\sigma}/\hbar) \\ G^{0A}_{kL\sigma}(\omega) &= (\omega^{+}-\epsilon_{kL\sigma}/\hbar)^{-1} \end{aligned} \tag{A.56}$$

where $f_L(\omega)$ is the Fermi function in the left lead. Substituting this in the current gives the expression

$$I_L = \frac{ie}{2\pi\hbar}\sum_{\sigma}\int_{-\infty}^{\infty} d\omega\,\mathrm{Tr}\big\{\Gamma_{L\sigma}(\omega)\left[f_L(\omega)\left(G^{R}_{d\sigma}(\omega)-G^{A}_{d\sigma}(\omega)\right)+G^{<}_{d\sigma}(\omega)\right]\big\} \tag{A.57}$$

where the hybridisation function $\Gamma_{L\sigma} = \frac{2\pi}{\hbar}\sum_k |V_{kL}|^2\delta(\omega-\epsilon_{kL\sigma})$.

For the resonant level model, we have $U = 0$ and the self energy is given by

$$\Sigma^{<}(\omega) = \frac{i}{\hbar}(f_L \Gamma^L + f_R \Gamma^R) \tag{A.58}$$

Therefore, substituting we get the symmetrised current

$$I = \frac{e}{2\pi\hbar^2} \int_{-\infty}^{\infty} d\omega [f_L(\omega) - f_R(\omega)] T(\omega) \tag{A.59}$$

where $T(\omega) = \sum_\sigma \mathrm{Tr}\left\{\Gamma_{L\sigma} G^R_{d\sigma}(\omega) \Gamma_{R\sigma} G^A_{d\sigma}\right\}$, is the transmission probability. We see that the Landauer formula[6] for the current is recovered.

# Bibliography

[1] L. V. Keldysh *et al.*, Sov. Phys. JETP **20**, 1018 (1965).

[2] R. A. Jishi, *Feynman diagram techniques in condensed matter physics* (Cambridge University Press, 2013).

[3] G. Stefanucci and R. van Leeuwen, *Nonequilibrium Many-Body Theory of Quantum Systems: A Modern Introduction* (Cambridge University Press, 2013).

[4] L. P. Kadanoff, *Quantum statistical mechanics* (CRC Press, 2018).

[5] D. C. Langreth *et al.*, "Linear and nonlinear electron transport in solids," (1976).

[6] R. Landauer, IBM Journal of Research and Development **1**, 223 (1957).

# Appendix B

# Second order perturbation theory for the SIAM coupled to chiral leads with DC bias

In this appendix chapter, we look at the system studied in chapters 2 and 3, which is a single impurity Anderson model connected to leads with spin-orbit coupling and subject to a DC bias. The Keldysh second order perturbation theory (KPT2) forms the basis of the methods used in both these chapters and will be dealt with in detail here.

## B.1 Hamiltonian

We consider a quantum dot system connected to two 2D leads with SOC, for which the Hamiltonian, $H$, is given in standard notation as

$$H = H_0 + H_{\mathrm{d}} + H_{\mathrm{SO}} + H_{\mathrm{hyb}}\,, \tag{B.1}$$

where, the two-dimensional conduction band reservoir is represented by

$$H_0 = \sum_{\alpha\mathbf{k}\sigma} \epsilon_{\mathbf{k}} c^{\dagger}_{\alpha\mathbf{k}\sigma} c_{\alpha\mathbf{k}\sigma} \tag{B.2}$$

and the isolated quantum dot is given by

$$H_{\mathrm{d}} = \sum_{\sigma} (\epsilon_d) d^{\dagger}_{\sigma} d_{\sigma} + U n_{d\uparrow} n_{d\downarrow}. \tag{B.3}$$

The Rashba spin-orbit interaction in the two-dimensional conduction band may be described as

$$H_{\mathrm{SO}} = \sum_{\alpha\mathbf{k}} \lambda \psi^{\dagger}_{\alpha\mathbf{k}} (\mathbf{k} \times \vec{\sigma})_z \psi_{\alpha\mathbf{k}}\,, \tag{B.4}$$

where $\mathbf{k} = (k_x, k_y)$, and $\psi^\dagger_{\alpha\mathbf{k}} = (c^\dagger_{\alpha\mathbf{k},\sigma}\ c^\dagger_{\alpha\mathbf{k},\bar{\sigma}})$. Finally the hybridization between the quantum dot and the conduction band is given by

$$H_{\text{hyb}} = \sum_{\alpha\mathbf{k}\sigma} \left( V_{\mathbf{k}} c^\dagger_{\alpha\mathbf{k}\sigma} d_\sigma + \text{h.c} \right) . \tag{B.5}$$

The conduction band terms, namely $H_0$ and $H_{\text{SO}}$ may be combined and simplified using the angular momentum expansion for the conduction band operators as[1]:

$$c_{\mathbf{k}\sigma} = c_{k_x k_y \sigma} = \frac{1}{\sqrt{2\pi k}} \sum_{m=-\infty}^{\infty} c_{km\sigma} \exp(im\theta_{\mathbf{k}}) , \tag{B.6}$$

where $k = |\mathbf{k}|$. The inverse transform is defined as $c_{km\sigma} = \sqrt{\frac{k}{2\pi}} \int_0^{2\pi} d\theta_{\mathbf{k}} c_{\mathbf{k}\sigma} e^{-im\theta_{\mathbf{k}}}$ Substituting the above expansion (equation B.6) into the Hamiltonian, and assuming an isotropic dispersion, such as $\epsilon_{\mathbf{k}} = \hbar^2 k^2/2m$, the following form of the Hamiltonian is obtained:

$$\begin{aligned} H = &\sum_{khm} \epsilon_{kh} (c_{kh}^{m+\frac{1}{2}})^\dagger c_{kh}^{m+\frac{1}{2}} \\ &+ \sum_{khm} \delta_{m,0} \tilde{V}_k \left( (c_{kh}^{m+\frac{1}{2}})^\dagger d_\uparrow + h (c_{kh}^{m-\frac{1}{2}})^\dagger d_\downarrow + \text{h.c} \right) \\ &+ H_{\text{d}} , \end{aligned} \tag{B.7}$$

where $h = \pm 1$ is an emergent chiral quantum number, and $j_m = m + h/2$ is the angular momentum quantum number. Thus, the system can be thought of as a quantum dot coupled to emergent chiral leads with a DC bias between them.

The dispersion, now depends on $h$ and the spin-orbit interaction, $\lambda$ as $\epsilon_{kh} = (\epsilon_k + h\lambda k)/k = \tilde{\epsilon}_k + h\lambda$. Hence the SOC introduces a Zeeman-type splitting of the conduction band.

The hybridization matrix elements are assumed to be isotropic, i.e $V_{\mathbf{k}} = V_k$, and $\tilde{V}_k = V_k \sqrt{\frac{2\pi}{k}}$, with $V_k \in \mathbb{R}$. The above expression shows that the bands with $j_m = \pm 1/2$ couple to the dot, while the rest are decoupled and do not affect the dot dynamics at all. Thus, we rewrite the Hamiltonian, with only those bands that couple to the dot to highlight this aspect. In order to study the interplay between the SO and a D.C. bias, we consider two copies of the conduction bath acting as a left and right lead with a common $\pm\mu$ chemical potential applied to all the emergent $h, j_m$ channels in each lead. This leads to the Hamiltonian

$$H_{\text{eff}} = \sum_{\alpha=L,R} \tilde{H}_\alpha + \tilde{H}_{\text{hyb}} + H_{\text{dot}} \tag{B.8}$$

Where we have

$$\begin{aligned}\tilde{H}_\alpha &= \sum_{khj_m} (\epsilon_{kh}) c^\dagger_{\alpha khj_m} c_{\alpha khj_m} \\ \tilde{H}_{hyb} &= \sum_{\alpha kh} \tilde{V}_{k\alpha} \left[ (c^\dagger_{\alpha kh \frac{+1}{2}} d_\uparrow + h.c.) + h(c^\dagger_{\alpha kh \frac{-1}{2}} d_\downarrow + h.c.) \right]\end{aligned} \tag{B.9}$$

and

$$H_{dot} = \sum_\sigma (\epsilon_d - \bar{\mu_0}) n_\sigma + U n_\uparrow n_\downarrow \tag{B.10}$$

To simplify the notation, we define $\epsilon_{k\alpha h} = \epsilon_{kh} + \mu_\alpha$.

## B.2 Current

The central quantity to be calculated in order to study transport is the current. This can be calculated by using the Meir-Wingreen formula[2]

$$j_\alpha = \frac{2e}{\hbar} \int \frac{d\omega}{2\pi} \operatorname{Re} \left\{ \sum_{(khj_m)(d\sigma)} \tilde{V}^2_{k\alpha} [G^r_{d\sigma}(\omega) g^<_{k\alpha hj_m}(\omega) + G^<_{d\sigma}(\omega) g^a_{k\alpha hj_m}(\omega)] \right\} \tag{B.11}$$

Where the $G^{r/<}_{d\sigma}$ are the retarded and lesser than interacting Green's functions of the dot and the $g^{</a}_{k\alpha hj_m}$ are the free lesser than and advanced Green's functions of the leads defined as

$$\begin{aligned} G^r_{d\sigma}(t,t') &= -\imath\Theta(t-t')\langle\{d_\sigma(t), d^\dagger_\sigma(t')\}\rangle \\ G^<_{d\sigma}(t,t') &= \imath\langle d^\dagger_\sigma(t') d_\sigma(t)\rangle \\ g^a_{k\alpha hj_m}(t,t') &= \imath\Theta(t'-t)\langle\{c_{k\alpha hj_m}(t), c^\dagger_{k\alpha hj_m}(t')\}\rangle \\ g^<_{k\alpha hj_m}(t,t') &= \imath\langle c^\dagger_{k\alpha hj_m}(t') c_{k\alpha hj_m}(t)\rangle \end{aligned} \tag{B.12}$$

The lead Green's functions can be exactly calculated using the equation of motion approach

$$\begin{aligned} g^<_{k\alpha hj_m}(t,t') &= \imath f_\alpha(\epsilon_{khj_m}) \exp\{[-\imath\epsilon_{khj_m}(t-t')]\} \\ g^{a,r}_{k\alpha hj_m}(t,t') &= \pm\imath\Theta(\mp t \pm t') \exp\{[-\imath\epsilon_{khj_m}(t-t')]\} \end{aligned} \tag{B.13}$$

Since we are studying the steady-state regime, we can Fourier transform into frequency space to get

$$\begin{aligned} g^<_{k\alpha hj_m}(\omega) &= 2\pi\imath f_\alpha(\epsilon_{khj_m}) \delta(\omega - \epsilon_{khj_m}) \\ g^{a,r}_{k\alpha hj_m}(\omega) &= \frac{1}{\omega^\mp - \epsilon_{khj_m}} \end{aligned} \tag{B.14}$$

From this we see $g^r(\omega) = [g^a(\omega)]^*$ and $g^<(\omega)$ is purely imaginary. These observations also hold true for the dot Green's functions. Since we can write for any complex number $z \in \mathbb{C}$, $\mathrm{Re}\{z\} = \frac{z+z*}{2}$, we can rewrite eqn (B.11) as

$$j_\alpha = \frac{e}{\hbar} \int \frac{d\omega}{2\pi} \sum_{(khj_m)(d\sigma)} \tilde{V}^2_{k\alpha} \Big\{ [G^r_{d\sigma}(\omega) g^<_{k\alpha hj_m}(\omega) + G^<_{d\sigma}(\omega) g^a_{k\alpha hj_m}(\omega)] - [G^a_{d\sigma}(\omega) g^<_{k\alpha hj_m}(\omega) + G^<_{d\sigma}(\omega) g^r_{k\alpha hj_m}(\omega)] \Big\} \tag{B.15}$$

Which can be simplified to get

$$j_\alpha = \frac{e}{\hbar} \int \frac{d\omega}{2\pi} \sum_{(khj_m)(d\sigma)} \tilde{V}^2_{k\alpha} \Big\{ [G^r_{d\sigma}(\omega) - G^a_{d\sigma}(\omega)] g^<_{k\alpha hj_m}(\omega) + G^<_{d\sigma}(\omega) [g^a_{k\alpha hj_m}(\omega) - g^r_{k\alpha hj_m}(\omega)] \Big\}. \tag{B.16}$$

We now define the hybridisation function,

$$\Gamma_\alpha(\omega) = \sum_{khj_m} \frac{\tilde{V}^2_{k\alpha}}{\omega^+ - \epsilon_{k\alpha hj_m}} \equiv E_\alpha(\omega) - \imath\Delta_\alpha(\omega) \tag{B.17}$$

$$\Delta_\alpha(\omega) = 2\pi \sum_{khj_m} \tilde{V}^2_{k\alpha} \delta(\omega - \epsilon_{k\alpha hj_m}) \tag{B.18}$$

From eqn (B.14), we see that $g^a_{k\alpha hj_m}(\omega) - g^r_{k\alpha hj_m}(\omega) = 2\pi\imath\delta(\omega - \epsilon_{k\alpha hj_m})$. This allows us to recast the current expression in terms of the hybridisation function as

$$j_\alpha = \frac{e}{\hbar} \int \frac{d\omega}{2\pi} \imath\Delta_\alpha(\omega) \sum_{d\sigma} \Big\{ [G^r_{d\sigma}(\omega) - G^a_{d\sigma}(\omega)] f_\alpha(\omega) + G^<_{d\sigma}(\omega) \Big\} \tag{B.19}$$

Substituting this and using the $G^r = (G^a)^*$ property of Green's functions, gives us the equation of the current which we implement

$$j_\alpha = \frac{2\imath e}{h} \int d\omega \Delta_\alpha(\omega) [G^<_{d\sigma}(\omega) + 2\imath f_\alpha(\omega) \,\mathrm{Im}\{G^r_{d\sigma}(\omega)\}] \tag{B.20}$$

In order to be able to calculate the current, it is apparent that we need a way of calculating the interacting dot's Green's functions $G^{<,r}_{d\sigma}(\omega)$ and the hybridisation function $\Gamma_\alpha(\omega)$. The calculation of these two quantities is given in the following sections

## B.3 Dot Green's functions

The full Green's functions include the interaction on the dot and can be treated via a self energy. The Keldysh formalism (see appendix A for a detailed treatment) allows us to make use of the matrix Dyson equation

$$\begin{aligned}\boldsymbol{G} = \begin{pmatrix} 0 & G^a_d \\ G^r_d & 2G^<_d + G^r - G^a \end{pmatrix} = \\ \begin{pmatrix} 0 & g^a_d \\ g^r_d & 2g^<_d + g^r - g^a \end{pmatrix} + \boldsymbol{g} \begin{pmatrix} \Sigma^r - \Sigma^a - 2\Sigma^< & \Sigma^r \\ \Sigma^a & 0 \end{pmatrix} \boldsymbol{G} \\ = \boldsymbol{g} + \boldsymbol{g}\boldsymbol{\Sigma}\boldsymbol{G} \end{aligned} \tag{B.21}$$

Where the upper/lower case G stand for the interacting and free Green's functions respectively and $\Sigma$ is the self-energy. Since the advanced and retarded Green's functions are conjugates of each other, the independent quantities are only the retarded and lesser than Green's functions.

One can calculate the free Green's functions using the equation of motion technique (EOM) with $U = 0$ in the Hamiltonian. In the frequency domain, we have the expressions for a general dot Green's function $G^{r/<}_{AB} = \langle\langle A : B\rangle\rangle^{r/<}$ in the Zubarev[3] notation from Niu et al[4].

$$\begin{aligned} \langle\langle A : B\rangle\rangle^r_\omega &= \mathrm{g}^r_0\langle\{A, B\}\rangle + \mathrm{g}^r_0\langle\langle[A, H_{\mathrm{int}}] : B\rangle\rangle^r_\omega \\ \langle\langle A : B\rangle\rangle^<_\omega &= \mathrm{g}^<_0(\omega)\langle\{A, B\}\rangle + \mathrm{g}^r_0(\omega)\langle\langle[A, H_{\mathrm{int}}] : B\rangle\rangle^<_\omega \\ &\quad + \mathrm{g}^<_0(\omega)\langle\langle[A, H_{\mathrm{int}}] : B\rangle\rangle^a_\omega \end{aligned} \tag{B.22}$$

Where the $\mathrm{g}^{r,<}_0$ are the retarded and lesser than Green's functions of the non-interacting uncoupled dot and $H_{\mathrm{int}}$ is the coupling and interaction parts of the Hamiltonian.

The $\mathrm{g}^{r,<}_0$ can be calculated by using the EOM on the Hamiltonian $H_{\mathrm{dot}} = \sum_\sigma(\epsilon_d - \bar{\mu}_0)d^\dagger_\sigma d_\sigma$. This gives us

$$\mathrm{g}^r_0(\omega) = \frac{1}{\omega^+ - \epsilon_d + \bar{\mu}_0} \tag{B.23}$$

$$\mathrm{g}^<_0(\omega) = 2\pi\imath f(\omega)\delta(\omega - \epsilon_d + \bar{\mu}_0) \tag{B.24}$$

Since we are working with a non-interacting dot, $H_{\mathrm{int}} = \tilde{H}_{hyb}$. Using the retarded part of equation (B.22) in order to calculate the free dot retarded Green's function, we have

$$\langle\langle d_\sigma : d^\dagger_\sigma\rangle\rangle^r_\omega = (\omega^+ - \epsilon_d + \bar{\mu}_0)^{-1}[\{d_\sigma, d^\dagger_\sigma\} + \langle\langle[d_\sigma, \tilde{H}_{hyb}] : d^\dagger_\sigma\rangle\rangle^r] \tag{B.25}$$

which for the up and down spins gives

$$\begin{aligned}(\omega^+ - \epsilon_d + \bar{\mu}_0) g^r_{d\uparrow}(\omega) &= 1 + \sum_{k\alpha h} \tilde{V}_k \left( g^r_{(k\alpha h)(d\uparrow)}(\omega) \right) \\ (\omega^+ - \epsilon_d + \bar{\mu}_0) g^r_{d\downarrow}(\omega) &= 1 + \sum_{k\alpha h} h\tilde{V}_k \left( g^r_{(k\alpha h)(d\downarrow)}(\omega) \right)\end{aligned} \tag{B.26}$$

Where the mixed Green's functions $g^r_{(k\alpha h)(d\sigma)}$ are calculated recursively as follows

$$\begin{aligned}(\omega^+ - \epsilon_{k\alpha h}) g^r_{(k\alpha h)(d\uparrow)}(\omega) &= \tilde{V}_k \left( g^r_{d\uparrow}(\omega) \right) \\ (\omega^+ - \epsilon_{k\alpha h}) g^r_{(k\alpha h)(d\downarrow)}(\omega) &= h\tilde{V}_k \left( g^r_{d\downarrow}(\omega) \right)\end{aligned} \tag{B.27}$$

Which when substituted gives the expression for the dot Green's function

$$(g^r_{d\sigma}(\omega))^{-1} = \omega^+ - \epsilon_d + \bar{\mu}_0 - \sum_{k\alpha h} \frac{|\tilde{V}_{k\alpha}|^2}{\omega^+ - \epsilon_{k\alpha h}} \tag{B.28}$$

Similarly one can do the calculation for the lesser than Green's function to get the expressions

$$\begin{aligned}\langle\langle d_\sigma : d^\dagger_\sigma \rangle\rangle^<_\omega = 2\pi\imath f(\omega)\delta(\omega - \epsilon_d + \bar{\mu}_0)\{d_\sigma, d^\dagger_\sigma\} \\ + (\omega^+ - \epsilon_d + \bar{\mu}_0)^{-1} \langle\langle [d_\sigma, \tilde{H}_{hyb}] : d^\dagger_\sigma \rangle\rangle^< \\ + 2\pi\imath f(\omega)\delta(\omega - \epsilon_d + \bar{\mu}_0) \langle\langle [d_\sigma, \tilde{H}_{hyb}] : d^\dagger_\sigma \rangle\rangle^a\end{aligned} \tag{B.29}$$

Using the mixed Green's functions $g^{a/<}_{(k\alpha h)(d\sigma)}$ and calculating recursively as done for the retarded case gives

$$\begin{aligned}[g^r_{d\sigma}(\omega)]^{-1} &= \omega^+ - \epsilon_d + \bar{\mu}_0 - \sum_\alpha \Gamma_\alpha(\omega) \\ g^<_{d\sigma}(\omega) &= 2\imath |g^r_{d\sigma}(\omega)|^2 \sum_\alpha \Delta_\alpha(\omega) f(\omega - \mu_\alpha)\end{aligned} \tag{B.30}$$

Where we have used the hybridisation function

$$\begin{aligned}\Gamma_\alpha(\omega) &= \sum_{kh} \frac{V^2_{k\alpha}}{\omega^+ - \epsilon_{k\alpha h}} \\ \Delta_\alpha(\omega) &= 2\pi \sum_{kh} \tilde{V}^2_{k\alpha} \delta(\omega - \epsilon_{k\alpha h})\end{aligned} \tag{B.31}$$

In order to calculate the full interacting Green's functions, we can use the properties $[G^r]* = G^a, [\Sigma^r]^* = \Sigma^a$ to reduce the matrix Dyson equation (eqn

(B.21)) to two Dyson equations, one for the retarded and the lesser than Green's functions given by

$$[G_d^r(\omega)]^{-1} = [g_d^r(\omega)]^{-1} - \Sigma^r(\omega) \tag{B.32}$$

$$G_d^<(\omega) = |G_d^r(\omega)|^2 \left( \frac{g_d^<(\omega)}{|g_d^r(\omega)|^2} - \Sigma^<(\omega) \right) \tag{B.33}$$

## B.4 Hybridization

The effect of coupling the dot to the leads is given by the hybridisation function, which can be written as

$$\begin{aligned} \Gamma_\alpha(\omega) &= \sum_{kh} \frac{\tilde{V}_k^2}{\omega^+ - \epsilon_{k\alpha h}} \\ &= \sum_k \tilde{V}_k^2 \left[ \frac{1}{\omega^+ - \tilde{\epsilon}_{k\alpha} + \lambda} + \frac{1}{\omega^+ - \tilde{\epsilon}_{k\alpha} - \lambda} \right] \\ &= \sum_h \Gamma_{h\alpha}(\omega)\,. \end{aligned} \tag{B.34}$$

We can see from the above expression that the hybridisation depends crucially on the dispersion of the leads. A simple choice would be to work with a uniform flat band dispersion would correspond to

$$\Gamma_\alpha = i\frac{\Delta_0}{2} \tag{B.35}$$

where $\Delta_0$ is the constant parameter. But, this choice removes the effect of bias on the hybridisation and would be less interesting than the finite bandwidth case. This led us to consider a Gaussian density of states for the leads which can be thought of as an abstraction of the hybridising lead orbitals. We also work with a free electron like dispersion, which gives us

$$\tilde{V}_k = \frac{V}{\sqrt{k}} e^{-\chi(k-k_F)^2/2} \tag{B.36}$$

$$\tilde{\epsilon}_k = \frac{\epsilon}{k} = ak \tag{B.37}$$

$$\tilde{\epsilon}_{k\alpha} = ak + \mu_\alpha \tag{B.38}$$

Where $a, \chi$ are undetermined constants and $k_F$ is the Fermi momentum. Substituting these in the expression for hybridisation, we have

$$\Gamma_\alpha(\omega) = \sum_{kh} \frac{V^2 e^{-\chi(k-k_F)^2}}{k(\omega^+ + \mu^0 - (ak + \mu_\alpha) + h\lambda)} \tag{B.39}$$

$$\Gamma_\alpha(\omega) = \sum_{h} \frac{L^2}{(2\pi)^2} \int_0^\infty 2\pi k dk \frac{V^2 e^{-\chi(k-k_F)^2}}{k(\omega^+ + \mu^0 - (ak + \mu_\alpha) + h\lambda)} \tag{B.40}$$

By changing variables $a\bar{k} = k - k_F$ and choosing the lattice reference energy $\mu^0 = ak_F$, we can write

$$\Gamma_\alpha(\omega) = \sum_{h} \frac{L^2 V^2}{2\pi} \int_{-ak_F}^\infty \left(\frac{dx}{a}\right) \frac{e^{-\chi(x/a)^2}}{\omega^+ - \mu_\alpha + h\lambda - x} \tag{B.41}$$

Where $L$ is the corresponding length. Denoting the coefficients $a, \chi$ via an effective hopping by $a = \sqrt{2\chi} t_*$, we have

$$\Gamma_\alpha(\omega) = \sum_{h} \frac{L^2 V^2}{\sqrt{2\chi}} \frac{1}{2\pi t_*} \int_{-t_* 2\pi k_F}^\infty dx \frac{e^{-x^2/2t_*^2}}{\omega^+ - \mu_\alpha + h\lambda - x} \tag{B.42}$$

Since $\sqrt{\chi} k_F \gg 1$, the exponential ensures negligible contribution at large negative values of $x$ and allows us to take the lower limit of the integral to $-\infty$. Representing the numerical coefficient $\frac{L^2 V^2}{\sqrt{2\chi}} = V_0^2$, we can write

$$\Gamma_\alpha(\omega) = \sum_{h} V_0^2 \frac{1}{2\pi t_*} \int_{-\infty}^\infty dx \frac{e^{-x^2/2t_*^2}}{\omega^+ - \mu_\alpha + h\lambda - x} \tag{B.43}$$

Which can be calculated as a Hilbert Transform $\mathcal{H}(z)$ which is defined as follows

$$\Gamma_\alpha(\omega) = \sum_{h} V_0^2 \mathcal{H}(z_h) \tag{B.44}$$

$$z_h = \omega^+ - \mu_\alpha + h\lambda \tag{B.45}$$

$$\mathcal{H}(z_h) = \int dx \left(\frac{\rho_0(x)}{z_h - x}\right) \tag{B.46}$$

$$\rho_0(x) = \frac{1}{2\pi t_*} e^{-x^2/2t_*^2} \tag{B.47}$$

Where we have $\rho_0$ being the Gaussian density of states

## B.5 Self Energy

The most important ingredient needed to calculate the current is the self energy which can be used in the Dyson equations to calculate the interacting dot Green's functions. We calculate the self-energy upto second order, which forms the basis for the calculations in chapters 2 and 3. We recall from eqn (B.32) that the Dyson's equations are

$$\begin{aligned}[G_d^r(\omega)]^{-1} &= [g_d^r(\omega)]^{-1} - \Sigma^r(\omega) \\ G_d^<(\omega) &= |G_d^r(\omega)|^2\left(\frac{g_d^<(\omega)}{|g_d^r(\omega)|^2} - \Sigma^<(\omega)\right)\end{aligned} \tag{B.48}$$

where the free Green's functions $g_d^{r,<}(\omega)$ are given by

$$\begin{aligned}[g_{d\sigma}^r(\omega)]^{-1} &= \omega + \bar{\mu}_0 - \sum_\alpha \Gamma_\alpha(\omega) \\ g_{d\sigma}^<(\omega) &= 2\imath|g_{d\sigma}^r(\omega)|^2 \sum_\alpha \Delta_\alpha(\omega) f(\omega - \mu_\alpha)\end{aligned} \tag{B.49}$$

We can write the dot energy as $\epsilon_d - \bar{\mu}_0 = E_d + \varepsilon_{eff}$ where $E_d = -U/2 + \frac{1}{2}\sum_\alpha \mu_\alpha$, which is the dot energy corresponding to the particle hole symmetric limit in equilibrium and an arbitrary constant $\varepsilon_{eff}$ which is used for the perturbation. Recasting the equations in terms of $\varepsilon_{eff}$, we get

$$\begin{aligned}[g_{d\sigma}^r(\omega)]^{-1} &= \omega - E_d - \varepsilon_{eff} - \sum_\alpha \Gamma_\alpha(\omega) \\ g_{d\sigma}^<(\omega) &= 2\imath|g_{d\sigma}^r(\omega)|^2 \sum_\alpha \Delta_\alpha(\omega) f(\omega - \mu_\alpha)\end{aligned} \tag{B.50}$$

### B.5.1 First order perturbation

We begin with the first order perturbation in interaction. This gives us

$$\Sigma^{r1}(\omega) = E_d - \varepsilon_{eff} + U\langle n_d \rangle \tag{B.51}$$

$$\Sigma^{<1}(\omega) = 0 \tag{B.52}$$

Where the $\Sigma^{r,<1}$ are the first order self energies corresponding to the retarded and lesser than Green's functions and $\langle n_d \rangle$ is the average dot occupation given by the expression

$$\begin{aligned}\langle n_d^0 \rangle &= \frac{1}{2\pi}\int d\omega\, \mathrm{Im}\{g_d^<(\omega)\} \\ \langle n_d \rangle &= \frac{1}{2\pi}\int d\omega\, \mathrm{Im}\{G_d^<(\omega)\}.\end{aligned} \tag{B.53}$$

The $\langle n_d^0 \rangle$ calculated from the free Green's functions corresponds to the Hartree-Fock term. The $\langle n_d \rangle$ uses the interacting Green's functions and is evaluated self-consistently.

### B.5.2 Second order perturbation

In order to simplify the calculation of the second order perturbation, we switch to the density of states representation

$$g_d^r(\omega) = \int d\epsilon \frac{\rho^0(\epsilon)}{\omega^+ - \epsilon} \tag{B.54}$$

$$g_d^<(\omega) = 2\imath\pi\rho^0(\omega)\tilde{f}(\omega) \tag{B.55}$$

Where we have $\rho^0(\omega) = -1/\pi \, \mathrm{Im}\{g_d^r(\omega)\}$ and the weighted Fermi function is given by

$$\tilde{f}(\omega) = \frac{\Delta_L(\omega) f(\omega - \mu_L) + \Delta_R(\omega) f(\omega - \mu_R)}{\Delta_L(\omega) + \Delta_R(\omega)} \tag{B.56}$$

With this, we can evaluate the second order perturbative terms to be

$$\Sigma^{r2}(\omega) = U^2 \int d\epsilon_1 d\epsilon_2 d\epsilon_3 \frac{\rho^0(\epsilon_1)\rho^0(\epsilon_2)\rho^0(\epsilon_3)}{\omega^+ + \epsilon_3 - \epsilon_2 - \epsilon_1} \times [\tilde{f}(-\epsilon_1)\tilde{f}(-\epsilon_2)\tilde{f}(\epsilon_3) + \tilde{f}(\epsilon_1)\tilde{f}(\epsilon_2)\tilde{f}(-\epsilon_3)] \tag{B.57}$$

and

$$\Sigma^{<2}(\omega) = -2\imath\pi U^2 \int d\epsilon_1 d\epsilon_2 \rho^0(\epsilon_1)\rho^0(\epsilon_2)\rho^0(\epsilon_1 + \epsilon_2 - \omega) \times [\tilde{f}(\epsilon_1)\tilde{f}(\epsilon_2)\tilde{f}(\omega - \epsilon_1 - \epsilon_2)] \tag{B.58}$$

where we have used the identity $1 - f(\epsilon) = f(-\epsilon)$. These are the required KPT2 self-energies.

# Bibliography

[1] M. Zarea, S. E. Ulloa, and N. Sandler, Phys. Rev. Lett. **108**, 046601 (2012).

[2] Y. Meir and N. S. Wingreen, Phys. Rev. Lett. **68**, 2512 (1992).

[3] D. N. Zubarev, Soviet Physics Uspekhi **3**, 320 (1960).

[4] C. Niu, D. L. Lin, and T.-H. Lin, Journal of Physics: Condensed Matter **11**, 1511 (1999).